

Towards a combined estimation of Greenland's ice sheet mass balance using GRACE and ICESat data

MSc. Geomatics

Thesis



Delft University of Technology

Cornelis Slobbe
October 2007

Mathematical Geodesy and Positioning & Physical and Space Geodesy
Department of Earth Observation and Space Systems (DEOS)
Faculty of Aerospace Engineering, Delft University of Technology

Cover: Artists impressions of both GRACE and ICESat satellites (up). East Greenland (below) photo taken by Christian Morel

Graduation Professor: prof. dr.-ing. habil. R. Klees
Delft Supervisor (GRACE): dr. P.G. Ditmar
Delft Supervisor (ICESat): dr. R.C. Lindenberg
Co-reader: dr. L.L.A. Vermeersen

Abstract

The Greenland ice sheet is sensitive to climate change. Global heating is expected to result in ice mass losses that will contribute to global sea level rise. For this reason monitoring Greenland's ice mass balance is of utmost importance.

Data of both the Ice, Cloud, and land Elevation Satellite (ICESat) laser altimetry mission and the Gravity Recovery and Climate Experiment (GRACE) gravity mission are used to create two independent estimates of Greenland's ice sheet mass balance over the full measurement period of about 2003 until 2007.

For ICESat data, a processing strategy is developed that uses the elevation differences of geometrically overlapping footprints of both crossing and repeated tracks. The dataset is cleaned using quality flags defined by the Geoscience Laser Altimeter System (GLAS) science team. (The GLAS is the sole scientific instrument on ICESat). The cleaned dataset reveals some strong, spatially correlated signals that are shown to be related to physical phenomena like melting glaciers. On the other hand, strong correlation is also visible between the observed elevation differences and the combined effect of roughness and surface slope.

Different processing strategies applied to different sets of laser campaigns are used to convert the observed temporal elevation differences to mass changes for 6 different drainage systems, further divided into a region above and below 2000 meter elevation. Here all available laser campaigns are used and outliers are removed using N-sigma thresholding. Both a uniform and non-uniform weighting scheme, used to estimate the elevation changes with respect to a reference epoch, is evaluated. The non-uniform weighting scheme is developed to account for the influence of roughness and surface slope, but it turns out that also signals of interest are sometimes suppressed. In order to obtain our final estimates based on ICESat data, the uniform weighting scheme is applied. For the whole of Greenland the estimated mass change rate is equal to -142.6 Gton/year. This value can be mainly attributed to strong mass losses in the region below 2000 meter elevation. On the other hand we show that for different processing strategies this value ranges between approximately 0 and -200 Gton/year. In general, the obtained results confirm trends discovered by other authors who use altimetry. Differences can be explained by different time spans of the used datasets, but mainly by differences in sampling of the data in the region below 2000 meter.

Furthermore, GRACE based monthly variations of the Earth's gravity field as processed by CNES, CSR, DEOS and GFZ are used to estimate the mass change rate for North and South Greenland. Here, both a Gaussian filter, for half-widths of 300, 500 and 800 km, and a Wiener filter is used. It turns out that the Gaussian filter with a half-width of 500 km has the best performance. The final estimates obtained after application of this filter for the different GRACE solutions range between -60.9 and -93.1 Gton/year. The differences in estimates among different GRACE solutions can be mainly explained by differences in processing strategies used by the processing centers to obtain the monthly gravity fields. Only for the DEOS solutions, these differences can also be attributed to the different time span of this dataset. In any case the estimates are low compared with recently published GRACE estimates, which can be explained by an unaccounted leakage effect in our estimates.

The unaccounted leakage effect also mainly explains the differences between estimates based on ICESat

and GRACE data.

Due to their global coverage and high temporal resolution both the ICESat and GRACE mission have improved the estimations of Greenland's ice sheet mass balance. Further improvements are possible when both datasets are combined. Hence an attempt is made for a joint inversion of both datasets. Depending on the used GRACE solution the estimated combined mass change rates range between -114.3 and -124.7 Gton/year.

Samenvatting

De ijskap op Groenland is gevoelig voor veranderingen in het klimaat. De verwachting is dat wereldwijde opwarming resulteert in het smelten van de ijskap wat zal bijdragen aan het stijgen van de zeespiegel. Daarom is het monitoren van de massa balans van de Groenland ijskap van groot belang.

Data van zowel de Ice, Cloud, and land Elevation Satellite (ICESat) laser altimetrie missie en de Gravity Recovery and Climate Experiment (GRACE) zwaartekracht missie over de volledige meetperiode zijn gebruikt, om twee onafhankelijke schattingen te doen van de massa balans van de Groenland ijskap. De meetperiode loopt van ongeveer 2003 tot 2007.

Voor ICESat is een processing strategie ontwikkeld, die gebruik maakt van de hoogteverschillen tussen geometrisch overlappende signalen uit zowel kruisende als herhaalde satellietbanen. De data is opgeschoond aan de hand van kwaliteitsvlaggen, zoals gedefinieerd door het Geoscience Laser Altimeter System (GLAS) science team. (De GLAS is het enige wetenschappelijke instrument aan boord van de ICESat satelliet). De opgeschoonde dataset vertoont enige sterke, ruimtelijk gecorreleerde signalen, die gerelateerd kunnen worden aan fysische fenomenen zoals smeltende gletsjers. Er is tevens een sterke correlatie zichtbaar tussen de waargenomen hoogteverschillen en het gecombineerde effect van ruwheid en helling van het oppervlak.

Verskillende strategieën, toegepast op verschillende sets van laser campagnes zijn gebruikt, om de waargenomen temporele hoogteverschillen te converteren naar massa veranderingen. Dit is gedaan voor 6 verschillende stroomgebieden, verder onderverdeelt in een gebied boven en beneden 2000 meter. Hiervoor zijn alle beschikbare laser campagnes gebruikt en om uitbijters te verwijderen N-sigma thresholding. Voor het schatten van de hoogteveranderingen ten opzichte van een referentie tijdstip, zijn twee wegingschema's geëvalueerd. Een wegingschema dat uniforme gewichten toekent en een die niet-uniforme gewichten toekent aan de gemeten hoogteverschillen. Het laatstgenoemde wegingschema is ontwikkeld, om de invloed van de ruigheid van het oppervlak en de helling mee te nemen. Het blijkt echter dat soms ook de belangrijke signalen onderdrukt worden. Om onze uiteindelijke schatting van de massa balans, gebaseerd op ICESat data, te verkrijgen, is het uniforme wegingschema toegepast. Voor heel Groenland is de geschatte snelheid waarmee de massa balans veranderd gelijk aan -142.6 Gton/jaar. Deze waarde kan voornamelijk worden toegeschreven aan sterke massa verliezen in het gebied beneden de 2000 meter. Aan de andere kant laten we zien, dat voor verschillende strategieën deze waarde varieert tussen 0 en -200 Gton/jaar. Over het algemeen bevestigen de verkregen trends de resultaten van andere auteurs, die altimetrie gebruiken. Verschillen kunnen worden verklaard door de verschillende tijdspannes van de gebruikte datasets, maar voornamelijk door de verschillen in sampling van de data in het gebied beneden de 2000 meter.

Verder zijn op GRACE gebaseerde maandelijkse variaties van het gravitatieveld van de aarde, zoals berekend door CNES, CSR, DEOS en GFZ, gebruikt om de snelheid waarmee de massa balans verandert te schatten voor het noorden en zuiden van Groenland. Hiervoor zijn zowel het Gaussisch filter, met filter halfbreedtes van 300, 500 en 800 km, gebruikt als het Wiener filter. Het blijkt, dat het Gaussisch filter met een halfbreedte van 500 km het beste resultaat geeft. De uiteindelijke schattingen voor de verschillende GRACE oplossingen, die met dit filter verkregen zijn, variëren tussen -60.9 en -93.1 Gton/jaar. De verschillen in schattingen tussen de verschillende GRACE oplossingen kunnen voornamelijk worden verklaard door de verschillende strategieën, die de rekencentra hebben gebruikt, om de maandelijkse

schattingen van het gravitatieveld te verkrijgen. Alleen voor de oplossingen van DEOS kunnen de verschillen eveneens worden toegeschreven aan de verschillende tijdsperiode van deze dataset. In ieder geval zijn onze schattingen laag, vergeleken met recent gepubliceerde schattingen gebaseerd op GRACE data, wat kan worden toegeschreven aan het feit, dat wij in onze schattingen geen rekening houden met het 'lek effect' (leakage effect).

Het feit, dat wij geen rekening houden met het 'lek effect', verklaart eveneens voornamelijk de verschillen tussen de schattingen gebaseerd op ICESat en GRACE data.

Als gevolg van de globale bedekking en de hoge temporele resolutie, hebben zowel de ICESat als de GRACE missie de schattingen van de snelheid waarmee de massa balans van de Groenland ijskap verandert, verbeterd. Verdere verbeteringen zijn mogelijk als beide datasets gecombineerd worden. Vandaar dat er een aanzet is gedaan om de massa balans te schatten door gebruik te maken van beide datasets. Afhankelijk van de verschillende GRACE oplossingen variëren de geschatte snelheden van de massa balans veranderingen tussen -114.3 en -124.7 Gton/jaar.

Preface

Probably the increased attention to climate changes can be attributed to Al Gore's "An Inconvenient Truth", however, it cannot be denied, climate changes are today's topic. In all parts of the world and by all kind of people, the possible causes and consequences of global warming are discussed, relativised and exaggerated. And when one hears the positiveness of people in these discussions, one might wonder whether further research is really necessary. Because it seems beyond doubts that the ice sheets are melting and so sea level is rising. Of course this is of major concern, because even a small sea level rise can harm the lives, wealth and welfare of many people. This makes the question how fast the ice sheets are melting, formulated on a poster at the wall of the Aerospace Engineering building, an important and urgent question. In this graduation project we want to get insight into this question, where we focus on the Greenland ice sheet.

The subject chosen for this thesis is: "Towards a combined estimation of Greenland's ice sheet mass balance using GRACE and ICESat data". The ice sheet mass balance is the difference of mass gain due to accumulation and mass loss due to sublimation, melting/evaporation and discharge, as a function of time.

At Delft University of Technology (DUT) research is performed on the application of Gravity Recovery and Climate Experiment (GRACE) and Ice, Cloud, and land Elevation Satellite (ICESat) data. Both missions are, among others, designed to determine with high precision the changes in the polar ice sheets mass. Before this project, no research was performed at DUT to this application of GRACE and ICESat datasets. This project explores the possibilities how both datasets can be used to estimate a mass balance. The experience obtained by this project will be used in future research work.

Is the Greenland ice sheet really melting? How can you measure that, what is the accuracy of these estimates and how can these estimates be improved? These questions cross my mind when I started this project. Now, at the end of this project these questions can only partly be answered and new questions take the places of the old ones. Beside new questions, I also left with amazement and gratitude. Amazement about the beauty of an ice sheet and its environment. Amazement that was already expressed by the poet of Psalm 147: "*...He giveth snow like wool: he scattereth the hoarfrost like ashes. He casteth forth his ice like morsels: who can stand before his cold? He sendeth out his word, and melteth them: he causeth his wind to blow, and the waters flow...*".

But also gratitude towards the people that helped me during this project. First of all, I would like to thank my supervisors Pavel Ditmar and Roderik Lindenbergh for their supervision and support during this project. I will surely miss the discussions around the laptop about the interpretation of the pictures during our weekly meetings.

Also I would like to thank professor Roland Klees and Bert Vermeersen for their contribution as graduation professor and co-reader respectively.

Furthermore, I am grateful to some members of the group Physical and Space Geodesy for their help and support with software issues and other questions. Especially Elena Zapreeva for her software that I used for the processing of the GRACE data and her support for getting it work on my PC. Erna Oudman, Tobias Wittwer and Xianglin Liu are gratefully acknowledged for their scripts and answers of

my questions about practical issues of the GRACE processing.

I would like to thank Riccardo Riva for the PGR corrections he calculated for me. But also our long discussions about the combination of the GRACE and ICESat datasets were very useful for me.

Beside the people of DUT, also other people contributed to this thesis. Here I want to mention the name of my brother Arthur Slobbe who created an artist impression about the topic of this project. The result of his work is visible on the cover of this report. Also I am grateful to my girlfriend Janneke Kuijntjes for her continuous support and understanding. Beside that she helped me with typing of parts of this report. Here I want to excuse for my horrible writing.

And last but surely not least I would like to thank my parents for their patience and common sense when they were listening to my interpretations. Especially I want to mention my mother who provided me with sufficient coffee every day. Also our talks during these drinks are stored as a dear memory.

Cornelis Slobbe
Brakel, October 2007

Contents

Abstract	iii
Samenvatting	v
Preface	vii
Used abbreviations	xxi
Glossary	xxiii
Used symbols	xxv
1 Introduction	1
1.1 Why polar ice sheet monitoring	1
1.2 Determination of ice sheet mass balance	1
1.3 The status of current research	3
1.4 Objective and Research Questions	3
1.5 Methodology	4
1.6 Outline	5
2 The ICESat and GRACE mission	7
2.1 The ICESat mission	7
2.1.1 Mission science objectives	7
2.1.2 Orbit characteristics	8
2.1.3 Measurement principle and instruments	8
2.1.4 Data processing and products	10
2.2 The GRACE mission	12
2.2.1 Mission science objectives	13
2.2.2 Orbit characteristics	13
2.2.3 Measurement principle and instruments	14
2.2.4 Data processing and products	15
3 The preparation of the ICESat data	17

3.1	The raw data product	17
3.2	Convert to ASCII	18
3.3	Organize and Split	18
3.4	Calculation of the potential CTPs and OTPs	20
3.5	The real overlap test	25
3.6	Cleaning of the dataset	25
3.6.1	OPs not on Ice sheet	25
3.6.2	Quality flags	27
3.6.3	Remaining criteria	35
4	Mass balance estimation with ICESat data	37
4.1	Case Studies, slope and roughness	37
4.1.1	Case studies: outliers	39
4.1.2	Case studies: systematic effects	39
4.1.3	Surface slope	41
4.1.4	Roughness	45
4.2	Mass balance estimation	48
4.2.1	Ice sheet division	48
4.2.2	Removal of outliers	50
4.2.3	Weighting scheme	51
4.2.4	Mass balance estimation	54
5	Mass balance estimation with GRACE data	59
5.1	Used GRACE solutions	59
5.1.1	Monthly solutions	59
5.1.2	Static solutions	60
5.1.3	The coefficients of degree 0 and 1	60
5.2	From gravitational potential variations to mass change	60
5.2.1	The used equations	61
5.2.2	Region function	62
5.2.3	Estimation of the trend	64
5.2.4	Error propagation	64
5.3	Filtering	65
5.4	GRACE error sources and corrections	69
5.4.1	PGR correction	70
5.4.2	Destriping	71
5.4.3	Leakage	72
6	Results and Discussion	75

6.1	Results and discussion ICESat	75
6.1.1	Results ICESat	75
6.1.2	Comparison with other altimetry based estimates	79
6.1.3	Comparison with mascon solutions	83
6.1.4	The uncertainty of the ICESat estimates	87
6.2	Results and discussion GRACE	89
6.2.1	Filter performance	89
6.2.2	Results GRACE	91
6.2.3	Comparison with other GRACE based estimates	92
6.2.4	The uncertainty of the GRACE estimates	94
6.3	A comparison of ICESat and GRACE	96
6.4	A joint inversion of ICESat and GRACE	97
6.4.1	Method for a joint inversion	97
6.4.2	Results and discussion of joint inversion	98
7	Conclusions and recommendations	101
7.1	Conclusions	101
7.1.1	Conclusions ICESat	101
7.1.2	Conclusions GRACE	103
7.1.3	Conclusions comparison ICESat and GRACE	103
7.1.4	Conclusions joint inversion ICESat and GRACE	103
7.2	Recommendations	104
7.2.1	Recommendations for ICESat processing	104
7.2.2	Recommendations for GRACE processing	105
A	Maps Case Studies	109
B	Time series ICESat	127
C	Time series GRACE	133
D	Time series joint inversion	137
	Bibliography	141

List of Figures

1.1	Processes contributing to ice mass balance and applied measurement methods, taken and adapted from [63].	2
2.1	The GLAS instrument, taken and adapted from [36].	9
2.2	Schematic overview of the waveform processing.	11
2.3	The GRACE satellites in orbit, taken from [32].	13
3.1	Schematic overview of the process to retrieve the overlapping footprints.	19
3.2	Schematic overview of the calculation of the potential CTPs and OTPs.	21
3.3	The creation of the bounding boxes.	22
3.4	Principle of the bounding box overlap test.	23
3.5	The iterative procedure used to estimate the location of the crossing of one ascending and one descending track.	24
3.6	Overlapping and non-overlapping footprints.	25
3.7	Digital Elevation Model (DEM), where elevations are defined with respect to the mean sea level.	26
3.8	Ratio between the received and transmitted energy for the data points acquired at the end of the ablation season. The unit of the received energy is in 0.01 fJoules while the unit of the transmitted energy is in counts. Notice that the color bar is adapted for visualization purposes, i.e. the maximum value of this ratio is 50.	28
3.9	Surface mask of the Greenland continent. If an OP is not located on the ice sheet or a glacier, then the OP is removed from the dataset.	29
3.10	Overview of the OPs that are indicated to have a large off-nadir angle (upper image). Histograms of the elevation differences for the case that <i>AttFlg1</i> does not indicate a large off-nadir angle (left) and otherwise (right). Notice that the axes of both histograms are adapted for visualization purposes.	31
3.11	Overview of OPs that are probably contaminated by clouds (upper image). Histograms of the elevation differences for the case that <i>Elfflg</i> does not indicate probable cloud contamination (left) and otherwise (right). Notice that the axes of the histograms are adapted for visualization purposes.	33

3.12	Means and standard deviations of the elevation differences for a fixed value of <i>cld1_mswf</i> , without (left) and with (right) applying the cleaning criteria of the third group. Notice that there are two flag values per elevation difference, here we took the value corresponding with the worst situation. The minimum number of points used to calculate the mean and standard deviations for all cases is larger than 1 575. For most cases this number is in the order of thousands. For the left plot, the error bars are truncated for visualization purposes. For flag values 1 and 2 the standard deviation are equal to 4.2 an 5.1 meter respectively, while for flag values 10, 12 and 15 the standard deviations are equal to 19.6, 21.0 and 34.1 meter respectively.	34
3.13	Means and standard deviations of the elevation differences for a fixed value of <i>FRir_qaFlag</i> , without (left) and with (right) applying the cleaning criteria of the third group. Notice that there are two flag values per elevation difference, here we took the value corresponding with the worst situation. The minimum number of points used to calculate the mean and standard deviations for all cases is larger than 173. For most cases this number is in the order of thousands.	34
3.14	Means and standard deviations of the elevation differences for an increasing number of cloud layers, without (left) and with (right) applying the cleaning criteria of the third group. Notice that there are two numbers per elevation difference, here we took the maximal value. The minimum number of points used to calculate the mean and standard deviation equals 394. The lower the number of detected clouds, the larger the number of used points.	35
4.1	Overview of all elevation differences with the corresponding histograms for the region above (left) and the region below (right) 2000 meter. The thick black line is the 2000 meter elevation contour. Notice that the color bar is adapted for visualization purposes.	38
4.2	Two not completely overlapping footprints, separated by a distance D_{footpr} on a mountain with slope α causes an expected slope bias (SIB).	41
4.3	The expected slope bias as a function of both surface slope and distance between the footprint centers.	42
4.4	The computation of α_{GLOBE} based on the GLOBE DEM.	43
4.5	The north and east gradient components are assigned to each footprint using a nearest neighbor operation. The color of the arrows, pointing in the directions of the gradient components, indicates which values of the gradient components are assigned to the OPs.	44
4.6	Histogram of the expected slope biases based on the GLOBE DEM.	45
4.7	Scatterplot of the expected slope biases and the observed elevation differences. The red crosses indicate the mean elevation differences per interval. The numbers refer to the used number of points to calculate the mean.	46
4.8	The error in the expected slope bias, introduced when the slope changes over the line that connects both centers of the footprints.	46
4.9	Large sastrugi on Antarctica, taken from [18].	47
4.10	Scatterplots of the roughness values and the observed elevation differences for the region above 2000 meter (upper image) and below 2000 meter (lower image). Estimates of the roughness parameter are only available for the first two laser campaigns. In cases where two roughness values were available, the mean roughness value is used. The red crosses indicate the mean elevation difference per roughness interval.	49
4.11	Greenland divided into 6 drainage systems, further divided into a region above (a) and below (b) 2000 meter, taken from [34].	50
4.12	Correlation between the roughness parameter and the elevation differences on the left (blue line) and right side (red line) of a threshold, as a function of this threshold. The left and right plots are for the region above and below 2000 meter respectively.	52

4.13	Map where the color is indicating the weights assigned to the observed elevation differences. Notice that we added both regions together, but that the estimation is done separately. This figure shows clearly that for the region above 2000 meter mostly uniform weights are used. For the region below 2000 meter, weights in general decrease toward the margins.	53
4.14	PGR-induced radial velocities, calculated using Peltiers ICE-5G ice model and the VM2 Earth model [43].	56
5.1	Degree amplitudes of the exact averaging kernels for disc-shaped regions with a different radius of (a) 1000 km, (b) 500 km, and (c) 100 km. The maximum amplitude has been normalized by $1/\vartheta_0$. Taken and adapted from [55]	63
5.2	Smoothed region function for the region below 2000 meter. The 2000 meter elevation contour is indicated with the thick black line. Here L_{max} equals 50, corresponding with the maximum degree of the CNES models. For smoothing, a Wiener filter is used, see section 5.3.	64
5.3	Average degree-power spectra for all used GRACE solutions, in terms of geoid-height squared in mm^2 . The blue dots represent the degree variances for all monthly solutions. The green crosses are the averages per degree based on all monthly degree amplitude spectra. The black and red solid are respectively the modeled inverse-power function for the signal part and the modeled linear function in a logarithmic scale for the noise part.	67
5.4	Average degree-power spectra for all used GRACE solutions, in terms of geoid-height squared in mm^2	68
5.5	PGR-induced rates of geoid height changes, calculated using Peltiers ICE-5G ice model and the VM2 Earth model.	70
6.1	Time series for drainage system 4b using processing strategy IIIc. The bad performance of the used model to estimate the trend is caused by the small number of points of the time series.	77
6.2	Ice-sheet elevation change rate in cm/year , derived from 11 years of ERS-1/ERS-2 satellite radar altimeter data (1992 to 2003), excluding some ice-sheet marginal areas (white). The spatially averaged rate is $5.4 \pm 0.2 \text{ cm}/\text{year}$, or $5 \text{ cm}/\text{year}$ when corrected for PGR. The white areas between the color-coded pixels and the thick line delimiting the ice sheet indicate no observations. Taken from [24].	80
6.3	Estimated elevation change rates averaged over 50-km grid squares. Taken and adapted from [62].	81
6.4	Flight tracks (outlined in black) of airborne laser altimetry surveys, taken and adapted from [30]. Swaths range between 150 and 200 meter [29]. Interpolation is used in order to obtain an area covered map of the rate of change in surface elevation.	84
6.5	Mascon solutions versus estimates based on ICESat data for the individual regions.	85
6.6	Mascon solutions versus estimates based on ICESat data for the individual drainage systems. Here we used the mascon solutions that are corrected for potential signal loss ($\sim 9\%$) as determined from simulation analyses.	88
6.7	Smoothed monthly models based on different filters, expressed in variations of thickness of an equivalent water layer for CNES and DEOS solutions of April 2004. Maps are in a polar stereographic projection.	90
6.8	GRACE long-term mass rates over Greenland and surrounding regions during the period April 2002 to November 2005, determined from mass change time series on a 1° grid, taken from [9].	95

- A.1 First track acquired on 24-Feb-2004, second on 26-Feb-2005. The erratic behavior is probably due to the combined effect of surface slope and roughness in combination with the fact that the footprints do not overlap exactly. At the end of the elevation profiles we can probably see the effect of undulation, see section 4.1.4. 110
- A.2 First track acquired on 01-Mar-2004, second on 04-Mar-2005. Overlapping tracks located at the margin of the ice sheet. On the Landsat images we can see that a part of the OTPs are located on the rocks that rise above the ice sheet. Here steep slopes and roughness might explain the large elevation differences. 111
- A.3 First track acquired on 09-Mar-2004, second on 12-Mar-2005. Overlapping tracks located at the margin of the ice sheet. On the Landsat images we can see that a part of the OTPs are is located on the rocks that rise above the ice sheet. Here steep slopes and roughness might explain the large elevation differences. 112
- A.4 First track acquired on 19-Oct-2003, second on 24-Oct-2005. The first increasing elevation differences that become constant and decrease after a while are probably due to the effect of saturation. Notice that for only one track a saturation correction is applied. Probably here also the glacier dynamics play a role. 113
- A.5 First track acquired on 23-Oct-2003, second on 24-Feb-2004. The first increasing elevation differences that become constant and decrease after a while are probably due to the effect of saturation. Notice that for only one track a saturation correction is applied. . . 114
- A.6 First track acquired on 28-Oct-2003, second on 08-Mar-2004. The first increasing elevation differences that become constant and decrease after a while are probably due to the effect of saturation. Notice that for only one track a saturation correction is applied. 115
- A.7 First track acquired on 28-Oct-2003, second on 10-Nov-2005. The first increasing elevation differences that become constant and decrease after a while are probably due to the effect of saturation. Notice that for only one track a saturation correction is applied. 116
- A.8 First track acquired on 21-Mar-2004, second on 27-Mar-2006. Surface lakes at the West Greenland ice margin. The smoothness of the upper elevation profile can be interpreted as a water surface. In the left example the lake disappeared while in the right example a new lake is formed. 117
- A.9 First track acquired on 21-Mar-2004, second on 27-Mar-2006. Thinning inlet of Jakobshavn Isbræ glacier. 118
- A.10 First track acquired on 21-Mar-2004, second on 23-Nov-2005. Thinning inlet of Jakobshavn Isbræ glacier. 119
- A.11 First track acquired on 27-Feb-2005, second on 29-Oct-2005. Thinning inlet of Jakobshavn Isbræ glacier. 120
- A.12 First track acquired on 01-Mar-2005, second on 05-Mar-2006. Thinning inlet of Jakobshavn Isbræ glacier. 121
- A.13 First track acquired on 07-Mar-2005, second on 10-Mar-2006. Thinning inlet of Jakobshavn Isbræ glacier. 122
- A.14 First track acquired on 25-Sep-2003, second on 03-Oct-2003. Most likely explanation here is that the blocked flow of the glacier results in an uplift of the glacier. 123
- A.15 First track acquired on 21-Oct-2003, second on 26-Oct-2005. Probable effect of undulation. 124
- A.16 First track acquired on 29-Oct-2003, second on 07-Mar-2006. Probable effect of undulation. 125

- B.1 Elevation change time series for drainage systems 1 to 3 based on ICESat data. Units of vertical axis are in meter. The letters a and b stand for above and below 2000 meter respectively. The time series are computed according to processing strategy Ic, see table 6.1. The estimated trend (straight dotted line) is computed using all available laser campaigns. The solid green line is the trend plus the seasonal cycle. The solid and dotted red curve represents the 95%- and 99%-confidence regions. 128
- B.2 Elevation change time series for drainage systems 4 to 6 based on ICESat data. Units of vertical axis are in meter. The letters a and b stand for above and below 2000 meter respectively. The time series are computed according to processing strategy Ic, see table 6.1. The estimated trend (straight dotted line) is computed using all available laser campaigns. The solid green line is the trend plus the seasonal cycle. The solid and dotted red curve represents the 95%- and 99%-confidence regions. 129
- B.3 Elevation change time series for drainage systems 1 to 3 based on ICESat data. Units of vertical axis are in meter. The letters a and b stand for above and below 2000 meter respectively. The time series are computed according to processing strategy Id, see table 6.1. The estimated trend (straight dotted line) is computed using all available laser campaigns. However, due to the used processing strategy mostly the values of the first laser campaign are out of range. The solid green line is the trend plus the seasonal cycle. The solid and dotted red curve represents the 95%- and 99%-confidence regions. . 130
- B.4 Elevation change time series for drainage systems 4 to 6 based on ICESat data. Units of vertical axis are in meter. The letters a and b stand for above and below 2000 meter respectively. The time series are computed according to processing strategy Id, see table 6.1. The estimated trend (straight dotted line) is computed using all available laser campaigns. However, due to the used processing strategy mostly the values of the first laser campaign are out of range. The solid green line is the trend plus the seasonal cycle. The solid and dotted red curve represents the 95%- and 99%-confidence regions. 131
- C.1 Time series of all used GRACE solutions for the northern part of Greenland. This region is defined as the combination of the drainage systems 1, 2 and 6, see figure 4.11. The variations are expressed in terms of variations of thickness of an equivalent water layer, with units in meters. For spatial smoothing a Gaussian filter with a half-width of 500 km is used. Time series are corrected for PGR, see also table 5.3 and table 5.4. The estimated trend is represented as the straight dotted line. The solid green line is the trend plus the seasonal cycle. The solid and dotted red curve represents the 95%- and 99%-confidence regions. 134
- C.2 Time series of all used GRACE solutions for the southern part of Greenland. This region is defined as the combination of the drainage systems 3, 4 and 5, see figure 4.11. The variations are expressed in terms of variations of thickness of an equivalent water layer, with units in meters. For spatial smoothing a Gaussian filter with a half-width of 500 km is used. Time series are corrected for PGR, see also table 5.3 and table 5.4. The estimated trend is represented as the straight dotted line. The solid green line is the trend plus the seasonal cycle. The solid and dotted red curve represents the 95%- and 99%-confidence regions. 135
- C.3 Time series of all used GRACE solutions for whole Greenland. The variations are expressed in terms of variations of thickness of an equivalent water layer, with units in meters. For spatial smoothing a Gaussian filter with a half-width of 500 km is used. Time series are corrected for PGR, see also table 5.3 and table 5.4. The estimated trend is represented as the straight dotted line. The solid green line is the trend plus the seasonal cycle. The solid and dotted red curve represents the 95%- and 99%-confidence regions. 136

- D.1 Time series of the whole of Greenland based on joint inversion of the ICESat dataset (all releases + N-sigma thresholding applied) and all GRACE solutions. Here no variance component estimation is applied to estimate the relative weights between both datasets. The vertical axes are in terms of gigatons. For spatial smoothing of the GRACE data a Gaussian filter with a half-width of 500 km is used. Time series are corrected for PGR. The yellow crosses mark the epochs for which only GRACE data is available. The black crosses mark the epochs for which both ICESat and GRACE data is available. The estimated trend is represented as the straight dotted line. The solid green line is the trend plus the seasonal cycle. The solid and dotted red curve represents the 95%- and 99%-confidence regions. 138

- D.2 Time series of the whole of Greenland based on joint inversion of the ICESat dataset (all releases + N-sigma thresholding applied) and all GRACE solutions. Here variance component estimation is applied to estimate the relative weights between both datasets. The vertical axes are in terms of gigatons. For spatial smoothing of the GRACE data a Gaussian filter with a half-width of 500 km is used. Time series are corrected for PGR. The yellow crosses mark the epochs for which only GRACE data is available. The black crosses mark the epochs for which both ICESat and GRACE data is available. The estimated trend is represented as the straight dotted line. The solid green line is the trend plus the seasonal cycle. The solid and dotted red curve represents the 95%- and 99%-confidence regions. 139

List of Tables

2.1	Single-shot error budget for ICESat elevation measurements, taken from [79]	12
2.2	ICESat/GLAS standard data products.	12
3.1	Laser operation campaign summary. Notice that there are more laser campaigns, but not all campaigns are available to the public.	18
3.2	Maximum values of axes footprint ellipses for the different laser campaigns	23
3.3	The number of potential and real CTPs and OTPs.	25
3.4	Overview of the quality flags available for GLA12. Notice that mostly one flag consists of several bits, all indicating different aspects. So the flags are in fact generic terms for a subset of flags.	27
3.5	Overview total number of removed OPs for different groups of cleaning criteria.	36
4.1	PGR corrections in mm/year for the different regions.	57
5.1	Main properties of used GRACE monthly solutions.	60
5.2	For all used GRACE solutions this table provides the boundaries of the signal and noise part plus the estimated parameters of the inverse-power function (x_1 and x_2) and the linear function in a logarithmic scale (x_3 and x_4). These functions are used to model the signal and noise part respectively.	69
5.3	PGR corrections in Gton/year for the different GRACE solutions per region when the Wiener filter is used.	71
5.4	PGR corrections in Gton/year for different half-widths of the Gaussian filter.	71
6.1	Different possible processing strategies.	76
6.2	Overview of estimated elevation/mass change rates obtained with different processing strategies using different sets of laser campaigns. The elevation change rates ($\overline{\Delta H}$) and mass change rates (ΔM) are expressed in cm/year and Gton/year respectively. The mass change rates are calculated according to the methodology of section 4.2.4. The arrows \uparrow and \downarrow indicate the region above and below 2000 meter respectively. In order to convert the elevation change rates into mass change rates, densities of 600 kg/m^3 and 917 kg/m^3 are used for the regions above and below 2000 meter respectively. The last two columns contain the total mass change rates and accompanying standard deviations. Estimates are corrected for PGR.	77

6.3	Overview of estimated elevation/mass change rates per drainage system for the region above (\uparrow) and below (\downarrow) 2000 meter, using processing strategy 1c and 1d. The elevation change rates ($\overline{\Delta H}$) and mass change rates (ΔM) are expressed in cm/year and Gton/year respectively. In order to convert the elevation change rates to mass change rates, densities of 600 kg/m^3 and 917 kg/m^3 are used for the regions above and below 2000 meter respectively. The last two columns contain the total mass change rates and accompanying standard deviations. Estimates are corrected for PGR.	78
6.4	Overview total mass change rates for the region above (\uparrow) and below (\downarrow) 2000 meter, using processing strategy 1c and different densities. The mass balance change rates (ΔM) are expressed in Gton/year respectively. Estimates are corrected for PGR.	79
6.5	Overview elevation change rates provided in different studies using altimetry datasets, for the region above (\uparrow) and below (\downarrow) 2000 meter.	82
6.6	Summary of Greenland drainage system mascon solutions (corrected for PGR) above and below 2000 meter elevation (July 2003 to July 2005), taken from [34]. The values in the last column are corrected for potential signal loss ($\sim 9\%$) as determined from simulation analyses. This is the reason why the value of the last column is not equal to the sum of the values in the second and third column.	83
6.7	Estimated mass change rates for all used GRACE solutions and different regions (Reg.), i.e. North (N), South (S) and the whole of Greenland (WG). Both the Wiener filter and Gaussian filter are used to suppress the noise. Estimates are in Gton/year and ordered in alphabetical order, i.e. 1: CNES, 2: CSR, 3: CSR destriped, 4: DEOS, 5: GFZ.	91
6.8	Estimated mass change rates for all used GRACE solutions and different regions (Reg.), i.e. North (N), South (S) and the whole of Greenland (WG). A Gaussian filter with a half-width of 500 km is used and the estimates are obtained for different time spans. Estimates are in Gton/year and ordered in alphabetical order, i.e. 1: CNES, 2: CSR, 3: CSR destriped, 4: DEOS, 5: GFZ.	92
6.9	Overview estimated mass change rates provided in different studies. All estimates are solely based on GRACE data.	93
6.10	Estimated mass change rates and accompanying uncertainties in Gton/year with and without application of VCE.	99

Used abbreviations

AVHRR	Advanced Very High Resolution Radiometer
CNES	Centre National d'Études Spatiales
CSR	Center for Space Research
CTP	Crossing Track Pair
CWAMP	Challenging Mini Satellite Payload
DEM	Digital Elevation Model
DEOS	Department of Earth Observation and Space Systems
DS	Drainage System
DUT	Delft University of Technology
ECCO	Estimation of the Circulation and Climate of the Ocean
GFZ	GeoForschungsZentrum
GLAS	Geoscience Laser Altimeter System
GPS	Global Positioning System
GRACE	Gravity Recovery and Climate Experiment
ICESat	Ice, Cloud, and land Elevation Satellite
ID	Identifier
InSAR	Interferometric Synthetic Aperture Radar
LAGEOS	Laser Geodynamics Satellite
LIDAR	LIght Detection And Ranging or Laser Imaging Detection And Ranging
JPL	Jet Propulsion Laboratory
OP	Overlapping Pair (both Crossing Track Pairs and Overlapping Track Pairs)
OTP	Overlapping Track Pair
PGR	Post Glacial Rebound
SAR	Synthetic Aperture Radar
SDS	Science Data System
SGG	Satellite Gravity Gradiometry
SLR	Satellite Laser Ranging
SST	Satellite-to-Satellite Tracking
TOF	Time-Of-Flight
VC-matrix	Variance-Covariance matrix
VCE	Variance Component Estimation

Glossary

Ablation	All processes that remove snow, ice, or water from a glacier, snowfield, etc.; in this sense, the opposite of accumulation.
Ablation zone	Area or zone of a glacier where snow and ice ablation exceed accumulation.
Accumulation	All processes by which snow or ice are added to a glacier, this is typically the accumulation of snow, which is slowly transformed into ice; other accumulation processes can include avalanches, wind-deposited snow, and the freezing of rain within the snow pack.
Accumulation zone	Area of a glacier where more mass is gained than lost.
Albedo	The fraction of solar radiation that is reflected by the Earth's surface.
Cryosphere	One of the Earth's spheres of irregular form existing in the zone of interaction of the atmosphere, hydrosphere and lithosphere, distinguished by negative or zero temperature and the presence of water in the solid or super-cooled state; the term refers collectively to the portions of the earth where water is in solid form, including snow cover, floating ice, glaciers, ice caps, ice sheets, seasonally frozen ground and perennially frozen ground (permafrost).
Discharge	The flow of ice across the grounding line.
Equilibrium line	Boundary between the accumulation area and ablation area where the mass balance is zero.
Evaporation	In meteorology, evaporation usually is restricted in use to the change of water from liquid to gas.
Firn	Rounded, well-bonded snow that is older than one year; firn has a density greater than 550 kilograms per cubic-meter.
Ice sheet	A dome-shaped mass of glacier ice that covers surrounding terrain and is greater than 50 000 square kilometers (e.g., the Greenland and Antarctic ice sheets).
Ice shelf	Portion of an ice sheet that spreads out over water.
Grounding line	The location where glacial ice resting on solid Earth gives way to floating ice.
Mass balance	The difference of mass gain due to accumulation and mass loss due to sublimation, melting/evaporation and discharge, as functions of time.
Sastrugi	Complex, fragile shapes of snow on top of sea ice that resemble sand dunes; they form parallel to the prevailing wind direction; sastrugi can also form on snow cover over land.
Runoff	Meltwater that flows from land to the ocean. It can come from melting snow or ice anywhere on the ice sheet, and can flow over or through the ice, perhaps even collecting in reservoirs under the ice.
Sublimation	The transition of a substance from the solid phase directly to the vapor phase, or vice versa, without passing through an intermediate liquid phase.

Used symbols

a	y-intercept
A	design matrix
A_m	amplitude
b	trend of linear model
c	first parameter that accounts for seasonal cycle
\overline{C}_{lm}	Stokes coefficients
\overline{C}_{lm}^n	spherical harmonic coefficients associated with noise $n(\theta, \lambda)$
C_l^W	spherical harmonic coefficients of filter function
d	second parameter that accounts for seasonal cycle
D_{footpr}	distance between footprint centers
\underline{e}	noise
e_i	enlargement of bounding box
$\#E$	number of evaluations
$\mathcal{E}[\cdot]$	expectation operator
E_{reg}	angular area of the region
\underline{f}	the sum of gravitational and non-gravitational accelerations
f_0	mass variation inside the region of interest
f_i	mass variation outside the region of interest
G	gravitational constant
$\delta\overline{h}_w$	average variation of thickness of the equivalent water layer
$h_w(\theta, \lambda)$	variations of surface density expressed in terms of equivalent water layer thickness
$h_{w\overline{w}}(\theta, \lambda)$	smoothed variations of surface density expressed in terms of equivalent water layer thickness
$\hat{\delta}h_w(\theta, \lambda)$	estimation of true variation of thickness of the equivalent water layer after filtering
$\overline{\Delta H}$	average elevation change trend
$\overline{\Delta H}_{ij}$	observed elevation difference between month j and i
H_i^r	height on month i , defined with respect to a fixed height of reference epoch r
k'_l	load Love numbers
l	degree
l_c	thickness of the firn/ice column
L_{max}	maximum or truncation degree
m	order
M	mass
M_E	total mass of the Earth
$\#N$	total number of months
N	geoid height
N_a	number of ascending tracks
N_d	number of descending tracks
$\overline{\delta\text{PGR}}$	average PGR correction in mm/year expressed in variation of thickness of an equivalent water layer
$q(\theta, \lambda)$	region function that is 1 inside and 0 outside the area Ω
$q_w(\theta, \lambda)$	smoothed region function
$Q_{\hat{x}\hat{x}}$	variance-covariance matrix of the estimated parameters

Q_{yy}	variance-covariance matrix of observations
r	spherical coordinate of given point (distance from the origin of the coordinate system)
r'	spherical coordinate of integration point (distance from the origin of the coordinate system)
\bar{r}	the position vector in an Earth-centered inertial frame
R	major semi-axis of a reference ellipsoid
\bar{R}	mean Earth radius
R_s	spatial resolution of the gravity field
$\delta s(\theta, \lambda)$	variation of surface density
SIB	expected slope bias
ΔT_{Tr}	time difference between first and last shot of track
t_i	epoch i
T	period of seasonal cycle, i.e. one year
T_h	threshold that defines boundary between second and third part in weighting scheme
v	volume of the Earth
V	gravitational potential
V_g	ground velocity
w_{ij}	weight assigned to a particular elevation difference between epoch i and j
W	weight matrix
$W(\cos \psi)$	filter function
x_i	unknown parameter with index i
y_i	observation on epoch i
\bar{Y}_{lm}	4π -normalized surface spherical harmonics
α	slope
$\bar{\epsilon}_0$	bias in $\delta \bar{h}_w$ over the region of interest
λ	spherical coordinates of given point (longitude)
λ'	spherical coordinates of integration point (longitude)
ϕ	phase
θ	spherical coordinates of given point (co-latitude)
θ'	spherical coordinates of integration point (co-latitude)
ϑ_l	degree amplitude l
ρ_{\uparrow}	average density above 2000 meter elevation (600 kg/m^3)
ρ_{\downarrow}	average density below 2000 meter elevation (917 kg/m^3)
ρ_a	average density of the firn/ice column
ρ_{ave}	average Earth's density
ρ_w	the water density
$\sigma_{lm}^2(\delta h_w)$	signal variances
$\sigma_{lm}^2(n)$	noise variances
$\sigma_{GS,l}^2$	averaged degree amplitude for degree l with $2 \leq l \leq L_{max}$
Ω	unit sphere
Ω_R	mean Earth sphere
Ω_{reg}	area on the unit sphere
Ψ	azimuth between center of first footprint in time to second footprint in time
ψ_0	characteristic filter width of Gaussian filter

Chapter 1

Introduction

For long, the determination of the ice sheets mass balance was the work of glaciologists. However, due to the increased usage of remote sensing in this research area, more disciplines are involved. Therefore, a short introduction into this research area is necessary to understand the backgrounds and current status of the research. This makes the position of this thesis work, which will be explained in the remainder of this chapter, more clear.

First the relevance of mass balance monitoring is described in section 1.1. Section 1.2 provides a short description of the methods used to determine the mass balance of an ice sheet, followed by an overview of the status of current research. This leads to the formulation of the research objective and research questions in section 1.4. After that the methodology is described that is used during this research. The chapter ends with an outline of the report.

1.1 Why polar ice sheet monitoring

The ice sheet mass balance is the difference of mass gain due to accumulation and mass loss due to sublimation, melting/evaporation and discharge, as a function of time. The Antarctic and Greenland ice sheets together hold 33 million km³ of ice, representing enough water to raise global sea level by 70 m [46]. Annual snowfall on the ice sheets is equivalent to 6.5 mm of sea level decline, so only a small imbalance between snowfall and discharge of ice and melt water into the ocean could be a major contributor to present day sea level rise (3.1 ± 0.4 mm/year [7]). Because most human activities are concentrated along the coasts, even small amounts of sea level rise have substantial societal and economic impacts through coastal erosion, increased susceptibility to storm surges, groundwater contamination by salt intrusion, and other effects. By the end of the 21st century, sea level is predicted to rise by 0.5 ± 0.4 m in response to additional global warming [10], with potential contributions from the Greenland and Antarctic ice sheets dominating the uncertainty of that estimate. Consequently, a detailed knowledge and understanding of the evolution of polar ice sheets is of considerable societal importance.

1.2 Determination of ice sheet mass balance

Figure 1.1 shows the wide variety of data connected to ice mass changes. Some measurement techniques are used to determine just one term of the mass budget, others can be related more or less directly to the mass balance. Basically there are three different ways to determine the mass balance that will be briefly discussed ([46]).

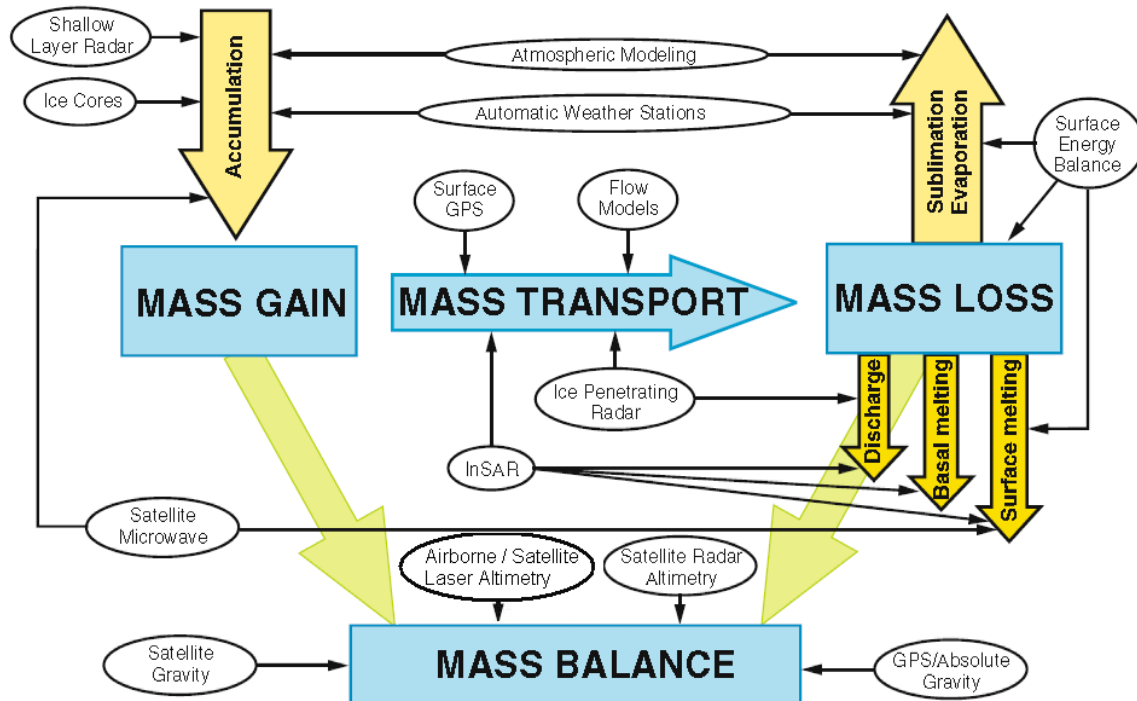


Figure 1.1: Processes contributing to ice mass balance and applied measurement methods, taken and adapted from [63].

1. **The mass budget method** compares the mass gain due to accumulation to mass loss due to sublimation, meltwater runoff and ice flowing into the ocean. Net accumulation is inferred primarily from ice core measurements. Loss by melting is more complex because of meltwater refreezing after draining into near-surface snow. To estimate ice discharge, the velocity of the glaciers is combined with ice thickness data and data on the width of the glaciers. Nowadays the ice surface velocity can be measured by GPS or interferometric synthetic aperture radar (InSAR). The mass budget method is hampered by a lack of accurate accumulation and ice thickness data.
2. **Measurements of elevation changes over time**, which are translated into volume/mass changes. The measurements are acquired by radar or laser altimetry on both satellites and aircraft. Satellite radar altimeters (Seasat, Geosat, and European Remote Sensing Satellites ERS-1 and -2) have been used over Greenland and Antarctica since 1978 ([11], [74]). One of the problems with satellite radar altimetry is that coverage is limited to the interior of the ice sheets, where surface slopes are low. Aircraft altimeters do not suffer from this problem and they were used extensively over Greenland in the 1990s [30]. With the launch of NASA's Ice, Cloud, and Land Elevation Satellite (ICESat), with a laser altimeter onboard and nearly global coverage, the measurement precision is increased and surveys cover the full extent of the ice sheet, so also the ice sheet margins [79]. Basically there are three problems intrinsically related to this method. The first problem, also related to gravity change data, is the separability of the signals of current and past ice load change. Past ice load change, in particular the deglaciation after the last ice age, continues to act through Post Glacial Rebound (PGR), i.e. vertical land movements due to removed ice loads and related lateral mass shifts in the Earth's interior. Secondly, decadal variations in snow accumulation rate make a conversion to mass changes more difficult because the density of snow differs from that of ice by a factor three. And so decadal variations in accumulation are exaggerated in the observed volume fluctuations over those due to ice dynamics in the same ratio. A correction is only possible if the snowfall is known independently. The third problem is related to the compaction of snow over time and due to variable accumulation rates. Snow compaction results in elevation changes unrelated to mass changes. Firn compaction models can be used to reduce this term. In addition also a non-zero surface slope is a point of concern related to the use of elevation changes over time. When pairs of footprints do not overlap perfectly, a non-zero surface slope will

introduce an elevation difference.

3. **Weighting of the ice sheets.** Since 2002, NASA/DLR's (Germany's aerospace research agency) Gravity Recovery and Climate Experiment (GRACE) satellite mission measures the spatiotemporal changes of the Earth's gravity field. Over the ice sheets, this change can be converted into an ice-mass change, assuming that the gravity field change results from a change in surface mass. However, current estimates of the mass balance based on GRACE data are highly scattered, caused by different processing techniques and the relatively short time span of the analyses. They are also inaccurate, caused by contamination from the PGR and other effects like variations in atmosphere, adjacent oceans and (for areas free of ice today) continental hydrology. Furthermore, the GRACE estimates are biased by the so-called 'leakage error'. This error is caused by the small signals of the surrounding oceans and the strong signals on ice sheet in combination with the coarse resolution (400-600 km).

1.3 The status of current research

Compared to the mass budget method, the use of GRACE and ICESat data allows to directly determine the ice volume and mass changes with a nearly complete coverage of ice sheets and glaciers, with high spatial resolution and with sufficient temporal resolution (monthly sampling of mass changes by GRACE, whereas the temporal resolution of ICESat depends on the availability of the laser campaigns and the type of cross-over analysis).

The situation becomes even better when both datasets are combined. Simulations of GRACE and ICESat data show that when both datasets are combined, a separation of the PGR signal and ice mass trend is possible ([72] and [65]). When using simulated GRACE data alone, the achieved precision for ice mass and sea level change (0.6 mm/year sea level change) is not much better than the precision with mass budget methods. When using GRACE and ICESat together, the precision improves considerably (0.2 mm/year sea level change). Further improvements can be achieved by adding a set of GPS vertical movement data [65].

Currently, several estimates are available using GRACE ([66], [44], [9], [68], [67], [69] and [34]) or ICESat data ([62]), sometimes in combination with other data sources. The interpretation of these estimates result in a lot of discussion about, and improvements of the used processing strategies. However, until now, no results are published where both datasets are integrated.

1.4 Objective and Research Questions

At the start of this research a complete integration of GRACE and ICESat, which results in a combined estimate of the mass balance of the polar ice sheets, was believed to be too ambitious. There was also no experience at DUT with mass balance estimation at all. However, during the project it became clear that a joint inversion of both datasets was feasible. Therefore we add one question to our subquestions. The research objective is defined as:

Compare the estimations of the ice sheet mass balance based on GRACE and ICESat data.

The main research question of this graduation project will be:

What is the mass balance of the Greenland ice sheet using GRACE and ICESat data over the full measurement period of both satellite missions and how can differences between both estimates be explained.

Here we focus on the way how these estimates can be derived. This means that for this research it does not matter whether we focus on the Antarctic or Greenland ice sheet. The reason why we prefer Greenland is that only Greenland is completely covered by both satellites. To get a complete coverage for Antarctica, other data sources have to be used or we could only focus on a part of this ice sheet. Both situations are not desirable, because the first makes a good comparison between both methods more difficult, while the last option hampers the validation of the estimates. Another reason why Greenland is preferred is the fact that Greenland presently makes the largest contribution to sea level rise [2].

The main research question is divided into the following subquestions:

1. **What is the mass balance of the Greenland ice sheet based on only ICESat data.** In this step it will be determined whether it is necessary to use all data, because by data reduction the feasibility is increased. During the development of the methodology it must become clear what the problems are and which assumptions have to be made using only ICESat data. Also error sources have to be specified and the precision of the estimate will be assessed. This step results in an estimate of the mass balance of the Greenland ice sheet and a computational scheme.
2. **What is the mass balance of the Greenland ice sheet based on only GRACE data.** Here the level-2 data product will be used. During the development of the methodology it must become clear what the problems are and which assumptions have to be made using only GRACE data. Also error sources have to be specified and the precision of the estimate will be assessed. This step results in an estimate of the mass balance of the Greenland ice sheet and a computational scheme.
3. **How can the differences between both estimates be explained and how can these differences be reduced.** From the previous steps we derived two independent estimates of the mass balance of the Greenland ice sheet. For both estimates different assumptions have to be made and also the error sources are different. From this step the weak points of both methods become clear.
4. **What is the mass balance of the Greenland ice sheet based on a joint inversion of ICESat and GRACE data.** During the development of the methodology it must become clear what the problems are and which assumptions have to be made using a joint inversion of ICESat and GRACE data. This step results in an estimate of the mass balance of the Greenland ice sheet and a computational scheme.

1.5 Methodology

This graduation project can be divided according to the subquestions defined in section 1.4. These subquestions can be tackled in four steps:

1. **Literature study:** here the method is studied to become familiar with current processing techniques and already recognized problems.
2. **Development of the algorithms:** at this stage the algorithms needed to estimate the mass balance are developed. If possible, current known processing techniques and existing routines or software packages are used.
3. **Interpretation, validation and improvements:** the estimates and processing techniques are evaluated and the results are compared with other estimates. Possible differences are explained and necessary improvements are made.
4. **Writing:** each step is closed by a description of the processing techniques, results and interpretation.

To get the best estimate of the mass balance, all available and useful data is used from both satellites. For GRACE, launched on March 17, 2002, there is data available from 2002 to present. For ICESat, launched on January 12, 2003, there is data available from different laser campaigns spread over a time period of 2003 to present. For both studies level-2 data is used, using the latest releases.

For the ICESat processing, Matlab is used to develop the algorithms. This set of scripts form an extensive toolbox that can be used to process ICESat data.

For the GRACE processing, existing Fortran programs are used. Additional programs and scripts are developed in Fortran and Matlab respectively.

1.6 Outline

Because of the fact that a part of the readers might not be familiar with the ICESat and/or GRACE mission, chapter 2 starts with an overview of both missions. It contains a general overview of the characteristics of the missions, on-board instruments and explains what kind of data is obtained from these missions.

In contrast to the GRACE data, the ICESat dataset cannot be used immediately. First the overlapping footprints have to be retrieved from the original data product. In order to obtain an unbiased estimate of the ice sheet mass balance also some cleaning steps are necessary. The procedures used to retrieve the overlapping footprints, developed in the course of this project, and the used cleaning steps are described in chapter 3.

Chapter 4 focuses on the method how the overlapping footprints can be used to obtain the mass balance. Beside that, the results are presented of some case studies we conducted to explain some random and systematic behaving features in the observed elevation differences.

In chapter 5 we explain how GRACE data can be used to estimate the mass balance. After an overview of the used GRACE solutions the used equations are provided. This is followed by a description of the necessary filter step and a discussion of some error sources.

The results of the estimated mass change rates using ICESat and GRACE data separately are both discussed in chapter 6. Here the used processing strategies are evaluated and the results are compared with already published estimates. Finally, a method for a joint inversion of both datasets and the corresponding results are presented.

The last chapter contains the conclusions and some recommendations for future work. The maps of the case studies and plots of the time series belonging to ICESat and GRACE are incorporated in the appendices.

Chapter 2

The ICESat and GRACE mission

The Ice, Cloud, and land Elevation Satellite (ICESat) mission, part of NASA's Earth Observing System, is launched on January 13, 2003, and still in orbit. The primary goal of ICESat is to quantify the ice sheet mass balance and understand how changes in the Earth's atmosphere and climate affect the polar ice masses and global sea level. Approximately one year earlier (March 17, 2002), the Gravity Recovery and Climate Experiment (GRACE) mission was launched and is also still in orbit. The primary science objective of this mission is to provide global and high-resolution estimates of the mean and time-variable part of the Earth's gravity field. This chapter provides an overview of both missions and their main characteristics.

2.1 The ICESat mission

This section provides an introduction to the ICESat mission, mainly focused on the altimetry part. Section 2.1.1 starts with an overview of the mission science objectives, followed by an overview of the main characteristics of this mission in section 2.1.2. In section 2.1.3 the measurement principle and instruments are described. This chapter ends with a short introduction into the processing of the raw measurements and an overview of the available data products

2.1.1 Mission science objectives

The science objectives of the ICESat mission can be divided in objectives related to the cryosphere, land processes and atmospheric sciences. However, the primary purpose of this mission is the determination of inter-annual and long-term changes in the polar ice sheet mass, the causes of changes in the mass balance, and the impact of these changes on global sea level [79]. A specific objective of ICESat is to reduce the uncertainty in the known ice sheet mass balance through the determination of the polar ice elevation changes with better than 2 cm/yr accuracy over 100 km × 100 km areas, averaged over three or more years of seasonal and interannual variability. A further goal is to provide a precise elevation topography of the Greenland and Antarctic ice sheets and describe the nature of surface characteristics (e.g., roughness and reflectivity), including sea ice.

The primary land processes science goal is to conduct topographic measurements of the Earth's land surface on a global basis in order to contribute to a global grid of ground control points for georeferencing of topographic maps and digital elevation models. The secondary land processes science goal is to detect topographic change at the meter per year level or better in selected regions of limited spatial extent.

The last group of science objectives is related to the atmospheric sciences. The primary science goal of the Geoscience Laser Altimeter System (GLAS) cloud and aerosol measurement is to determine the radiative forcing and vertically resolved atmospheric heating rate due to clouds and aerosols by directly observing the vertical structure and magnitude of cloud and aerosol parameters. These parameters are important for the radiative balance of the Earth-atmosphere system, but are ambiguous or impossible to obtain from existing or planned passive remote sensors. A further goal is to directly measure the height of atmospheric transition layers (inversions) which are important for dynamics and mixing, the planetary boundary layer, and lifting condensation level.

2.1.2 Orbit characteristics

ICESat was launched on January 13, 2003, into a 600 km altitude orbit with a 94° inclination. This inclination is a compromise between the desire for a true polar orbit and the need for orbital crossovers points (intersections between ascending and descending tracks) necessary to determine elevation changes. To provide adequate coverage of the West Antarctic Ice Sheet, it was determined that the ground tracks should provide coverage to at least 86° S. This inclination causes an uncovered area between 86° and the both poles.

The satellite has the opportunity for off-nadir pointing maneuvers up to $\pm 5^\circ$, i.e., to locations up to ± 50 km away from the reference track. However, in the polar regions ICESat is commanded to always point at the reference track (ideal, exact repeat track) to compensate for natural orbit drift and enable near repeats (± 150 m) of the tracks.

The nominal orbit altitude of 600 km is a compromise between the GLAS instrumental preference for lower altitudes and the orbit determination and spacecraft control preferences for higher altitudes. A higher altitude requires more laser power to achieve the required signal to noise ratio of reflected light that is proportional to the second power of the altitude. On the other hand, a lower altitude requires more fuel for more frequent orbit adjustments to compensate for atmospheric drag. Also, the accuracy of the precision orbit determination degrades at lower altitudes due to greater perturbations from atmospheric drag and undetermined gravity anomalies.

Originally, the ICESat mission was designed for a 183-day ground track repeat cycle yielding 14.5 km spacing between repeated tracks at the equator. However, problems with the first laser early in the mission forced a reduced schedule of operations [1], [52]. To complete a global coverage, the orbit was changed to a 91-day exact repeat orbit, with a 33 day sub-cycle. And instead of continuous measurements, the ICESat mission was replanned to operate the remaining two GLAS lasers for three 33-day campaigns per year. In a complete 91-day cycle there will be global data coverage with 30 km spacing between ascending tracks at the equator. For the 33-day sub-cycle this distance equals 90 km.

2.1.3 Measurement principle and instruments

ICESat uses laser altimetry to perform range measurements to determine the elevation of a spot on the Earth's surface. The elevation of the spot, illuminated by the laser, is determined from the sum of two vectors: the position vector of the laser instrument plus the range or altitude vector (the position vector of the illuminated spot centroid with respect to the instrument). The resultant vector is the position of the spot (or footprint), which can be readily transformed into geodetic latitude, longitude and elevation with respect to a reference ellipsoid.

In conventional laser altimetry systems, the range measurements are performed by measuring the time-of-flight (TOF) of a short pulse of infrared laser radiation. The instrument emits laser pulses that are reflected by the surface. Part of the reflected radiation returns to the laser altimeter, is detected, and stops a time counter, which was started when the pulse was sent out. The one-way range is then calculated by multiplying half the TOF with the speed of light. However, instead of just measuring the

TOF of the laser pulse until its first or last echo arrives, the reflected signal is sampled with a 1 GHz sampler. So, instead of measuring only the first or last pulse, the full pulse (also called laser waveform) is digitized. This waveform is used to derive the range to the surface. The advantage of this approach is that the vertical structure of the surface can be derived with high accuracy. Assume for example that the satellite is above a forest. In that case, a laser waveform of a single emitted pulse holds information about possible cloud layers, the density of a tree canopy at different heights, the height and density of understory vegetation, and even about surface slope and roughness.

The ICESat satellite consists of a spacecraft with only one scientific instrument, the Geoscience Laser Altimeter System (GLAS). Additionally there are star trackers, and an on-board GPS receiver, see figure 2.1. GLAS has three lasers (mentioned as Laser 1, 2 and 3), with only one laser operating at a time. Each laser produces a 1064 nm pulse for altimetry and lidar, but a doubler crystal converts this to a 532 nm wavelength pulse, which yields a more sensitive determination of the vertical distribution of clouds and aerosols [54]. The operating laser pulses at 40 Hz and the transmitted laser pulse illuminates a spot on the Earth's surface with a diameter of ~ 65 m, except when optically thick clouds obscure the surface. Successive spots are separated on the Earth's surface by 172 m, which results from the 7 km/sec orbital motion and the 40 Hz laser pulse repetition rate. The echo pulse is captured by a 1 m diameter telescope and directed to an analog detector, digitized along with a digitized record of the transmitted pulse and telemetered to the ground.

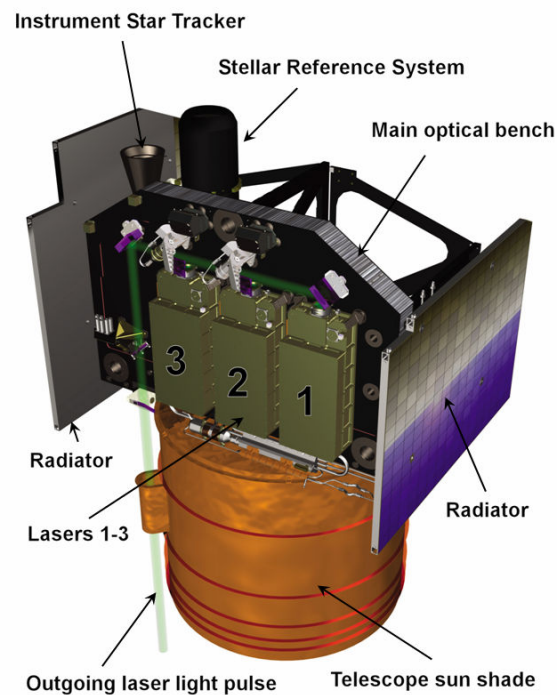


Figure 2.1: *The GLAS instrument, taken and adapted from [36].*

The position vector of the laser instrument is determined using a "Blackjack" dual frequency GPS receiver. The ground-based Satellite Laser Ranging (SLR) network provides tracking data that will support validation of the GPS-determined orbit as well as a passive backup tracking system.

To be able to calculate the location of the GLAS footprint and its associated elevation, also the laser-pointing direction has to be known. To achieve the mission science requirements, it is necessary to determine this direction with a precision better than 1.5 arc second (1σ) [79]. This angle is measured relative to inertial space by the GLAS stellar reference system. The orientation of the rigid GLAS optical bench is determined relative to the star field using a zenith-viewing star camera (Instrument Star Tracker) and precise gyroscopes for noise smoothing. A laser reference sensor measures the orientation of each laser beam with respect to the same optical bench. Although, the mounting of the GLAS instrument

to the spacecraft will distort in response to thermal variations in orbit, the distortions can be monitored and modeled. More details about this process and the used instrumentation can be found in [53].

2.1.4 Data processing and products

This section treats the basics of the processing of the raw laser waveforms. Here also the error budget is given for a single-shot measurement, followed by an overview of the available data products.

Data processing

All parameters are derived from the digitized waveform in ground-based data processing, done by the ICESat Science Investigator Processing System with support from the Center for Space Research at the University of Texas. For a schematic overview of the ICESat mission operations, see [81].

The range to the mean surface within the laser footprint is determined from one-half the measured time from the transmitted pulse to the time of receipt of the echo pulse reflected from the surface, taking into account the pulse spreading. The transmitted pulse has a Gaussian shape that is affected by for instance the surface height distribution within the footprint, forward scattering in the atmosphere, but also saturation. Saturation is related to the fact that measurements made with high transmit energies to flat ice surfaces through a clear atmosphere produce stronger than expected echo pulses. Due to saturation, the waveforms become distorted (flat-topped and broadened, followed by an abrupt signal decrease and oscillations) when the return energy exceeds the linear response range of the receiver [1]. To minimize occurrences of saturation, GLAS uses an automated detector gain adjustment. Rapid shot-to-shot changes from low to high peak received energy (due to transitions from low to high reflectance, steep to flat relief, and/or cloudy to clear sky) can cause the gain to be too high, resulting in "high-gain" saturation. "Low-gain" saturation occurs when the energy exceeds the receiver dynamic range at the lowest gain. Basically it can be assumed that under ideal circumstances, i.e. a clear atmosphere and a non-sloped and smooth surface, the returned waveform has a Gaussian shape as well. It turns out that over oceans, sea ice, and most of the ice sheets, the returned waveform is a single Gaussian. But also when these circumstances are less ideal, it turns out that the returned waveform can be described as a sum of Gaussian components. This is the case over land and more complicated ice sheet regions.

Figure 2.2 provides a schematic overview of the waveform processing. For a detailed discussion of the algorithms and equations, see [6]. Notice that for the different ICESat altimetry data products different parameterizations are used. So the algorithms are the same for all surface types; the differences in the final results come from the use of different sets of parameters to drive these algorithms. Two sets of parameters are used, one that satisfies the ice sheets, sea ice and ocean processing requirements (standard parametrization), and one that satisfies the land requirements (the alternative parametrization).

The accuracy of the derived position vector of the footprint depends on the contribution of various error sources, see table 2.1. For these values it is assumed that the laser pointing error is 1.5 arc second and the surface slope is 1° . The nature of these errors is a combination of random and systematic. The GLAS range measurement precision is characterized as random, but most of the other errors are systematic for successive pulses. However, the components of the error budget are mostly uncorrelated with each other. For those errors that are correlated on successive pulses, the errors for a series of measurements over a given location during the life of the mission tend to be random rather than systematic. One exception to this are geographically-correlated errors in the absolute height of the orbit calculations. However, these errors can be mostly time-independent if the orbits are systematically processed with the same gravity model calculation procedures and therefore not important for elevation change measurements. Another exception is the atmospheric forward scattering if the scattering clouds have significant seasonal or interannual variations. For a more detailed discussion of the separate error sources see [79].

Data products

Table 2.2 provides an overview of the ICESat/GLAS data products. The raw data collected on ICESat and transmitted to the ground are level-0 and these data are archived at the ICESat Science Investigator-led Processing System and the National Snow and Ice Data Center. A level-1A product is generated from

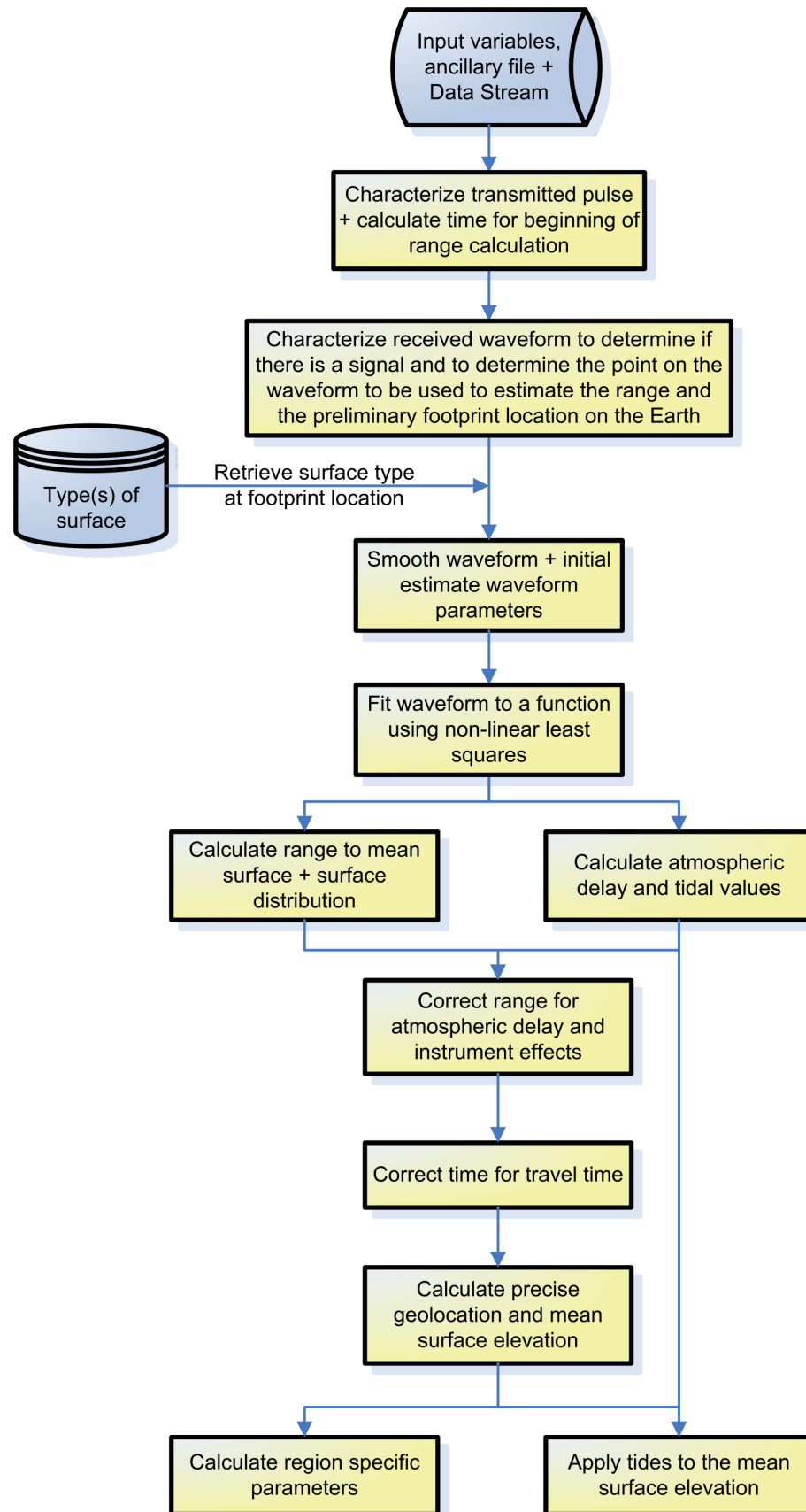


Figure 2.2: Schematic overview of the waveform processing.

Source	Error (cm)
GLAS range measurement precision	10
Radial orbit determination	5
Pointing determination	7.5
Atmospheric delay	2
Atmospheric forward scattering	2
Other (tides, etc.)	1
Root Sum Square	13.8

Table 2.1: Single-shot error budget for ICESat elevation measurements, taken from [79]

Product ID	Level	Content
GLA00	0	Global Instrument Packet (Telemetry data)
GLA01	1A	Global Altimetry Data
GLA02	1A	Global Atmosphere Data
GLA03	1A	Global Engineering Data
GLA04	1A	Global Laser Pointing Data
GLA05	1B	Global Waveform-based Range Corrections Data
GLA06	1B	Global Elevation Data
GLA07	1B	Global Backscatter Data
GLA08	2	Global Planetary Boundary Layer and Elevated Aerosol Layer Heights
GLA09	2	Global Cloud Heights for Multi-layer Clouds
GLA10	2	Global Aerosol Vertical Structure Data
GLA11	2	Global Thin Cloud/Aerosol Optical Depths Data
GLA12	2	Antarctic and Greenland Ice Sheet Altimetry Data
GLA13	2	Sea Ice Altimetry Data
GLA14	2	Global Land Surface Altimetry Data
GLA15	2	Ocean Altimetry Data

Table 2.2: ICESat/GLAS standard data products.

level-0 with reversible conversions to engineering units. The level-1A altimetry data (GLA01) include the transmitted and received waveforms from the instrument. Level-1B waveform parametrization data (GLA05) include output parameters from the waveform characterization procedure and other parameters required to calculate surface slope and relief characteristics. Level-1B elevation data (GLA06) include surface elevation, surface roughness assuming no slope, surface slope assuming no roughness, and geodetic and atmospheric corrections for range measurements. Both level-1B products are geolocated to the center of the laser footprint. GLA06 is used in conjunction with GLA05 to create the level-2 altimetry products (GLA12-15). Level-2 altimetry data provide surface elevations for ice sheets (GLA12), sea ice (GLA13), land (GLA14), and oceans (GLA15). Data also include the laser footprint geolocation and reflectance, as well as geodetic, instrument, and atmospheric corrections for range measurements.

2.2 The GRACE mission

The GRACE mission, a joint project between NASA and the DLR, is the second mission under the NASA Earth System Science Pathfinder program. This program is intended to address unique, specific, highly focused scientific issues and provide measurements required to support Earth science research. This section provides an overview of the GRACE mission and its main characteristics. Section 2.2.1 starts with an overview of the mission science objectives, followed by an overview of the main characteristics of this mission in section 2.2.2. In section 2.2.3 the measurement principle and instruments are described. This section ends with a short introduction into the processing of the raw data and an overview of the available data products.

2.2.1 Mission science objectives

The primary science objective of the GRACE mission is to provide, with unprecedented accuracy, global, and high-resolution estimates of the mean and time-variable part of the Earth's gravity field. Secondary objective is the measurement of several hundred globally distributed profiles per day of the excess delay or bending angle of GPS measurements caused by the ionosphere and atmosphere [15].

The data obtained by GRACE is used for many scientific applications. Estimates of time variable components of the gravity field help for a better understanding of time variable processes in oceanography, hydrology, glaciology or solid Earth sciences like deep ocean current changes, soil moisture changes, mass balance of ice sheets and glaciers, mantle and lithospheric density variations and Post Glacial Rebound. The improved knowledge of the mean geoid is useful for precise positioning, orbit determination, leveling etc. The profiles of the excess delay of GPS measurements are used in atmospheric/climate research, but also for weather forecasting.

2.2.2 Orbit characteristics

The twin satellites, see figure 2.3, were launched on March 17, 2002, into a ~ 500 km altitude orbit with an 89.5° inclination, separated from each other by 220 ± 50 km along track. The near-polar orbit was chosen to get a homogeneous and global coverage, necessary for a precise estimate of the gravitational potential.

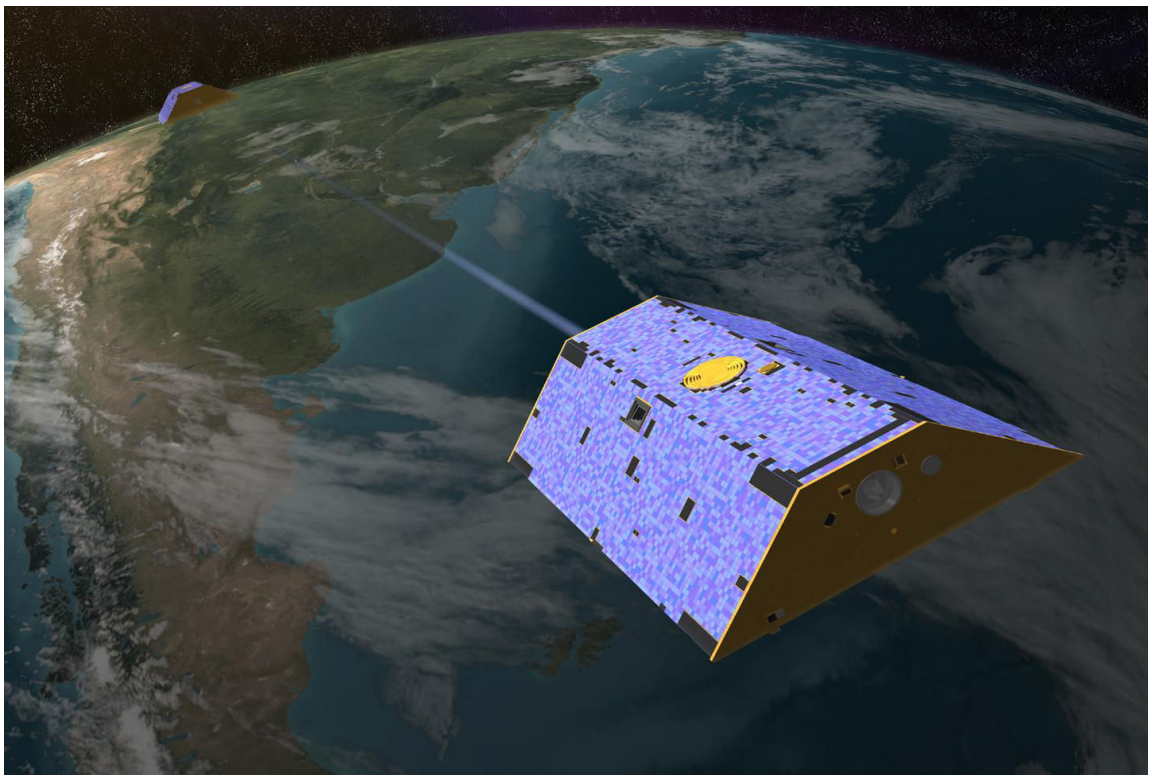


Figure 2.3: *The GRACE satellites in orbit, taken from [32].*

The altitude is a compromise between gravity field solutions, that desire an even lower altitude, and atmospheric/ionospheric applications, that would benefit from a higher altitude. Due to atmospheric drag the altitude of the GRACE satellites decreases. The predicted natural decay depends on the magnitude of the actual solar activity maximum. The initial altitude of about 485 - 500 km was chosen

in order to guarantee a multi-year mission duration even under severe solar activity conditions. To ensure the mission lifetime of 5 years, the altitudes of both satellites can be re-boosted once, if deemed to be necessary. At the moment of writing, the satellites are already longer than 5 years in orbit and because of the fact that there is no successor of this mission yet, the mission lifetime is recently extended to 2014.

2.2.3 Measurement principle and instruments

For some decades the use of satellites for gravitational field determination was based on tracking the satellite orbit and comparing the observed orbit with a reference one, which would have been obtained if the satellite moves in a reference gravitational field. The differences between the observed orbit and the reference orbit allowed to determine the difference between the actual gravitational field and the reference one. Currently, there are two concepts, which are based on the same physical principle: satellite-to-satellite tracking (SST) and satellite gravity gradiometry (SGG). Both concepts use as observable the relative motion of test masses under the influence of the gravitational field: ranges, range-rates, and changes of range-rates for SST and acceleration differences of very short baselines for SGG [27].

For SST, the relative motion along the line-of-sight of two or more satellites is measured. There are two variants of this concept. The high-low variant uses one low-flying satellite, whereas the other satellite(s) (for instance GPS satellites) are in a high altitude orbit. This concept is realized in the Challenging Mini Satellite Payload (CHAMP) satellite gravity field mission. The low-low variant, realized with GRACE, uses two satellites flying in orbits of about the same altitude (200-500 km).

As the GRACE satellites fly in formation over the Earth, the precise speed of each satellite and the distance between them is constantly communicated via a microwave K-band ranging instrument. A change in mass of the surface beneath results in a change of the orbital motion of each satellite. Notice that an increase in mass causes an increase in the gravitational force exerted, which keeps the satellites in orbit. The change in orbital motion causes a change in distance between the two satellites that can be measured using the K-band instrument. So, when the front satellite approaches an area of higher gravity, it will be pulled toward the area of higher gravity and speed up, resulting in an increased distance between both satellites. As the satellites straddle the area of higher gravity, the front satellite will slow down and the trailing satellite will speed up, so the distance becomes smaller. As the trailing satellite passes the area of higher gravity, it will slow down and the lead satellite will not be affected. In this case the distance becomes larger again.

In order to derive the Earth's gravitational field, the range measurements are used in combination with accurate measurements of the satellites positions as well as accelerometer data to correct for the non-gravitational accelerations.

The K-band ranging system is the major instrument on-board the two identical GRACE satellites that measures the dual one-way range change between both satellites with a precision of a few μm . (The precision of the range rates is equal to $\sim 0.3\mu\text{m/s}$). Here carrier phase signals on two frequencies are used, allowing for ionospheric corrections.

The accelerometer measures all non-gravitational accelerations, for instance caused by atmospheric drag. For the correct interpretation of the accelerometer measurements, the attitude of the accelerometer is measured with high precision by a star camera assembly. The attitude data is also needed to project the offsets between the center of mass of each satellite and the K-band instrument/antenna, on the line of sight between both satellites.

A GPS TurboRogue Space Receiver is used for precise orbit determination with cm-accuracy, coarse positioning ($<50\text{m}$) for real time use by the attitude and orbit control system, time tagging of all payload data and atmospheric and ionospheric profiling.

The GRACE satellites also have a laser retro reflector that enables Satellite Laser Ranging (SLR). This data is used for precise orbit determination in combination with GPS tracking data and for calibration

of the on-board GPS Space Receiver.

2.2.4 Data processing and products

The observed ranges or range rates within a certain time span are used to estimate the Earth's gravity field for that corresponding time span. Subsequent estimations of the Earth's gravity field enable us to derive temporal variations that can be related to mass changes. First some general ideas behind the estimation of the Earth's gravity field are discussed. We will provide only a very limited introduction into this topic and the interested reader is referred to literature, see for instance [13] and [27]. The last part of this section provides an overview of the available data products.

Data processing

In section 2.2.3 it was explained how the distance between both satellites changes due to a change in mass at the surface beneath. These range or range rate measurements are directly related to the instantaneous position and velocity (or trajectory) of both satellites. These trajectories contain the influence of the total exterior gravitational potential (and other forces) on each satellite. So, the satellites acceleration caused by the Earth's attraction is equal to the gravitational field at a particular point. The gravitational field is equal to the gradient of the Earth's gravitational potential.

Outside of the attracting masses, the gravitational potential of the Earth is a harmonic function and can be expanded into an infinite series of spherical harmonics ([21]):

$$V(r, \theta, \lambda) = \frac{GM_E}{R} \sum_{l=0}^{\infty} \sum_{m=-l}^l \bar{C}_{lm} \left(\frac{R}{r}\right)^{l+1} \bar{Y}_{lm}(\theta, \lambda) \quad (2.1)$$

Where:

V	gravitational potential
r, θ, λ	spherical coordinates of given point (distance from the origin of the coordinate system, co-latitude, and the longitude, respectively)
GM_E	geocentric gravitational constant, product of the gravitational constant G and the mass of the Earth M_E
R	major semi-axis of a reference ellipsoid
L_{max}	maximum or truncation degree
\bar{C}_{lm}	Stokes coefficients: \bar{c}_{lm} for $m \geq 0$, and \bar{s}_{lm} for $m < 0$
l, m	degree and order
$\bar{Y}_{lm}(\theta, \lambda)$	4π -normalized surface spherical harmonics

In practice this series expansion is truncated at a certain maximum degree L_{max} . The maximum degree of this representation indicates the spatial resolution R_s of the gravity field, see equation 2.2. Here 20 000 is approximately half the circumference of the Earth.

$$R_s [\text{km}] = \frac{20\,000}{L_{max}} \quad (2.2)$$

The mathematical model for the dependence between the range measurements (and so the trajectories of both satellites) and the influence of the total exterior gravitational potential is given by the dynamic equation of motion for each satellite,

$$\ddot{\vec{r}}_i = \vec{f}_i, \quad i = 1, 2 \quad (2.3)$$

Where:

\vec{r}	the position vector in an Earth-centered inertial frame for satellite i
\vec{f}	the sum of gravitational and non-gravitational accelerations for satellite i

Therefore, a collection of range measurements, over a suitable time span, with suitable or sufficient geographical coverage, and properly corrected for non-gravitational effects, is implicitly representative of the exterior gravity field of the Earth and its variations within that time span. Mostly, one month of measurements is used to estimate the gravity field for that month.

A proper parametrization enables to estimate the gravitational potential parameters from the selected data span. In practice different approaches are used that will not be discussed here. Amongst other differences, for instance in noise reduction strategies, the different used orbits mainly causes the differences between the different GRACE solutions [51]. Normally the estimates of the gravitational potential parameters are made of updates to an a priori best-known gravitational potential model, which is part of the so-called background model. The background model consists of mathematical models and the associated parameter values, which are used along with numerical techniques to predict a best-known value for the observed ranges or range rates. The background model incorporates, amongst others, the knowledge about the static gravitational potential and its secular variations, solid earth tides, ocean tides, atmospheric tides, non-tidal atmosphere and oceanic variability, pole tides and influences of the Sun, Moon and planets. This background model differs from the true gravity field of the Earth by errors of omission of either certain geophysical phenomena or spatial components; and by errors of commission by having incorrect models or parameter values for these phenomena [3].

The updates to the background model are computed such that the differences between the observed and predicted values are minimized in a least-squares sense. This update may be regarded as the new gravity information available from GRACE.

Data products

The responsibility for extraction of Earth gravity models is with the GRACE project Science Data System (SDS). The SDS is distributed between the University of Texas Center for Space Research (CSR), Jet Propulsion Laboratory (JPL) and the GeoForschungsZentrum (GFZ).

The GRACE data is divided into three levels. The level-0 data are the result of the data reception, collection and decommutation by the raw data center of the mission operation system. The raw data is calibrated and time-tagged in a reversible sense, and labeled level-1A. These data undergo extensive and irreversible processing, and are converted to edited and cleaned data products at 1-5 second rates. The products, labeled level-1B, include among others, the inter-satellite range, range-rate, range-acceleration, the non-gravitational accelerations from each satellite, the pointing estimates, the orbits, etc. The level-1B products are processed to produce the monthly gravity field estimates in form of spherical harmonic coefficients. These estimates are labeled level-2. Occasionally, several months of data are combined to produce an estimate of the mean or static gravity field.

Chapter 3

The preparation of the ICESat data

In order to be able to estimate the mass balance using ICESat data, elevation differences between overlapping footprints are needed. This chapter describes the methodologies and procedures that are developed in the course of the project to retrieve these overlapping footprints from the GLA12 data product. Starting with a short description of the raw data products in section 3.1, this chapter continues with the conversion of the raw data products to the ASCII format. The steps to organize and split these converted files are described in section 3.3. After that the newly developed methodology to retrieve Crossing Track Pairs (CTPs) and Overlapping Track Pairs (OTPs) is explained in section 3.4. This step results in two sets of points that fulfill the criterion that each point in the first set, has a distance smaller than 120 meter to its corresponding point in the second set. From these sets, subsets are retrieved, based on the stricter criterion of real overlap of the actual corresponding footprints. This procedure is explained in section 3.5.

To get an unbiased estimate of Greenland's mass balance, not all Overlapping Pairs (OPs = both CTPs and OTPs) can be used. First of all, only the OPs located on the ice sheet are of interest. Secondly, some observations are biased by errors from different sources, so they must be removed. During the processing of the raw waveforms, these measurements are indicated as bad by several quality flags. Beside these quality flags, also other parameters are used to clean up the dataset. All cleaning criteria are discussed in section 3.6.

CPU times in this chapter refer to a 2GHz CPU, 1024 RAM PC.

3.1 The raw data product

The raw input consists of the so called 'data granules' of the GLA12 product [80]. In principle the latest releases of all the available data granules (at 01-02-2007) from the different laser campaigns are used. Table 3.1 provides an overview of the available data, the release numbers and some other characteristics of the data. So, we have data from seven different laser campaigns and three different releases. The GLA12 data granules are archived at 14 orbits per granule, starting and stopping at a demarcation of $\pm 50^\circ$ latitude. This corresponds to approximately one day of data. In total there are 273 data granules with an approximate file size of 52 mB per granule.

The GLAS products are binary files where all records have the same length. The data records contain elements in scaled integer binary format. One record consists of one second of data. With a laser frequency of 40Hz this means that each record contains 40 laser shots of data. Besides of the actual elevations, each record consists of 90 parameters, see [39] for an overview of all parameters that are available for the latest release (28). Parameters are stored per shot or per record, for instance the elevations are stored per shot while the surface temperature is stored per record. During the time more parameters become available, e.g. the surface temperature is not available for release 18.

Laser	Duration (days)	Start Date	End Date	Orbit Repeat (days)	Release Nr.
1	38	2003-02-20	2003-03-29	8	18
2A	9	2003-09-25	2003-10-04	8	26
2A	45	2003-10-04	2003-11-18	91/33	26
2B	34	2004-02-17	2004-03-21	91/33	28
3A	37	2004-10-03	2004-11-08	91/33	28
3B	36	2005-02-17	2005-03-24	91/33	28
3D	35	2005-10-21	2005-11-24	91/33	28
3E	34	2006-02-22	2006-03-27	91/33	28

Table 3.1: *Laser operation campaign summary. Notice that there are more laser campaigns, but not all campaigns are available to the public.*

These data granules form the actual input for the processing steps that will be discussed in the next sections. A schematic overview of these steps is given in figure 3.1.

3.2 Convert to ASCII

The so called 'IDL - reader' [41] is used to convert the data granules to ASCII format. This reader can run under the software environment Interactive Data Language (IDL) or IDL Virtual Machine (IDL VM). This program needs a so called 'control file' where the input file, output file and release number have to be specified. To speed up this step, a simple program was written that automatically writes a new control file based on a file that contains all the file names. After that the IDL reader was started manually (running under IDL VM).

The GLA12 distribution contains both the Greenland and Antarctic ice sheets. This means that a significant reduction of the file sizes can be reached by removing the data on the Antarctic ice sheet. Because of the fact that both ice sheets are on a different hemisphere, the data screening is based on the latitude of the shot locations. Due to this screening procedure the amount of information is reduced 10 times. In total this step takes approximately 2 hrs of CPU time.

3.3 Organize and Split

Despite the fact that the file sizes are halved to 25 MB, the files are still too large for processing in Matlab. Therefore, the files are split per track and based on the information type, i.e. information per shot or per record. A track means one pass over of the ICESat satellite over the Greenland area.

For this step a program is written in the Delphi programming language Object Pascal. This program reads all the converted data granules, stores the shot info and the record info in two separate arrays, splits the arrays per track and prints the tracks to a file.

During the reading process, the parameters are stored in two different arrays; the first array contains all the shot info while the second array contains the record info. The link between these two arrays is established by storing a record identifier (ID) in the shot info array. As a result of this step, two arrays are filled with the data on only the Greenland ice sheet. In the second step the arrays are split into different tracks. This splitting step is based on the time difference between the successive records. Due to gaps in the data this time difference is not constant. However, assuming a track length of maximal 40 latitudinal degrees and a distance of 170 meter between the footprints, the approximated maximal time difference between 2 points of the same track can be computed with equation 3.1. Here the Earth is

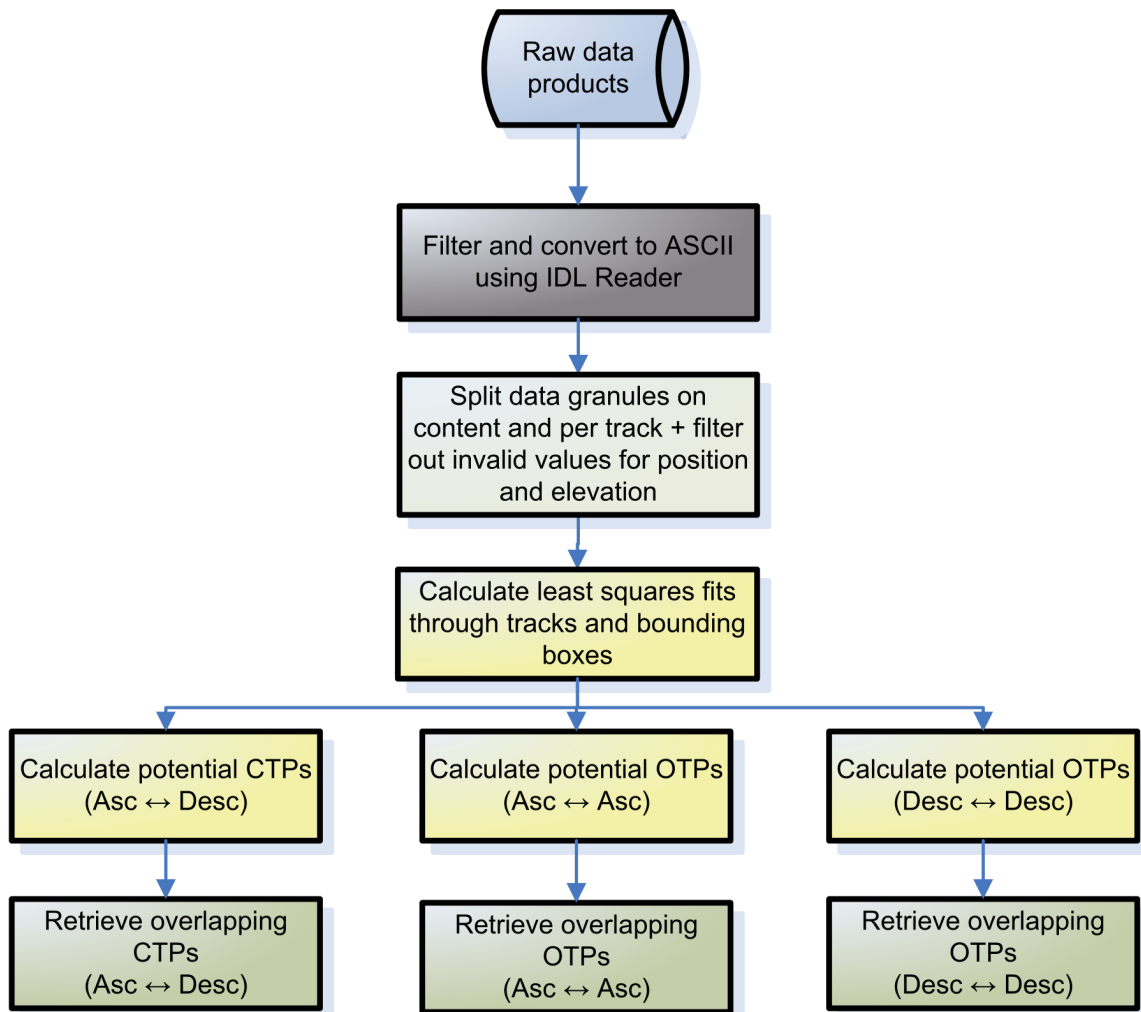


Figure 3.1: Schematic overview of the process to retrieve the overlapping footprints.

approximated as a perfect sphere with a circumference of 40 000 km.

$$\Delta T_{Tr} = \frac{40 \cdot 10^6 \cdot 40^\circ}{360^\circ V_g} \quad (3.1)$$

Where:

ΔT_{Tr} time difference between first and last shot of a track
 V_g ground velocity, i.e. 40 Hz · 170 m

So, when the time difference between two successive shots is larger than 1000 seconds, both shots belong to different tracks. By taking the order of the latitudes into account, it is determined whether the track is an ascending or descending track.

In the last step of the procedure, the split arrays are stored. When a data granule consists of 5 tracks, it is stored in 5 files that contain the shot info and 5 files that contain the record info.

Not all data from GLAS are suitable for processing and some data may be missing. This is indicated by so called 'invalid values', large numbers that vary with the data type. Only when the latitude, longitude and elevation values are all valid, all shot info is stored.

This step takes approximately 1hr of CPU time and results in 1404 different tracks; 764 ascending and 640 descending tracks.

3.4 Calculation of the potential CTPs and OTPs

Our calculation of the mass balance change with altimetry data is based on the elevation changes at the Overlapping Pairs (OPs). These OPs are footprints from different tracks, where the footprints have a nonempty intersection. A distinction is made between two kinds of OPs, the Crossing Track Pairs (CTPs) and the Overlapping Track Pairs (OTPs). The CTPs are defined as OPs that result from the crossing between the ascending and descending tracks. OTPs are defined as OPs that occur when two tracks of the same orientation do overlap, i.e. two ascending or two descending tracks. Here it is assumed that there is maximal one CTP per combination of one ascending and one descending track. When the angle between the two tracks is small it might be that there are more OPs in both tracks, but this is mostly not the case in practice.

To find all the CTPs and OTPs it is necessary to collate every track with all the other tracks. If N_a is the number of ascending tracks and N_d is the number of descending tracks the number of evaluations ($\#E$) to find all the CTPs equals:

$$\#E_{CTPs} = N_a \cdot N_d \quad (3.2)$$

To find all the OTPs the number of evaluations equals:

$$\#E_{OTPs} = \frac{1}{2}(N_a - 1)N_a + \frac{1}{2}(N_d - 1)N_d \quad (3.3)$$

For performance reasons another strategy is chosen. In this strategy the potential CTPs and OTPs are selected in a two step procedure. First the track combinations are identified that possibly hold a potential CTP or some potential OTPs. In the second step these combinations are evaluated, which results in the real potential candidates. Figure 3.2 provides a general overview of this procedure.

Without mentioning, further calculations are done in a local Cartesian coordinate system. This implies a conversion from the geographical coordinates to the local Cartesian system. The local Cartesian coordinate system is chosen such that the Z-axis is pointing through the center of Greenland (71° N, 42° W), the X-axis is pointing through (19° S, 42° W) and the origin is in the center of the Earth. When we calculate a distance, this distance is the projected distance between two points on the XY-plane.

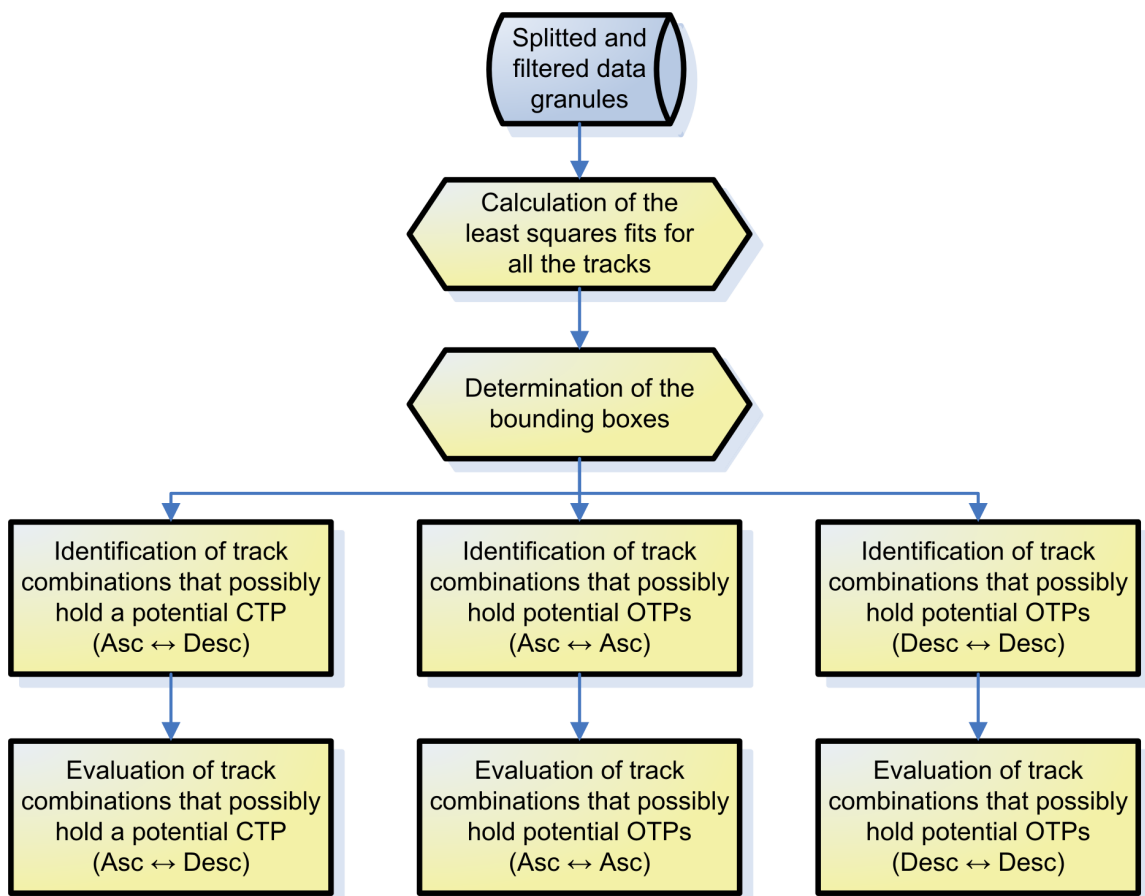


Figure 3.2: Schematic overview of the calculation of the potential CTPs and OTPs.

The track combinations are selected based on a bounding box overlap test. The centerline of such a bounding box is the best fitted line in the least squares sense through all the points in the track, while the maximal residuals determine the width of the box. In figure 3.3 the least squares fit is indicated with a black dotted line, the maximal residuals are indicated in green.

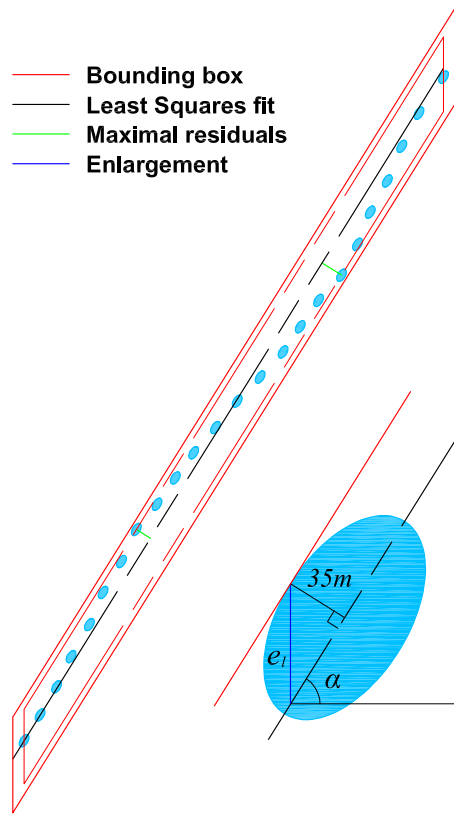


Figure 3.3: *The creation of the bounding boxes.*

Because of the size of the footprints, the bounding boxes are enlarged to ensure that no overlapping footprints are disregarded. The enlargement, indicated with e_l in figure 3.3, depends on the slope (α) of the least squares fit and the minor semi-axis of the ellipsoidal footprint. The latter value is fixed to 35 meter, which results in the following formula for e_l :

$$e_l = \frac{35}{\cos \alpha} [m] \quad (3.4)$$

If the area of intersection of two bounding boxes is larger than zero, the combination of both tracks holds a potential CTP or potential OTPs. The principle of the bounding box overlap test is visualized in figure 3.4. The red area is the intersection of the two bounding boxes.

The number of track combinations that possibly hold a potential CTP equals 291 117. This means that roughly 60% of the ascending tracks cross with the descending tracks. The total number of ascending track combinations that possibly holds a potential OTP is equal to 5 486, for the descending tracks this number is 4 078.

The next step in this procedure holds a brute force evaluation of all the potential track combinations, to retrieve the set of potential CTPs and OTPs. These pairs do not necessarily overlap in practice, but fulfill the criterion that the centers of their footprints are within a distance of 120 meter of each other. This distance is based on the maximum distance between two ellipses that results in an overlap, i.e. two times the maximum major semi-axis of the footprints. Notice that the shape of the footprint differs for the different laser campaigns [1]. In order to ensure that no potential CTPs and OTPs are disregarded, the maximum value of the major semi-axis is chosen that occurs in the dataset. Table 3.2 provides an

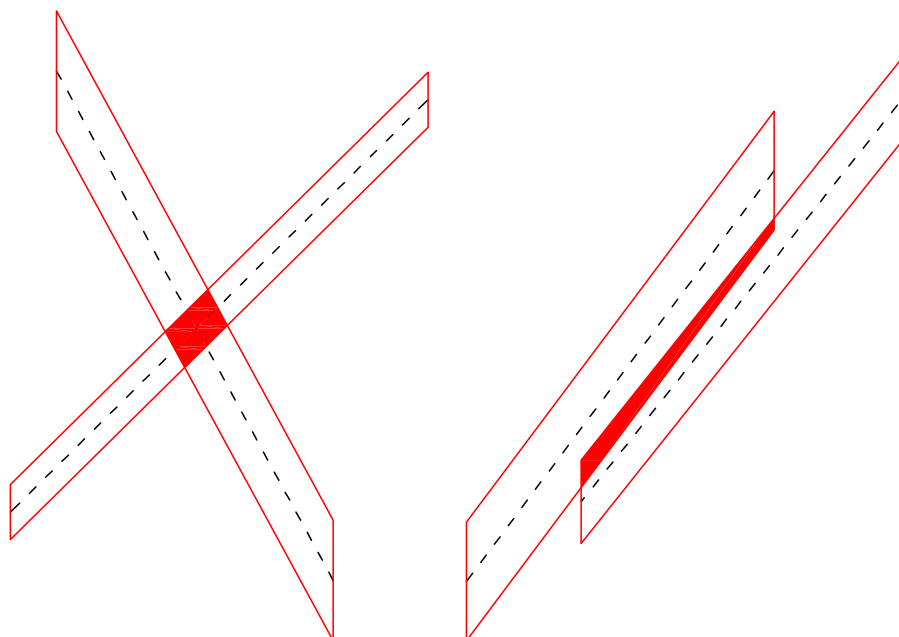


Figure 3.4: Principle of the bounding box overlap test.

Laser	Major semi-axis (m)	Minor semi-axis (m)
1	44.9	23.1
2A	56.6	27.3
2B	53.1	33.1
3A	11.5	11.3
3B	50.3	29.7
3D	27.8	23.7
3E	27.1	24.2

Table 3.2: Maximum values of axes footprint ellipses for the different laser campaigns

overview of the maximum values of the major and minor semi-axes of the footprints for the different laser campaigns.

For the validation of the potential CTPs and OTPs different algorithms are used, so both are discussed separately. The retrieval of the potential OTPs is rather straightforward. Given are two tracks for which it holds that the area of intersection of the bounding boxes is larger than zero. Required are the points of track 1 and track 2 that are within a distance of 120 meter of each other. Points outside the intersection of the bounding boxes of these tracks never overlap with points in the other track. Therefore only the distances between the points in the intersection are evaluated. If the smallest distance between a point of track 1 and the points of track 2 is smaller than 120 meter, all the information of the two points is stored in two separate arrays.

In principle the same procedure can be used for the determination of the potential CTPs. However, the strategy discussed here tries to determine the location of the crossing of the two tracks and evaluates a point pair most close to this location. This procedure is faster and provides also the location of the crossing of the two tracks. Again two tracks are given and two points, one of each track, are required that are within a distance of 120 meter of each other. It makes sense that these points are close to the location of the crossing. For computational efficiency it was assumed that there was one CTP per combination of two tracks. To estimate the location of the crossing of the two tracks, an iterative scheme is used. The location of the crossing between the least squares fits of a line through both tracks, using all the points in the track, is used as the initial estimate. Now for both tracks the point is

identified most close to this initial estimated location. A new estimate of the location of the crossing is estimated, based on the least squares fits of a line through both tracks, using the identified points and the 25 previous and next points in the track. So instead of all the points, a limited set of points is used to estimate the parameters of the line, called a local fit. For all iterations, the same number of points is used. After each iteration the location of the estimated crossing becomes closer to its 'true' location. After some iterations, the same points in both tracks are used for the estimation, which means that the estimated location will not change anymore. Figure 3.5 illustrates this procedure.

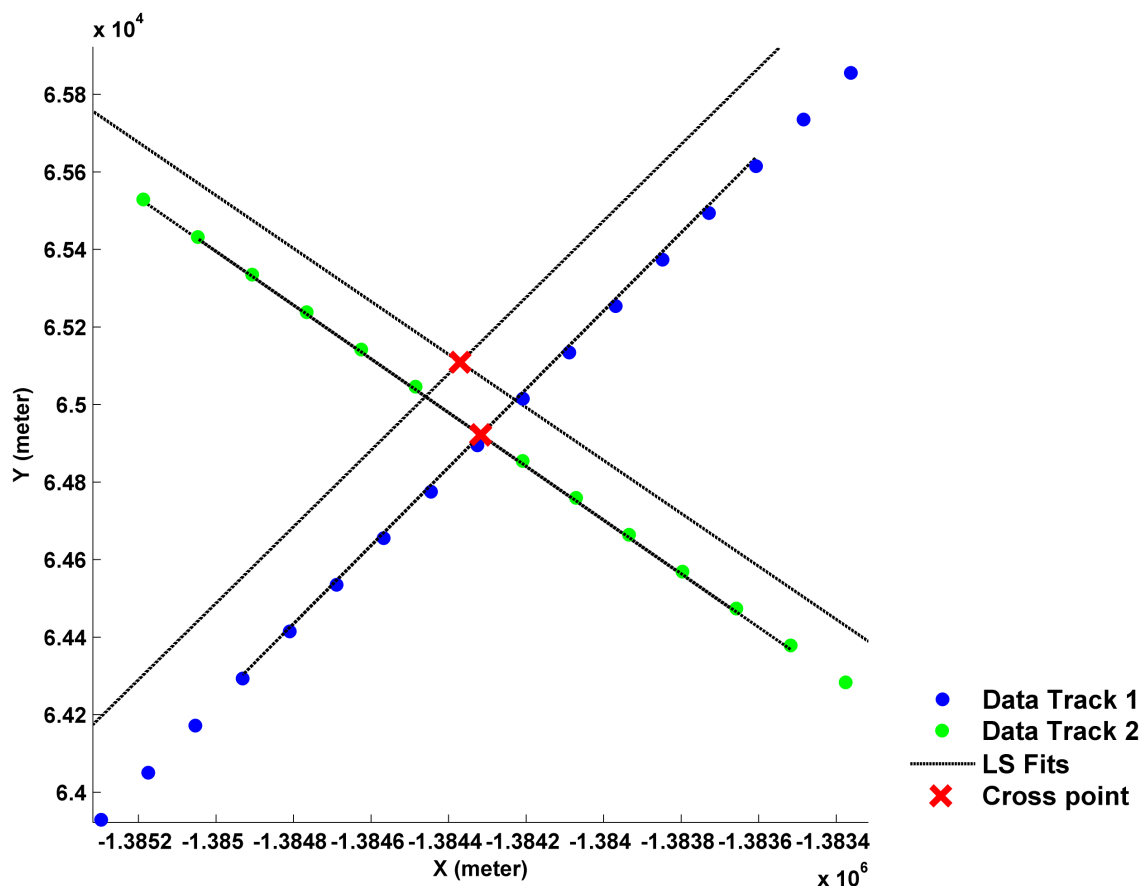


Figure 3.5: *The iterative procedure used to estimate the location of the crossing of one ascending and one descending track.*

In the last step, three points in both tracks are identified and used to evaluate whether there is a point pair that fulfill the distance criterion. The middle one of these three is the point in the track most close to the crossing of the tracks. The other ones are the previous and next one in the track.

The information of the identified potential CTPs is stored in the same way as for the OTPs. For both the potential CTPs and OTPs an array is stored that holds the track IDs and point/shot IDs. This array in combination with the record IDs is used to retrieve the record info. Table 3.3 provides an overview of the identified track combinations and the number of potential CTPs and OTPs. Also this table provides an overview of the reduction of possible evaluations by using the bounding box overlap test. In terms of performance both the determination of the potential CTPs and OTPs can be done in one day, i.e. 12 hrs of CPU time for the CTPs and 12 hrs of CPU time for the OTPs.

Type OP	Total #Tr. Combi.	#Pot. Tr. Combi.	Reduction	#Pot. Cand	#Real OP
CTPs	488 960	291 117	40%	206 384	19 446
OTPs-Asc	291 466	5486	98%	4 138 911	276 338
OTPs-Desc	204 480	4078	98%	4 885 689	352 648

Table 3.3: The number of potential and real CTPs and OTPs.

3.5 The real overlap test

The validation whether two footprints really overlap, requires a brute force evaluation of the potential CTPs and OTPs. The information about the footprints is stored in the record info files. Based on the array with the track IDs, point IDs and record IDs this information is retrieved. Because of the fact that no standard algorithms are available, an approximation is used. That is, the analytical ellipses are approximated by a polygon with a finite number of vertices. When this number is sufficiently large, the error is negligible. Using this approximation two footprints are said to overlap when the area of intersection of both polygons is unequal to zero, see figure 3.6.

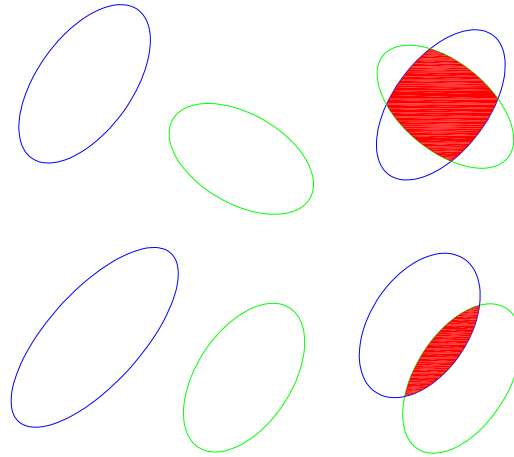


Figure 3.6: Overlapping and non-overlapping footprints.

It makes sense that there is a trade off between the number of vertices of the polygon and the performance of this step. When the number of vertices equals 100, the evaluation of all potential CTPs requires 3 hrs of CPU time, for the OTPs this is 60 hrs of CPU time. However, this step can be easily divided over different computers. Table 3.3 provides an overview of the number of real overlapping points.

3.6 Cleaning of the dataset

In total we have 648 432 geometrically overlapping footprints. This dataset still contains unusable data due to for instance the fact that not all corrections could be applied properly. This section provides an overview of all criteria used to clean up the dataset.

3.6.1 OPs not on Ice sheet

Figure 3.7 shows a Digital Elevation Model (DEM) based on all points from the MAIN file (file that contains the first points in time). This figure shows that a significant part of OPs are not located on

the Greenland ice sheet, even not on the mainland of Greenland itself. Obviously these OPs should not be taken into account for the estimation of the mass balance. In the first step of the cleaning process, these pairs will be removed.

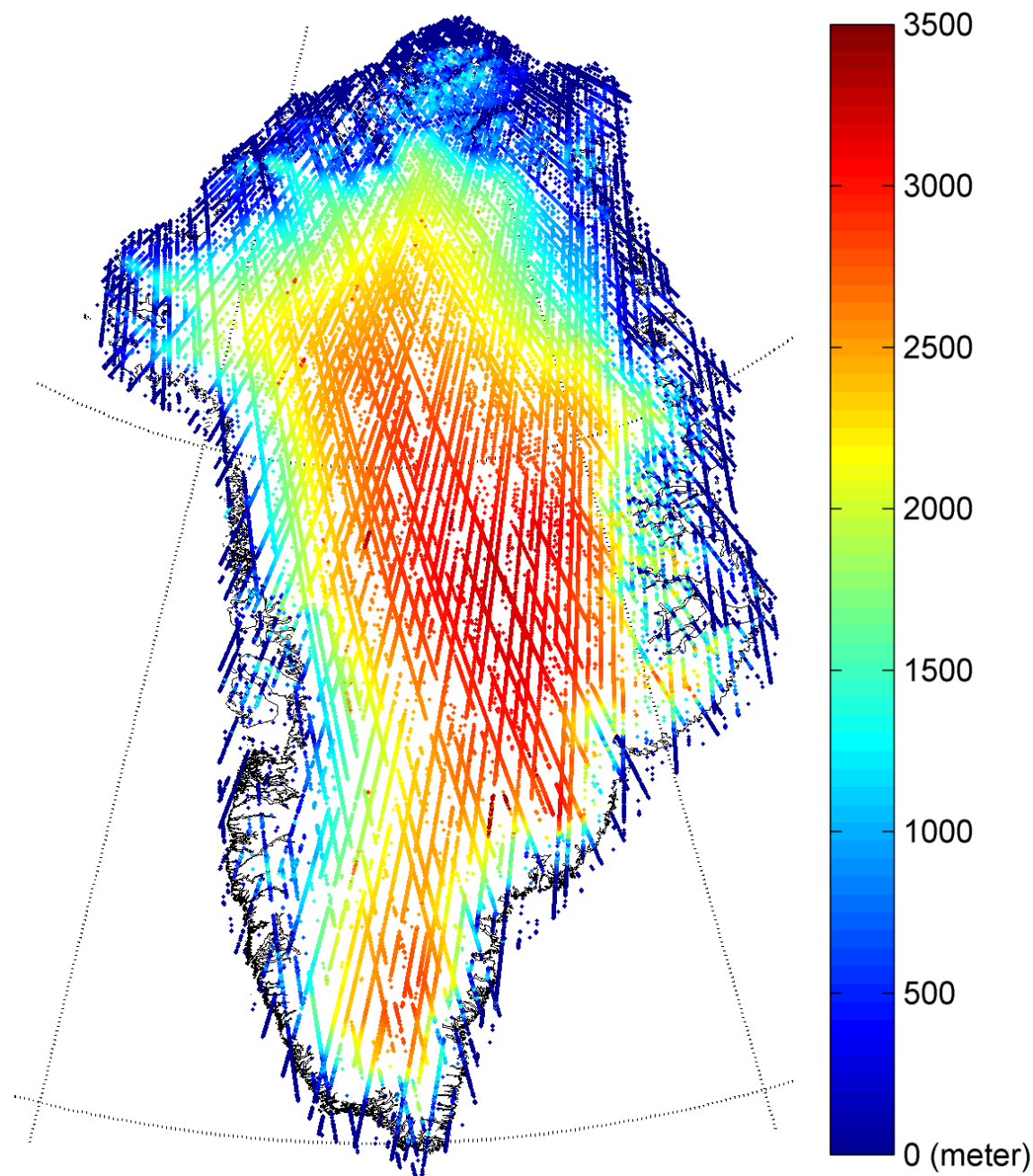


Figure 3.7: *Digital Elevation Model (DEM), where elevations are defined with respect to the mean sea level.*

One idea to remove these OPs is by classifying the waveforms to retrieve the surface type of the footprint. Only the footprints classified as ice sheet will be used for further processing. Due to the fact that we only use the GLA12 data product, consisting of elevations only, this idea cannot be implemented. However, this data product contains several parameters related to the waveform. In this study we made an attempt to use the ratio between the received and transmitted energy. The ratio between the received and transmitted energy has to be used because of the fluctuations in the transmitted energy, [1]. It makes sense that due to the better reflection properties of ice, this ratio is higher for an ice sheet surface as for a rock surface. Here it must be noticed that snow cover influences the results of this classification,

Flag name	Group	Indicates
<i>atmQF</i>	1	from LIDAR channel if conditions for forward scattering were favorable.
<i>AttFlg2</i> ^{*1}	1	whether attitude is calculated/predicted, and if there are noted problems with attitude sensor.
<i>CorrStatFlg</i>	1	for each geophysical correction which algorithm or model was used.
<i>ElvuseFlg</i>	1	whether elevations on record should be used or not.
<i>OrbFlg</i>	1	quality of orbit, whether predicted or precision orbit is used, loss of GPS data, maneuver-degraded, etc.
<i>rngCorrFlg</i>	1	applied geophysical or instrument corrections to the range in the calculation of the elevation on this record.
<i>APID_AvFlg</i>	2	for each second, available, missing or filled level-0 packets.
<i>timecorflg</i>	2	instrument or bias corrections applied to the times on this record.
<i>FrameQF</i>	3	all bad data (no signal in whole frame), or all data good and all science team recommended corrections applied.
<i>rng_UQF</i>	3	data quality for the range offsets on this record.
<i>AttFlg1</i>	4	whether attitude angle is large, and whether it is the result of a programmed ocean sweep, target of opportunity, or steering to a reference track.
<i>cld1_mswf</i>	4	potential severity of multiple scattering.
<i>ElvFlg</i>	4	used location on the received echo to calculate the elevation on the record.
<i>FRir_qaFlag</i> ^{*2}	4	whether clouds are detected based on 1064 nm pulse (Full Resolution 1064 Quality Flag).
<i>sigmaatt</i>	4	attitude quality.

^{*1} consists of quality flags: *padUseFlg*, *calcPadFlg*, *LPAprobFlg*
^{*2} not available for release 18

Table 3.4: Overview of the quality flags available for GLA12. Notice that mostly one flag consists of several bits, all indicating different aspects. So the flags are in fact generic terms for a subset of flags.

i.e. rock covered by snow will show similar reflection properties as ice covered by snow. To reduce this problem, only the observations at the end of the ablation season are used, i.e. the points in the MAIN and SLAVE file that belong to one of the laser campaigns in the autumn. (The MAIN and SLAVE files contain the first and second points in time respectively, of all OPs). For the MAIN and SLAVE file, this holds for 177 412 and 89 716 points respectively.

Figure 3.8 shows the ratio between the received and transmitted energy for those observations. It must be noticed that we only make use of a limited subset of observations, because we only use the observations that are in the subset of geometrically overlapping footprints. From figure 3.8 it follows that there is no significant difference visible between the inland and coastal region of Greenland. Thus, we decided not to use the waveform information for data cleaning. A more detailed study of the waveforms is necessary to figure out whether other waveform parameters can be used.

Instead of the waveforms we use a surface mask of the Greenland continent that has a resolution of 1 by 1 kilometer, see figure 3.9. In this surface mask, kindly provided by J. L. Bamber, a distinction is made between ocean, land, glacier/ice cap and ice sheet.

All OPs that fall in a grid cell for which it holds that the mask indicates ocean or land are removed from the dataset. In total 145 747 OPs are removed, which imply that 502 685 OPs remain.

3.6.2 Quality flags

The GLA12 data files contain flags that indicate the quality of input data, output data and data corrections. If the quality is acceptable, the data use and record quality flags are set to zero. A non-zero data use and record flag indicates an abnormal situation during processing. Table 3.4 provides an overview of the quality flags that are available for the GLA12 data product [39]. These quality flags

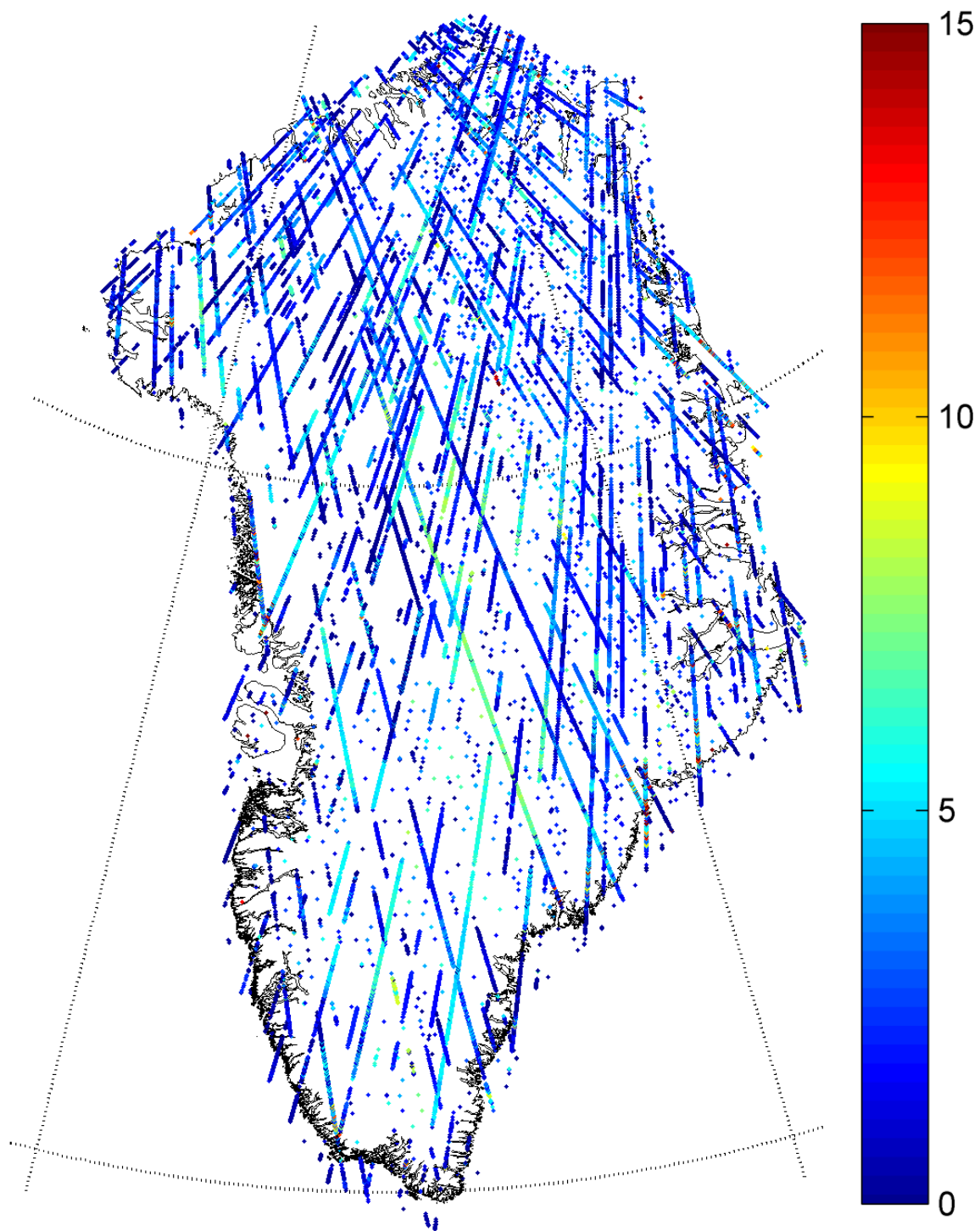


Figure 3.8: Ratio between the received and transmitted energy for the data points acquired at the end of the ablation season. The unit of the received energy is in 0.01 fJoules while the unit of the transmitted energy is in counts. Notice that the color bar is adapted for visualization purposes, i.e. the maximum value of this ratio is 50.

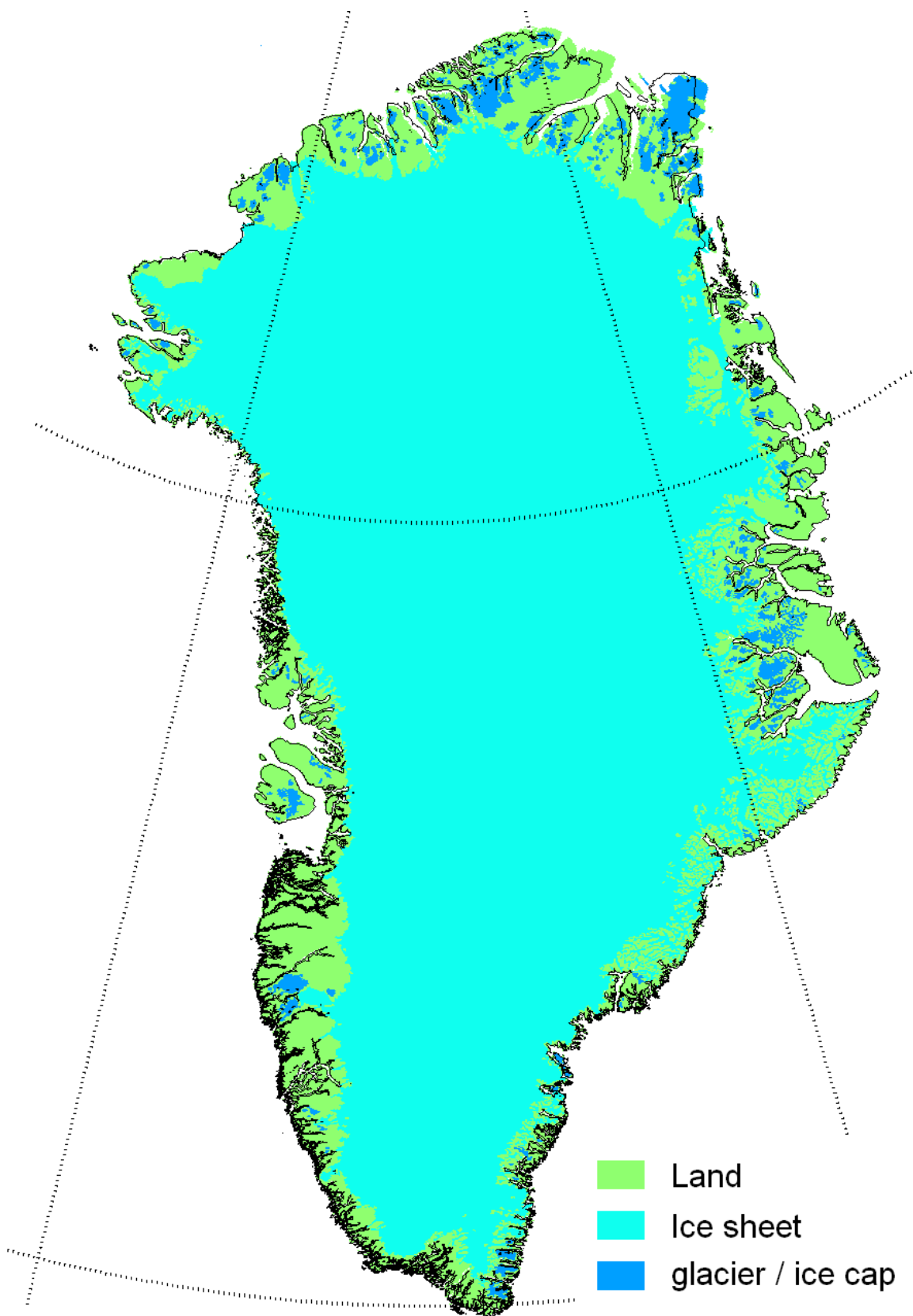


Figure 3.9: Surface mask of the Greenland continent. If an OP is not located on the ice sheet or a glacier, then the OP is removed from the dataset.

can be divided into four different groups. First there is a group of quality flags that have no capability to distinguish, i.e. all values are the same. This holds for the quality flag *ElvuseFlg* that indicates that all elevations are valid. Furthermore, according to the quality flag *atmQF*, for all observations the conditions are favorable for forward scattering. A similar statement holds for the quality flags *AttFlg2*, *CorrStatFlg*, *OrbFlg* and *rngCorrFlg*.

Secondly, there is a group of quality flags that have the capability to distinguish but they are not directly related to the main parameter of interest, i.e. the elevations. This is the case for the quality flags *timecorflg* and *APID_AvFlg*.

FrameQF

The third group has the capability to distinguish and is directly related to the elevations. So, this group provides clear criteria to remove bad data. From *FrameQF* it follows that some of the data is not corrected or has measurement problems. So also here, there is no capability to distinguish. However, for a part of the records this quality flag also indicates that all elevations in the record are bad due to problems with corrections. This situation mostly occurs at the margins of the ice sheet and in the South of Greenland, which is understandable because the cloud conditions are worse in those regions. Also the topography of the ice sheet becomes more complicated to the margins of the ice sheet, i.e. there are the glaciers, mountains etc. So all OPs for which one of the elevations is indicated as bad are removed from the dataset.

rng_UQF

According to the GLAS Altimetry Product Usage Guidance [40] it is better to remove OPs for which *rng-UQF* indicates that the received return may be saturated or have significant forward scattering. This is because the points do not represent the surface characteristics and will give less accurate elevations. Both saturation due to 'high-gain' and 'low-gain' occurs (see section 2.1.4), however the last situation occurs significantly more often than the first, especially closer to the smoother center of the ice sheet. Forward scattering results in a delay of the signal due to the fact that particles like cloud droplets and aerosols, scatter the incoming signal. So all OPs for which one or both of the elevations are contaminated by saturation or forward scattering, are removed from the dataset.

With the combination of those two criteria, 149 849 OPs are removed from the dataset.

AttFlg1

The last group of quality flags does not indicate bad data directly but is related to effects that might influence the derived elevations. To determine whether these quality flags should be used, more detailed analysis is necessary. Because we are interested in the elevation differences, these quantities will be used to study the possible relation with the quality flags of this group.

The *AttFlg1* quality flag is related to the direction of the laser beam that is, within certain limits, directed to nadir. Due to the steering of the laser beam to a reference track this direction often exceeds the limits and in that case the *AttFlg1* quality flag indicates a large off-nadir angle. Figure 3.10 shows the histograms of the elevation differences for the case that the quality flag does not indicate a large off-nadir angle and otherwise. From the histograms and the derived statistics, it becomes clear that a difference in the mean of 6 centimeter is significant with respect to the standard deviation of the mean that is in the order of millimeters. However, from figure 3.10 it follows that the spatial distribution of OPs for which the *AttFlg1* quality flag indicates a large off-nadir angle is rather inhomogeneous. So possibly the bias in the mean is caused by spatial differences in the ablation and accumulation signal. Therefore these OPs are not removed from the dataset.

ElvFlg

With regards to the used location on the received echo the *ElvFlg* does not have the capability to distinguish. According to [6], the range to the surface is half the time between the centroid of the transmitted pulse and the center of the Gaussian fitted to the last peak of the received pulse multiplied with the velocity of light. However, *ElvFlg* indicates for all elevations that the location associated with the Gaussian with the largest peak is used. Also this flag indicates the elevations that are probably contaminated by clouds and so these elevations are probably biased. In accordance with the cloud cover conditions most contaminated elevations show up at the margins and in the South of the ice sheet,

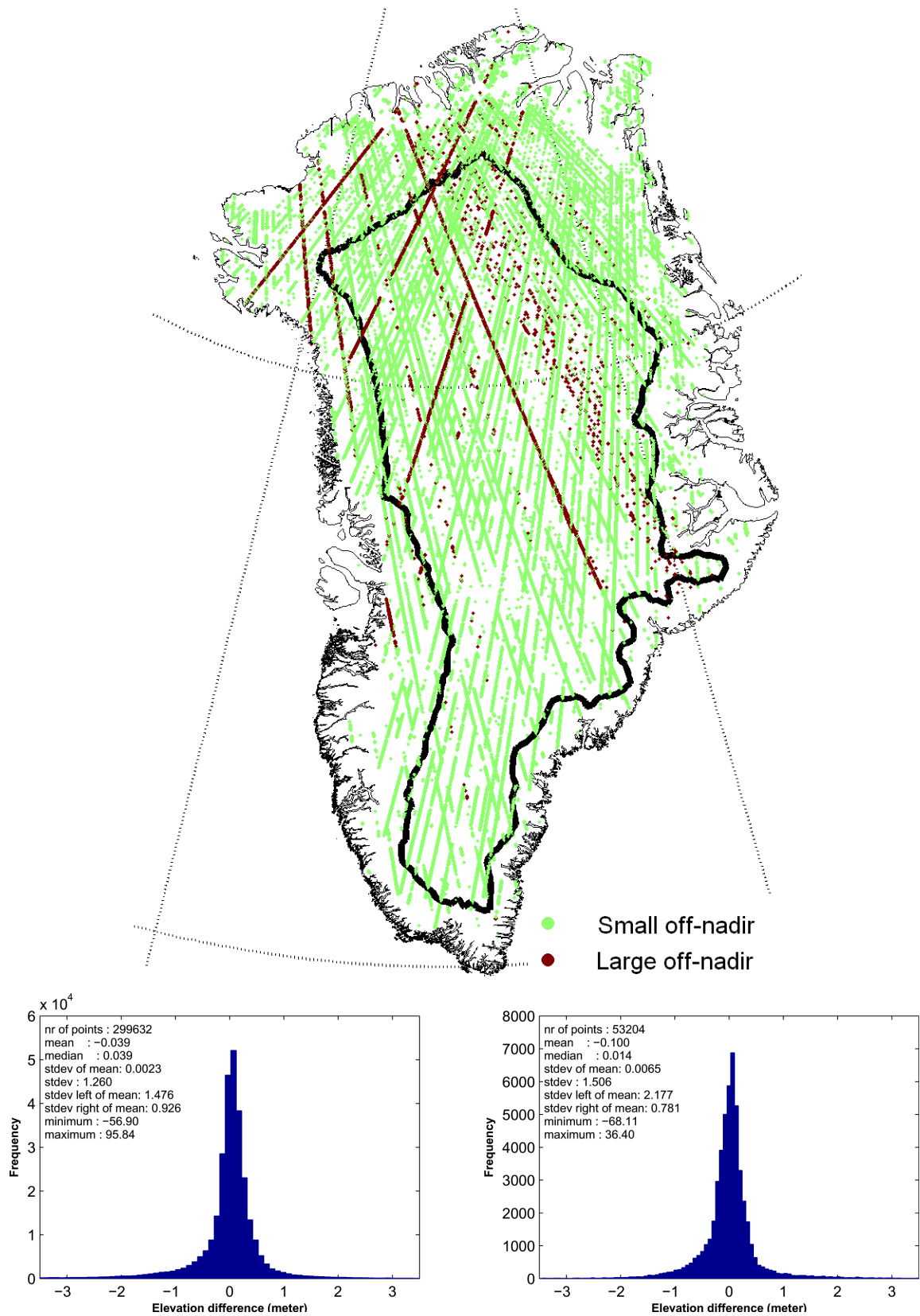


Figure 3.10: Overview of the OPs that are indicated to have a large off-nadir angle (upper image). Histograms of the elevation differences for the case that AttFlg1 does not indicate a large off-nadir angle (left) and otherwise (right). Notice that the axes of both histograms are adapted for visualization purposes.

see figure 3.11. The corresponding histograms show that the means of the elevation differences for the case with and without cloud contamination are slightly different, only the standard deviations differ significantly. However, notice that at the margin of the ice sheet also other effects influence the elevation differences, like increased surface slopes. Furthermore, there might be spatial differences in the ablation and accumulation signals. This makes it difficult to derive any clear criteria to remove data based on this quality flag.

cld1_mswf

The multiple scattering warning flag (*cld1_mswf*) is based on the total column optical depth calculated in GLA11 using the 532 nm signal. The optical depth expresses the quantity of light removed from the transmitted laser beam by scattering or absorption during its path through a medium of aerosols plus clouds. In such a medium, the scattering centers are grouped together and so the radiation may scatter many times. This is known as multiple scattering. The *cld1_mswf* flag is intended as a way to quickly obtain information about the potential severity of multiple scattering with regards to the range-to-surface calculated by the altimetry processing software. This flag will have values ranging from 0 - 15; the higher the number, the higher the optical depth. A warning flag of zero is a good indicator of no layers or a layer so thin it will not cause any range delays. A warning flag value of 15 will signify "invalid", which is the default value when no 532 nm signal is available. It could also occur that there is a total extinction of the signal due to optically thick clouds. In the last case the number of detected cloud layers is larger than zero.

We expect that when the optical depth increases also the range delay increases. In other words, the elevations are more biased for a larger optical depth. Figure 3.12 show the means and standard deviations of the elevation differences for the values of *cld1_mswf*. Notice that for one elevation difference, two *cld1_mswf* values are available referring to two different epochs. Here we used the value that indicates the worst situation, i.e. the situation with the highest optical depth.

To see the influence of the third group of quality flags a similar plot is created without applying the cleaning criteria of this group (left plot figure 3.12). The difference is clearly visible, for some larger values of the *cld1_mswf* flag, e.g. flag values 10 and 15, the mean is biased and also the standard deviations are significantly larger. It might be that this quality flag, in combination with other flags and parameters, is used to indicate whether the data is bad (*FrameQF*) and what the quality is for the range offsets (*rng-UQF*). Further removal of data based on this quality flag is therefore not necessary.

FRir_qaFlag

A similar conclusion can be drawn from the *FRir_qaFlag* quality flag. Also this flag has values ranging from 0 - 15 where 15 means no clouds, 14 the likely presence of low clouds, 13 the possible presence of a cloud and the values 0 - 12 that a cloud is detected by the cloud search algorithm. Here the higher numbers indicate a stronger average signal from the region starting at the cloud top and extending 500 meters below the cloud top. We expect that the elevations become more biased when this quality flag runs up to 12. From figure 3.13 it follows that there are only strong biases in the left plot that show the means and standard deviations before applying the cleaning criteria of the third group of quality flags. Notice that for the right plot in figure 3.13 the standard deviations significantly increase for larger values of the *FRir_qaFlag* quality flag. However, this mostly occurs at the margins of the ice sheet where also other effects influence the elevation differences.

sigmaatt

The flag *sigmaatt* is the last quality flag of this group and has three distinctive values to indicate the quality of the attitude; the quality is good, bad or there is a warning. All OPs for which the quality of the attitude is bad are removed from the dataset. It turns out that no OPs are removed by this criterion. In the uncleaned dataset only a few OPs have a bad attitude quality and these are already removed based on the criteria derived from the third group of quality flags.

Concluding we can say that the last group of quality flags do not provide more criteria to clean up the data set. Basically these quality flags provide a more detailed insight in the observations and the related error sources.

The study of the quality flags shows that the quality flags are not consistent with respect to each other. It sounds rather contradictory that *ElvuseFlg* indicates that all elevations can be used while based on

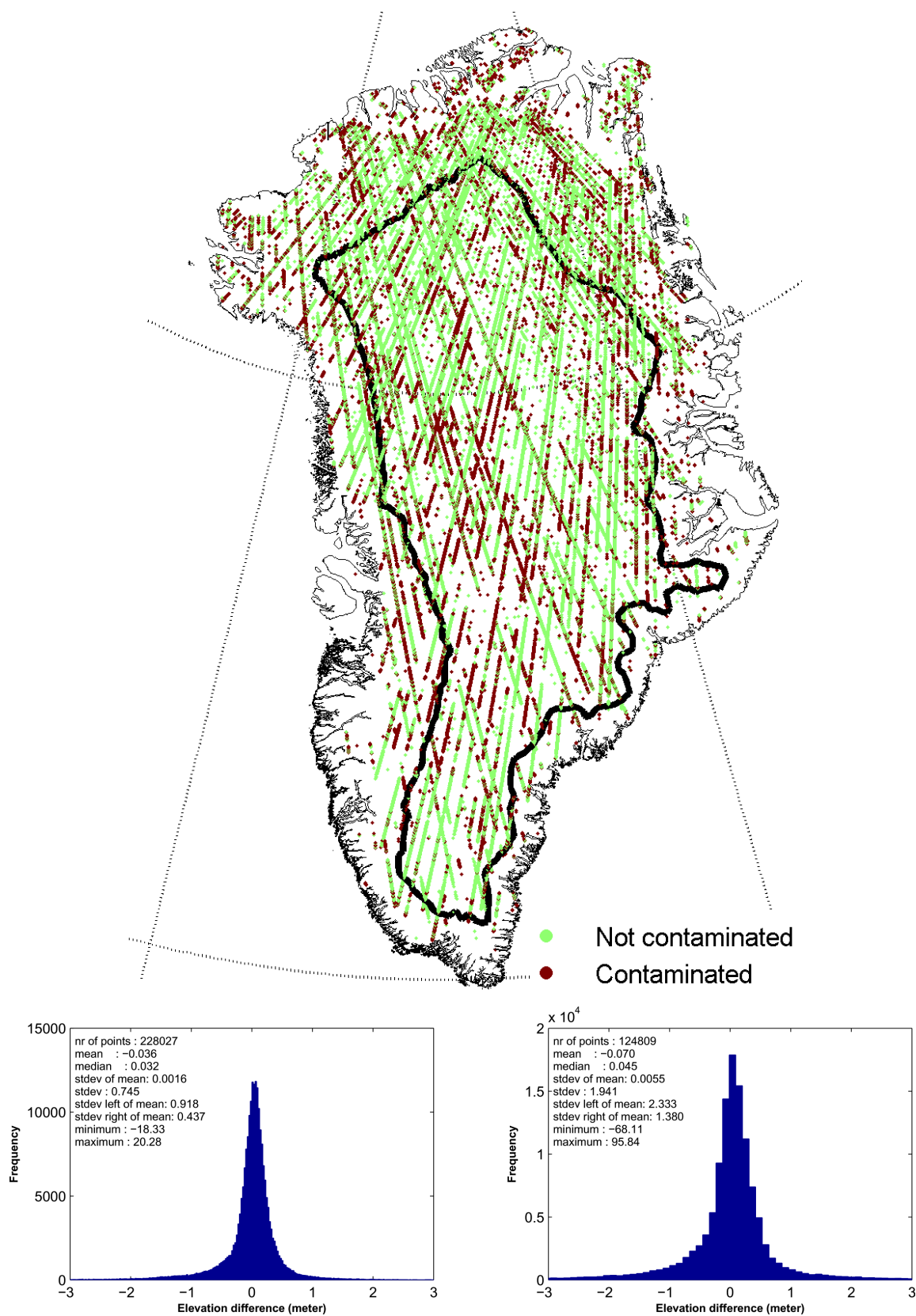


Figure 3.11: Overview of OPs that are probably contaminated by clouds (upper image). Histograms of the elevation differences for the case that `ElfFlg` does not indicate probable cloud contamination (left) and otherwise (right). Notice that the axes of the histograms are adapted for visualization purposes.

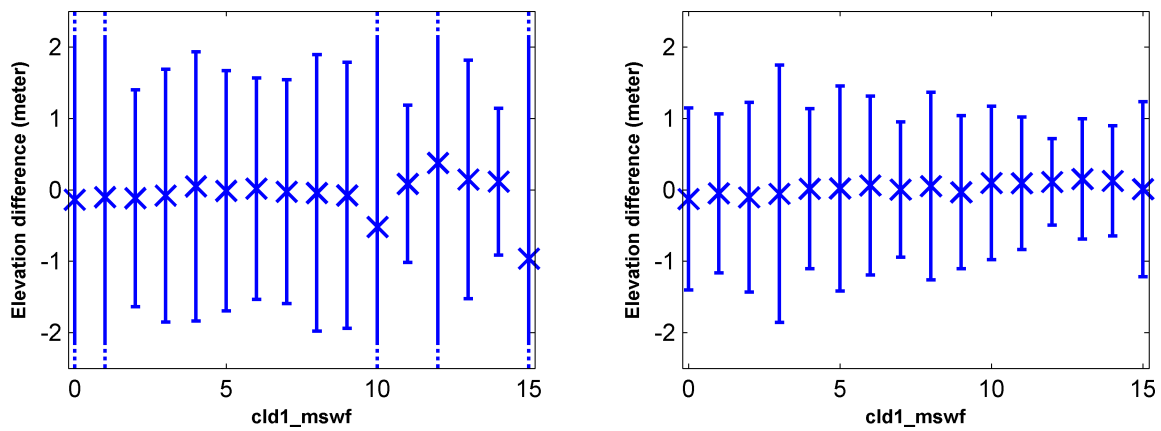


Figure 3.12: Means and standard deviations of the elevation differences for a fixed value of `cld1_mswf`, without (left) and with (right) applying the cleaning criteria of the third group. Notice that there are two flag values per elevation difference, here we took the value corresponding with the worst situation. The minimum number of points used to calculate the mean and standard deviations for all cases is larger than 1 575. For most cases this number is in the order of thousands. For the left plot, the error bars are truncated for visualization purposes. For flag values 1 and 2 the standard deviation are equal to 4.2 an 5.1 meter respectively, while for flag values 10, 12 and 15 the standard deviations are equal to 19.6, 21.0 and 34.1 meter respectively.

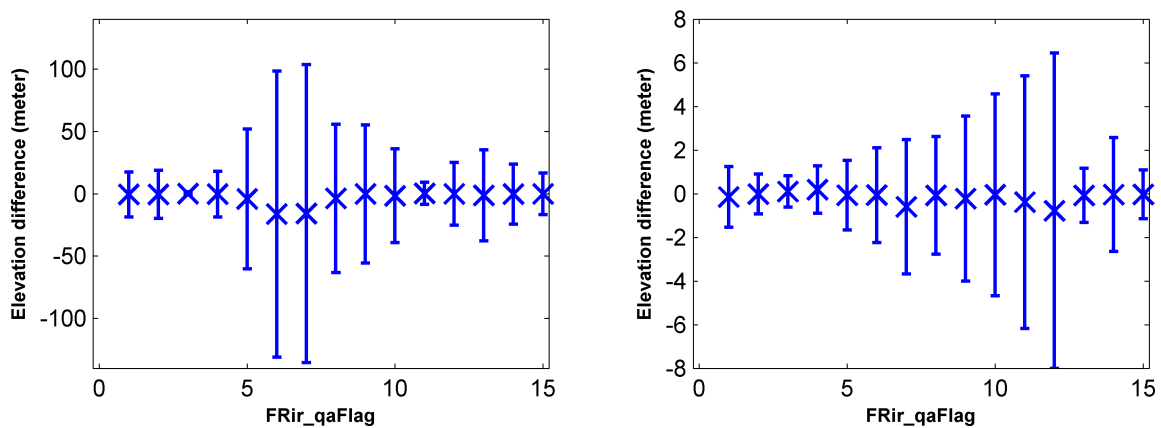


Figure 3.13: Means and standard deviations of the elevation differences for a fixed value of `FRir_qaFlag`, without (left) and with (right) applying the cleaning criteria of the third group. Notice that there are two flag values per elevation difference, here we took the value corresponding with the worst situation. The minimum number of points used to calculate the mean and standard deviations for all cases is larger than 173. For most cases this number is in the order of thousands.

FrameQF and *rng_UQF*, 138 750 OPs are removed from the dataset. A similar statement holds for the three flags related to clouds. Situations occur where *FRir_qaFlag* indicates no clouds while *ElvFlg* indicates a possible contamination by clouds. Or that the number of cloud layers is equal to zero and also *FRir_qaFlag* indicates no clouds while *ElvFlg* still indicates a possible contamination by clouds. But also that *clد1_mswf* indicates no layers or a layer so thin it will not cause any range delays while *FRir_qaFlag* indicates that a cloud is detected. In future research the algorithms to derive these quality flag values must be evaluated, to see whether it is possible to remove these contradictions.

3.6.3 Remaining criteria

Finally there are two other parameters in the GLA12 data product that might indicate possible biased data. First, the number of peaks in the return echo found by the Gaussian fitting procedure might be an indication. Multiple peaks mean that there are multiple reflections of the transmitted signal. Mostly this number is equal to one, but a few situations occur where this number equals two. On an ice sheet this situation can occur when the footprint is located on a crevassed surface. It would be reasonable to remove these OPs from the dataset.

Secondly, we can study the relation between the elevation differences and the number of clouds. Figure 3.14 show the means and standard deviations of the elevation differences with a fixed number of clouds, before (left plot) and after (right plot) the application of the cleaning criteria of the third group. Notice that there are two values per elevation difference, here we take the maximal number of clouds. This plot shows that after the application of the cleaning criteria of the third group, the elevation differences are still biased when the number of detected cloud layers is larger than four. So these OPs will be removed from the dataset.

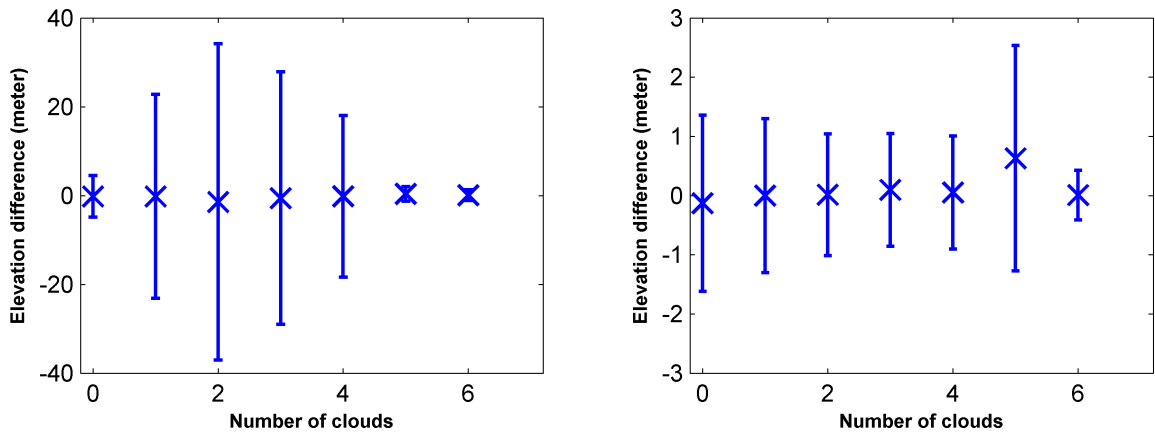


Figure 3.14: Means and standard deviations of the elevation differences for an increasing number of cloud layers, without (left) and with (right) applying the cleaning criteria of the third group. Notice that there are two numbers per elevation difference, here we took the maximal value. The minimum number of points used to calculate the mean and standard deviation equals 394. The lower the number of detected clouds, the larger the number of used points.

In total 1 200 OPs are removed from the dataset using these criteria. This makes the total number of removed OPs equal to 296 796, approximately 46% of all overlapping pairs. Table 3.5 provides an overview of the total number of removed OPs per group of cleaning criteria.

Group of cleaning criteria	Total # of removed OPs
OPs not on ice sheet	145 747
Cleaning criteria of first group	0
Cleaning criteria of second group	0
Cleaning criteria of third group	149 849
Cleaning criteria of fourth group	0
Cleaning criteria of remaining group	1 200

Table 3.5: *Overview total number of removed OPs for different groups of cleaning criteria.*

Chapter 4

Mass balance estimation with ICESat data

The cleaned dataset, obtained by the methods described in chapter 3, is used for further processing. Section 4.1 presents the results of some case studies we conducted to explain the occurrence of random and systematic elevation differences. These case studies show the usefulness of ICESat data to study local phenomena. But also they indicate the significant influence of the surface slope and roughness on the observed elevation differences. Based on these results we made an attempt to develop a weighting scheme to estimate the mass balance. The method to calculate this mass balance is explained in section 4.2.

The elevation differences are defined as the last measurement in time minus the first one. The elevations are corrected for saturation, but notice that only for release 28 these corrections are available.

4.1 Case Studies, slope and roughness

Figure 4.1 provides an overview of the elevation differences in the cleaned dataset. Notice that for this plot all elevation differences between all laser campaigns are added together, so the signals can be contradictory, i.e. the laser campaigns fall in different seasons and also the time difference is not constant.

The enclosed histograms of the regions above and below 2000 meter show that in both regions there are elevation differences up to tens of meters. Detailed investigation shows that these relatively large differences behave in some cases like outliers; in other cases they have a more systematic character along track. This systematic behavior is already visible in figure 4.1. Of course these elevation differences might indicate a strong local accumulation or ablation spot. However, some case studies, conducted to identify possible causes of these large differences, show that this is not always a likely explanation. Notice that for all case studies we make use of overlapping tracks, so the time difference is more or less constant. First, the features are discussed that show a random character, followed by the features that show a systematic character. In the course of this project we made an attempt to correct for the influence of surface slope. The developed method and results are presented and discussed in section 4.1.3. Finally, more background information about roughness is provided in section 4.1.4.

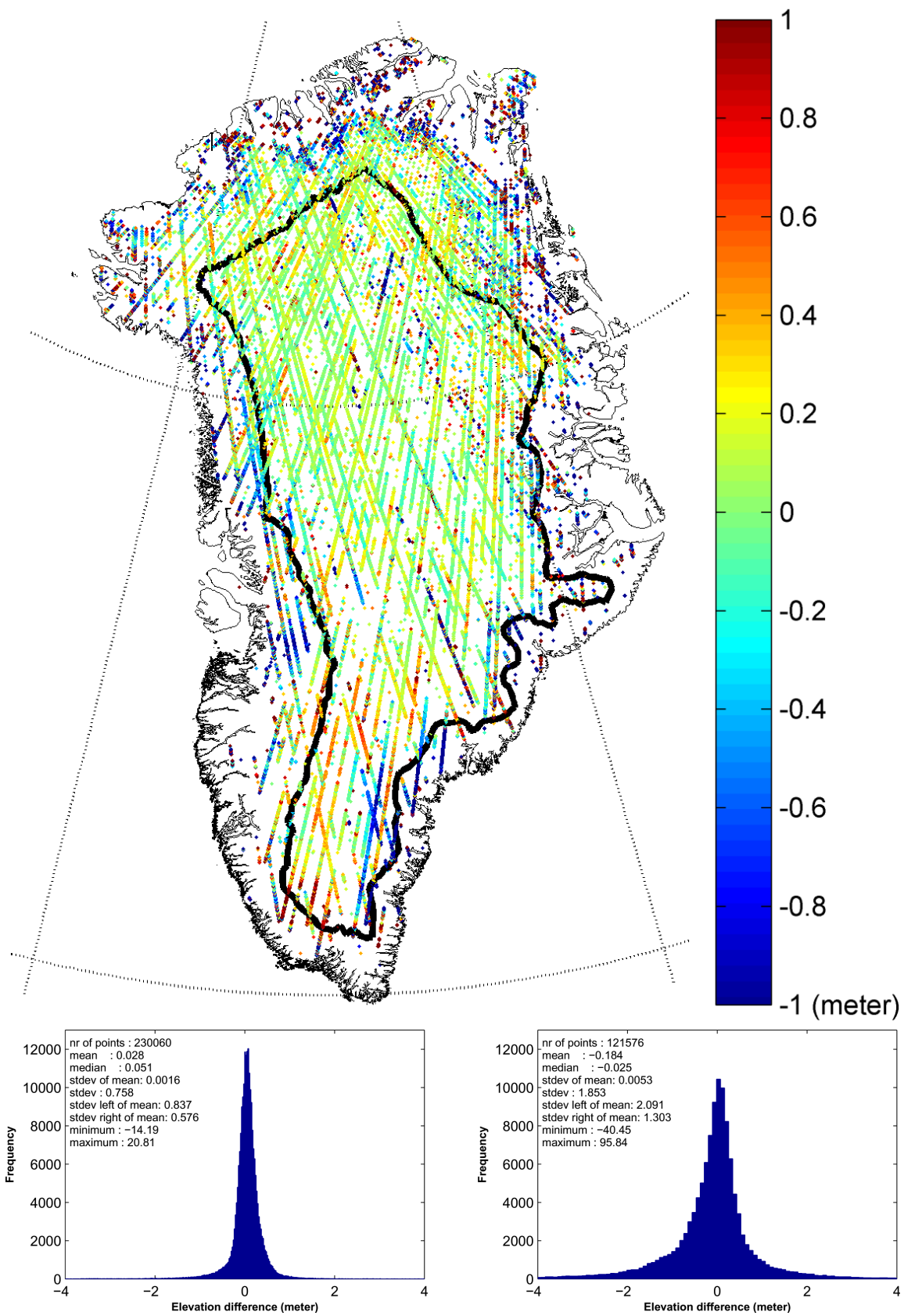


Figure 4.1: Overview of all elevation differences with the corresponding histograms for the region above (left) and the region below (right) 2000 meter. The thick black line is the 2000 meter elevation contour. Notice that the color bar is adapted for visualization purposes.

4.1.1 Case studies: outliers

The figures related to these case studies can be found in appendix A. In fact these figures show clearly the cause of the 'outliers' in the elevation differences. The random character excludes the possibility that these large elevation differences are due to atmospheric effects or other effects where spatial correlation is expected. Looking to the Landsat images we can conclude that these outliers are related to surface characteristics as slope and roughness.

In the first case study, see figure A.1, the overlapping tracks, with a time difference of one year, are located on a glacier. Even on the Landsat image, the crevasses on this glacier are clearly visible. The elevation difference profile shows an erratic pattern with elevation difference changes in successive points of several meters, sometimes even ten meter. Here a mixture of effects might play a role. First, steep surface slopes (see the elevation profiles) at different parts of the glacier cause large elevation differences if the footprints do not overlap exactly. Second, the roughness of this glacier due to crevasses influences the elevation differences. Finally, the dynamics of the glacier play a role, which is most clearly visible at the end of the elevation profiles. Here the bulge is shifted to the right when the satellite passed the second time. This feature will be discussed in more detail as an example for the second type of roughness in section 4.1.4.

The other two case studies, see figures A.2 and A.3, are both located at the margin of the ice sheet. On the Landsat images we can see that a part of the OTPs are located on the rocks that rise above the ice sheet. From the elevation profiles it become clear that in both cases there are steep slopes of even more than 6° . Depending on the distance between both footprint centers, this can give rise to errors in the meter level. But also here roughness might play a role. In section 4.1.3 and section 4.1.4 respectively, both error sources will be discussed in more detail.

4.1.2 Case studies: systematic effects

Detailed analysis of the overlapping tracks shows that there are cases where systematic elevation differences of more than 10 meter occur. A limited set of case studies is conducted at different locations on the ice sheet to identify possible causes for these differences. The corresponding figures related to these case studies can be found in appendix A.

Figures A.4, A.5, A.6 and A.7 show some examples of overlapping tracks with elevation differences that increase at first, than stabilize and finally decrease again. For all examples this behavior stretches over several kilometers along track while the order of magnitude of the elevation differences ranges from several meters to twenty meters. First it must be noticed that all these examples have a gap in the plotted elevation difference profiles. It turns out that the OPs at the locations of these gaps are removed because the range offset quality/use flag (*rng_UQF*) indicates that the saturation flag is set due to "Low-gain" saturation, see section 2.1.4. The fact that already a part of the data is indicated as bad, poses the question whether it is possible that not all bad data is recognized. This becomes more likely due to the fact that already those OPs are removed for which the elevation differences are largest. For these OPs the situation was probably worst. Notice that saturation is an along track correlated feature.

Another observation that supports this interpretation is the fact that in all cases there is one track of release 26 and one of release 28, so for one track a saturation correction is applied and for one not. There are no examples that have similar characteristics and where both tracks are from release 28. Also the magnitude of the applied saturation correction is comparable with the observed elevation differences, i.e. the maximal applied correction equals approximately 14 meter.

The fact that some OPs are removed due to "Low-gain" saturation excludes the possibility that these effects are related to clouds, i.e. "Low-gain" saturation only occurs when the atmosphere is clear. On the other hand, increased cloud cover reduces the saturation range error but can increase the forward scattering range error.

Based on the Landsat image in figure A.4, one may argue that there is another explanation. It turns

out that this track is located on a glacier. For sure this area is a dynamic environment, due to the flow of the glacier. This might be an explanation for this particular example, but is not likely for the other examples that are located more to the center of the ice sheet. That is also the reason why no clear Landsat images are available.

A well-known feature on the West Greenland ice margin are surface lakes that form in each summer melt season, in closed basins on the surface of the ice sheet. Many of these lakes drain rapidly, potentially supplying a substantial influx of water to the basal zone, and providing a mechanism for rapid response of the Greenland ice sheet to climate change. Lake sizes range from several hundred meters to several kilometers in diameter and their locations extend from close to the ice margin up to further inland [26]. On the Landsat images these features are clearly visible as dark spots due to the lower albedo of these lakes with respect to the ice sheet.

Figure A.8 provides two examples where the observed elevation differences can be related to these surface lakes. Striking is the smoothness of the upper elevation profile that we interpret as the water surface. So for the left example this means that the lake disappeared while for the right example a new lake is formed. It turns out that both lakes are not visible on the Landsat images that are formed by a compilation of images taken from 1999 to 2003. But according to [26], the lakes fill rapidly, retain water for a period of several weeks, and then drain rapidly (e.g. overnight). Interannual behavior varies significantly among individual lakes with some filling and draining regularly, some filling only occasionally, and others occasionally freezing over without draining.

The same overlapping tracks that possibly show the surface lakes reveal another feature. Figure A.9 shows that over a length of approximately 65 km the elevation differences are gradually increasing and decreasing to a maximum of approximately -14 meter. The elevation profiles show that this feature is located in a kind of valley. Furthermore, also surrounding overlapping tracks show a similar pattern, see figures A.10, A.11, A.12 and A.13. This fact illustrates that saturation, cloud cover or undetected instrumental errors are not likely. The corresponding Landsat images show that this feature is located at the inlet of the Jakobshavn Isbræ glacier. This glacier is one of the world's fastest flowing glaciers and Greenland's largest outlet glacier [64], draining 6.5 percent of Greenland's ice sheet area. Observations of the glacier velocity showed that the glacier slowed down from a velocity of 6 700 meters per year in 1985 to 5 700 meters per year in 1992. This latter speed remained somewhat constant until 1997. From 2000 up to 2003 the glacier sped up again from 9 400 to 12 600 meters per year, [25]. According to [23], the Jakobshavn Isbræ glacier has maintained these high speeds for several years now. So, what we are observing here is the thinning of the inlet of this glacier as a result of the increased velocity.

Figures A.14, A.15 and A.16 show three case studies on different glaciers for which multiple explanations can be given. In figure A.14 we can see two overlapping tracks on a glacier in the northwest of Greenland. Notice that the time difference between those tracks is just eight days. On the Landsat image we can see that the glacier flow is blocked by a rock. This poses the explanation that the observed uplift is caused by the blocked flow. From the elevation profile it follows that the bulge is located in a kind of pit. Furthermore, the elevation difference profile shows an increasing trend that becomes constant after a while. From this it follows that the uplift can also be caused by local accumulation in combination by snow deposition, so the wind had blown the snow in the pit. Notice however that then the snowfall is really local, because at the start of the overlapping tracks and behind the rock, where the track passes again the glacier, the elevation differences are zero.

The last two maps, see figures A.15 and A.16, show two overlapping tracks located near each other. Both elevation difference profiles show a similar pattern; negative elevation differences in the beginning that become positive at the end. This pattern can be caused by differences in snow compaction, but a relation with the glacier dynamics is more likely. This kind of behavior (sinusoidal pattern) can be recognized as an undulation, described in section 4.1.4 as the second type of roughness. Notice that a similar feature is visible in figure A.1. Here at the end of the elevation profiles it can be seen that the bulge has flowed down. In the elevation difference profile this give rise to a negative pattern that becomes positive.

4.1.3 Surface slope

The case studies show that a non-zero surface slope can explain a part of the observed elevation differences. In this section we will study this influence in more detail.

The expected bias due to the influence of surface slope, called the expected slope bias, can be calculated by a simple relation between the slope and the distance between the centers of the footprints. Figure 4.2 shows two not completely overlapping footprints, separated by a certain distance (D_{footpr}) on a mountain with surface slope α . The expected slope bias (SIB) equals:

$$\text{SIB} = \tan \alpha \cdot D_{\text{footpr}} \quad (4.1)$$

Where:

SIB	expected slope bias
α	surface slope
D_{footpr}	distance between the footprints

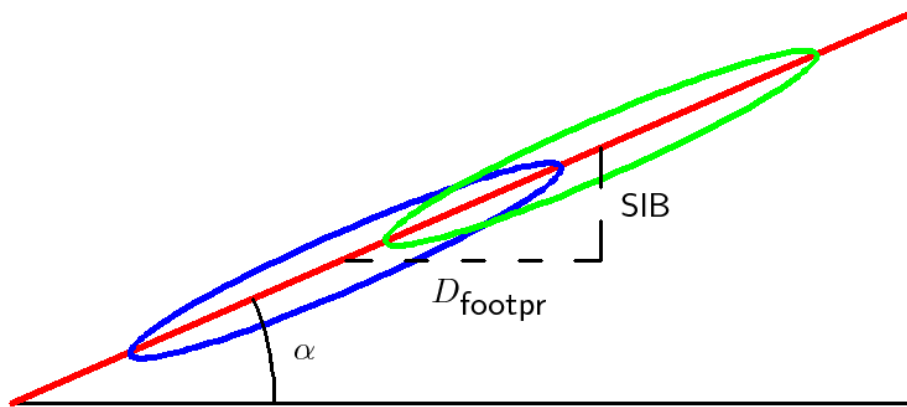


Figure 4.2: Two not completely overlapping footprints, separated by a distance D_{footpr} on a mountain with slope α causes an expected slope bias (SIB).

When we assume a maximal distance between the footprints of 60 meter and a maximal slope of 20 degrees, than the expected slope bias as a function of both slope and distance between the footprints can be visualized according to figure 4.3. This figure shows that even low surface slope angles already cause elevation differences at the decimeter level. Notice that the maximal distance between the footprint centers can be larger than 60 meter due to the different values of the axes of the footprint ellipses for the different laser campaigns, see table 3.2. The influence of surface slope might be characterized both as random and systematic. When the topography (and so the slope) will change over short distances, than the errors introduced by surface slope will have a random character. This might be the case in the coastal region. On the other hand, when the slope between the centers of the footprints for a particular overlapping track combination is constant, than the influence will be systematic.

The kind of influence and the possible magnitudes of these expected slope biases poses the question whether it is possible to correct for it. Therefore we need the slope of the line that connects both centers of the footprints that form an overlapping pair. The calculation of this slope requires an independent DEM with a comparable resolution as the distance between the footprints. The DEM with the highest resolution (1 km) available for whole Greenland is the Global Land One-kilometer Base Elevation (GLOBE) DEM [17]. To get an idea of the possibility to correct for the influence of surface slope, this DEM model is used to calculate the required slope (α_{GLOBE}). The procedure to calculate α_{GLOBE} is rather straightforward with the help of the 'gradientm' routine of the Matlab Mapping Toolbox [35]. This routine computes amongst others north and east components of the gradient for a regular data grid. When the grid contains elevations in meters, the north ($\|\vec{P}\vec{P}'\|$) and east ($\|\vec{Q}\vec{Q}'\|$) gradient components are the change in elevation per meter of distance in the north and east directions, see figure 4.4. In this

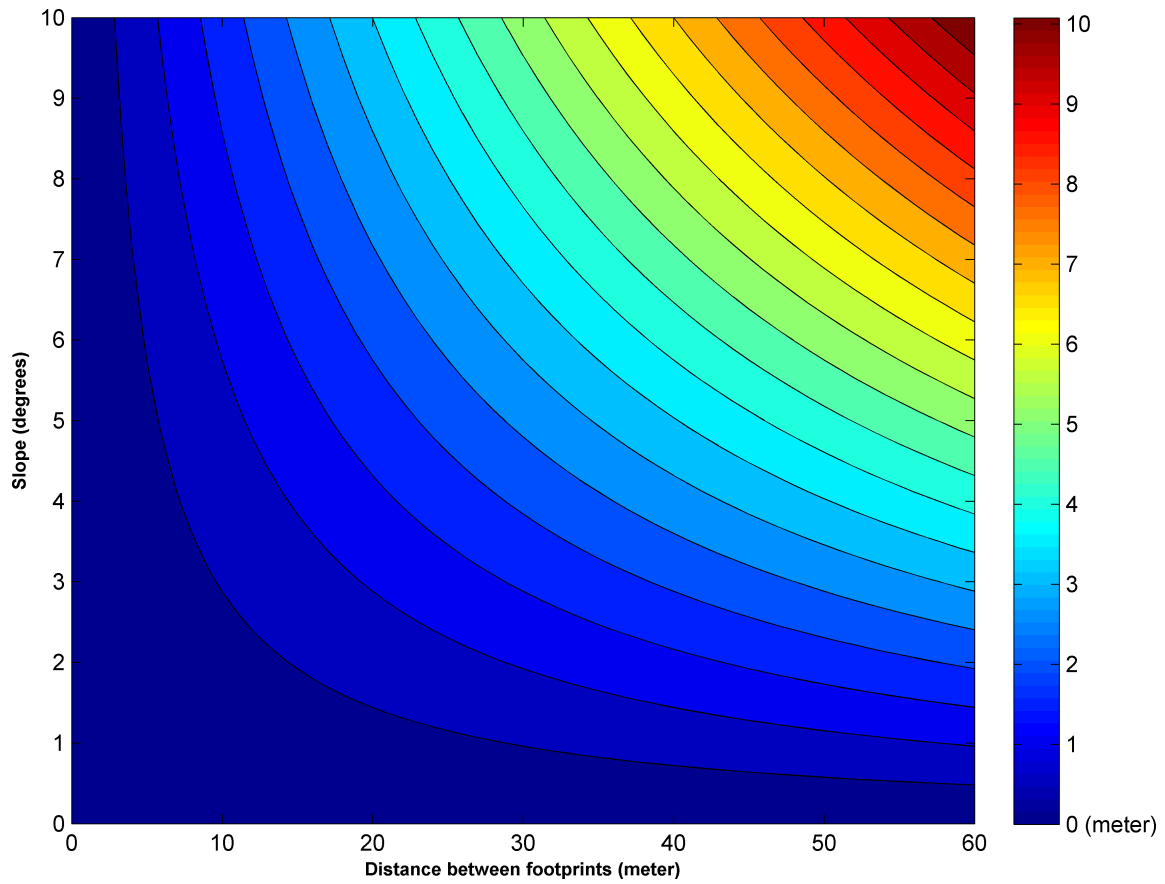


Figure 4.3: The expected slope bias as a function of both surface slope and distance between the footprint centers.

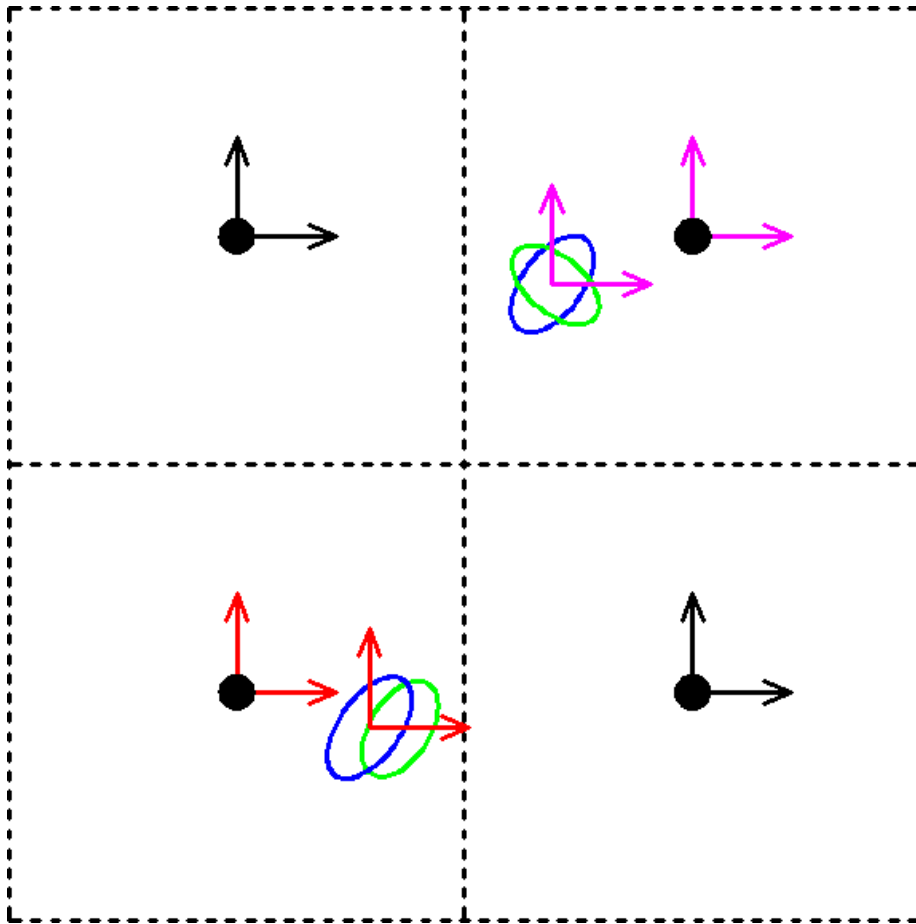


Figure 4.5: The north and east gradient components are assigned to each footprint using a nearest neighbor operation. The color of the arrows, pointing in the directions of the gradient components, indicates which values of the gradient components are assigned to the OPs.

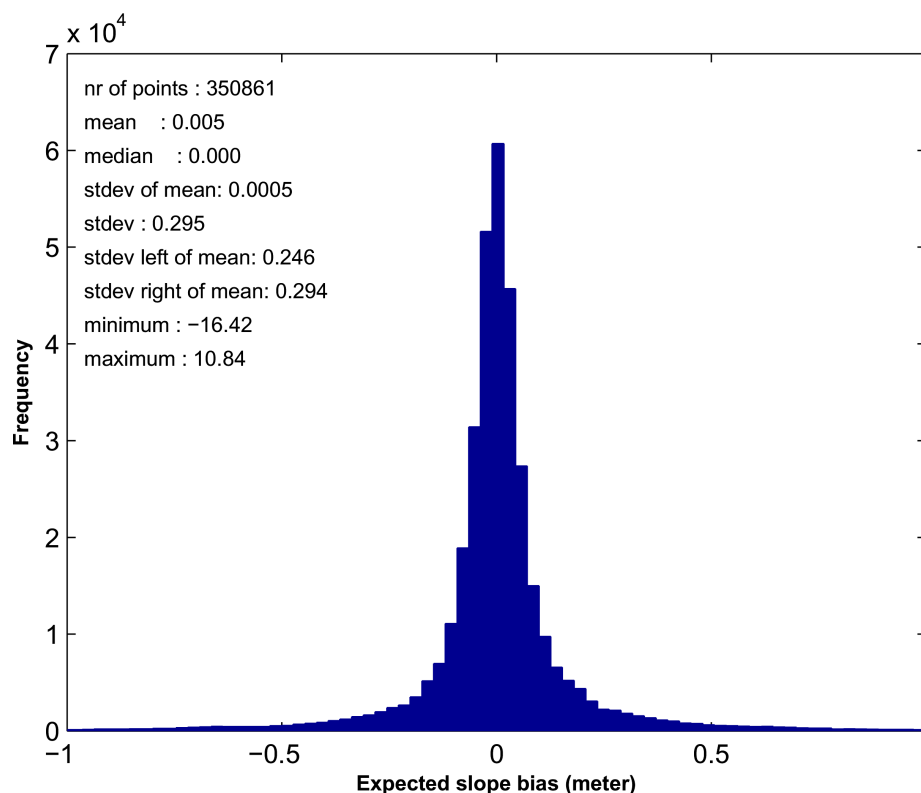


Figure 4.6: Histogram of the expected slope biases based on the GLOBE DEM.

crosses indicate the mean elevation differences per interval. Notice that the expected slope bias is calculated from the second point in time to the first point in time. This implies that when the real surface slope is exactly known and the elevation difference is purely due to the influence of this slope, the sign and magnitude of the elevation difference and the expected slope bias are equal. So, when slope is the only cause of the elevation differences, all points in the scatterplot are on a straight line. In reality the slope is based on a DEM with a poor resolution and the elevation differences are caused by multiple sources. Still the scatterplot in figure 4.7 shows that there is correlation.

The limited resolution and poor quality of the GLOBE DEM does not allow us to use this DEM to correct for the influence of slope. According to [16], the estimated absolute vertical accuracy, expressed by the root mean square error (RMSE), of the GLOBE DEM for Greenland equals 91 meter. For our purpose we need the relative vertical accuracy that is not specified but probably better.

Due to the limited resolution of the GLOBE DEM we adapted the assumption that the slope between the footprints was constant. When the slope is not constant, an error is introduced, indicated by SIB_{error} in figure 4.8. Here two, not exactly overlapping, footprints are plotted on a non-constant sloped terrain. When a higher quality dataset becomes available with a higher resolution it might be possible to correct for the slope. Probably airborne laser altimetry can be used to validate this procedure, but this is a topic for further research. Here we do not apply the calculated corrections, but we make an attempt to reduce the influence of the surface slope by a weighting scheme.

4.1.4 Roughness

Ice sheets are roughened in three fundamentally different ways [6]. On the smallest scale there is the roughness caused by wind and variations in the rate of snow accumulation, which comprises irregular features called 'sastrugi' and 'snow dunes'. Sastrugi are erosional or erosional/depositional features that vary widely in size, both vertically and horizontally, depending on the wind characteristics in a particular

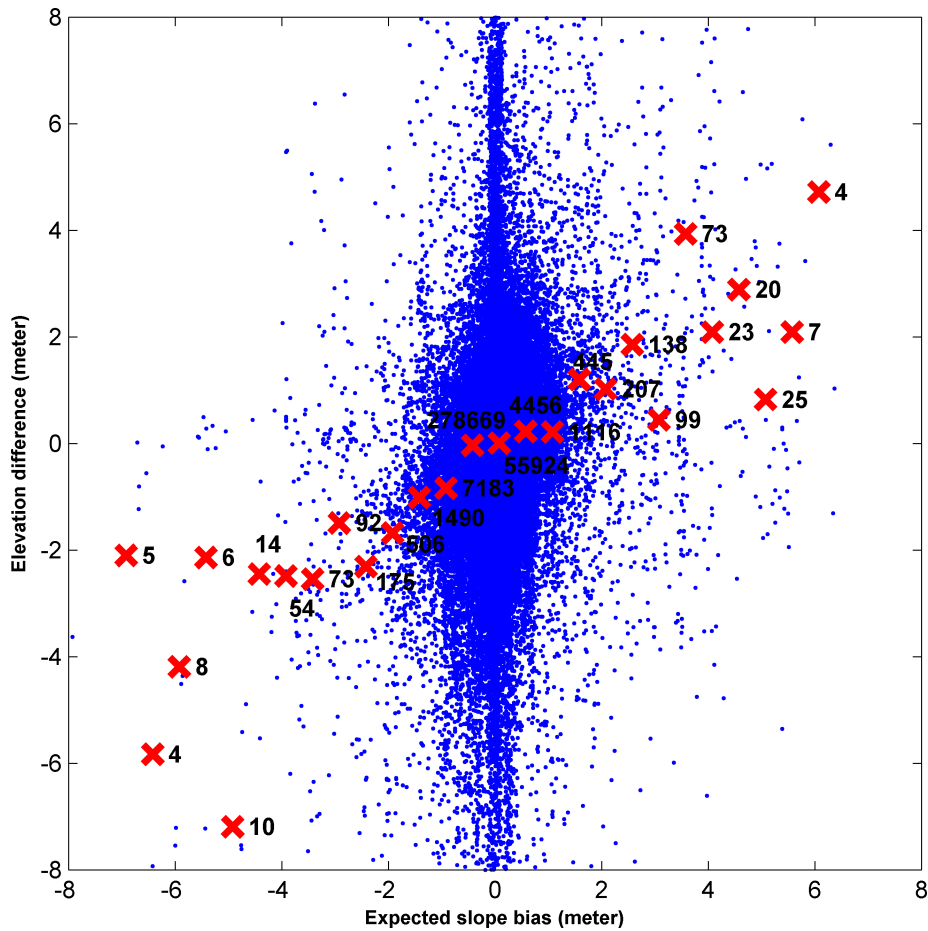


Figure 4.7: Scatterplot of the expected slope biases and the observed elevation differences. The red crosses indicate the mean elevation differences per interval. The numbers refer to the used number of points to calculate the mean.

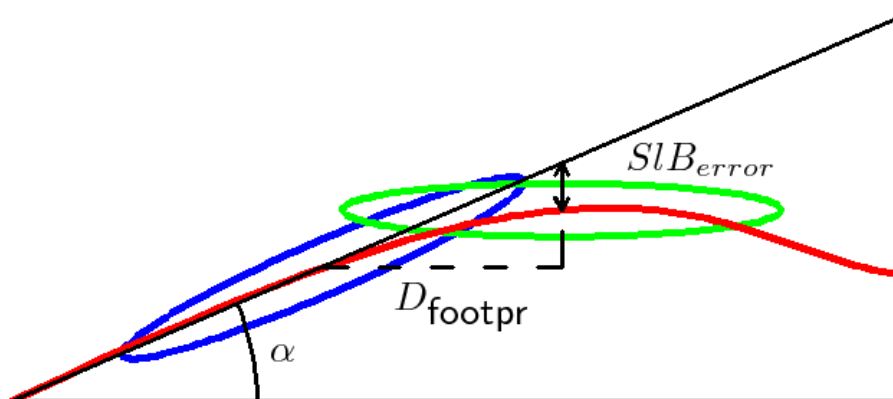


Figure 4.8: The error in the expected slope bias, introduced when the slope changes over the line that connects both centers of the footprints.

region, see figure 4.9. In many areas the irregularities of the surface are 0.1 m or less in height, with typical horizontal wavelengths on the order of several meters. Roughness due to sastrugi is anisotropic; sastrugi ridges are elongated in the direction of the wind, so the roughness characteristics are different along, and normal to, that direction. Snow dunes are accumulative features that are somewhat larger than sastrugi; they can be up to several meters in amplitude and tens of meters in wavelength.



Figure 4.9: *Large sastrugi on Antarctica, taken from [18].*

The second type of roughness has much longer wavelengths and has two different causes. The first cause are the megadunes, identifiable on AVHRR and SAR images, which are comparable in size to the flow-produced undulations but more regularly sinusoidal in form. Megadunes however, have not been found in Greenland. Second, there exist undulations of the surface that result from the flow of the ice over topographic irregularities in the bed. Although the flow characteristics of the ice are such that the vertical scale of the relief of the surface is much less than that of the bed, surface relief nevertheless exists and in many places is pronounced. Amplitudes of this relief are commonly a few meters to tens of meters, with horizontal wavelengths of hundreds of meters to many kilometers. The thickness of the ice sheet modulates the surface relief in two ways; the thicker the ice, the smaller the amplitude of the surface relief and the greater its dominant horizontal wavelengths. The ice sheet acts like a band pass filter; subglacial relief of wavelengths short compared to the ice thickness is damped by the strength of the ice sheet. On the other hand, very long wavelengths are attenuated by the plastic flow of the ice. It is the long-wavelength roughness, which grows more pronounced in the coastal regions where the ice is thinner and moving faster.

The third type of roughness stems from cracks in the surface; crevasses. These develop anywhere where the stresses in the ice due to variations in flow exceed the breaking strength of the ice. Crevasses vary widely in scale, from millimeters to tens of meters across and from tens of meters to kilometers long. Like the undulations, crevassing has a strong tendency to be more pronounced in locations nearer to the coast. In extreme cases, (e.g. the Jakobshavn ice tongue in Greenland) the crevassing is so severe that the surface becomes a jumbled series of sharp ridges of ice among the crevasses of a glacier; seemingly more crevasse than ice. In the waveforms, multiple reflections will provide a warning of the presence of crevasses.

So roughness can cause a systematic behavior in the elevation differences (second type), but for the first type the influence can be characterized as random. The third type can cause both types of behavior but this will depend on the orientation of the crevasses with respect to the crossing or overlapping tracks.

The measure of the first type of roughness is indicated by the roughness parameter in the GLA12 data product. Due to the fact that roughness and surface slope cannot be separated when they are estimated using the waveforms, this parameter represents a combined effect of both roughness and surface slope. Unfortunately there are some problems with both the roughness and the surface slope parameters [38]. A known problem with release 26 is that the estimates of slope and roughness are not correct. The equations in this release do not use the real laser footprint information and do not correct for the difference between the estimated and true pointing direction. For release 28 both parameters are output as invalid values because a new surface slope algorithm for flat surfaces estimated larger slope and roughness values than expected.

So we can only use the valid values of release 18 and release 26 to study the relation between the roughness parameter and the elevation differences, which implies that we have for only 69 030 OPs a roughness value. The valid roughness values are selected with the surface roughness and slope quality flag (*SurfRuf_slpQF*). Figure 4.10 shows the scatterplot between the valid roughness values and the absolute values of the elevation differences. The correlation is clearly visible, especially for larger values of the roughness. It turns out that the dataset contains a part that can be almost completely explained by the combined effect of roughness and surface slope. In this study we make an attempt to use this information in a weighting scheme.

4.2 Mass balance estimation

The case studies show that the elevation differences are contaminated by different effects that are sometimes not related to the ablation/accumulation signal we are looking for. Especially the influence of slope and roughness on the elevation differences is significant. It makes sense that suspect elevation differences get less weight in the estimation of the ice sheet mass balance. Due to the mixture of effects and the lack of information such weighting is not a straightforward task.

To account for the inhomogeneous distribution of OPs on the ice sheet, a trend is estimated for 6 drainage systems, further divided into a region above and below 2000 meter elevation. The problem of the inhomogeneous distribution and the used approach will be discussed in section 4.2.1. After that we explain how big outliers will be removed. In section 4.2.3 the proposed weighting scheme is discussed. To retrieve the time series of elevation changes, least squares techniques are used. In a second step a trend is estimated through these time series. The used techniques and models are discussed in section 4.2.4.

4.2.1 Ice sheet division

The map in figure 4.1 shows that the distribution of OPs is not homogeneous over the Greenland ice sheet. The further to the south, the less the density of OPs, which is simply caused by the orbital configuration of the satellite. When we simply add together all OPs, most signal will come from the northern part, because with this approach only the number of OPs is important. However, also the location of the OPs must be taken into account, which implies that the total estimated mass balance will be the sum of all different signals all over the ice sheet. Several approaches can be used to deal with this problem, here we will discuss only one approach.

One approach, often used in practice, is to divide the ice sheet in grid cells and estimate a trend for each of them. The total mass balance will be the integral over the whole surface. In this case, it is assumed that the inhomogeneous distribution of OPs for whole Greenland will be homogeneous for the individual grid cells. In this case you get rid of the effect on the distribution of OPs caused by the orbital configuration. On the other hand, you are still left with a non-isotropic sampling of the OPs, i.e. in

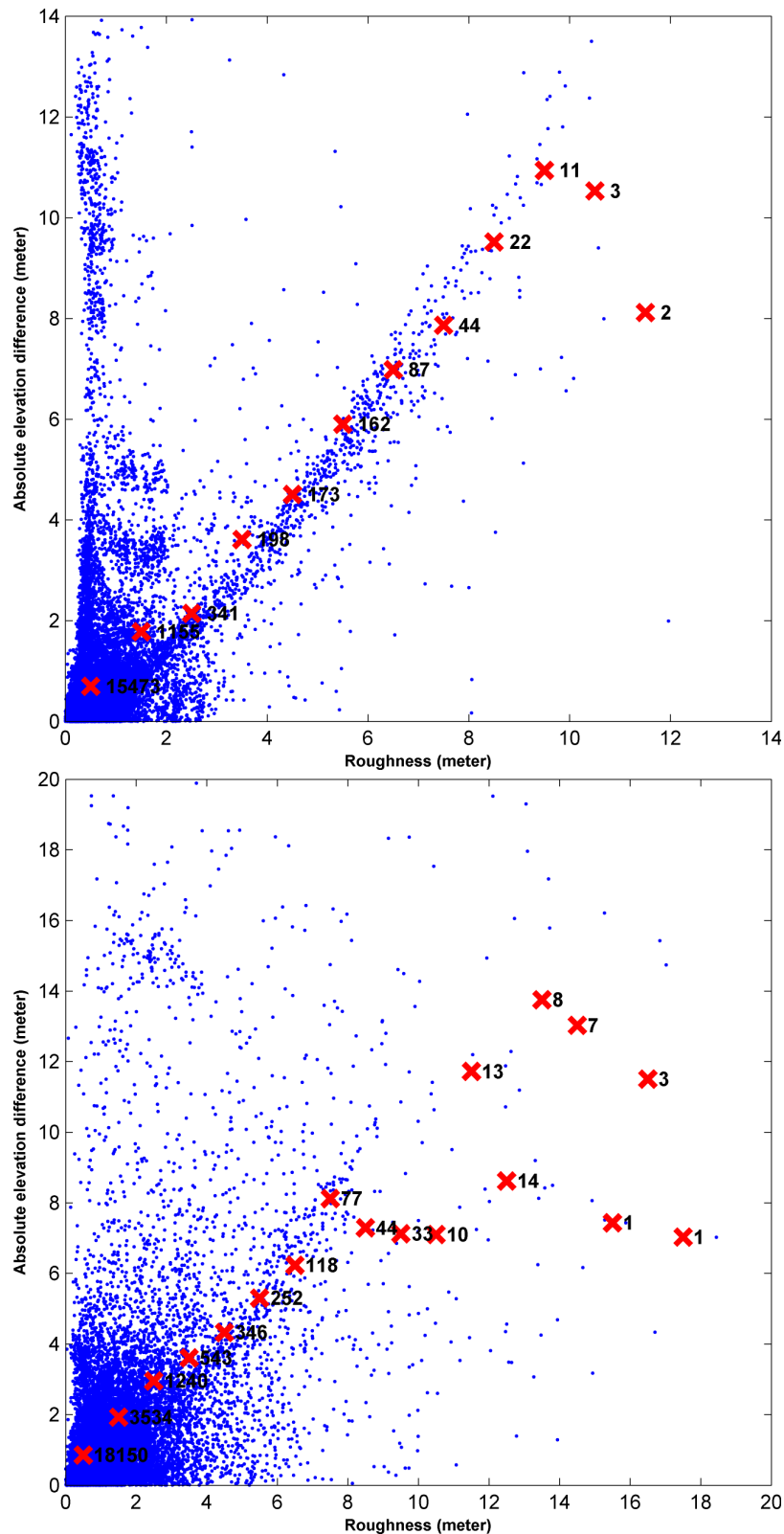


Figure 4.10: Scatterplots of the roughness values and the observed elevation differences for the region above 2000 meter (upper image) and below 2000 meter (lower image). Estimates of the roughness parameter are only available for the first two laser campaigns. In cases where two roughness values were available, the mean roughness value is used. The red crosses indicate the mean elevation difference per roughness interval.

North-South direction the sampling is better than in East-West direction due to the fact that also OTPs are used.

Furthermore, also the distribution of OPs in the temporal domain is important. This is a significant issue due to the reduced operational activities of the ICESat satellite. Especially at the glaciers, where large signals are expected due to accelerated flow speeds, this will be a problem ([23] and [45]). When we have only elevation differences on a fast moving glacier between two epochs, the signal shows up as an outlier in the estimated time series. In any case, a bad temporal sampling causes gaps in the time series, so it will be more difficult to estimate the trend.

To account for this, one can make the area of the grid cell sufficiently large. We follow a slightly different approach. Instead of a trend per grid cell, we will estimate a trend for 6 drainage systems (DSs), further divided into a region above and below 2000 meter ([34]), see figure 4.11. The DSs are defined according to climatology and with respect to the ice sheets flow direction from the interior toward the coasts. When these DSs are used, we will have no gaps in the time series and it will make validation of our estimates more feasible. In the remainder we refer to a particular DS by the abbreviation DS, followed by its number. The letters a and b are used to refer to the region above (a) and below (b) 2000 meter elevation.

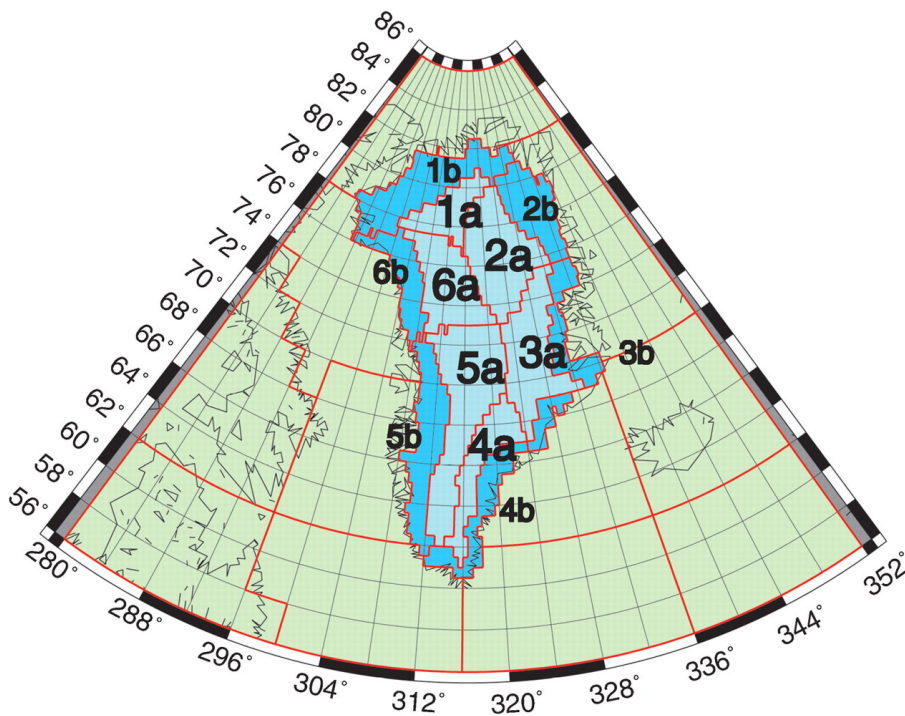


Figure 4.11: Greenland divided into 6 drainage systems, further divided into a region above (a) and below (b) 2000 meter, taken from [34].

4.2.2 Removal of outliers

To detect outliers, N-sigma thresholding is used. Elevation differences larger than the thresholds will not be used any more. The thresholds are set by adding and subtracting k times the standard deviation to/from the mean that is obtained from the elevation differences themselves. In order to avoid a contamination of the mean and standard deviation, first a large value of k is used to remove extreme outliers, here we used k equals 10. After that the mean and standard deviation are recomputed again. In the second step, this mean and standard deviation are used with k equals 3 to remove the remaining

outliers. In our situation this procedure is done separately for all individual DSs for both the region above and below 2000 meter.

The main problem with this approach is that no distinction is made between random outliers and systematic patterns, i.e. all elevation differences larger than the mean plus or minus k times the standard deviation are regarded as outliers. In this case, possible real signals will be removed too. Probably this can be avoided by a more advanced outlier detection method like data snooping. However, this approach requires a processing of the individual crossing and overlapping tracks. Due to the fact that we work with a subset of the data, the gaps in the elevation difference profiles limit the application of such a method. Also it is impossible to use data snooping to detect outliers in the CTPs. To avoid these problems as much as possible one might consider to apply this method on the raw tracks. In other words, before the OPs are derived, the outliers in the individual tracks are detected and removed. Still there will be gaps in the raw elevation profiles, because of invalid elevations. However, the situation will be improved significantly.

4.2.3 Weighting scheme

In section 4.1 the relation between the observed elevation differences and the slope/roughness was studied. The combined influence of both effects is visualized in figure 4.10, that shows a scatterplot between the roughness parameter and the elevation differences. These plots reveal that the elevation differences for the larger roughness values can almost completely be attributed to the combined effect of roughness and surface slope. Here, we make an attempt to use this information to develop a weighting scheme.

Uniform weights for all elevation differences do not take into account that the contribution of the roughness to larger elevation differences is relatively large. This is visualized in figure 4.12, that shows the correlation between the roughness parameter and the elevation differences on the left and right side of a threshold T_h , as a function of this threshold. When the threshold becomes larger, the correlation on the left side becomes larger too. Notice that for these plots only data of release 18 and 26 is used, because only for these releases an estimate of the roughness parameter is available. That is also the reason why we subdivided the whole of Greenland in only two regions, a region above and below 2000 meter. When these plots were made for individual DSs, no reliable correlations can be calculated. Notice that for the calculation of these curves, we make use of the elevation differences remaining after the N -sigma thresholding. The N -sigma thresholding corresponds to a horizontal cut-off of the scatterplot visualized in figure 4.10. For the left plot, corresponding to the region above 2000 meter, the crossing between the red and blue curve corresponds to a threshold that is equal to ± 0.7 meter. This shows that for the region above 2000 meter, the influence of roughness is especially strong for elevation differences of a few decimeters (0.3 meter up to 0.7 meter). This corresponds with the magnitude of wind-driven surface sastrugi. For the region below 2000 meter, both curves cross when the threshold is ± 1.7 meter. This shows that the influence of roughness and slope is more spread. Also here wind-driven surface sastrugi may play a role, but especially closer to the margins the influence of surface slope can become more severe.

Figure 4.12 shows that it makes sense to make the weights dependent on the observed elevation differences itself; the smaller the elevation difference, the higher the weight. To avoid the problem of very high weights for small elevation differences, two separate weight regions are defined that will have a distinctive weighting scheme, see equation 4.3. This approach is also more realistic due to the fact that figure 4.12 does not provide a basis for the proposed weighting scheme when the elevation differences are small. The figure shows that the correlation is comparable for elevation differences of 0.1 and 0.2 meter, while the elevation differences of 0.2 meter will get weights that are four times lower when the weights are inversely proportional to the squared elevation differences themselves.

So our observed elevation differences are divided in three parts. The first part is already detected and removed by N -sigma thresholding. The second part shows partly the signal of interest but partly the observed differences can be attributed to the combined effect of surface slope and roughness. Here the weights are assigned to be inversely proportional to the squared elevation differences. The last part

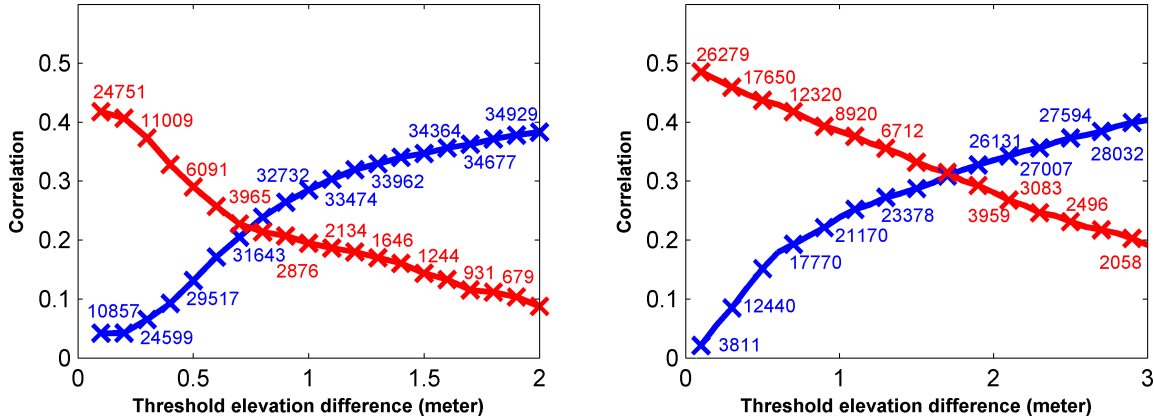


Figure 4.12: Correlation between the roughness parameter and the elevation differences on the left (blue line) and right side (red line) of a threshold, as a function of this threshold. The left and right plots are for the region above and below 2000 meter respectively.

shows mainly the signal of interest, here uniform weights are applied.

To indicate the boundary between the second and the third part, figure 4.12 was used. Notice that the choice of the boundary is arbitrary but we chose to assign uniform weights when the correlation between the roughness and the elevation differences is lower than 0.15. For the region below 2000 meter this corresponds to an elevation difference of 0.5 meter. For the region above 2000 meter this value equals 0.55 meter. Now, the weights are computed according to equation 4.3. Figure 4.13 shows a map where the color is indicating the weight assigned to each measurement. From this map it follows that the largest part of the observations will get uniform weight.

$$w_{ij} = \begin{cases} \frac{1}{\overline{\Delta H}_{ij}^2} & \text{if } |\overline{\Delta H}_{ij}| > T_h; \\ \frac{1}{T_h^2} & \text{if } |\overline{\Delta H}_{ij}| \leq T_h; \end{cases} \quad (4.3)$$

Where:

- w_{ij} weight assigned to a particular elevation difference between epoch i and j
- $\overline{\Delta H}_{ij}$ observed elevation difference between epoch j and i
- T_h threshold for which it holds that the correlation between the roughness parameter and the observed elevation differences is equal to 0.15

This weighting scheme is referred to as the non-uniform weighting scheme. Beside the non-uniform weighting scheme, also an uniform weighting scheme is used. In this weighting scheme the observations are divided in only two parts. The first part is already detected and removed by N-sigma thresholding, while all elevation differences of the second part will get uniform weight.

Drawback of the non-uniform weighting scheme is that it tries to account for the combined effect of surface slope and roughness based on the observed elevation differences itself. This will lead to a kind of reasoning that is not longer valid, i.e. a large elevation difference is interpreted as noise because it is large. The fact that this is unreasonable is proved by the case studies, see section 4.1.2. A strong ablation signal is observed for the Jakobshavn Isbræ glacier. With the non-uniform weighting scheme, this signal is strongly reduced, see figure 4.13.

Obviously this drawback is caused by a lack of information, i.e. we only have information about the roughness and surface slopes for two laser campaigns. When the roughness values were available for all releases, these values could be used to assign weights to all elevation differences.

For now, we are left with a trade-off. The non-uniform weighting scheme will reduce strong ablation/accumulation signals. On the other hand uniform weights for all elevation differences propagate the uncertainty and possible bias introduced by the combined effect of surface slope and roughness to

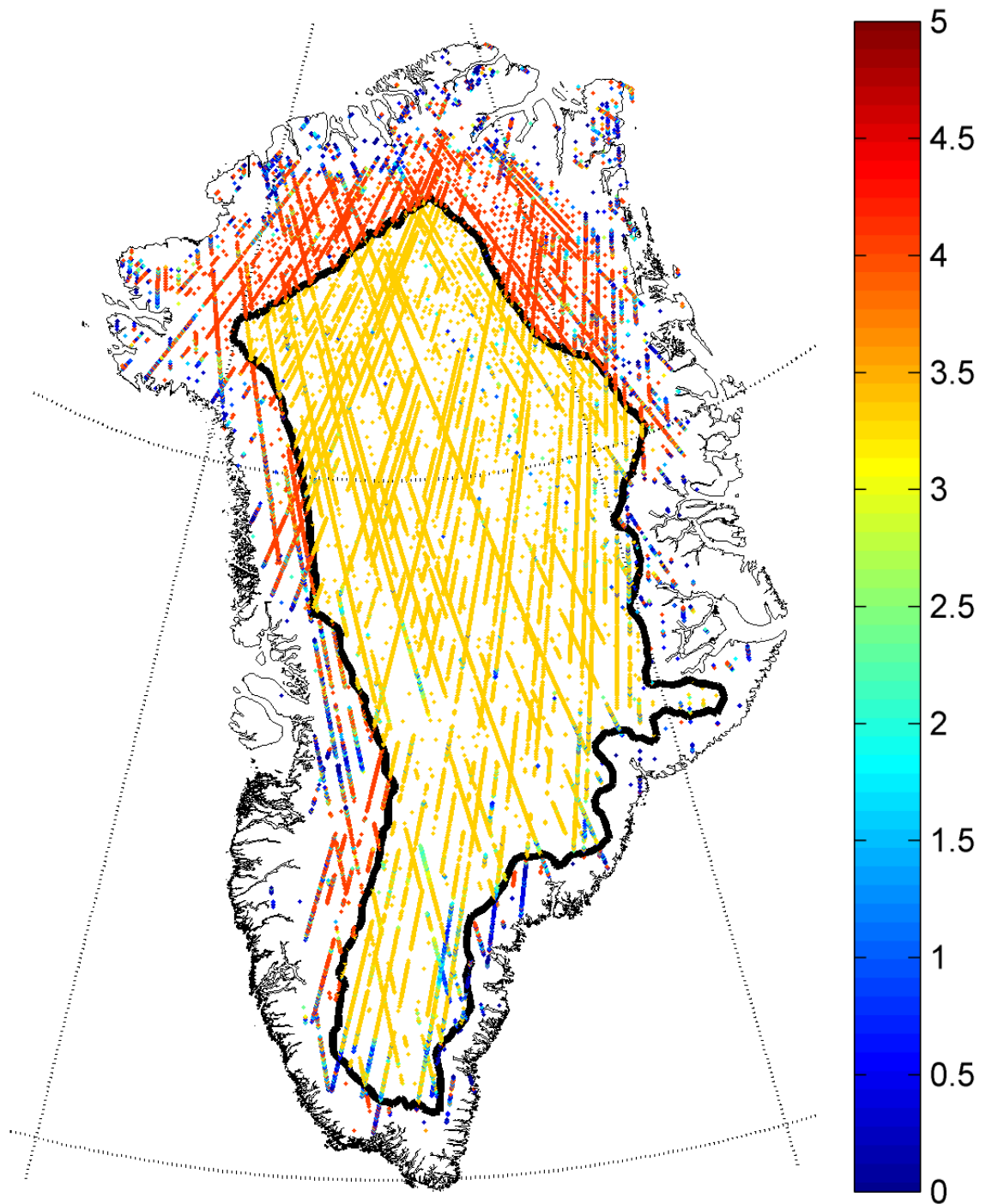


Figure 4.13: Map where the color is indicating the weights assigned to the observed elevation differences. Notice that we added both regions together, but that the estimation is done separately. This figure shows clearly that for the region above 2000 meter mostly uniform weights are used. For the region below 2000 meter, weights in general decrease toward the margins.

the estimated mass balance. (See section 4.1.3 and section 4.1.4 for a more detailed discussion about the nature of these effects). In section 6.1.1 both weighting schemes are evaluated.

4.2.4 Mass balance estimation

To be able to estimate the mass balance from the observed elevation differences, a two step estimation procedure is developed. In the first step the time series for all DSs above and below 2000 meter are reconstructed using weighted least squares. The time series are parameterized in months. Using the propagation law, also the uncertainty of the mass balance estimate can be propagated from the uncertainties in the observations. The estimated heights and corresponding uncertainties form the input for the Best Linear Unbiased Estimation (BLUE) of the trend parameters, using a combined linear and sinusoidal/cosinusoidal model. This trend is used to calculate the elevation change rate and in a next step the mass change rate. In the following, these steps are discussed in more detail. Notice that we use the elevation differences as our observations, which is not totally true because we measured elevations.

Estimating time series

To discuss the first step, we can use the parallel with the estimation of heights in a leveling network [60]. Based on only the leveled elevation differences this problem cannot be solved, but one minimal constraint is needed in order to eliminate the rank deficiency, i.e. one has to fix the height of one point. Instead of elevation differences in the spatial domain, we have to deal with elevation differences in the time domain. In order to eliminate the rank deficiency we choose to fix the height of one epoch (r) at zero. So our general observation equation becomes:

$$\overline{\Delta H}_{ij} = H_j^r - H_i^r + \bar{e}, \text{ with } i < j \quad (4.4)$$

Where:

$\overline{\Delta H}_{ij}$	observed elevation difference between month j and i
H_j^r	height in month j
H_i^r	height in month i
\bar{e}	noise

Due to the elimination of the reference epoch, the design matrix is of full rank. The remaining heights are given the upper index r to show that they are defined with respect to the fixed height of the reference epoch.

Notice that the parametrization in months implies that 7 138 elevation differences within one month ($i = j$) are disregarded. One might consider a parametrization in weeks, because the number of point pairs falling into the same week is only 235. The main problem of this solution is that a weekly trend will contain other signals that do not represent the trend we are looking for.

Weighted least squares techniques are used to estimate the unknown heights, where both the uniform and non-uniform weighting scheme (see section 4.2.3) are used.

In order to apply error propagation, a variance-covariance matrix (VC-matrix) has to be defined. Unfortunately all standard deviations of the elevations in the GLA12 data product are invalid. Therefore we assumed that the VC-matrix can be given as a scaled unit matrix where the scale factor is obtained from the standard deviation of the elevation differences with a time difference smaller than 30 days. Error propagation becomes now straightforward, using equation 4.5. Notice that when uniform weights are used, equation 4.5 reduces to equation 4.9.

$$Q_{\hat{x}\hat{x}} = (A^T W A)^{-1} A^T W Q_{yy} W A (A^T W A)^{-1} \quad (4.5)$$

Where:

$Q_{\hat{x}\hat{x}}$	VC-matrix of the unknown heights
A	design matrix of the time series model
W	weight matrix
Q_{yy}	VC-matrix of the observed elevation differences

Estimation of trend parameters

In the second step a trend is estimated through the time series. Here the combined linear and sinusoidal/cosinusoidal model is used, given in equation 4.6

$$y_i = a + b \cdot t_i + c \cdot \sin\left(\frac{2 \cdot \pi \cdot t_i}{T}\right) + d \cdot \cos\left(\frac{2 \cdot \pi \cdot t_i}{T}\right) \quad (4.6)$$

Where:

- y_i estimated height on epoch i
- a y-intercept
- b trend of linear model
- c first parameter that accounts for seasonal cycle
- d second parameter that accounts for seasonal cycle
- t_i epoch i , with t_0 at January 2003
- T period of seasonal cycle, i.e. one year

In this equation the last two terms account for the seasonal cycle. The corresponding parameters c and d are calculated from the more common wave parameters amplitude (A_m) and phase (ϕ) as:

$$c = A_m \sin \phi \quad d = A_m \cos \phi \quad (4.7)$$

Where:

- A_m amplitude
- ϕ phase

The advantage of using c and d instead of the amplitude and phase is that now a linear relationship exists. Inversely, the amplitude and phase of the wave can be calculated from c and d as:

$$A_m = \sqrt{c^2 + d^2} \quad \phi = \arctan\left(\frac{c}{d}\right) \quad (4.8)$$

Due to the limited amount of points in our time series and the fact that we only have laser campaigns in the period February - March and October - November, this model might not perform well. Another choice would be to only consider the points at the end of the ablation season and using only a linear model. However, in that case too much data will be removed from the dataset.

To propagate the uncertainties of our time series to the estimated trend parameters, equation 4.5 is used. Notice that Q_{yy} represents here the full VC-matrix of the time series, derived in the first step. Due to the fact that we used the BLUE, the weight matrix W is equal to the inverse of the full VC-matrix of the time series. In that case equation 4.5 reduces to:

$$Q_{\hat{x}\hat{x}} = (A^T Q_{yy}^{-1} A)^{-1} \quad (4.9)$$

PGR correction

Past ice load change, in particular the deglaciation after the last ice age, continues to act through Post Glacial Rebound (PGR), i.e. vertical land movements due to removed ice loads and related lateral mass shifts in the Earth's interior. The PGR-induced radial velocities (velocities in the direction of the satellite), see figure 4.14, kindly provided by Riccardo Riva, are calculated using Peltiers ICE-5G ice model and the VM2 Earth model [43]. The ice model describes the ice-load history, while the Earth model describes, amongst others, the mantle viscosity. From this grid, we are able to calculate the average PGR correction over our region of interest, by taking the average PGR-induced radial velocity ($\overline{PGR}_{\Delta H \downarrow}$) of the grid points in this region. So we are left with a linear trend that can be subtracted from the estimated time series or trend. See table 4.1 for an overview of the average PGR-induced radial velocities for the individual regions.

The rates are small, corresponding with the prevailing opinion. For the Antarctic ice sheet this error source is of much more concern [68]. To be able to derive a measure of uncertainty, it is common practice (R. Riva, personal communication) to use half the value of the maximum difference among the PGR rates based on different Earth and ice models. However, for Greenland only different Earth models were available. See table 4.1 for an overview of the estimated uncertainties.

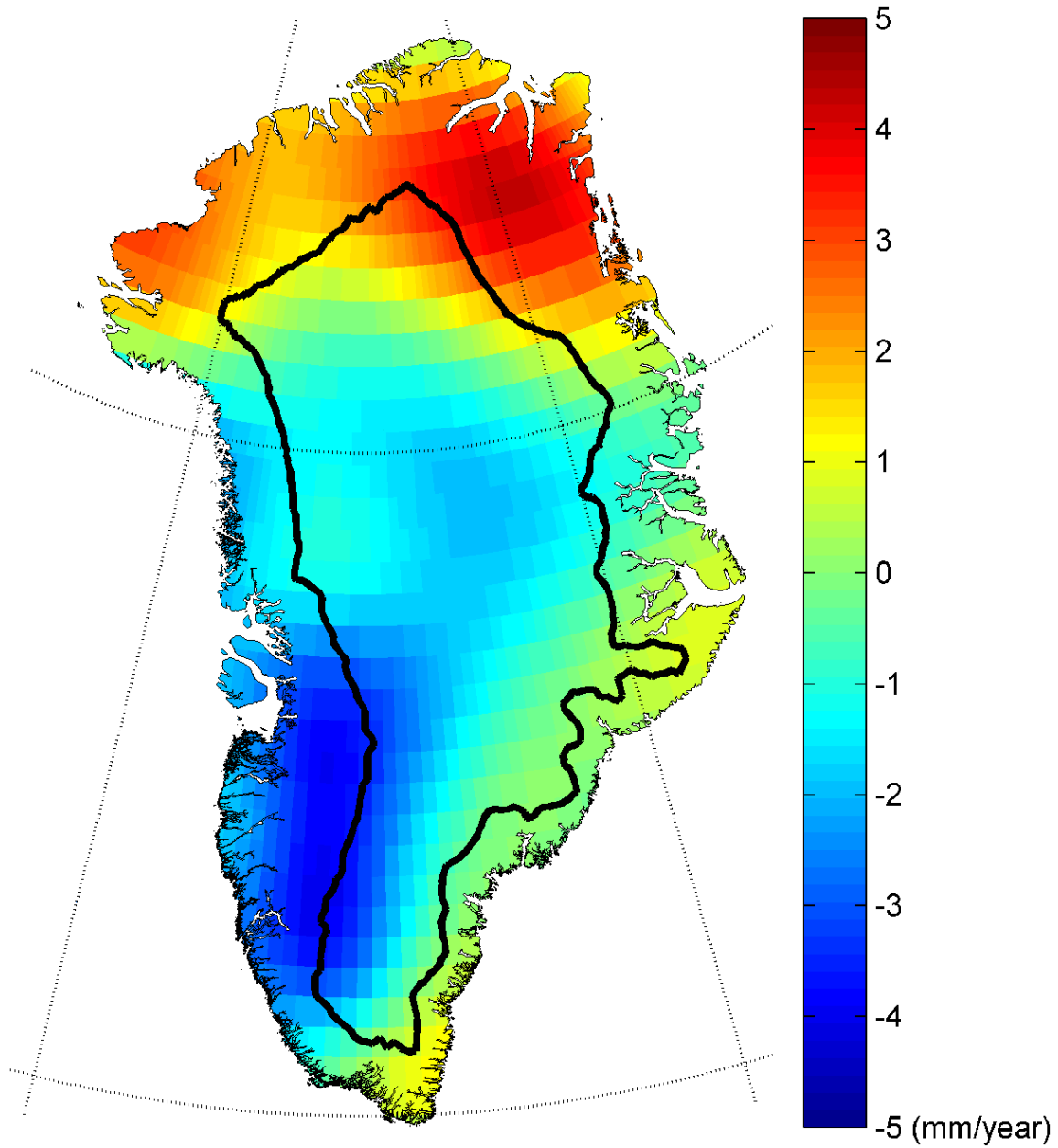


Figure 4.14: PGR-induced radial velocities, calculated using Peltiers ICE-5G ice model and the VM2 Earth model [43].

DS	$\overline{\text{PGR}}_{\Delta\text{H}\uparrow}$	$\sigma_{\overline{\text{PGR}}_{\Delta\text{H}\uparrow}}$	$\overline{\text{PGR}}_{\Delta\text{H}\downarrow}$	$\sigma_{\overline{\text{PGR}}_{\Delta\text{H}\downarrow}}$
1	0.7	1.1	2.2	0.9
2	-0.2	1.0	2.8	1.6
3	-0.8	0.5	0.0	1.1
4	-0.4	0.9	0.5	1.0
5	-2.0	1.0	-2.9	1.8
6	-1.3	0.8	-1.2	0.9

Table 4.1: PGR corrections in mm/year for the different regions.

From elevation change to mass change

The conversion from elevation changes to mass changes is not trivial and therefore different approaches exist, see [75]. In short the problem is caused by the fact that a proper density is needed to convert from elevation/volume changes to mass changes. The question is now whether the changes in elevation of the firn/ice column are caused by ice dynamics, not being in balance with the long-term multi-decadal accumulation rate, or are caused by shorter-term (decadal) variability in accumulation. In the last case, another density has to be used to convert to a mass change. Notice that the density of newly fallen snow is about three times smaller than the density of ice (300 kg/m³ versus 917 kg/m³ [75]). In other words, the estimated elevation change trend is the sum of a trend caused by ice loss, variability in the accumulation rate and also a rest term of the corrected PGR effect. This rest term is the difference between the real PGR contribution and the contribution obtained from the model that is used in the previous step to correct for PGR. From figure 4.14 it follows that the PGR corrections are small. Knowledge about the accumulation rate is limited, so this term cannot be determined completely. Wingham et al., [75] showed that, in the absence of other data, an altimeter estimate covering 73% of the Antarctic interior could vary by 90 Gton/year without contradicting the observed volume change. To get more insight into this issue we will discuss some of existing approaches before we will discuss our approach.

Zwally et al., [77] uses ~10 years of satellite radar plus airborne laser altimetry data to estimate the mass balance for the Greenland and Antarctic ice sheet. To convert the observed elevation differences to ice-thickness changes, they correct both for PGR and for temporal variations in the rate of firn compaction. These last corrections are calculated using a firn compaction model that is sensitive to variations in firn temperature and surface melting. The model also accounts for the effects of vapor transport in the firn and the effects of near-surface melting.

The ice-thickness changes are converted to mass changes using the approximation in equation 4.10. Here it is assumed that when the time series are sufficiently long, short-term stochastic fluctuations in accumulation rate average out over the full period. And that over large regions their nett effect will average out.

$$\frac{dM}{dt} = \rho_a \frac{dl_c}{dt} \text{Area} \quad (4.10)$$

Where:

- M mass
- ρ_a average density of the firn/ice column, 900 kg/m³
- l_c thickness of the firn/ice column

However, Helsen et al., [22] conclude that accumulation anomalies can cause large decadal elevation change rates, using the same firn compaction model without later advances made by Zwally and Jun [78].

Thomas et al., [62], used elevation changes from satellite radar and satellite and aircraft laser altimetry to estimate the mass balance change on the Greenland ice sheet. They do not account for temporal variations in the rate of firn compaction. So after subtraction of the PGR effect, they immediately convert the observed elevation differences to mass changes by using a similar approximation as Zwally et al. [77]. However, with this difference that they use different densities for different regions. For the interior (the region above 2000 meter) they used a density of 600 ± 300 kg/m³, but as they stated,

this density is probably at the lower end of the indicated range. This density is chosen because they conclude that increased snowfall causes the observed elevation differences. In the coastal region, where ice is lost by melting and increased discharge, they used a density of 900 kg/m^3 .

In our case, we have very short time series of elevation change. Recent observations show that the signal below 2000 meter is mainly caused by fluctuations in flow velocity of the glaciers ([34], [23] and [45]). For the region above 2000 meter a positive elevation change trend is reported ([77], [62] and [24]). We believe that the approach of [62] is more applicable for this situation. Here we use for all DSs above 2000 meter a density of 600 kg/m^3 , for the DSs below 2000 meter a density of 917 kg/m^3 is used. In section 6.1.1 we will discuss the influence of the underlying assumptions.

Now, equation 4.11 is used to convert the estimated elevation change rate ΔH_{DS} (indicated with b in equation 4.6) to a mass change rate for each individual DS above (\uparrow) and below (\downarrow) 2000 meter elevation.

$$\begin{aligned}\Delta M_{DS\uparrow} &= \text{Area}_{DS\uparrow} \cdot \Delta H_{DS\uparrow} \cdot \rho_{\uparrow} \\ \Delta M_{DS\downarrow} &= \text{Area}_{DS\downarrow} \cdot \Delta H_{DS\downarrow} \cdot \rho_{\downarrow}\end{aligned}\quad (4.11)$$

Where:

- ΔM_{DS} estimated mass change rate for a particular DS above (\uparrow) and below (\downarrow) 2000 meter
- ΔH_{DS} estimated elevation change rate for a particular DS above (\uparrow) and below (\downarrow) 2000 meter
- ρ_{\uparrow} average density above 2000 meter elevation (600 kg/m^3)
- ρ_{\downarrow} average density below 2000 meter elevation (917 kg/m^3)

In order to retrieve the mass change rate of whole Greenland, we simply sum up all estimated mass change rates for all different DSs both for the region above and below 2000 meter elevation.

In literature sometimes only the elevation change rates are provided. For validation purposes we provide both the estimated elevation and mass change rates. The average elevation change rate $\overline{\Delta H}$ over whole Greenland is computed according to equation 4.12.

$$\overline{\Delta H} = \frac{\sum_{DS=1}^6 (\text{Area}_{DS\uparrow} \Delta H_{DS\uparrow} + \text{Area}_{DS\downarrow} \Delta H_{DS\downarrow})}{\sum_{DS=1}^6 (\text{Area}_{DS\uparrow} + \text{Area}_{DS\downarrow})}\quad (4.12)$$

Chapter 5

Mass balance estimation with GRACE data

This chapter describes the methodologies and procedures that are used to estimate the mass balance change using GRACE data. Starting with a short description of the used data products in section 5.1, this chapter continues with an explanation how temporal gravity field variations can be used to estimate the mass balance change. As a consequence of noise, a filter step is necessary. This filter step will be explained in section 5.3. The GRACE mass balance change estimates are affected by different error sources that will be discussed in section 5.4.

5.1 Used GRACE solutions

To estimate the mass balance change using gravimetric data, monthly models of the Earth's gravity field derived from GRACE data are used. The monthly gravity variations are obtained by subtracting a static or mean field from the monthly solutions. Each solution consists of a set of gravity (Stokes) coefficients C_{lm} , see equation 2.1. Different GRACE solutions independently computed by several research groups are available that will be briefly discussed and summarized in this section. After that the most important details of the used static fields are given. In the remainder of this section it is explained how we deal with temporal variations of the coefficients of degree 0 and 1.

5.1.1 Monthly solutions

Several datasets of GRACE monthly solutions are available to the public. Here we used the solutions of the Bureau Gravimétrique International of the Centre National d'Études Spatiales (CNES) [5], Center for Space Research (CSR) [4] and GeoForschungsZentrum (GFZ) [50]. Also we have access to the DEOS GRACE solutions ([33]), but the time span of this dataset is only 3 years. The used GRACE solutions are referred to by the processing center. The main properties of the used solutions are summarized in table 5.1.

The CNES fields are given every 10 days and are based on the running average of three 10-day data periods with weights 0.5/1.0/0.5. They are recovered from GRACE data and from Laser Geodynamics Satellite-1/2 (LAGEOS) Satellite Laser Ranging (SLR) data. The SLR data provide over 90% of the information on degree 2 of the gravity field, whereas GRACE data provide nearly 100% of the information on all other harmonic coefficients. The CSR, DEOS and GFZ monthly solutions are given every month and are solely based on GRACE data.

Solution	Release	Time span	Max. degree	Static
CNES	1	Aug 2002 - Oct 2006	50	EIGEN-GL04C
CSR	4	Apr 2002 - Feb 2007	60	mean 2003 - 2004
CSR-ds ^{*1}	4	Apr 2002 - Dec 2006	60	GGM02C
DEOS	1	Feb 2003 - Nov 2005	120 ^{*2}	EIGEN-GL04C
GFZ	4	Aug 2002 - Feb 2007	120	EIGEN-GL04C

^{*1} CSR destribed (CSR-ds) solutions, see section 5.4.2.
^{*2} maximum degree differs per month, values of 50, 60, 70 but mostly 120 occur.

Table 5.1: *Main properties of used GRACE monthly solutions.*

5.1.2 Static solutions

Three different static fields are used in order to determine the temporal variations. For CNES, GFZ and DEOS the combined gravity field EIGEN-GL04C ([58]) is used, complete to degree and order 360. The model is a combination of GRACE (February 2003 to February 2005) and LAGEOS data plus gravimetry and altimetry surface data.

For the CSR destribed (CSR-ds) solutions (see section 5.4.2) the GGM02C static field ([59]) is used. This model is a combined solution of the GGM02S gravity model, estimated using 363 days (spanning April 2002 through December 2003) of GRACE data and terrestrial gravity information (surface gravity and surface altimetry data). The GGM02C model is complete to degree and order 360. From Xianglin Liu (personal communication) it follows that the GGM02C static field contains some biases. He advised to compute a mean field over a couple of years of GRACE solutions and use that to compute the monthly variations of the undestribed CSR solutions. We tested this approach using a mean field of 2 and 3 years of GRACE solutions. It turns out that the differences between both mean fields are negligible, so we used a mean field over 2 years. In this way, an alternative time series of CSR solutions was produced.

5.1.3 The coefficients of degree 0 and 1

For all GRACE solutions, the degree 0 and 1 coefficients are not available. The degree 0 coefficients are not important, because they reflect the total mass of the Earth that is constant. The degree 1 terms are proportional to the position of the Earth's center of mass relative to the center of the reference frame. They may change, but their behavior depends on the choice of the reference frame. The most realistic situation is to define the reference frame in such a way that its origin coincides with the center of figure of the solid Earth surface. This is because in practice the reference frame is defined primarily from GPS data, which refer to positions of GPS stations all over the world. In this case, the degree 1 terms describe the offset between the center of mass of the surface mass plus deformed solid Earth and the center of figure of the deformed solid Earth surface.

So our only concern is about the degree 1 coefficients, but they can in principle not be estimated from GRACE data. In order to incorporate these coefficients in the estimation of the mass balance change, sometimes empirical relations ([8]) are used. However, according to P. Ditmar (personal communication) the contribution of the degree 1 coefficients in the context of this study is negligible, so we will not regard them.

5.2 From gravitational potential variations to mass change

In this section we briefly discuss the way how the monthly variations in gravitational potential can be used to estimate the mass balance change. Here we focus on the practical implementation. For a

thorough derivation of the equations, we refer to [13], [55] and [70]. In section 5.2.1 we start with a short overview of the used equations, followed by a discussion about the used region functions. In section 5.2.3 we will discuss how the mass change rates are estimated. This section ends with some remarks about the error propagation.

5.2.1 The used equations

The most common way to represent the gravitational potential at the global scale is a linear combination of spherical harmonics, truncated at a certain maximum degree (L_{max}), see equation 2.1.

The Stokes coefficients (\overline{C}_{lm}) describing the Earth's gravity field can be linked to the distribution of masses inside the Earth. When this relation is substituted in equation 2.1, it can be shown that the Stokes coefficients are equal to:

$$\overline{C}_{lm} = \frac{1}{M_E(2l+1)} \iiint_v \rho(r', \theta', \lambda') \left(\frac{r'}{R}\right)^l \overline{Y}_{lm}(\theta', \lambda') dv \quad (5.1)$$

Where:

- M_E total mass of the Earth
- (r', θ', λ') location of integration point in spherical coordinates
- v volume of the Earth
- $\rho(r', \theta', \lambda')$ density at location of integration point

Most of the mass transport takes place at the Earth's surface, in the atmosphere, oceans and shallow sub-surface, i.e. in a relatively thin (± 10 km) near-surface layer. With GRACE, the gravity field is observed from space, so we can assume that this layer can be approximated by a thin spherical layer of radius $r = \tilde{R}$ (the mean radius of the Earth). Then, the mass transport can be represented as a variation of surface density $\delta s(\theta, \lambda)$ (amount of mass per unit area) in this thin layer:

$$\delta s(\theta, \lambda) = \int_{r_1}^{r_2} \delta \rho(r, \theta, \lambda) dr \quad (5.2)$$

Where:

- r_1 and r_2 radii that limit the layer where the actual mass transport takes place

When the integration in radial direction is done, equation 5.1 becomes a 2-D integral that describes the direct influence of the mass transport on the gravitational field. However, the Earth experiences elastic deformations due to an extra surface load that also cause variations of the gravity field. To account for this effect, an additional factor $(1 + k'_l)$ has to be included, where the coefficients k'_l are called load Love numbers. The values for these load Love numbers are provided by [70]. So, the total expression relating variations of the surface density to variations of the Stokes coefficients is:

$$\delta \overline{C}_{lm} = \frac{\tilde{R}^2(1 + k'_l)}{M_E(2l+1)} \left(\frac{\tilde{R}}{R}\right)^l \iint_{\Omega} \delta s(\theta, \lambda) \overline{Y}_{lm}(\theta, \lambda) d\Omega \quad (5.3)$$

Where:

- \tilde{R} radius of sphere $\Omega_{\tilde{R}}$ at which the mass transport takes place
- Ω unit sphere

Instead of the total mass of the Earth M_E , the average Earth's density ρ_{ave} is used (more precisely, the average density within the sphere of radius R), where $M_E = \frac{4}{3}\pi R^3 \rho_{ave}$.

When we expand the surface density variations into a series of surface spherical harmonics, with spherical harmonic coefficients $\overline{C}_{lm}^{\delta s}$ (see equation 5.4), and we neglect the difference between the radius of the sphere at which the mass transport takes place (\tilde{R}) and the major semi-axis of a reference ellipsoid

(R), the relationship between the Stokes coefficients $\delta\bar{C}_{lm}$ and the coefficients $\bar{C}_{lm}^{(\delta s)}$ can be written according to equation 5.5.

$$\delta s(\theta, \lambda) = \sum_{l,m=0}^{\infty} \bar{C}_{lm}^{\delta s} \bar{Y}_{lm}(\theta, \lambda) \quad (5.4)$$

$$\delta\bar{C}_{lm} = \frac{3(1+k'_l)}{R\rho_{av}(2l+1)} \bar{C}_{lm}^{(\delta s)} \quad (5.5)$$

Equation 5.5 allows to transform variations of the gravitational potential into variations of surface density. Usually these variations are expressed in terms of equivalent water layer thickness $h_w(\theta, \lambda)$, i.e. we assume that the surface density has changed solely due to a changing thickness of a water layer at the Earth surface. In that case we can write equation 5.5 as:

$$\bar{C}_{lm}^{(\delta h_w)} = \frac{\bar{C}_{lm}^{(\delta s)}}{\rho_w} = \frac{R(2l+1)\rho_{av}}{3(1+k'_l)\rho_w} \delta\bar{C}_{lm} \quad (5.6)$$

Where:

ρ_w the water density

5.2.2 Region function

In our case, we are interested in the average variation of thickness of the equivalent water layer within Greenland or a part of it. By definition, the average variation of thickness of the equivalent water layer $\delta\bar{h}$ within the area Ω_{reg} on the unit sphere is given by:

$$\delta\bar{h}_w = \frac{1}{E_{reg}} \int_{\Omega_{reg}} \delta h_w(\theta, \lambda) d\Omega = \frac{1}{E_{reg}} \int_{\Omega} \delta h_w(\theta, \lambda) q(\theta, \lambda) d\Omega \quad (5.7)$$

Where:

E_{reg} angular area of the region

$\delta h_w(\theta, \lambda)$ variation of thickness of the equivalent water layer as a function of location

$q(\theta, \lambda)$ region function that is 1 inside and 0 outside the area Ω

When the region function is represented as a series of surface spherical harmonics with spherical harmonic coefficients \bar{C}_{lm}^q , equation 5.7 can be rewritten as:

$$\delta\bar{h}_w = \frac{4\pi}{E_{reg}} \sum_{l,m=0}^{\infty} \bar{C}_{lm}^{\delta h_w} \bar{C}_{lm}^q \quad (5.8)$$

One effect of the region coefficients in equation 5.8 is a reduced contribution from the Stokes coefficients for large degrees to $\delta\bar{h}_w$. This is visualized in figure 5.1 that shows the degree amplitude spectrum for disc-shaped regions having radii of 1000, 500 and 100 km. The degree amplitude is defined as:

$$\vartheta_l = \sqrt{\sum_{m=-l}^l [(\bar{C}_{lm}^q)^2]} \quad (5.9)$$

From figure 5.1 it follows that for larger region sizes, the degree amplitude is concentrated at relatively smaller degrees, corresponding with longer wavelengths. This means that averages over larger regions are less influenced by poorly known short-wavelength signals.

Later we will see that the averages are biased by mass variations inside and outside the region. The magnitude of this bias depends amongst others on the size of the region [28]. In section 5.4.3 this bias will be discussed in more detail.

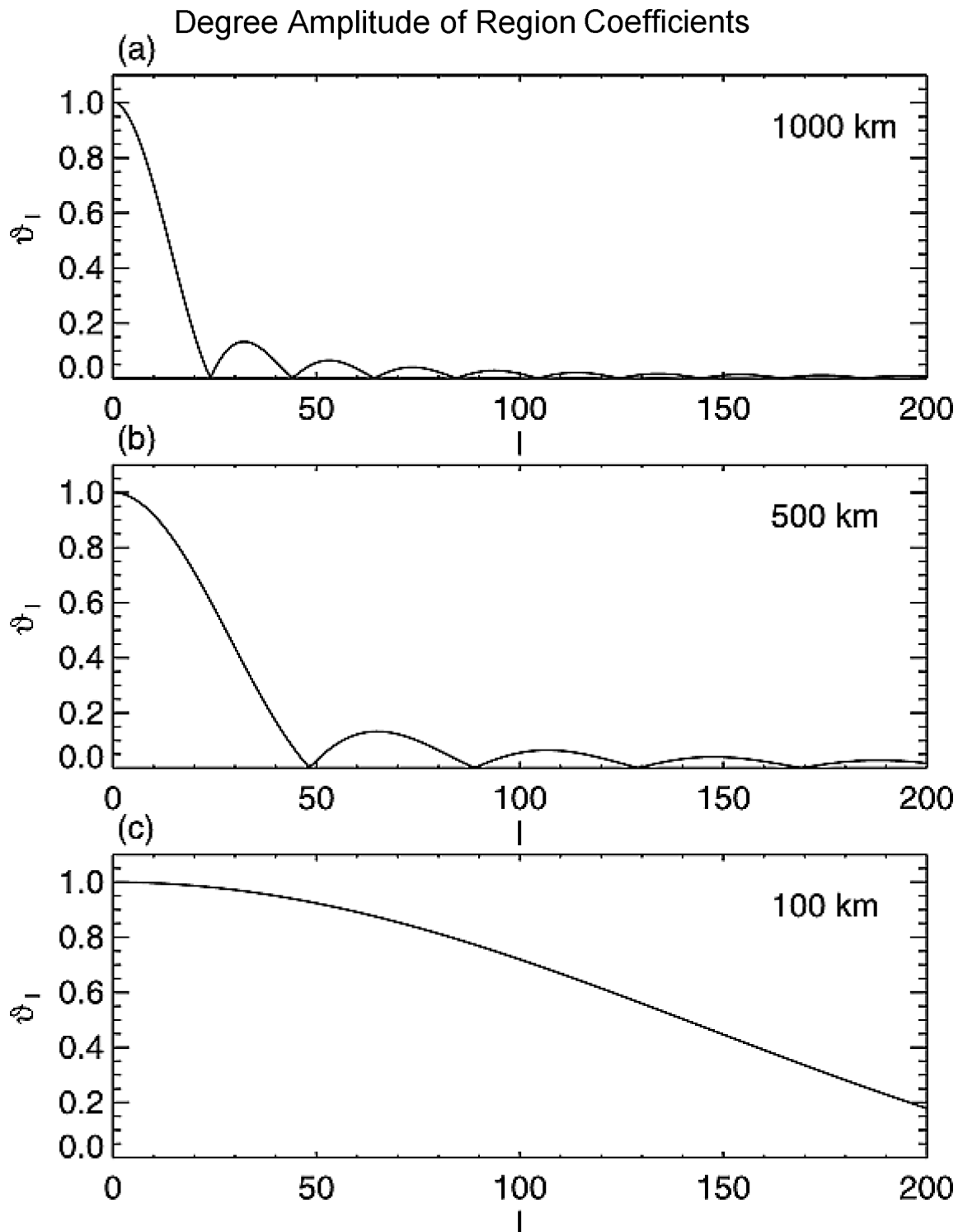


Figure 5.1: Degree amplitudes of the exact averaging kernels for disc-shaped regions with a different radius of (a) 1000 km, (b) 500 km, and (c) 100 km. The maximum amplitude has been normalized by $1/\vartheta_0$. Taken and adapted from [55]

From this, it follows that the size of the region may not be too small. One approach would be to take the largest region, i.e. the coast line of Greenland. However, then we will not see any spatial difference in the signal of possible mass changes. Another option would be to divide Greenland in regions above and below 2000 meter. The problem with this division is illustrated in figure 5.2. This figure shows a smoothed region function for the region below 2000 meter. As we can see, most of the signal comes from the northern part of Greenland.

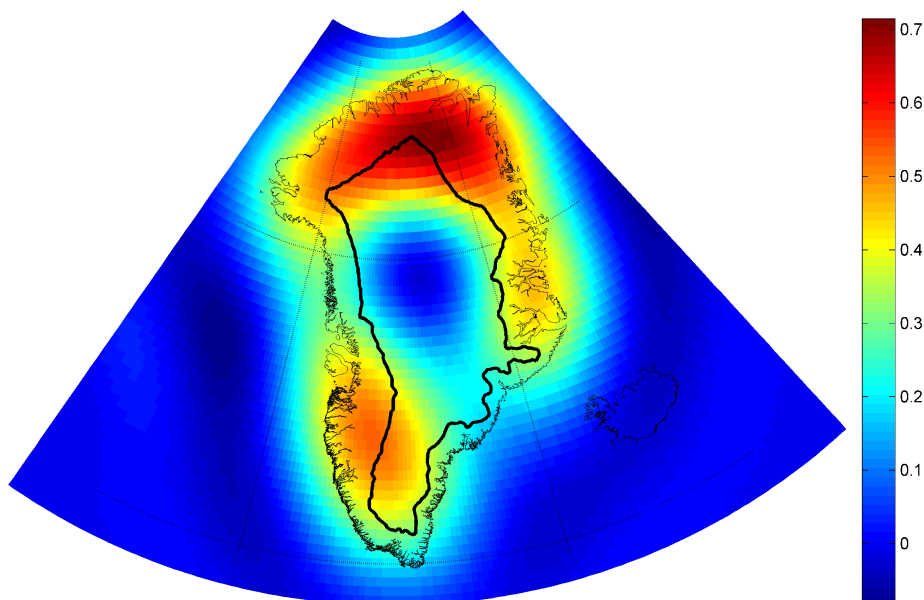


Figure 5.2: Smoothed region function for the region below 2000 meter. The 2000 meter elevation contour is indicated with the thick black line. Here L_{max} equals 50, corresponding with the maximum degree of the CNES models. For smoothing, a Wiener filter is used, see section 5.3.

To avoid these problems, Greenland is divided in a northern and southern part. Here we make use of the drainage systems as discussed in section 4.2.1. The northern part is defined as the combination of drainage systems 1,2 and 6 both a and b. The southern part as the combination of drainage systems 3,4 and 5 both a and b.

5.2.3 Estimation of the trend

With equation 5.8 we obtain the variations of thickness of an equivalent water layer within our region of interest. To estimate the mass change rate, basically the same procedure can be used as for the ICESat dataset. For ICESat the elevation change rate was estimated in a two step procedure. In the first step we estimated the time series, which is not necessary here, because the GRACE variations are defined with respect to a mean field. In other words, the design matrix to estimate the GRACE time series will be equivalent to the identity matrix. In the second step the elevation change rate of ICESat was estimated using a combined linear and sinusoidal/cosinusoidal model (see equation 4.6). For GRACE the same model is used. The estimated trend, expressed in variations of thickness of an equivalent water layer, can be converted to a mass change rate by multiplication with the area of the region and the density of water.

5.2.4 Error propagation

For most GRACE solutions we only have the formal and calibrated standard deviations of the spherical harmonic coefficients. The formal standard deviations are the uncertainties of the raw data, propagated

to the monthly gravity fields. However, in practice these errors are quite optimistic so they are calibrated (= rescaled). For all epochs these calibrated standard deviations are used to estimate the uncertainty of the averaged mass variation over the region of interest. This can be done by the propagation law of variances [42], given in equation 5.10.

$$Q_{zz} = A Q_{xx} A^T \quad (5.10)$$

For the DEOS solutions, the calibrated standard deviations of the CNES models are used, which turns out to be a rough indication of their uncertainty (X. Liu, personal communication). Of course it would be better to use the available full variance-covariance matrix. However, these matrices are huge (e.g. 1.6 gigabyte for $L_{max} = 120$). Dealing with these kind of matrices require advanced processing schemes that could not be developed within the frame of this project.

Equation 5.10 provides a variance for all points in the time series, expressed in variations of thickness of an equivalent water layer. The uncertainty of the estimated trend through the time series can be calculated using equation 4.9. Now again equation 5.10 can be used in order to compute the uncertainty of the estimated mass change rate in Gton/year.

5.3 Filtering

Until now, we did not consider the fact that in practice we have to deal with noisy data. This means that our estimated average will differ from the true region average due to the presence of satellite measurement errors. This noise rapidly increases when degree l increases.

In order to reduce the contribution of noise, two solutions are implemented and evaluated. The first solution to this problem is to smooth the region function with a low-pass filter. When this filter function ($W(\cos \psi)$) is expressed in terms of spherical harmonic coefficients (C_l^W), the application of this filter is a simple scaling of the spherical harmonic coefficients of the original region function $q(\theta, \lambda)$. In practice, different low-pass filters can be used. Here we used a Gaussian filter, see equation 5.11 that is applied quite often in practice.

$$W(\cos \psi) = \frac{b}{2\pi} \frac{e^{-b(1-\cos \psi)}}{1 - e^{-2b}} \quad (5.11)$$

Where:

$$b = \frac{\ln(2)}{\cos \psi_0} \quad (5.12)$$

Here, ψ_0 is a characteristic filter width that needs to be defined beforehand. Normally the half-widths are specified, here we use half-widths of 300, 500 and 800 kilometer.

The ad-hoc definition of the half-width is a drawback of this solution. Also, the larger this value, the more the real signal is damped. The second solution offers an objective way to design a filter using a mathematically justified criterion. This solution provides a statistically optimal estimation of the variation of thickness of the equivalent water layer all over the globe. However, Sasgen et al. ([49]) show that in practice this approach resulted in only a minor improvement over the approach based on the low-pass Gaussian filter.

The second solution can be realized with the so-called Wiener filter ([49]). The idea of this filter is to filter the original function in such a way that the total error in the resulting function is as small as possible. This results in the following minimization condition:

$$\mathcal{E} \left[\int_{\Omega} \left(\delta \hat{h}_w(\theta, \lambda) - \delta h_w(\theta, \lambda) \right)^2 d\Omega \right] = \mathcal{E} \left[\sum_{l,m=0}^{\infty} \left(\overline{C}_{lm}^{\delta \hat{h}_w} - \overline{C}_{lm}^{\delta h_w} \right)^2 \right] = \min \quad (5.13)$$

Where:

- $\mathcal{E}[\cdot]$ expectation operator
- $\hat{\delta h}_w(\theta, \lambda)$ estimation of true variation of thickness of the equivalent water layer after filtering
- $\delta h_w(\theta, \lambda)$ true variation of thickness of the equivalent water layer

Where equality holds due to Parseval's identity for spherical harmonic series. Notice that the original function consists of signal and noise. When it is assumed that these are not correlated, we can write the minimization as:

$$\mathcal{E} \left[\sum_{l,m=0}^{\infty} \left(\left(\frac{4\pi}{2l+1} C_l^W - 1 \right) \overline{C}_{lm}^{\delta h_w} \right)^2 + \left(\frac{4\pi}{2l+1} C_l^W \overline{C}_{lm}^n \right)^2 \right] = \min \quad (5.14)$$

Where:

- C_l^W spherical harmonic coefficients of the Wiener filter
- \overline{C}_{lm}^n spherical harmonic coefficients associated with noise $n(\theta, \lambda)$

When this expression reaches minimum, the spherical harmonic coefficients of the Wiener filter become:

$$C_l^W = \frac{2l+1}{4\pi} \frac{\sigma_{lm}^2(\delta h_w)}{\sigma_{lm}^2(\delta h_w) + \sigma_{lm}^2(n)} \quad (5.15)$$

Where:

- $\sigma_{lm}^2(\delta h_w)$ signal variances
- $\sigma_{lm}^2(n)$ noise variances

The signal and noise variances can be estimated from the original model of gravity field variations. Figure 5.3 shows the average degree-power spectra of all used GRACE solutions, calculated by:

$$\langle \sigma_{GS,l}^2 \rangle = \frac{1}{\#N} \sum_{t=1}^{\#N} \sigma_{GS,t,l}^2 \quad (5.16)$$

Where:

- $\sigma_{GS,l}^2$ averaged degree amplitude for degree l with $2 \leq l \leq L_{max}$ for a particular GRACE solution
- $\#N$ total number of months
- $\sigma_{GS,t,l}^2$ degree amplitude for month t and degree l for a particular GRACE solution

In order to be able to compare the degree-power spectra for the different GRACE solutions, all spectra are added together in figure 5.4. Notice that in both figure 5.3 and figure 5.4, the degree-power spectra are expressed in terms of geoid-height squared in mm^2 . These spectra are calculated according to equation 5.17 [71].

$$\delta N_l = R^2 \sum_{m=-l}^l \left[(\overline{C}_{lm})^2 \right] \quad (5.17)$$

Where:

- δN_l degree variance expressed in geoid-height squared in mm^2
- R major semi-axis of the reference ellipsoid in mm

It can be assumed that the low-degree part of these average spectra contains information about gravity signals. The high-degree part reflects the noise contaminating the GRACE data. In between there is a part where signal and noise are mixed.

The signal part is modeled by an inverse-power function, where the unknown parameters x_1 and x_2 are estimated using non-linear least squares techniques ([49]).

$$\sigma_{lm}^2(\delta h_w) = \frac{10^{x_1}}{l^{x_2}} \quad (5.18)$$

The noise part is modeled by a linear function in a logarithmic scale, see equation 5.19. Here the unknown parameters x_3 and x_4 are also estimated using least squares techniques ([49]).

$$\log \sigma_{lm}^2(n) = x_3 + x_4 l \quad (5.19)$$

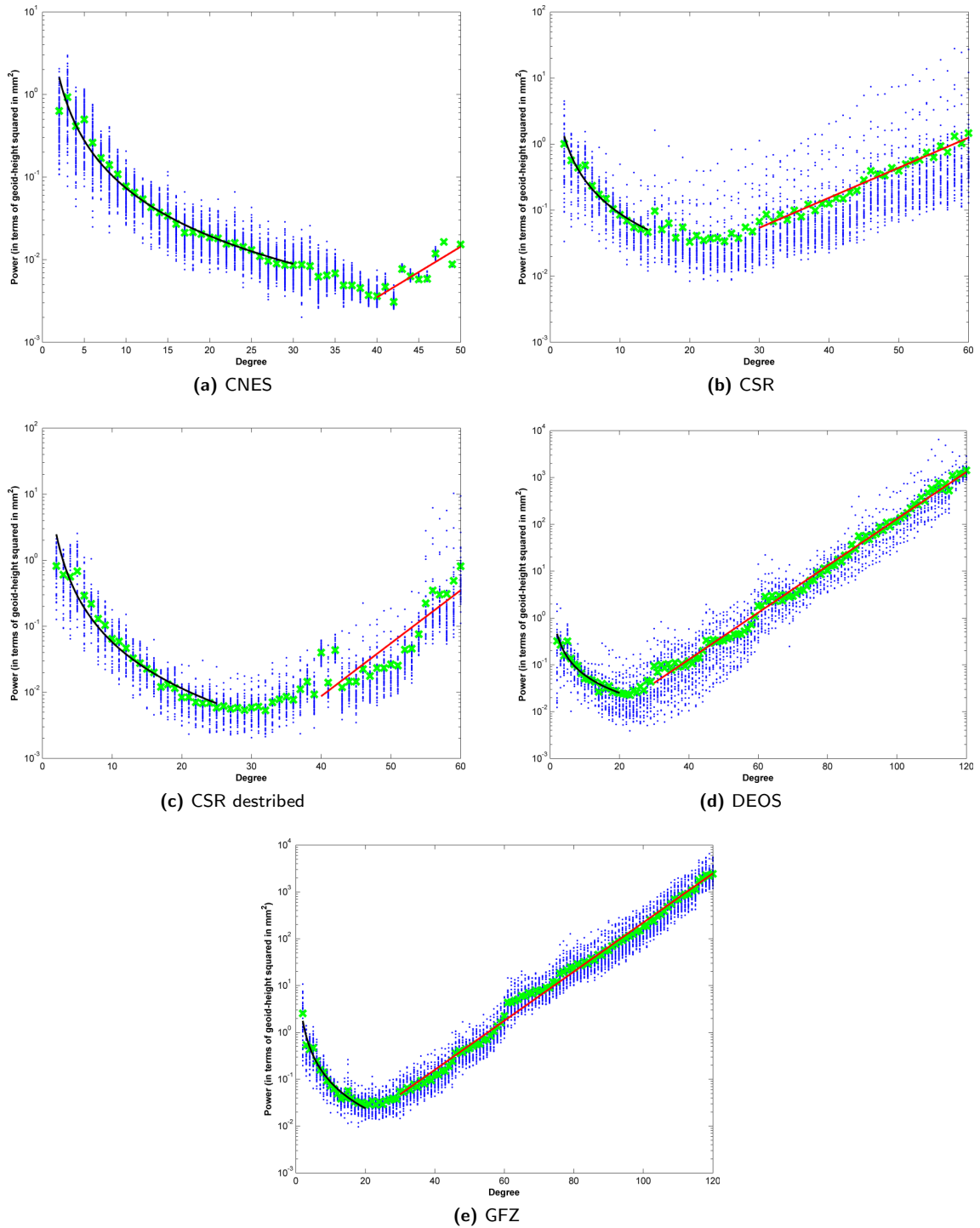


Figure 5.3: Average degree-power spectra for all used GRACE solutions, in terms of geoid-height squared in mm^2 . The blue dots represent the degree variances for all monthly solutions. The green crosses are the averages per degree based on all monthly degree amplitude spectra. The black and red solid are respectively the modeled inverse-power function for the signal part and the modeled linear function in a logarithmic scale for the noise part.

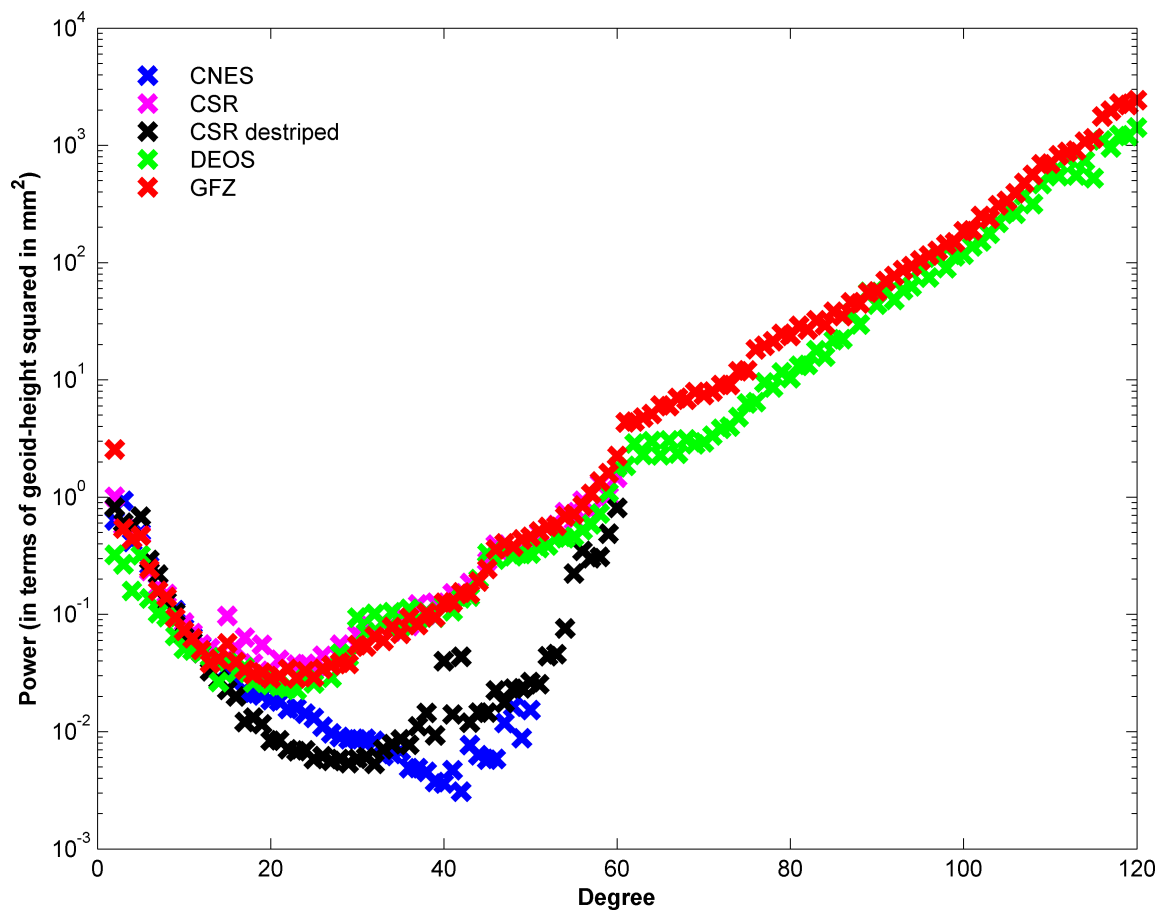


Figure 5.4: Average degree-power spectra for all used GRACE solutions, in terms of geoid-height squared in mm^2 .

Solution	$L_{\sigma_{lm}^2(s)}^{*1} \text{max}$	$L_{\sigma_{lm}^2(n)}^{*2} \text{min}$	x_1	x_2	x_3	x_4
CNES	30	40	0.79	1.92	-4.91	0.06
CSR	14	40	0.74	1.70	-1.76	0.03
GFZ	20	30	0.81	1.87	-2.90	0.05
DEOS	20	30	0.01	1.35	-3.23	0.05

*1 right boundary signal part used to estimate a and b (left boundary is 2).
*2 left boundary noise part used to estimate c and d (right boundary is L_{max}).

Table 5.2: For all used GRACE solutions this table provides the boundaries of the signal and noise part plus the estimated parameters of the inverse-power function (x_1 and x_2) and the linear function in a logarithmic scale (x_3 and x_4). These functions are used to model the signal and noise part respectively.

With the used models and the estimated parameters, the signal and noise degree variances are calculated for the whole spectrum, i.e. for $2 \leq l \leq L_{max}$. Now the spherical harmonic coefficients of the Wiener filter C_l^W are obtained by equation 5.15. This procedure is repeated for all GRACE solutions, see table 5.2 for an overview of the boundaries for the signal and noise part and the estimated parameters.

With the Gaussian or Wiener filter coefficients (C_l^W) the spherical harmonic coefficients of the smoothed variations of thickness of the equivalent water layer $\overline{C}_{lm}^{\delta h_{ww}}$ are calculated using equation 5.20 ([13]).

$$\overline{C}_{lm}^{\delta h_{ww}} := \frac{4\pi}{2l+1} \overline{C}_{lm}^{\delta h_w} C_l^W \quad (5.20)$$

To obtain the smoothed average variation of thickness of the equivalent water layer, we can apply equation 5.8 but now we use $\overline{C}_{lm}^{\delta h_{ww}}$ instead of $\overline{C}_{lm}^{\delta h_w}$.

Notice that both the Gaussian and Wiener filter are isotropic filters, i.e. they depend only on the spherical distance between the points. These kind of filters are also called degree-dependent filters, because in the spherical harmonics domain they only depend on degree l and not on the order m . However, there are inherent spherical harmonic degree-and-order-dependent error characteristics associated with the high inclination of the GRACE satellite orbits. In [19] it is shown that the orbits of the GRACE satellites cause larger errors in the potential coefficients of higher orders than of lower orders. This effect is visible e.g. in the longitudinal stripes, see section 5.4.2. To overcome these problems, more advanced filters are necessary.

Han et al. [19] developed an anisotropic filter that depends on both degree and order. However, the most general type of filter is when the information about the variances and covariances of the potential coefficients is fully exploited. In that case, the full noise variance-covariance matrix is needed, which is only available for the DEOS solutions. Notice that also mass variations inside and outside the region of interest contribute to the estimated average, see section 5.4.3. In order to minimize the total error caused by measurement errors and the mass variations inside and outside the region, also a-priori signal information is needed. Estimates of the signal may be obtained from models, observations or a combination of both. Due to a lack of time we did not implement these more advanced filters, which is a topic for further research. For more details about this topic, we refer to [57].

5.4 GRACE error sources and corrections

In this section different error sources are discussed together with some correction methods. We start with discussing Post Glacial Rebound (PGR) followed by an overview of the error known by the longitudinal stripes. This section ends with a discussion of the so-called leakage correction.

5.4.1 PGR correction

Post Glacial Rebound (PGR) causes lateral mass shifts in the Earth's interior for which we have to correct the observed mass changes. In order to be able to apply this correction, the PGR-induced rates of geoid height changes (δN) are calculated using Peltiers ICE-5G ice model and the VM2 Earth model [43], see figure 5.5. The PGR-induced rates of geoid height changes, kindly provided by Riccardo Riva, can be represented as a set of spherical harmonic coefficients as well. With these coefficients we are able

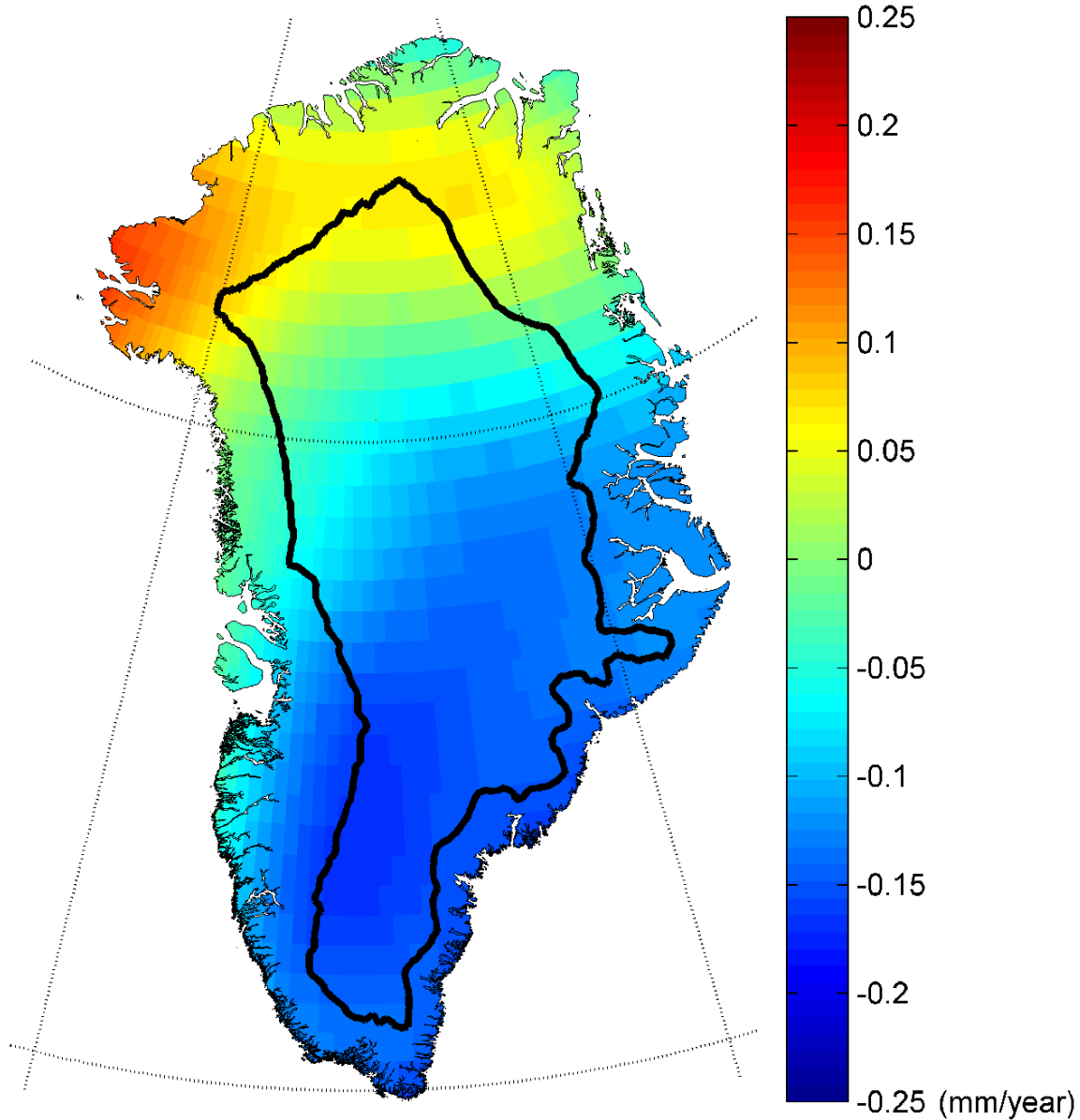


Figure 5.5: PGR-induced rates of geoid height changes, calculated using Peltiers ICE-5G ice model and the VM2 Earth model.

to calculate the average PGR correction over our region of interest. This correction can subsequently be subtracted from the estimated mass change. Due to the fact that the mass variations are expressed in variations of thickness of an equivalent water layer, a conversion step is necessary, see equation 5.21.

$$\overline{C_{lm}^{(\text{PGR}_{\delta h_w})}} = \frac{\rho_{av}(2l+1)}{\rho_w 3(1+k'_l)} \left(\frac{\tilde{R}}{R} \right)^{l+2} \overline{C_{lm}^{(\text{PGR}_{\delta N})}} \quad (5.21)$$

Where:

$\overline{C}_{lm}^{(PGR_{\delta h_w})}$	Stokes coefficients representing the PGR correction in mm/year expressed in variations of thickness of an equivalent water layer
\tilde{R}	mean Earth radius
R	major semi-axis of a reference ellipsoid
$\overline{C}_{lm}^{(PGR_{\delta N})}$	Stokes coefficients representing the PGR correction in mm/year expressed in rate of geoid height changes

The average PGR correction over the region of interest can be calculated using the following equation:

$$\overline{\delta PGR} = \frac{4\pi}{E_{reg}} \sum_{l,m=0}^{\infty} \overline{C}_{lm}^{(PGR_{\delta h_w})} \overline{C}_{lm}^q C_l^W \quad (5.22)$$

Where:

$\overline{\delta PGR}$	average PGR correction in mm/year expressed in variation of thickness of an equivalent water layer
-------------------------	--

As a consequence of the fact that the Wiener filter coefficients will differ for the different GRACE solutions, the PGR corrections are computed for all of them separately, see table 5.3. The PGR corrections for different half-widths of the Gaussian filter are provided in table 5.4. The uncertainties are derived

Region	CNES	CSR	CSR-ds	DEOS	GFZ
North* ¹	2.2	1.0	2.0	1.2	1.1
South* ¹	-5.4	-5.6	-5.5	-5.5	-5.8
Whole Greenland	-3.2	-4.6	-3.5	-4.4	-4.7

*¹ For a definition of these regions see section 5.2.

Table 5.3: PGR corrections in Gton/year for the different GRACE solutions per region when the Wiener filter is used.

Region	300 km	500 km	800 km
North* ¹	1.5	0.6	0.3
South* ¹	-5.2	-4.6	-2.7
Whole Greenland	-3.8	-3.9	-2.4

*¹ For a definition of these regions see section 5.2.

Table 5.4: PGR corrections in Gton/year for different half-widths of the Gaussian filter.

using the method explained in section 4.2.4. For the northern part, southern part and the whole of Greenland, these values are fixed at 3.3, 1.6 and 3.2 Gton/year respectively.

5.4.2 Destriping

We already mentioned the presence of longitudinal stripes in the GRACE solutions. The presence of stripes indicates a high degree of anisotropic spatial correlation in the GRACE errors and implies also correlation in the computed gravity field coefficients. The Wiener filter, but also the anisotropic filter of Han et al. ([19]) do not account for correlated errors in the data. Swenson and Wahr ([56]) developed a method to remove the correlated errors, referred to as destriping. To do this, smoothly varying coefficients for a particular order m of same parity are isolated and removed by smoothing the Stokes coefficients for that order with a quadratic polynomial in a moving window of a certain width centered about degree l . This had to be done manually, which takes a lot of time. Fortunately, the destriped CSR models were already available and kindly provided by Erna Oudman. Here it must be noticed that the C_{20} coefficients are replaced with values from SLR solutions.

It makes sense that this procedure changes the calibrated standard deviations that are used for error propagation. Unfortunately it is not clear how, so the original ones are used.

5.4.3 Leakage

The application of the Wiener filter was necessary to reduce the noise in the gravity field models. However, beside the reduction of noise, a bias is introduced ([28]) in the estimated average over the region of interest. This bias $\bar{\epsilon}_0$ can be written as:

$$\bar{\epsilon}_0 = -\frac{1}{E_{\text{reg}}} \int_{\Omega_{\text{reg}}} f_0(1 - q_w(\theta, \lambda)) d\Omega_R + \frac{1}{E_{\text{reg}}} \int_{\Omega_R - \Omega_{\text{reg}}} f_l q_w(\theta, \lambda) d\Omega_R \quad (5.23)$$

Where:

Ω_{reg}	area of region of interest
Ω_R	mean Earth sphere
f_0	mass variation inside the region of interest
$q_w(\theta, \lambda)$	smoothed region function
f_l	mass variation outside the region of interest

According to equation 5.23, the bias consists of two terms. The first term on the right-hand side is the so-called type 1 error. It expresses the contribution of mass variations inside the region of interest to the bias. Since $1 - q_w(\theta, \lambda)$ is always positive, it causes an underestimation of the amplitude of the monthly mean mass variation averaged over the region of interest. The second term on the right-hand side is called type 2 error. It represents the contribution of mass variations outside the region of interest to the bias. In literature this bias is mostly called the leakage error but sometimes only the second term get this name.

Due to the fact that this bias leads to a significant amplitude reduction in the estimated monthly mean, researchers investigate to rescale the amplitude variations. In [66] and [67] the smoothed region function is scaled such that if it is applied to a uniform mass change of 1 cm water thickness over all regions within a few hundred km off the Greenland coast, but zero in the interior, it returns an average value of 1 cm. This scaling is motivated by a study where airborne laser altimetry data is used that suggests that the largest mass changes are concentrated at the coast [31]. If it was assumed that the ice sheet was thinning uniformly, all trends would be reduced by 20%. Here, we do only partly agree with this approach, because recent studies show that the mass changes are not uniformly at the coast, e.g. [45], [34]. Mass losses are much stronger in the South, and there is also an accumulation signal in the interior of Greenland, [24] [34]. Therefore, this approach might be too simplistic. To define a proper scaling factor, simulations are needed that recover the measured signal. These simulations can be used to quantify what the estimated average should be. When this value is divided by the real estimated average, a proper scaling factor will be obtained. Due to a lack of time we were not able to implement this procedure.

Another approach to correct for this bias is to quantify the bias itself and add that to the estimated average. For this approach, a-priori information is needed about the mass variations inside and outside the region of interest. Information about mass variations outside the region of interest is only required within a certain distance from the region of interest. This distance depends on the used filter function. For the estimates of the northern and southern part of Greenland, the strongest mass variations outside the region of interest come from the southern and northern part respectively. The contamination from the surrounding oceans seems to be negligible [66].

The contamination of the continental hydrology can be obtained from hydrological models that can be understood as a kind of rain bucket. For every grid cell the water storage is calculated based on bottom coverage maps, precipitation fields, temperature fields etc. Variations in the water storage can be obtained by subtracting a mean field from the monthly models.

Unfortunately no reliable hydrological model of Greenland is available (Marc Bierkens and Rens van

Beek, personal communication). This is partly due to a lack of reliable datasets, but mainly due to the fact that the area is covered by ice. Due to the low temperatures just a part of the area is hydrologically active. So we are left with global hydrological models that have quite large uncertainties. When we take the GLDAS models [47] as an example, (used by [66] to remove leakage from the Greenland mass balance estimates), we see no signal in the interior of Greenland for all months, which is totally unreasonable. With this in mind, we decided not to apply this correction based on this approach, because when the correction is applied, additional errors will be introduced.

So, our estimates still contain the bias. According to [28], the bias increases when the size of the region decreases. Therefore, our estimates of the northern and southern part are more biased than the estimate of Greenland as a whole. Further research is necessary to quantify the bias, probably a scaling factor computed using simulations will do a better job. In section 6.2.3 it is shown, that in some studies this bias is approximately as large as the unscaled signal itself, which shows the importance of this correction.

Chapter 6

Results and Discussion

In this chapter, the estimated mass change rates are presented based on ICESat and GRACE data separately and based on a joint inversion on both datasets. In the discussion, the results are interpreted and compared with other studies, possible differences will be explained. We start with the estimates based on both ICESat and GRACE data separately. These parts form the answers to the first two subquestions, as defined in section 1.4. From these answers also the answer at the third subquestion can be derived, shortly summarized in section 6.3. In the final section we present a method for a joint inversion on both ICESat and GRACE data. These results form the answer to the last subquestion.

6.1 Results and discussion ICESat

In this paragraph we answer the question: What is the mass balance of the Greenland ice sheet based on only ICESat data? We start with an evaluation of different possible processing strategies. Here, the strategy that performs best is chosen and the time series of elevation changes are presented and discussed for the different drainage systems (DSs). First these results are compared with estimates from other studies where altimetry is used. After that we will compare our results with the so-called 'mascon solutions' for the different DSs [34].

6.1.1 Results ICESat

Using the methods described in chapter 4, the time series of elevation change are calculated for the different drainage systems. In order to evaluate the developed processing strategy, elevation change rates and corresponding mass change rates are computed using four different processing strategies for three sets of laser campaigns, see table 6.1. For the corresponding time frames that belong to these three datasets, we refer to table 3.1. We refer to the different strategies and datasets by the Roman numerals I-III followed by a letter (a-d) indicating the used dataset and processing strategy respectively.

Table 6.2 provides an overview of the estimated elevation change rates and corresponding mass change rates using the different strategies defined in table 6.1. It turns out that in most cases the data of release 18 (spring 2003) and also release 26 (autumn 2003) behave like outliers. This is visible in the time series belonging to strategy Ic and Id, provided in appendix B. Also the other time series belonging to processing strategy I and II show a similar behavior for these two laser campaigns. This behavior indicates the existence of unremoved data suffering from the aforementioned saturation effect for both releases, see section 2.1.4. For the release 18 data also former processing strategies are used.

ID	Used releases	N-sigma thresholding	Weighting
Ia	all	yes	non-uniform
Ib	all	no	non-uniform
Ic	all	yes	uniform
Id	all	no	uniform
IIa	R26,R28	yes	non-uniform
IIb	R26,R28	no	non-uniform
IIc	R26,R28	yes	uniform
IId	R26,R28	no	uniform
IIIa	R28	yes	non-uniform
IIIb	R28	no	non-uniform
IIIc	R28	yes	uniform
IIId	R28	no	uniform

Table 6.1: *Different possible processing strategies.*

As indicated in section 4.2.3, both releases are necessary to derive the non-uniform weighting scheme. It is possible to only use the data of release 18 and 26 for the non-uniform weighting scheme, but not for the estimation of the time series of elevation change. However, one problem with the removal of these laser campaigns is that fewer points are used to estimate unknown parameters of the combined linear and sinusoidal/cosinusoidal model, see equation 4.6. Figure 6.1 shows the time series for DS4b using processing strategy IIIc. This example shows that the estimated trend does not follow the data points at all. In general it turns out that the estimated model parameters perform better when both releases are left out. Therefore, we decided to use all available laser campaigns. Notice that a real outlier detection procedure for the time series points will remove most of the data points. This is because the uncertainties are quite optimistic and also the used model is too simplistic.

From table 6.2 it follows that the main differences in the estimated change rates are caused by the different processing strategies, rather than by the different sets of laser campaigns. Only the differences between strategies a and b for all sets of laser campaigns are small. This can be understood by the fact that in the case of processing strategy b, the additional elevation differences will get a low weight, so their contribution to the final estimate will be low.

The used weighting scheme has the largest influence, especially for the region below 2000 meter. Differences in total mass change rates can be more than 200 Gton/year. The main problem with the non-uniform weighting scheme is that it is based on the elevation differences itself instead on the roughness or slope values. In this case, all strong signals are smoothed, also the signals that show a real mass loss, like the example of the Jakobshavn glacier (see section 4.1.2). On the other hand, the estimates are biased by the combined effect of surface slope and roughness when uniform weights are used. The reason that mainly the estimates below 2000 meter are affected, is caused by the fact that in those regions the largest elevation differences are observed. This can be explained by the fact that in this region the influence of roughness and surface slope is much larger. On the other hand, the expected signal is much larger due to the acceleration of some glaciers as reported by [45]. Also, the signal is probably characterized there by a rough spatial pattern.

One might consider to adopt the non-uniform weighting scheme in such a way that larger elevation differences will get more weight. With this solution, we are able to produce any estimate between the estimates of strategy a and c. However, with this approach still no distinction is made between real signals and signals caused by surface slope and roughness. Probably future releases contain a reliable value for the roughness parameter that can be used to develop a weighting scheme. For now, we decided to use uniform weights for all OPs, corresponding with processing strategies c and d.

The differences between processing strategy c and d are caused by the removal of outliers with N-sigma thresholding. To get more insight into the performance of this step, table 6.3 provides the estimated

	$\overline{\Delta H}_{\uparrow}$	$\sigma_{\overline{\Delta H}_{\uparrow}}$	$\overline{\Delta H}_{\downarrow}$	$\sigma_{\overline{\Delta H}_{\downarrow}}$	ΔM_{\uparrow}	$\sigma_{\Delta M_{\uparrow}}$	ΔM_{\downarrow}	$\sigma_{\Delta M_{\downarrow}}$	TOTAL	σ_{TOTAL}
Ia	4.0	0.2	-4.4	0.7	25.5	1.3	-28.1	4.7	-2.6	4.9
Ib	4.1	0.4	-4.4	0.7	25.5	2.8	-28.2	4.9	-2.7	5.6
Ic	3.1	0.2	-25.3	0.5	19.5	1.2	-162.2	3.5	-142.6	3.7
Id	2.8	0.4	-34.7	0.5	17.5	2.7	-223.1	3.6	-205.6	4.5
IIa	4.3	0.1	-5.0	0.8	26.8	0.5	-32.4	5.2	-5.6	5.3
IIb	4.3	0.1	-5.1	0.8	26.9	0.9	-32.6	5.4	-5.6	5.5
IIc	3.4	0.1	-26.1	0.5	21.6	0.5	-167.3	3.7	-145.7	3.8
IId	4.9	0.1	-33.4	0.6	30.9	0.9	-214.7	3.9	-183.8	4.0
IIIa	3.7	0.1	-4.1	1.1	23.2	0.5	-26.1	7.1	-2.8	7.1
IIIb	3.7	0.1	-4.1	1.3	23.2	0.7	-26.2	8.2	-3.0	8.2
IIIc	2.7	0.1	-22.4	0.8	17.0	0.5	-144.1	5.4	-127.1	5.4
IIId	2.6	0.1	-28.5	1.0	16.4	0.7	-182.9	6.3	-166.6	6.3

Table 6.2: Overview of estimated elevation/mass change rates obtained with different processing strategies using different sets of laser campaigns. The elevation change rates ($\overline{\Delta H}$) and mass change rates (ΔM) are expressed in cm/year and Gton/year respectively. The mass change rates are calculated according to the methodology of section 4.2.4. The arrows \uparrow and \downarrow indicate the region above and below 2000 meter respectively. In order to convert the elevation change rates into mass change rates, densities of 600 kg/m^3 and 917 kg/m^3 are used for the regions above and below 2000 meter respectively. The last two columns contain the total mass change rates and accompanying standard deviations. Estimates are corrected for PGR.

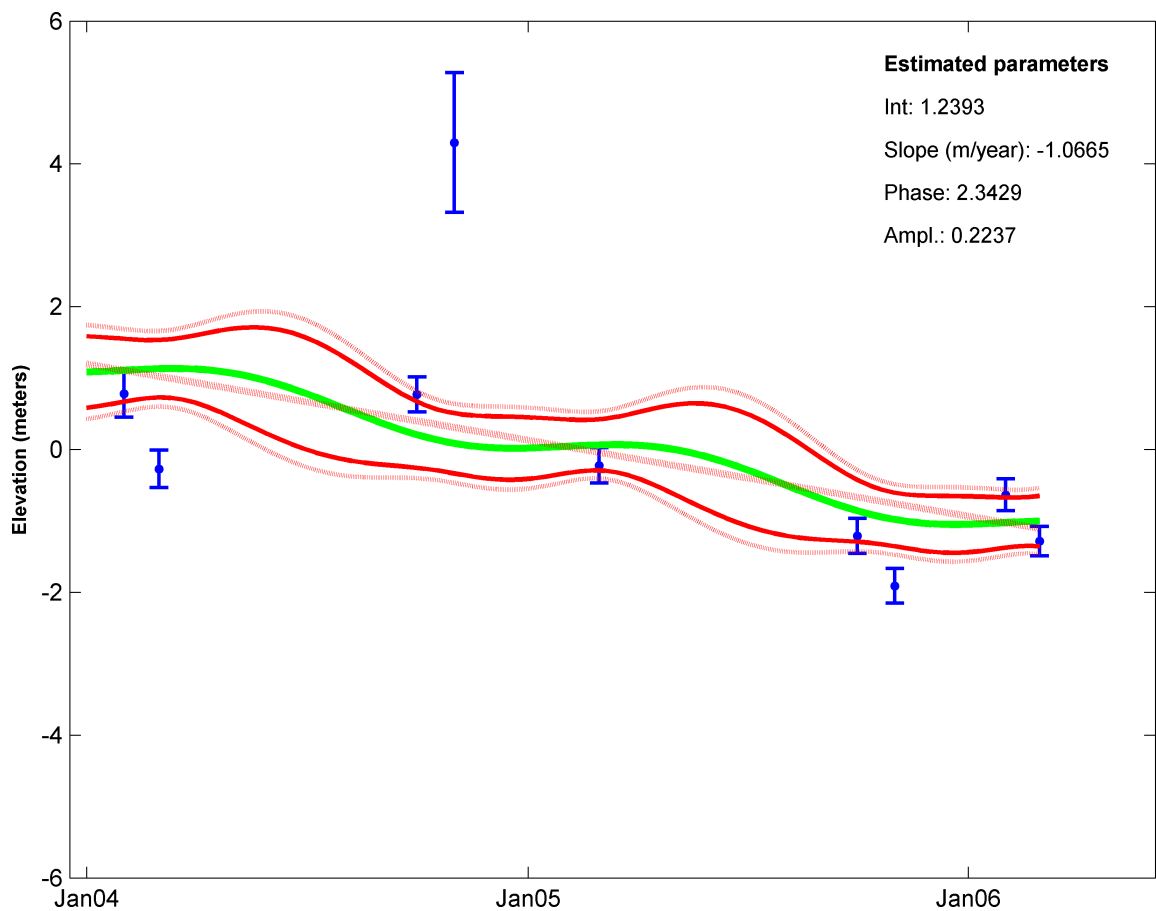


Figure 6.1: Time series for drainage system 4b using processing strategy IIIc. The bad performance of the used model to estimate the trend is caused by the small number of points of the time series.

	DS	$\overline{\Delta H}_{\uparrow}$	$\sigma_{\overline{\Delta H}_{\uparrow}}$	$\overline{\Delta H}_{\downarrow}$	$\sigma_{\overline{\Delta H}_{\downarrow}}$	ΔM_{\uparrow}	$\sigma_{\Delta M_{\uparrow}}$	ΔM_{\downarrow}	$\sigma_{\Delta M_{\downarrow}}$	TOTAL	σ_{TOTAL}
lc	1	8.5	0.2	-4.9	0.3	4.2	0.2	-8.0	0.5	-3.8	0.6
	2	4.1	0.3	-7.8	0.4	4.4	0.3	-8.9	0.8	-4.6	0.8
	3	1.1	0.3	-64.7	1.2	1.4	0.4	-52.4	1.0	-51.1	1.1
	4	-17.6	1.3	-85.8	4.7	-11.6	0.8	-50.4	2.8	-62.0	2.9
	5	10.2	0.3	-19.9	0.5	18.2	0.7	-29.0	1.3	-10.8	1.5
	6	3.0	0.1	-16.9	0.8	3.0	0.1	-13.4	0.8	-10.4	0.8
	TOTAL	3.1	0.2	-25.3	0.5	19.5	1.2	-162.2	3.5	-142.6	3.7
ld	1	8.3	0.9	-6.4	0.3	4.1	0.5	-10.4	0.6	-6.3	0.8
	2	2.8	0.6	-6.5	0.8	3.0	0.7	-7.4	1.1	-4.5	1.3
	3	0.3	0.5	-94.5	1.2	0.4	0.7	-76.5	1.0	-76.2	1.2
	4	-16.9	2.3	-91.8	4.7	-11.1	1.5	-54.0	2.8	-65.1	3.2
	5	10.0	1.0	-33.4	0.5	17.8	1.9	-48.8	1.3	-31.0	2.3
	6	3.3	0.2	-32.6	1.1	3.4	0.2	-25.9	1.0	-22.5	1.0
	TOTAL	2.8	0.4	-34.7	0.5	17.5	2.7	-223.1	3.6	-205.6	4.5

Table 6.3: Overview of estimated elevation/mass change rates per drainage system for the region above (\uparrow) and below (\downarrow) 2000 meter, using processing strategy lc and ld. The elevation change rates ($\overline{\Delta H}$) and mass change rates (ΔM) are expressed in cm/year and Gton/year respectively. In order to convert the elevation change rates to mass change rates, densities of 600 kg/m^3 and 917 kg/m^3 are used for the regions above and below 2000 meter respectively. The last two columns contain the total mass change rates and accompanying standard deviations. Estimates are corrected for PGR.

elevation change rates and mass change rates for the individual DSs using processing strategy lc and ld. The corresponding time series are provided in appendix B. From table 6.3 it follows that the influence of N-sigma thresholding is limited for the region above 2000 meter elevation. There, the maximal difference is 1.4 Gton/year for DS2. However, for the region below 2000 meter, the maximal difference between lc and ld is equal to 24.1 Gton/year for DS3. Also the differences are equal in sign, except for DS2. This indicates that not only noise is removed but probably also some signal. In section 4.2.2 it was already noticed that this could be a problem when N-sigma thresholding is used. On the other hand, the time series corresponding to processing strategy ld show that some points really behave like outliers, especially the points that belong to the first laser campaign. These outliers will influence the estimated trends. From table 6.2 we conclude that the differences between processing strategy c and d become smaller when the first two laser campaigns are removed. However, for these trends less points are used to estimate the model parameters. Probably the estimates based on processing strategy lc are too low, but the estimates of ld are not reliable. Therefore the estimates based on processing strategy lc are regarded as our final estimates. The spread in the estimates using different processing strategies indicates the uncertainty of the estimates. Notice that this uncertainty mainly affects the region below 2000 meter. Above 2000 meter, the differences caused by different strategies are maximal ~ 15 Gton/year.

A close look to the estimates based on processing strategy lc in table 6.3, reveals positive elevation change rates in the region above 2000 meter, except for drainage system 4a, and negative rates in the region below 2000 meter. When we combine the estimates of all drainage systems above 2000 meter we conclude that the interior of Greenland raises with a rate of 3.1 cm/year, corresponding with a mass change of 19.5 Gton/year.

In the region below 2000 meter, we conclude that the average elevation change equals -25.3 cm/year, corresponding with a mass change rate of -162 Gton/year. This change can be attributed to accelerated glaciers ([23] and [45]) and an increased number of icequakes [14]. Especially the contribution of the glaciers is believed to dominate the mass balance changes in this region.

When we sum up over the northern and southern part of the Greenland ice sheet as defined in section 5.2.2, we obtain a small mass loss in the North of -18.7 ± 1.3 Gton/year and a strong mass loss in the South of -123.9 ± 3.5 Gton/year. These results will be discussed in paragraph 6.3.

$\rho_{\uparrow} \text{ kg/m}^3$	$\rho_{\downarrow} \text{ kg/m}^3$	ΔM_{\uparrow}	ΔM_{\downarrow}	TOTAL
350	350	11.4	-61.9	-50.5
350	600	11.4	-106.1	-94.7
350	917	11.4	-162.2	-150.7
600	600	19.5	-106.1	-86.6
600	917	19.5	-162.2	-142.6
917	917	29.9	-162.2	-132.3

Table 6.4: Overview total mass change rates for the region above (\uparrow) and below (\downarrow) 2000 meter, using processing strategy 1c and different densities. The mass balance change rates (ΔM) are expressed in Gton/year respectively. Estimates are corrected for PGR.

Notice that the obtained mass changes strongly depend on the densities used to convert the observed volume change to mass change, see section 4.2.4. We used densities of 600 kg/m^3 and 917 kg/m^3 for the regions above and below 2000 meter elevation respectively. Here we assumed that the mass changes in the region above 2000 meter were mainly caused by variabilities in the accumulation rate, while for the region below 2000 meter the cause is mainly ice loss.

When we change these assumptions, also the estimated mass change rates will change. This is further illustrated in table 6.4 that provides an overview of the obtained results when different densities are used. The value of 350 kg/m^3 approximates the density of fresh snow, so it refers to the situation that the observed volume change is only due to variabilities in snow fall. For both regions this value is not realistic. For the region below 2000 meter the largest signals are expected from the glaciers ([34], [23] and [45]). Above 2000 meter elevation, there are no glaciers but still there is ice loss due to ice flow and surface melting. Furthermore, snow compacts, so density increases. On the other hand, the situation that in both regions the mass change is purely due to ice loss is also not realistic. Especially for the region above 2000 meter, because this region is in the accumulation zone of the ice sheet. Therefore we use densities of 600 and 917 kg/m^3 for the regions above and below 2000 meter respectively. The value of 600 kg/m^3 is a compromise between snow fall on one hand and ice loss and compaction on the other hand.

6.1.2 Comparison with other altimetry based estimates

The growth of the interior was already reported by other altimetry based studies, for an overview of these results see table 6.5.

In [24], the averaged elevation change above 2000 meter is equal to 6.5 cm/year (uncorrected for PGR), for the period 1992 to 2003, see figure 6.2. This estimate is based on satellite radar altimetry and not corrected for firn compaction.

Thomas et al., [62], also show positive trends for the interior of Greenland, see figure 6.3. They use a combination of airborne and satellite laser altimetry (Airborne Topographic Mapper and ICESat). Also here, no correction for the firn compaction was applied. The elevation change rates for the region above 2000 meter are equal to 2.4 ± 1.0 and $3.8 \pm 1.0 \text{ cm/year}$ over the periods of 1993 - 2004 and 1998 - 2004 respectively.

Finally, Zwally et al., [77], derived an averaged elevation change of $4.77 \pm 0.14 \text{ cm/year}$, based on both ERS radar altimetry and Airborne Topographic Mapper laser altimetry data, from mid-April 1992 to mid-October 2002. After the correction for temperature driven variations in the rate of firn compaction, the trend becomes $6.54 \pm 0.07 \text{ cm/year}$.

When we compare the estimates, we might draw the conclusion that our estimated trend compares well. Notice that the time span of these studies does not correspond with our time span. Only in [62] data is

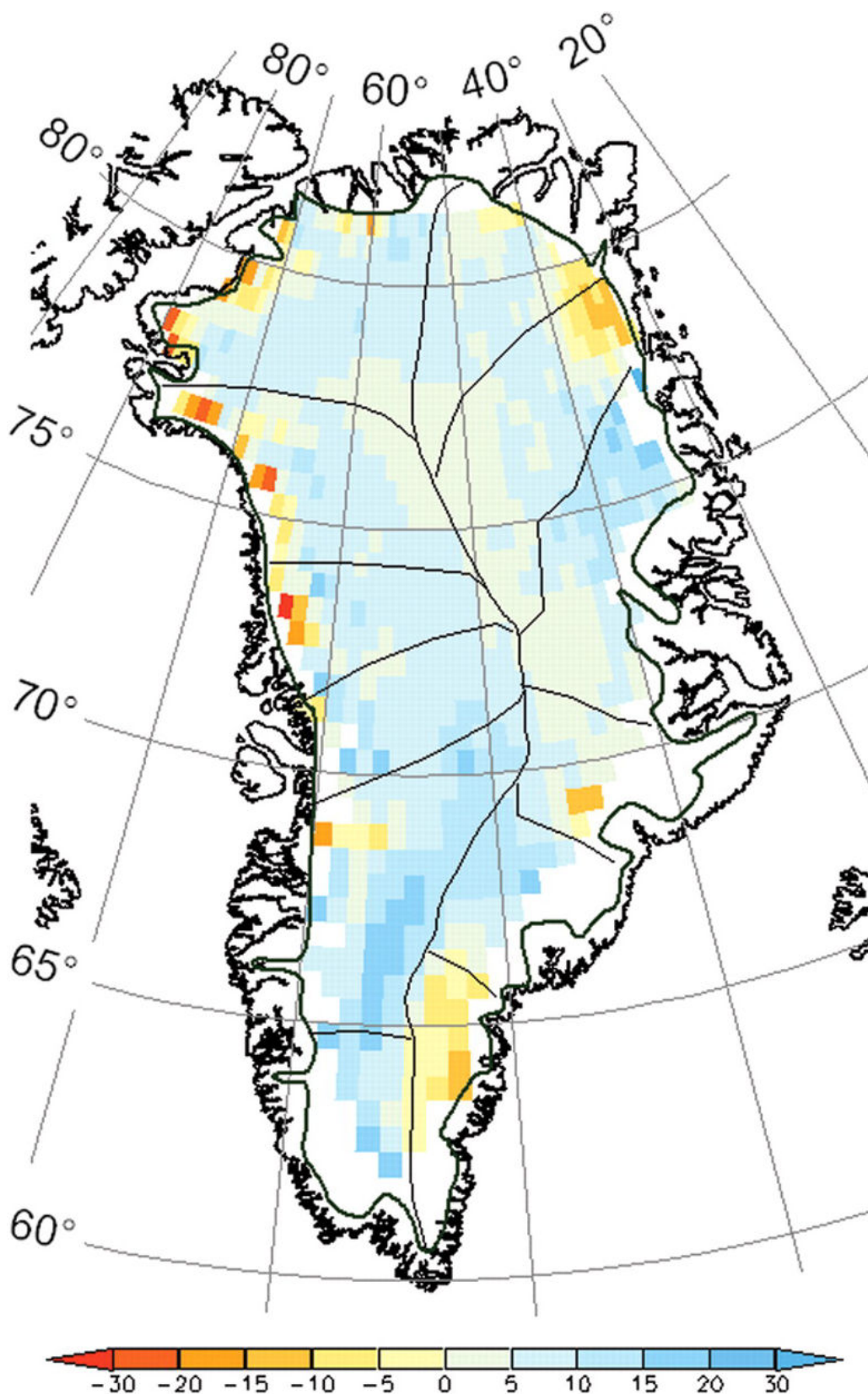


Figure 6.2: Ice-sheet elevation change rate in cm/year, derived from 11 years of ERS-1/ERS-2 satellite radar altimeter data (1992 to 2003), excluding some ice-sheet marginal areas (white). The spatially averaged rate is 5.4 ± 0.2 cm/year, or 5 cm/year when corrected for PGR. The white areas between the color-coded pixels and the thick line delimiting the ice sheet indicate no observations. Taken from [24].

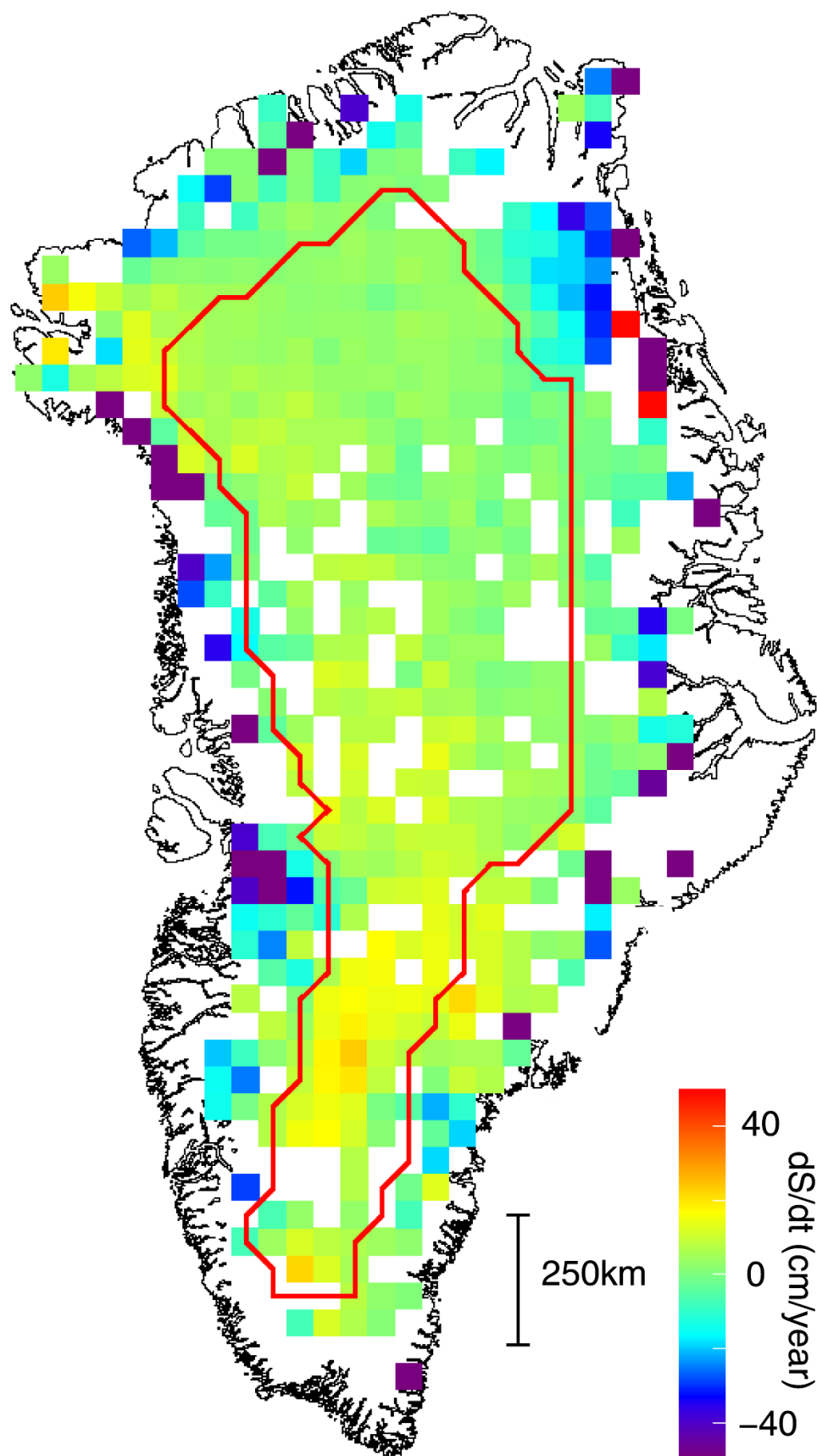


Figure 6.3: Estimated elevation change rates averaged over 50-km grid squares. Taken and adapted from [62].

Study	Region	Time span	Estimate (cm/year)
[24]	↑	1992 - 2003	6.5 ^{*1}
	↓		2.5 ^{*1}
[62]	↑	1993/4 - 2004	2.4 ± 1.0
	↑	1998/9 - 2004	3.8 ± 1.0
	↓	1993/4 - 2004	-15.3 ± 1.7
	↓	1998/9 - 2004	-21.1 ± 1.7
[77]	↑	1992 - 2003	6.54 ± 0.07 ^{*2}
	↑		-8.95 ± 0.85

^{*1} Uncorrected for PGR.
^{*2} Corrected for firn compaction.

Table 6.5: Overview elevation change rates provided in different studies using altimetry datasets, for the region above (↑) and below (↓) 2000 meter.

used up to 2004. So it might be that changes in the accumulation rate over time cause these differences in estimated trends. On the other hand, also different datasets and processing techniques are used. Furthermore, our and possibly also their reported uncertainties are far too optimistic, see section 6.1.4. In other words, when the uncertainties are larger the differences in estimated trends can be relaxed somewhat.

Notice also the spatial correspondence in the observed signals. We observed the largest positive trend in DS5a, averaged over the region this value is equal to 10.2 cm/year. In [24], the largest positive elevation change rates are observed in the southwestern ($<69^\circ\text{N}$) and eastern of Greenland (between 74°N and 77°N). In the southwestern, values up to 20 cm/year occurs. Notice that they estimated a trend per grid cell (see figure 6.2), resulting in more spatial detail. This value of 20 cm/year is the maximal trend of all grid cells in this region. We reported the average elevation change rate over the whole drainage system. This explains why our estimate is lower. The other strong positive trend in the East, see figure 6.2, is difficult to verify because this region falls in both DS3 and DS4. But in figure 4.1 we can see a yellow spot in this area, corresponding with positive elevation changes. Also in [77] and [62] strong positive trends are observed in drainage system 5a.

The observed negative trend in drainage system 4a is also confirmed by others. Here most signal comes from the southern part of this drainage system. From [24] we can learn that there is a negative trend in the southern part of DS4a, while for the northern part the trend is slightly positive. Also [77] conclude that this region is the principal region of elevation decreases above 2000 meter.

For the other DSs above 2000 meter, small positive values are reported. Also here, the order of magnitude is comparable with our estimates.

The situation changes for the region below 2000 meter. Johannessen et al., [24], reported a negative elevation change of -2.0 ± 0.9 cm/year for the region below 1500 meter. For the elevation band 1500-2000 meter, they reported a positive trend of 5.6 ± 0.5 cm/year. Weighted according to the area of these bands, the total estimate for the region below 2000 meter becomes 2.5 cm/year. In this case, the sign is even different from our trend. Notice however, that in this study the data at the margins of the ice sheet is not used, because this data is believed to be unreliable. The coastal areas form an inherent problem when radar altimetry is used, because radar altimetry misses narrow coastal glaciers because of inadequate ground resolution. Also the ice elevations measured by the radar are much less reliable over steep, undulated surfaces than over flat surfaces.

The correspondence becomes better when we compare our results with [62]. Based on airborne and satellite laser altimetry, values are estimated of -15.3 ± 1.7 cm/year and -21.1 ± 1.7 cm/year, over a period of 1993/4 - 2004 and 1998/9 - 2004 respectively. These values are slightly smaller than our trend

DS	ΔM_{\uparrow}	ΔM_{\downarrow}	TOTAL
1	13 ± 2	-4 ± 4	8 ± 5
2	40 ± 2	-32 ± 2	8 ± 4
3	50 ± 3	-75 ± 2	-25 ± 4
4	-38 ± 11	-33 ± 3	-77 ± 11
5	3 ± 3	-3 ± 13	7 ± 13
6	-27 ± 3	6 ± 5	-22 ± 7
TOTAL	41 ± 8	-140 ± 24	-101 ± 16

Table 6.6: Summary of Greenland drainage system mascon solutions (corrected for PGR) above and below 2000 meter elevation (July 2003 to July 2005), taken from [34]. The values in the last column are corrected for potential signal loss ($\sim 9\%$) as determined from simulation analyses. This is the reason why the value of the last column is not equal to the sum of the values in the second and third column.

of -25.3 cm/year. Also [77] comes up with a negative trend of -8.95 ± 0.85 cm/year (uncorrected for temperature driven variations in the rate of firn compaction) for this region. However, notice that this value is estimated using data of a different time span. Differences in the estimates might be caused by fluctuations in glacier speed ([23] and [45]), but also by variations in accumulation rates. On the other hand, notice that also the spatial distribution of the used airborne laser data in [62] and [77] is not homogeneous over Greenland, see figure 6.4. Probably in this dataset some signals are missed or undersampled. Especially for glaciers this is a large problem, because here the largest signals are expected.

Basically we conclude that the correspondence for the region above 2000 meter is good. For the region below 2000 meter, larger differences are observed but still the order of magnitude is the same for the most recent estimate [62]. The correspondence is less when we compare our estimates with estimates obtained by satellite radar interferometry ([45]) or GRACE ([66], [44], [67], [9] and [34]) However, the estimates based on GRACE data, using monthly gravity fields in spherical harmonic coefficients, will be addressed in section 6.2.3. In section 6.2.3 our ICESat estimates are compared with our GRACE estimates. Comparison with the estimates based on satellite radar interferometry ([45]) is more difficult because in this study only the ice discharge by the glaciers is based on real measurements. To derive a mass balance change over the whole of Greenland, the estimates for individual glaciers were combined with deviations in surface mass balance from the long-term average, computed using meteorological models taken from [20]. However, the satellite interferometry estimates provide good insights in the mass balance evolution of the DSs. In the following section we will compare our estimates with the so-called 'mascon solutions' [34].

6.1.3 Comparison with mascon solutions

The mascon solutions and accompanying uncertainties are given in table 6.6 [34]. These mascon solutions are based on a new approach of GRACE data processing. The mass concentrations are determined at a local scale by processing the raw GRACE observations, i.e. the range-rates between the two satellites. Notice that they used a 2-year period, from July 2003 to July 2005. When we compare these estimates with ours, immediately we can see large discrepancies that can only partly be explained by the characteristics of both methods, see figure 6.5. To get a good insight in the differences we want to discuss them for the different DSs.

For drainage system 1 and 2, the mascon solutions are not significantly different from zero, which, according to [34], is consistent with the lack of glacier acceleration [45] or detected icequacks [14] reported for these areas. For those drainage systems (DSs), our combined estimates are also close to zero, respectively -3.8 and -4.6 Gton/year for DS1 and DS2. However, when we consider the separate estimates for the regions above and below 2000 meter, the differences are striking, especially for DS2. For this DS a mass gain of 40 Gton/year is reported for the region above 2000 meter, while a mass

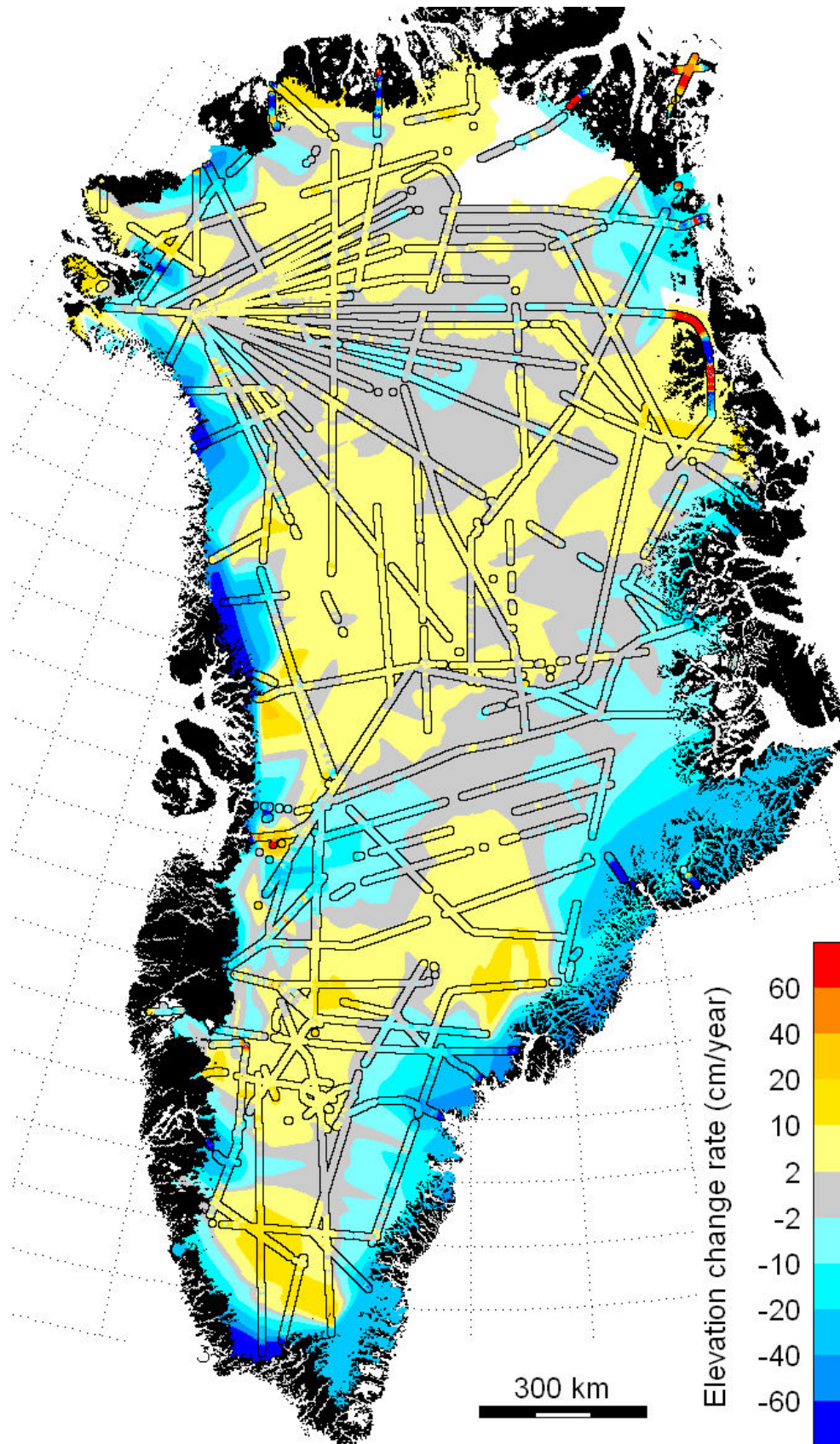


Figure 6.4: Flight tracks (outlined in black) of airborne laser altimetry surveys, taken and adapted from [30]. Swaths range between 150 and 200 meter [29]. Interpolation is used in order to obtain an area covered map of the rate of change in surface elevation.

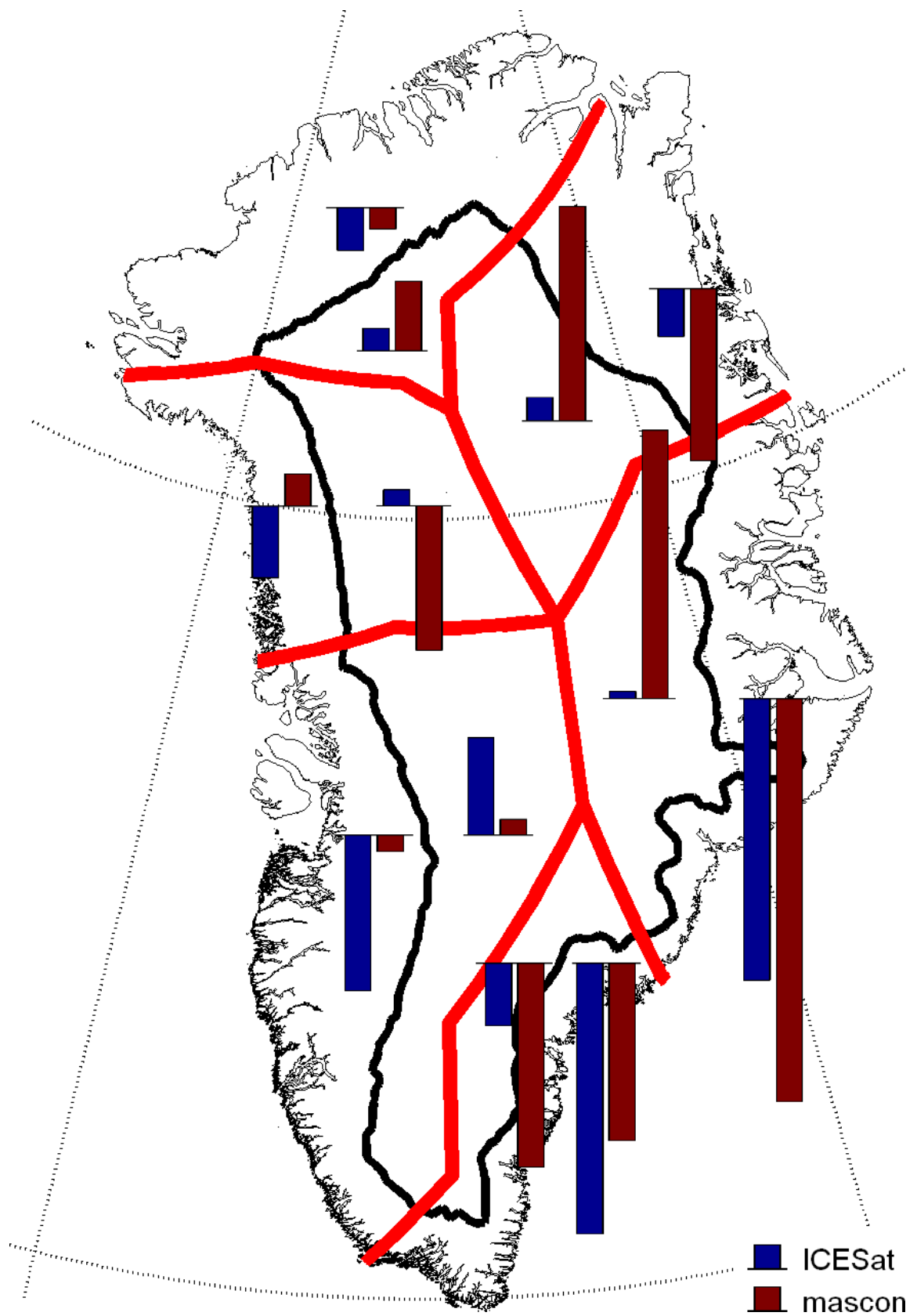


Figure 6.5: Mascon solutions versus estimates based on ICESat data for the individual regions.

loss of -32 Gton/year is reported for the region below 2000 meter. The difference for DS2b can be understood when we consider the fact that an averaged nett mass change not necessarily results in a corresponding nett volume change. When the mass loss of DS2b, based on the mascon solutions (-32 Gton/year), is purely caused by ice loss, the expected average elevation change would be ($\rho_{\text{ice}} = 917 \text{ kg/m}^3$ and area DS2b = 125 598 km²) -27.8 cm/year. This value is significantly larger as the -7.8 cm/year, observed with ICESat. However, when the volume change of ice is partly compensated by snow fall, the nett volume change does not correspond anymore to the computed mass change. This is caused by the different densities of snow and ice. So, the real nett mass loss will always be larger. Also, the lower estimate can be caused by the undersampling of the glaciers with ICESat.

However, for DS2a (179 687 km²) such a mechanism cannot explain the difference. A mass gain of 40 Gton/year roughly corresponds to an averaged elevation change of 0.37 meter/year (assuming an averaged density of 600 kg/m³) or 0.24 meter/year (assuming an averaged density of 917 kg/m³). These trends are ~ 9 and ~ 6 times our estimated trend of 4.1 cm/year. With these numbers it is unlikely that the differences can be completely contributed to unmodeled PGR effects. When this would be the case, we can think of a similar mechanism as for DS2b, due to the higher density of the lithospheric layer that causes the volume change. In that case the radial uplift due to PGR must be in the orders of centimeters instead of the modeled millimeters. Also compaction of the firn is not able to compensate the volume change by accumulation. Zwally et al., ([77]) uses a firn compaction model to estimate this term and came up with an average value of -1.71 cm/year for the accumulation zone of Greenland. This value corresponds with roughly -23.4 Gton/year (assuming an averaged density of 900 kg/m³), which is already smaller than the difference for only DS2. So we conclude that for the whole of DS1 and DS2 our estimates are comparable with the mascon solutions, but for the separate regions above and below 2000 meter the differences are large.

A similar statement holds for DS3, where the mascon solutions come up with a value of 50 and -75 Gton/year for DS3a and DS3b respectively. The large negative trend in DS3b is explained by one accelerating glacier [45] and icequakes in two glaciers [14]. We estimated a significantly lower negative trend for DS3b of -52.4 Gton/year. Here a similar explanation can be given as for DS2b.

The strong positive trend based on the mascon solutions for DS3a (50 Gton/year) is relaxed by the fact that this DS has a large average annual mass input of 42 Gton/year [77], and therefore is very sensitive to interannual variations or trends in precipitation and ice accumulation. Due to the fact that our time series do only partly overlap, a change in accumulation rate might cause a difference. But in that case, we have to see this change in our time series, because they are longer. Notice that this trend is not visible.

For DS4 the mascon solutions come up with the largest change (-77 Gton/year) that is mainly attributed to the acceleration of three glaciers. Rignot et al. ([45]), indicate an increase in the rate of loss in 2005, compared with that in 1996, of -56 Gton/year. For this DS, we estimated a rate of -11.6 and -50.4 for DS4a and DS4b respectively. In total this estimate is slightly smaller as the value provided by the mascon solutions, but agrees more or less with the value provided by [45]. Notice however once again the differences in estimates for the regions a and b. These differences are up to 26 and 17 Gton/year.

Notice that the sum of the mascon solutions for DS3 and DS4 roughly compares to the sum of our estimates, -102 Gton/year and -113.1 Gton/year respectively.

In DS5 there are only a few large glaciers because its ablation area is much broader and less steep than that in the southeast (DS4), so glacier ice discharge at the coast is low. Only the Jakobshavn Isbræ glacier, Greenland's largest outlet glacier, is an exception. From Rignot et al. ([45]) it follows that the mass balance deficiency of this glacier grew from -12.5 km³/year for 2000 to -16 km³/year for 2005. This increased deficiency is due to a 95% increase in frontal speed from 1996 to 2005 during the progressive breakup of its floating ice tongue ([25], [73]). However, also other glaciers in this DS accelerates, but due to a lack of thickness data there are no mass balance estimates available [45]. Based on this information, a positive mass balance for DS5b is unlikely.

However, the mascon solutions come up with a positive mass change of 7 Gton/year, here a correction

is applied for potential signal loss. For the regions a and b, values of 3 and -3 Gton/year are estimated. Notice however, the large uncertainty for the estimate of DS5b. For DS5a we observed the largest positive trend, 18.2 Gton/year. Striking is that we and also others ([24], [62] and [77]) observed a strong positive signal in DS5a, while this signal is not visible in the mascon solutions. On the other hand this value is more than compensated by a mass decrease in DS5b of -29 Gton/year. This last value is approximately two times the mass balance deficiency of the Jakobshavn Isbræ glacier ([45]). Probably the extra mass losses are caused by other glaciers in this DS. Also it could be possible that there is strong mass accumulation on the eastern side of DS5b. In that case the used density for this part of DS5b is too large, resulting in a mass change which is too large.

Notice that the sum of the mascon solutions for DS4 and DS5 compares very well to the sum of our estimates, -70 Gton/year and -72.8 Gton/year respectively.

For DS6, a contradictory signal is observed for both regions. For DS6a and DS6b, the mascon solutions provide a mass change of -27 Gton/year and 6 Gton/year respectively. These numbers are explained by glacier accelerations [45] and an increased number of icequakes [14]. Probably these numbers are interchanged, because as far as we can see, these glaciers do not appear in the region above 2000 meter.

Again, notice that the sum of the mascon solutions for DS1 and DS6 compares very well to the sum of our estimates, -14 Gton/year and -14.2 Gton/year respectively.

So basically we can conclude that there are large differences between our estimates and the mascon solutions. We showed that these differences mostly show up for the separate estimates of the regions above and below 2000 meter. Therefore, we draw the conclusion that the mascon solutions only provide a reasonable estimate for the whole DS or even combinations of DSs. This is visualized in figure 6.6 where our ICESat estimates are compared with the mascon solutions for the individual drainage systems.

On the other hand, when the mascon solutions only provide a reasonable estimate for the whole DS or even combinations of DSs, than we would expect that for larger regions the differences become smaller. In other words, the mass change rates for the whole of Greenland, obtained with the mascon solutions and ICESat, must be very close to each other. It turns out that this is not the case; -101 Gton/year and -142.6 Gton/year for the mascon solutions and ICESat respectively. Personal communication with Scott Luthcke learns that new mascon solutions over a time period of 2003 to 2007 provide a much stronger mass loss of -154 Gton/year over the whole of Greenland. The reason for this increased mass loss is a big summer melt in 2005. In contradiction to our estimates, the previous set of mascon solutions did not contain the summer of this year. In any case, this new estimate is much closer to our ICESat estimate. At the moment of writing, the new mascon solutions are not published yet, so we cannot compare with the individual estimates for the separate regions. However, we do not expect that only the big summer melt in 2005 will explain all differences between the individual estimates per region.

6.1.4 The uncertainty of the ICESat estimates

Due to several reasons, the propagated uncertainties do not reflect the real uncertainties of our estimates. First we want to recall the robustness analysis of the used processing strategy. Large differences in the estimates show up for different processing strategies, especially for the region below 2000 meter.

Secondly, the undersampling of the signal, both in spatial and temporal domain, biases our estimates for the region below 2000 meter. Furthermore, there is a direct relation between the number of overlapping pairs (OPs) and the uncertainty of the points in the time series. The larger this number, the smaller the uncertainty. This would be reasonable if the OPs were homogeneously distributed, but this is not completely the case. Therefore also the location of the OPs plays a role, see section 4.2.1.

An additional uncertainty is introduced by the fact that we did not correct for the firn compaction. Zwally et al. ([77]) compute a correction, averaged over the accumulation zone, of -1.71 cm/year corresponding with -23 Gton/year (using a averaged density of 900 kg/m³).

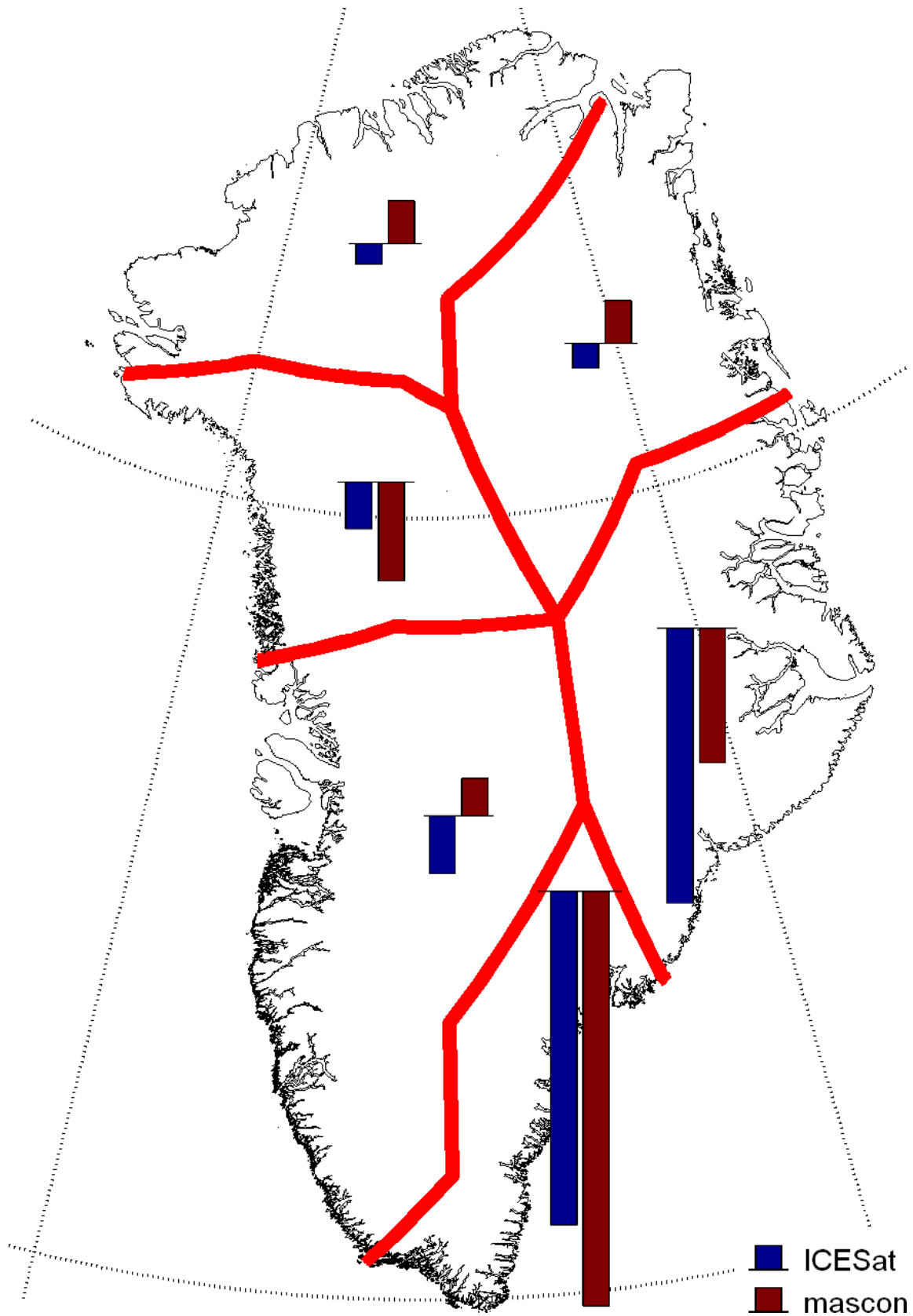


Figure 6.6: Mascon solutions versus estimates based on ICESat data for the individual drainage systems. Here we used the mascon solutions that are corrected for potential signal loss ($\sim 9\%$) as determined from simulation analyses.

The uncertainty of the PGR effect is unknown, we used an empirical derived value based on different Earth models. Probably this value is too low, because an additional uncertainty is introduced by the used ice model that reflects the ice history.

Finally, the conversion to mass changes introduces an error for two reasons. First due to the fact that a nett mass change not necessarily means that you will measure a volume change. Secondly, averaged values for the density are used for different regions. In reality this approximation is not correct, which directly introduces an error.

6.2 Results and discussion GRACE

In this section we answer the question: What is the mass balance of the Greenland ice sheet based on only GRACE data? First, we start with an evaluation of the different filters and filter settings used to reduce the noise. After that the time series and accompanying trends for the North, South and for the whole of Greenland are presented and discussed. The mass balance estimates of all regions will be compared with other studies and the differences will be explained. This section ends with some remarks about the estimated uncertainties.

6.2.1 Filter performance

In section 5.3 two possible solutions were given to reduce the noise in the Stokes coefficients at higher degrees. A Gaussian low-pass filter is used with the half-widths 300, 500 and 800 kilometer. Furthermore, a Wiener filter is used to obtain a statistically optimal solution. This last solution is preferred, because the Gaussian filter requires an ad-hoc definition of the half-width.

However, it turns out that the smoothed models, after application of the Wiener filter, contain significant influences of noise and stripes, see figure 6.7 for two examples. These influences will bias the estimates of the mass change rates. The problem with this filter is the fact that the GRACE solutions contain non-isotropic or degree-and-order dependent errors. In that case, the solution we obtain will not longer be the best solution. Notice that the existence of stripes decreases to the poles. This is caused by the orbital configuration of the satellites. The data density is higher towards the poles, resulting in less errors.

Table 6.7 provides an overview of the estimated mass change rates using different filters and filter settings for all used GRACE solutions. When we compare the Wiener filter estimates with the estimates using a Gaussian filter, we see that they are most close to the Gaussian filter with a half-width of 300 km. In fact this half-width is too small compared with the fundamental spatial resolution (400 km) of the GRACE data [48].

The use of 500 km provides most reasonable models, see figure 6.7 for two examples. In these models, most stripes and noise are suppressed. Higher values for the filter half-widths will also suppress the observed ablation/accumulation signals, which turns out to be the case when a half-width of 800 kilometer is used.

In the following we will use the results that are obtained by a Gaussian filter with a half-width of 500 kilometer as our best estimates.

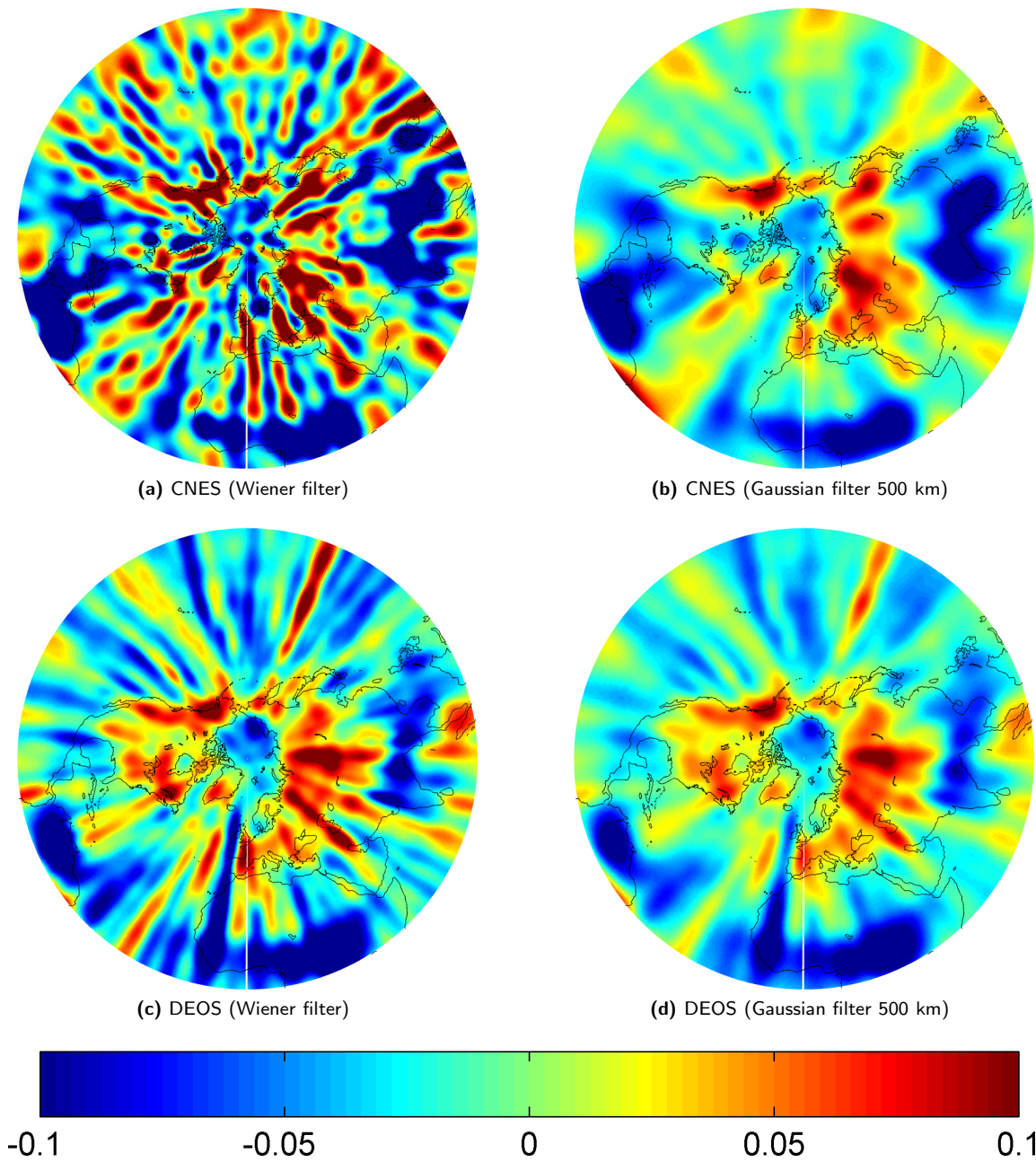


Figure 6.7: Smoothed monthly models based on different filters, expressed in variations of thickness of an equivalent water layer for CNES and DEOS solutions of April 2004. Maps are in a polar stereographic projection.

Filter	Reg.	ΔM_1	$\sigma_{\Delta M_1}$	ΔM_2	$\sigma_{\Delta M_2}$	ΔM_3	$\sigma_{\Delta M_3}$	ΔM_4	$\sigma_{\Delta M_4}$	ΔM_5	$\sigma_{\Delta M_5}$
W.	N* ¹	-32.3	3.4	-37.7	4.5	-34.8	4.6	-17.5	4.0	-21.8	3.5
	S* ¹	-89.3	2.2	-67.7	3.7	-65.5	3.9	-52.2	3.7	-65.1	2.4
	WG	-122.1	3.5	-105.0	6.9	-99.5	7.1	-69.8	4.9	-87.3	4.0
G300	N	-31.0	3.4	-37.9	4.5	-34.1	4.5	-18.7	3.7	-22.1	3.5
	S	-78.0	2.0	-71.4	3.8	-59.7	3.8	-54.5	2.8	-70.4	2.5
	WG	-109.2	3.4	-108.8	6.9	-93.2	7.0	-73.3	4.2	-92.9	4.0
G500	N	-29.2	3.3	-35.3	4.4	-31.5	4.4	-17.5	3.4	-21.2	3.4
	S	-63.2	1.9	-58.0	3.6	-51.3	3.6	-43.4	2.3	-52.8	2.2
	WG	-92.2	3.4	-93.1	6.8	-82.7	6.8	-60.9	3.8	-74.3	3.8
G800	N	-25.2	3.3	-31.0	4.4	-27.2	4.4	-16.7	3.4	-19.8	3.4
	S	-43.3	1.7	-42.6	4.3	-38.2	3.4	-30.6	1.9	-35.6	1.9
	WG	-68.3	3.3	-73.4	6.6	-65.4	6.6	-47.3	3.5	-55.5	3.7

*¹ For a definition of these regions see section 5.2.

Table 6.7: Estimated mass change rates for all used GRACE solutions and different regions (Reg.), i.e. North (N), South (S) and the whole of Greenland (WG). Both the Wiener filter and Gaussian filter are used to suppress the noise. Estimates are in Gton/year and ordered in alphabetical order, i.e. 1: CNES, 2: CSR, 3: CSR destriped, 4: DEOS, 5: GFZ.

6.2.2 Results GRACE

Using the methods described in chapter 5, the time series of the variations of thickness of an equivalent water layer are obtained, given in appendix C. The trends in those time series are converted to trends in Gton/year, which makes comparison with other studies more straightforward. The estimated trends and accompanying uncertainties are provided in table 6.8.

In the time series (see appendix C), we can see a clear seasonal cycle for South Greenland while for North Greenland this cycle is not visible. In fact this can be expected for higher latitudes where melting is less significant. In [34] a similar pattern is visible for the northern DSs. For DS1 and DS2 there is almost no seasonal cycle, for DS3 and DS6 the cycle becomes more visible and for DS4 and DS5 the cycle is very clear. Notice that there is also a relation with elevation, i.e. for lower elevations the cycle becomes more obvious.

Another striking fact is the relatively large difference between the different GRACE solutions, where large is defined with respect to the estimated uncertainties. Especially for the South, differences can be up to 32 Gton/year. Unaccounted effects, like leakage, cannot fully explain these differences because here the magnitudes must be comparable.

Except for the DEOS solutions, the time spans of all GRACE solutions are more or less comparable. For DEOS, monthly solutions are available from February 2003 to November 2005. This might explain a part of the differences between the DEOS solutions and the remaining GRACE solutions. For the remaining solutions, most likely the differences can be explained by different strategies and orbits used by the processing centers to obtain the monthly gravity fields. It is not clear yet what the optimal solutions are. Especially for the polar regions, verification is difficult due to a lack of reliable hydrological models. Future research might be focused at obtaining such a model that can be used as a forward model to evaluate different strategies and orbits.

Despite the fact that the magnitudes are different, all GRACE solutions agree on the sign of the mass balance change for both the northern and southern part of Greenland. The largest trend is observed in the South, which corresponds with observed glacier accelerations ([45]) and an increased number of icequakes ([14]). In the northern part, glacier accelerations and an increased number of icequakes are only reported in DS6.

Period	Reg.	ΔM_1	$\sigma_{\Delta M_1}$	ΔM_2	$\sigma_{\Delta M_2}$	ΔM_3	$\sigma_{\Delta M_3}$	ΔM_4	$\sigma_{\Delta M_4}$	ΔM_5	$\sigma_{\Delta M_5}$
full	N ^{*1}	-29.2	3.3	-35.3	4.4	-31.5	4.4	-17.5	3.4	-21.2	3.4
	S ^{*1}	-63.2	1.9	-58.0	3.6	-51.3	3.6	-43.4	2.3	-52.8	2.2
	WG	-92.2	3.4	-93.1	6.8	-82.7	6.8	-60.9	3.8	-74.3	3.8
before July04	N	-50.5	3.6	-54.0	8.5	-42.7	8.5	-14.4	4.7	-53.7	5.5
	S	-48.2	2.6	-34.8	8.4	-23.5	8.4	-15.5	5.0	-48.9	5.5
	WG	-98.5	4.2	-88.7	16.1	-66.2	16.1	-30.1	7.4	-103.2	9.4
after July04	N	-30.1	3.4	-35.1	7.8	-33.7	8.0	-21.7	4.1	-19.4	4.2
	S	-62.6	2.1	-78.8	7.6	-75.2	7.7	-45.5	3.7	-62.3	3.5
	WG	-93.0	3.6	-113.6	14.7	-109.0	15.0	-67.4	5.7	-82.2	6.1

*1 For a definition of these regions see section 5.2.

Table 6.8: Estimated mass change rates for all used GRACE solutions and different regions (Reg.), i.e. North (N), South (S) and the whole of Greenland (WG). A Gaussian filter with a half-width of 500 km is used and the estimates are obtained for different time spans. Estimates are in Gton/year and ordered in alphabetical order, i.e. 1: CNES, 2: CSR, 3: CSR destriped, 4: DEOS, 5: GFZ.

Also striking are the differences in estimates before and after July 2004. In [9] and [67] increased mass losses are reported for the South, starting approximately half 2004. Notice that this increased trend is not visible in the time series over the whole of Greenland. It turns out that this increased trend is more or less compensated by a decreased trend in the North, starting in 2005. Table 6.8 contain the estimates using only the data before and after July 2004. All GRACE solutions, except DEOS, show the decrease of the North. The increased trend of DEOS is probably caused by the short time span of this dataset (2003 - 2005). For the South, all GRACE solutions show the increased mass loss.

Also other studies show larger values for the southern part, see [34], [67] and [69]. However, the magnitude of these estimates differs considerably. In the next section our estimates will be compared with other GRACE based estimates. Here possible explanations for the large differences will be given.

6.2.3 Comparison with other GRACE based estimates

Table 6.9 provides an overview of the values provided in different studies. In the remainder of this chapter the IDs, preceded by GRACE, are used to refer to a particular study.

Table 6.9 may raise the conclusion that there are GRACE based estimates that show strong mass losses and on the other hand there are estimates that show moderate mass losses of approximately half these strong signals. Both GRACE I-II and GRACE VI belong to the last category, while GRACE III-V show significantly larger numbers. When we compare our estimates with the estimates of GRACE I-V, we conclude that our estimates are slightly low. Differences are up to 100 Gton/year.

Several explanations are possible that might explain the differences between the different GRACE estimates, including our estimates. Part of the differences might be caused by the different GRACE solutions that are used. We, but also the estimates of GRACE V show that differences for different GRACE solutions are up to tens of gigatons, (here we do not take into account the estimates of JPL).

Partly these differences could be attributed to the different time spans of the used datasets. In section 6.1.3 we mentioned already the big summer melt in 2005, which was the reason of the low estimate for GRACE VI. A new estimate for the whole of Greenland, over a period of 2003 to 2007, provide a mass change rate of -154 Gton/year (Scott Luthcke, personal communication). Also for GRACE I and GRACE II, which do not contain the summer of 2005, the big summer melt in this year might explain

ID	Study	Region	Time span	GRACE solution	Estimate (Gton/year)
I	[66]	whole	Apr 2002 - Jul 2004	CSR R01	-75 ± 21
II	[44]	whole	Jul 2002 - Mar 2005	CNES	-129 ± 15
III	[9]	whole	Apr 2002 - Nov 2005	CSR R01	$-219 \pm 21^{*1}$
IV	[67]	North ^{*2}	Apr 2002 - Apr 2006	CSR R01	-76 ± 17
		South ^{*2}			-148 ± 22
		whole			-227 ± 33
V	[69] ^{*3}	North ^{*4}	2002 - 2006	CSR	-50
		South ^{*4}			-160
		whole			-206
		North		GFZ	-23
		South			-155
		whole			-179
		North		Goddard	-27
		South			-144
		whole			-172
		North		JPL	11
South	-103				
whole	-92				
VI	[34] ^{*5}	North	Jul 2003 - Jul 2005	not applicable	-6 ± 16
		South			-95 ± 16
		whole			-101 ± 16
*1 uncorrected for PGR					
*2 border between North and South 73.25°					
*3 no uncertainty measures available					
*4 border between North and South latitude Summit station (72.5°)					
*5 mascon solutions, see also table 6.6					

Table 6.9: Overview estimated mass change rates provided in different studies. All estimates are solely based on GRACE data.

why these estimates are low.

Furthermore, in section 6.2.2 it was already noticed that the decrease in mass loss for the North starts somewhere in 2005. When only data is used up to 2005, this decreased trend will not be visible. This conclusion is supported by the sequence of estimates provided by Velicogna et al. (GRACE I, GRACE IV and GRACE V). For GRACE I and GRACE IV a more or less similar processing strategy is used, so here the differences are explained by an increased rate of mass loss, starting in spring 2004. A fit to the monthly averages for the whole of Greenland before and after April 2004 results in ice loss trends of -95 ± 50 Gton/year during April 2002 to April 2004 and -314 ± 61 Gton/year during May 2004 to April 2006 ([67]). Notice that there is a slight difference with the value provided in GRACE I, which is probably due to small changes in the processing. On the other hand, the estimates over the whole of Greenland for GRACE IV but also GRACE III are significantly larger as the values given in GRACE V. For GRACE V, data is used from 2002 - 2006.

Also the different approaches used to account for the leakage effect might explain a part of the differences, compare section 5.4.3. We did not take this effect into account. In GRACE II a negligible correction is calculated using a hydrological model. For GRACE I, GRACE III and probably also for GRACE V, a scaling of the smoothed region function is applied. This approach is already discussed in section 5.4.3. For GRACE III it is less clear how the final estimate is obtained. However, using their results we can try to figure out the influence of a possible scaling step. From figure 6.8, where mass changes are expressed in terms of variations of thickness of an equivalent water layer, it follows that the locations A and B are chosen in the regions with the largest mass changes. For location A the rate for the entire 3.5-year period is -4.59 ± 0.39 cm/year and for location B this rate equals -3.97 ± 0.27 cm/year. In the paper it is stated that prominent negative trends (about -3 to -4 cm/year of equivalent water height change) are observed over large parts of Greenland. When we take an average value of -4 cm/year and $2.2E6$ km² for the area of Greenland, this rate corresponds to a change of -88 Gton/year. When we take an average of -5 cm/year, the rate increases to -110 Gton/year. In the paper it is stated that these rates need to be adjusted for effects of spatial filtering. It is not known how they did it, but finally they come up with an estimate of -219 ± 21 Gton/year (uncorrected for PGR). This means an approximate doubling of the trend.

Furthermore, we can see that the mass loss is spread quite homogeneously over the entire Greenland continent, which is in contrast with other studies that indicate loss concentrated at the margins ([31], [77], [62] and [45]) and growth in the interior ([77], [62] and [24]).

When we finally compare the estimates of GRACE V with the new mascon solutions (-154 Gton/year for the whole of Greenland over a period of 2003 to 2007 (Scott Luthcke, personal communication)), the differences are significant. For the solutions of CSR, the magnitude differs considerably with roughly a factor 1.5. For the solutions of GFZ and Goddard the differences are lower.

It is not clear yet how these differences must be explained. Probably the GRACE estimates based on the monthly solutions in terms of spherical harmonics overestimate the real mass balance change by inappropriate scaling procedures used to account for the leakage effect. Or there might be some problems with the mascon solutions. Here further research is necessary.

Again we want to stress the point that for our estimates a correction for the leakage error is necessary. This unaccounted effect, mainly causes the differences between our estimates and the estimates of GRACE V and the new mascon solutions, for which the time spans are comparable with ours.

6.2.4 The uncertainty of the GRACE estimates

When we compare our uncertainty measures with the values in table 6.9 we see that they are quite low. In fact we simply propagate the uncertainties in the Stokes coefficients, see section 5.2.4. In GRACE IV, another approach is applied. Here the 1σ uncertainties, caused by errors in the gravity fields, are estimated by convolving the smoothed region functions with uncertainty estimates for the GRACE Stokes coefficients. The uncertainty in each Stokes coefficient was obtained by assuming that the scatter of all monthly values about their best-fitting annual cycle is entirely due to errors, with no contributions from

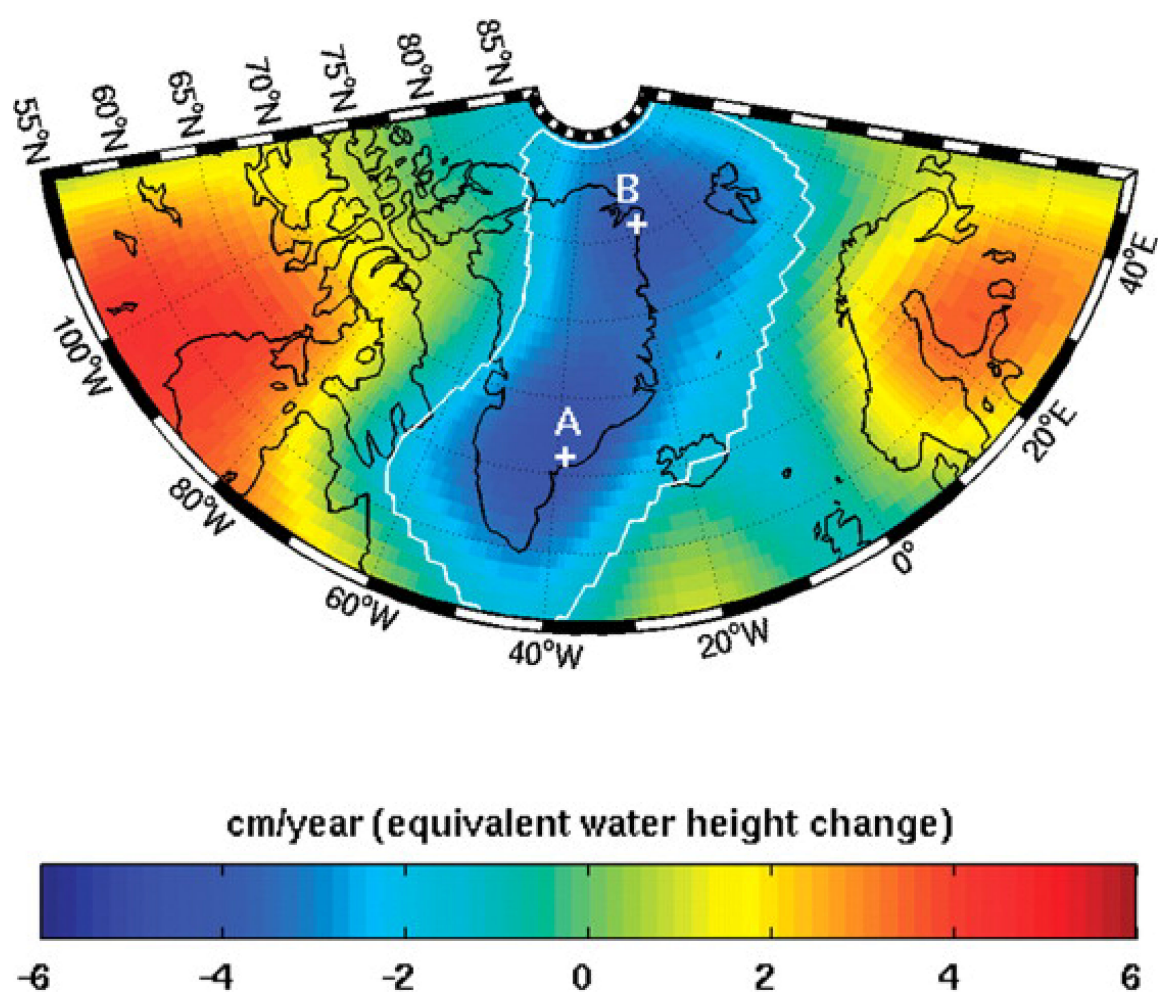


Figure 6.8: GRACE long-term mass rates over Greenland and surrounding regions during the period April 2002 to November 2005, determined from mass change time series on a 1° grid, taken from [9].

real geophysical signals. As they stated, this is certainly not true and led to overestimated errors. The convolution with a smoothed region function assumes that the errors in different Stokes coefficients are uncorrelated. This assumption is not true either, and this approach will therefore lead to error estimates for the mass results that oversimplify their spatial pattern.

Here we conclude that both approaches used to estimate the uncertainty have their drawbacks and it is for sure that our estimates are too optimistic. Errors are introduced by remaining GRACE measurement errors after spatial smoothing, uncertainty in the underlying background geophysical models used in GRACE, (e.g. errors in the atmospheric and ocean models over Greenland and surrounding regions), and unquantified leakage errors.

6.3 A comparison of ICESat and GRACE

The third subquestion of this thesis was: How can the differences between both estimates be explained and how can these differences be reduced. In fact, the answer to this question can be derived from our discussions in section 6.1 and 6.2. This paragraph will therefore provide a short summary of the main issues. The GRACE estimates mentioned in this paragraph are retrieved from table 6.8.

When we compare our estimates based on ICESat and GRACE data separately, we conclude that with ICESat a much stronger mass loss is observed, -142.6 ± 3.7 Gton/year and -93.1 ± 6.7 Gton/year for ICESat and GRACE respectively. For GRACE we mentioned the strongest mass loss, obtained when the CSR monthly solutions are used. For CNES, the difference is comparable, but for the solutions of CSR (destriped), DEOS and GFZ the difference is larger.

The differences between our ICESat and GRACE estimates are mainly caused by the unaccounted leakage effect for GRACE (see section 5.4.3), which makes that these estimates are too low. This also explains the differences between the individual estimates of the northern and southern part. For ICESat a small mass loss of -18.7 ± 1.3 Gton/year is observed. For GRACE, the estimates range from -17.5 ± 3.2 (DEOS) to -35.3 ± 4.2 (CSR) Gton/year. Except for DEOS, all GRACE estimates show a stronger mass loss for this region. Strong mass losses in the South will leak into the estimates of the North, making the trends more negative. A similar statement holds for the estimates of the southern part. For ICESat we obtained a mass loss of -123.9 ± 3.5 Gton/year, while the GRACE estimates range from -43.4 ± 3.4 (DEOS) to -63.2 ± 3.2 (CNES). This can be understood by the fact that strong mass losses in the coastal region leak to the surrounding oceans, making the trends more positive.

Table 6.9 provides the estimates for the North, South and the whole of Greenland for two studies that applied a correction for the leakage error, i.e. GRACE IV and GRACE V. Compared with our ICESat results they estimated much stronger ablation signals for all regions, except when the monthly solutions of JPL are used. For the southern part this can be understood by the fact that our ICESat results are believed to be too low. With the N-sigma thresholding, used to remove outliers, also a part of the signal is removed. Mainly in the southern part where strong ablation signals are observed, this leads to an underestimation of the real signal. For the northern part we have more doubts about the estimates provided by GRACE IV and GRACE V. For this region the assumption, used to apply the leakage correction is not valid, see section 5.4.3.

For sure the differences between our ICESat and GRACE estimates can be further reduced when parts of the processing are changed, see section 7.2. However, for some effects corrections in the near future might be difficult due to a lack of reliable models or independent data sources. As an example we refer to the conversion of the observed volume changes to mass changes, when ICESat data is used.

6.4 A joint inversion of ICESat and GRACE

One method to reduce the uncertainty in the estimated mass balance change rates for the separate datasets is to combine both datasets. Because more observations with the same number of unknowns will reduce the uncertainty of the estimated unknowns. In this section we propose a method for a joint inversion of ICESat and GRACE. This forms the answer to the final subquestion; what is the mass balance of the Greenland ice sheet based on a joint inversion of ICESat and GRACE data. In section 6.4.1 the method is briefly explained, followed by a presentation and discussion of the results.

6.4.1 Method for a joint inversion

In literature, [65], [72] and [76], several attempts are made to integrate ICESat and GRACE datasets in order to estimate both the mass balance change and the PGR contribution. For Antarctica, these procedures make sense due to the magnitude of the PGR effect with respect to the observed mass changes [68]. For Greenland, the PGR corrections are small compared with the observed mass changes. Therefore we did not estimate these corrections, but only the mass change rate with a joint inversion of both ICESat and GRACE datasets.

For ICESat and GRACE, two separate divisions of the ice sheet were used. For ICESat, the ice sheet was divided in 6 drainage systems (DSs), further divided into regions above and below 2000 meter. For GRACE, we combined DS 1, 2 and 6 and DS 3, 4 and 5 to a northern and southern part respectively. For the joint inversion, we combine all DSs, so we estimate the mass change rate for the whole of Greenland. In this case, the bias caused by leakage will be smaller as when we apply a joint inversion for both the northern and southern part separately.

The simplest approach for a combination of both datasets will be a joint inversion of the separate trends for the whole of Greenland. This is nothing else than the weighted mean of both trends, where the weights are inversely proportional to the inverse of the corresponding variances. However, this approach will not take into account the limited temporal coverage of the ICESat data, i.e. the number of points in the time series is significantly lower as for GRACE.

On the other hand, one might propose to simply combine the design-matrices for the different regions used to estimate the time series for both ICESat and GRACE and use that to estimate a new time series for the whole of Greenland, see equation 6.1. After that we use this time series to estimate the trend, using the procedures described in section 4.2.4. Here we assume that there is no correlation between the ICESat and GRACE dataset. Notice that with a joint inversion of both datasets it is not necessary to use a reference epoch (see section 4.2.4), because the matrix A_{JI} will be of full rank.

$$A_{JI} = \begin{pmatrix} A_{I,DS1a} \\ \dots \\ A_{I,DS6b} \\ A_{G,DS1-6} \end{pmatrix}, \quad y_{JI} = \begin{pmatrix} y_{I,DS1a} \\ \dots \\ y_{I,DS6b} \\ y_{G,DS1-6} \end{pmatrix}, \quad Q_{yy_{JI}} = \begin{pmatrix} Q_{yy_{I,DS1a}} & 0 & 0 & 0 \\ 0 & \ddots & 0 & 0 \\ 0 & 0 & Q_{yy_{I,DS6b}} & 0 \\ 0 & 0 & 0 & Q_{yy_{G,DS1-6}} \end{pmatrix} \quad (6.1)$$

With this solution it is necessary to convert both the ICESat and GRACE observables to mass changes. So, the observed elevation differences must be converted to mass changes using the procedure given in section 4.2.4 and the variations of thickness of an equivalent water layer must be multiplied with the area of Greenland and the density of water. Before the conversion to mass changes, both the observed elevation differences and the variations of thickness of an equivalent water layer are corrected for the PGR effect. For the correction of the observed elevation differences we used a slightly different approach as explained in section 4.2.4. In this case the PGR-induced radial velocities are interpolated to the positions of the OPs, using a nearest neighbor interpolation. The PGR correction is obtained by multiplying the interpolated radial velocities with the time differences between the points that form the OPs. For the correction of the variations of thickness of an equivalent water layer, see section 5.4.1.

The problem with this solution is related to the ICESat part, because here the solution does not take into account the inhomogeneous distribution of OPs over the Greenland area, see section 4.2.1 for more details about this problem. This problem can be solved by computing the mean mass change over a DS region per pair of epochs and sum these means up over all DS, see equation 6.2. With this approach we obtain the mass changes over the whole of Greenland for all epoch pairs.

$$\sum_{DS=1}^6 \left(\frac{1}{\#_{OP\uparrow}} \sum_{n=1}^{\#_{OP\uparrow}} \overline{\Delta M}_{\uparrow ij} + \frac{1}{\#_{OP\downarrow}} \sum_{n=1}^{\#_{OP\downarrow}} \overline{\Delta M}_{\downarrow ij} \right), \text{ with } i < j \quad (6.2)$$

Where:

$\overline{\Delta M}_{ij}$ estimated mass difference between month j and i for the region above (\uparrow) and below (\downarrow) 2000 meter

$\#_{OP}$ number of OPs for the region above (\uparrow) and below (\downarrow) 2000 meter

However, such a solution requires that for all regions the same pairs of epochs are available. Because, when a particular epoch pair is missing for a certain region, the sum of the mean mass changes for that epoch pair is not longer a sum over the whole of Greenland. For ICESat, we have data for 15 different epochs, resulting in 105 unique pairs of different epochs. For none of the DS areas, all pairs are available, the maximum is 104, while the minimum is only 55. Possibly the gaps can be filled with 'fake' data in such a way that the estimated trend without this fake data is not contaminated. But this idea has to be worked out in future.

Several approaches might be followed to solve this problem. We decided to merge DS 1, 2 and 6 and DS 3, 4 and 5 for the region above and below 2000 meter separately. After that, we calculate the mean and sum up over all regions. With this approach, the problem was not solved completely. In total we missed data for 9 epoch pairs, which were removed from the dataset. Besides the disadvantage that in this case not all data is used, another disadvantage is that we introduce problems related to the inhomogeneous distribution of OPs, see section 4.2.1.

So far, we assumed that the variance-covariance matrices of both the ICESat and GRACE datasets are known. Especially for ICESat this is a point of concern. Because here, we estimate the variances of the elevation differences for a particular DS area using the elevation differences over a time period shorter than 30 days, see section 4.2.4. When the number of OPs for a particular epoch pair is low and the variances of the observed elevation differences are high, it might happen that the variance of the summed mass change for that epoch pair is also high. In that case, it might happen that the influence of the ICESat data is negligible. However the other way around is also possible, resulting in an influence of the ICESat observations that is too high. In that case, the estimated trend will strongly rely on the epochs for which we have both ICESat and GRACE data.

Variance component estimation (VCE) is a well-known procedure to retrieve the relative weights between two datasets. Basically you estimate two scaling factors (σ_1 and σ_2) that are used to scale the variance-covariance matrices of each dataset accordingly. So the variance-covariance matrix of the observations is written according to equation 6.3. For more details about this procedure we refer to literature, see for example [12] and [61].

$$Q_{yy_{JI}} = \sigma_1 \begin{pmatrix} Q_{yy_{ICESat}} & 0 \\ 0 & 0 \end{pmatrix} + \sigma_2 \begin{pmatrix} 0 & 0 \\ 0 & Q_{yy_{GRACE}} \end{pmatrix} \quad (6.3)$$

6.4.2 Results and discussion of joint inversion

The joint inversion scheme, presented in the previous section, is applied with and without application of the VCE technique. Here all different GRACE solutions are used. Table 6.10 provides an overview of the estimated trends and accompanying uncertainties using both procedures. For the corresponding time series we refer to appendix D.

VCE	CNES	σ_{CNES}	CSR	σ_{CSR}	CSR-ds	$\sigma_{\text{CSR-ds}}$	DEOS	σ_{DEOS}	GFZ	σ_{GFZ}
no	-131.6	0.13	-132.4	0.13	-132.4	0.13	-132.4	0.13	-132.0	0.13
yes	-115.6	9.03	-121.5	10.06	-114.3	9.59	-124.7	11.72	-119.0	10.86

Table 6.10: *Estimated mass change rates and accompanying uncertainties in Gton/year with and without application of VCE.*

It turns out that without application of VCE, the estimated trends are almost similar for all different GRACE solutions. This means that the influence of the ICESat data is very strong, i.e. the estimates only rely on the data of those epochs. Based on the time series of figure D.2 in appendix D we conclude that the estimates obtained after application of VCE are more reasonable. Still the errorbars for the epochs for which both ICESat and GRACE data is available are smaller than for the remaining epochs, which is reasonable because for these epochs more information is available. But the VCE causes a stronger influence in the estimated trend of the epochs for which only GRACE data is available.

Also here, the reported uncertainties are too optimistic. In the previous paragraphs it is already mentioned that both the estimates of ICESat and GRACE are believed to be too small. The ICESat estimates due to the fact that with the N-sigma thresholding also a part of the signal is removed. The GRACE estimates due to the fact that they are biased by the so-called leakage error.

Chapter 7

Conclusions and recommendations

The previous chapters contain the methods and derived estimates of Greenland's ice sheet mass balance, using ICESat and GRACE data. Furthermore, the estimates of ICESat and GRACE are compared with each other and a method, with accompanying results, for a joint inversion of both datasets is presented and discussed. This chapter completes the thesis by giving final conclusions concerning the presented work. Furthermore, this chapter contains a list of recommendations for future work.

7.1 Conclusions

In this section the conclusions are presented per subquestion as defined in section 1.4. For each subquestion we start with the general conclusion followed by an explanation. Eventually some remaining conclusions are presented.

7.1.1 Conclusions ICESat

The estimated mass change rate of Greenland's ice sheet and its formal error based on ICESat data only is equal to -142.6 ± 3.7 Gton/year. This signal is mainly caused by strong mass losses in the region below 2000 meter (-162.2 ± 3.5 Gton/year). For the region above 2000 meter, a mass gain of 19.5 ± 1.2 Gton/year is observed.

In order to estimate these mass change rates, data of seven laser campaigns is used, obtained between February 2003 and March 2006. From this dataset a subset of 351 636 not exactly overlapping footprints is retrieved, after being cleaned using the quality flags defined by the GLAS science team.

The total estimate is a sum of estimates over 6 drainage systems, further divided into a region above and below 2000 meter elevation. This division of the Greenland ice sheet is necessary to account for the inhomogeneous distribution of overlapping footprints caused by the inclination of the satellite. Estimations for smaller areas were not possible, because in that case we were not able to retrieve complete time series of elevation change.

Outliers in the observed elevation differences are removed using N-sigma thresholding per drainage system. It turns out that with this method also real signal is removed. But the estimates obtained when no N-sigma thresholding is used turn out to be unreliable due to outliers in the first laser campaign, which is of an older release. A complete removal of this laser campaign results in less reliable trends due to the fact that far less data points are used to estimate the trend. Therefore we believe that current estimates underestimate the real mass change rates.

Uniform weights are assigned to all elevation differences in order to estimate the elevation changes with

respect to a reference epoch. Also a non-uniform weighting scheme was tested, developed to account for the combined influence of surface slope and roughness. Information about this combined influence was obtained from the GLAS roughness parameter that provides an estimate of the roughness assuming no surface slope. In practice, the assumption of no surface slope is not realistic. Therefore this parameter represents the combined influence of both surface slope and roughness. As a consequence of the fact that this parameter was only available for the first two laser campaigns, the correlation between the observed elevation differences and the roughness parameter was used to derive the weights. It turns out that for larger elevation differences, a relatively larger part of the difference could be explained by the combined influence of surface slope and roughness. Therefore the elevation differences itself were used to assign the weights. However, it turns out that with this weighting scheme also strong ablation and accumulation signals were suppressed.

The estimated time series are corrected for the contribution of Post Glacial Rebound (PGR). This correction, computed by Riccardo Riva, is based on Peltiers ICE-5G ice model and the VM2 Earth model. The uncertainty of the PGR correction is fixed as half the maximum difference between different PGR corrections based on different Earth models. For the individual areas the uncertainty ranges between 0.3 and 1.1 Gton/year. In reality these values will be larger because also the used ice model contains uncertainties. However, for Greenland only one ice model is available.

For the conversion of the elevation changes to mass changes an average snow/ice density of 600 kg/m^3 is used for the region above 2000 meter. Here it is assumed that the observed elevation change rates in this region are mainly caused by variability in the accumulation rate. The value of 600 kg/m^3 is a compromise among snow fall, influence of compaction and ice loss. For the region below 2000 meter a density of 917 kg/m^3 is used, based on the assumption that the observed elevation change rates are mainly caused by ice loss.

The formal errors are obtained by error propagation of the variances in the observed elevation differences to the estimated mass change rates. The variances in the observed elevation differences are estimated per region by taking the variance of all elevation differences over a time span shorter than 30 days. This approach is followed because the variances of the observed elevations are not available.

Remaining conclusions ICESat

- The conducted case studies show that it is difficult to distinguish between physically meaningful signals and noise in altimetric data.
- The ablation pattern is very inhomogeneous over the Greenland ice sheet. The conducted case studies show that sometimes strong mass losses can be related to a particular glacier. In order to obtain a representative estimation of the total mass change rate, all these spots need to be sampled sufficiently, both in spatial and temporal domain. With global approaches a good sampling of all these spots is not feasible. In fact the inhomogeneous ablation pattern stimulates to use spatiotemporal changes in the gravity field (as obtained with GRACE), in order to estimate the total mass change rate. Because the gravity method is insensitive for this inhomogeneity.
- The observed elevation change rates for the region above 2000 meter are confirmed by other altimetry based studies. Compared with the estimates of a study that uses satellite radar altimetry [24], the discrepancies with our estimates are large for the region below 2000 meter. The discrepancies become smaller when the estimates are compared with a satellite radar altimetry study that also uses airborne laser altimetry [77]. Only when we compare with a study that uses satellite radar altimetry in combination with satellite plus airborne laser altimetry [62], the comparison is good. Partly these discrepancies can be attributed to the different time spans of all studies, but the main reason are differences in the sampling of the region below 2000 meter where strong ablation signals are observed. In the study that uses satellite radar altimetry only [24], data at the margins of the ice sheet is not used. Furthermore, with satellite radar altimetry smaller glaciers are missed due to an inadequate ground resolution. Also the ice elevations measured by the radar are much less reliable over steep, undulated surfaces than over flat surfaces. The sampling of the airborne laser altimetry dataset, used by [77] and [62], is not homogeneous over the coastal region. In this case, not all signals will be taken into account.
- The formal errors of the estimated mass change rates are far too optimistic. The real uncertainty is dominated by the question whether all signals are taken into account and by the unknown errors in

the densities used to convert elevation changes to mass changes. The question whether all signals are taken into account depends on the sampling of the overlapping footprints in both spatial and temporal domain. Also the used processing strategy is important, because application of N-sigma thresholding and the non-uniform weighting scheme will suppress strong signals.

7.1.2 Conclusions GRACE

The estimated mass change rates of Greenland's ice sheet and accompanying formal errors using GRACE solutions of CNES, CSR, DEOS and GFZ range between -60.9 ± 3.8 Gton/year and -93.1 ± 6.8 Gton/year. This signal is mainly caused by strong ablation in the South; estimates for the different GRACE solutions range between -43.4 ± 2.3 Gton/year and -63.2 ± 1.9 Gton/year. For the northern part of the ice sheet, this range is between -17.5 ± 3.4 Gton/year and -35.3 ± 4.4 Gton/year.

In order to reduce the measurement errors, the monthly variations of the gravity field are smoothed with a degree-dependent Gaussian filter using a half-width of 500 km. The performance of the degree-dependent Wiener filter, that provides a statistically optimal solution, was limited due to degree-and-order-dependent error characteristics associated with the high inclination of the GRACE satellites. Higher values for the half-widths of the Gaussian filter also smoothed the real signal.

The estimates are corrected for the contribution of Post Glacial Rebound (PGR). For the different regions the uncertainty ranges between 1.6 and 3.3 Gton/year.

For the bias introduced by spatial smoothing (also called 'leakage error'), we did not correct due to lack of time. This leads to an underestimation of the real mass change rate.

The reported formal error of the estimates is far too optimistic. Several error sources are not taken into account like errors introduced by remaining GRACE measurement errors after spatial smoothing, uncertainty in the background geophysical models used in GRACE and unquantified leakage errors.

Remaining conclusions GRACE

- The estimated trends are low compared with other studies using GRACE monthly gravity fields in spherical harmonic coefficients. The differences are mainly caused by the unaccounted leakage effect in our estimates.
- For the southern part, our results confirm the increased mass loss, starting half 2004 ([67] and [9]). On the other hand, our results suggest a decrease in mass loss for the northern part starting in 2005.
- The spatial resolution of the mascon solutions [34] is limited. This is probably the reason why the ICESat results do not confirm these solutions for the individual drainage system regions.

7.1.3 Conclusions comparison ICESat and GRACE

The differences between the estimates of ICESat and GRACE for the northern part, southern part and the whole of Greenland can be explained by the unaccounted leakage effect in our GRACE estimates.

We believe that for both ICESat and GRACE our estimates underestimate the real mass loss. For ICESat this is due to the used method to remove outliers. For GRACE this is due to the unaccounted leakage effect.

7.1.4 Conclusions joint inversion ICESat and GRACE

The estimated mass change rates of Greenland's ice sheet and accompanying formal errors, obtained after a joint inversion of the ICESat dataset and GRACE solutions of CNES, CSR, DEOS and GFZ range

between -114.3 ± 9.6 Gton/year and -127.7 ± 11.7 Gton/year.

In order to apply a joint inversion for the whole of Greenland, the ICESat elevation differences are corrected for the contribution of PGR and converted to mass changes. For this last step, densities of 600 kg/m^3 and 917 kg/m^3 are used for the region above and below 2000 meter respectively.

The mass changes are averaged per pair of epochs for the combined drainage systems 1, 2, 6 and 3, 4, 5 both for the region above and below 2000 meter separately. These averages are summed up in order to obtain the total elevation change for the whole of Greenland. It was not possible to average and sum up over all individual drainage systems because of missing epoch pairs. With this approach we limit the error introduced by the inhomogeneous distribution of overlapping footprints and on the other hand only a few epoch combinations have to be removed because they are not available for all areas.

The GRACE variations of thickness of an equivalent water layer are also corrected for the contribution of PGR and converted to mass changes.

After that, both systems of observation equations are combined. Variance component estimation is used to estimate the relative weights both datasets get in the final estimation procedure. It turns out that the epochs for which only GRACE data is available, do have a negligible influence on the estimated mass change rates when no variance component estimation is used. This means that the relative precision of ICESat data is overestimated with respect to GRACE data. With the application of variance component estimation more weight is assigned to GRACE, which provide more realistic estimates of the mass change rates based on a combination of both datasets.

7.2 Recommendations

In this paragraph we will provide a short overview of ideas that could be tried in future research. We start with a list of recommendations for the ICESat processing, followed by a similar list for GRACE.

7.2.1 Recommendations for ICESat processing

- To remove the overlapping pairs (OPs) that are not located on the ice sheet a 1×1 km surface mask of the Greenland area is used. The limited resolution probably hits some useful points at the narrow glaciers in the coastal area. Possibly the waveforms can be used to classify the overlapping footprints into ice and non-ice points. By considering the temporal behavior of the OPs within a certain area, it might even be possible to distinct between rock covered with snow and ice covered with snow.
- N-sigma thresholding is currently used to remove outliers in the elevation differences. This method does not allow a well-considered distinction between physically meaningful signals and outliers. Instead of N-sigma thresholding, a data snooping procedure applied to all individual raw tracks might perform better, i.e. before the determination of the overlapping footprints and the application of the cleaning procedures. That is because these steps will create gaps in the individual tracks hampering the snooping.
- When no N-sigma thresholding is used, the estimated trends turn out to be unreliable due to outliers in the first laser campaign (old release). It makes sense to use different processing strategies when the stochastic properties for a particular laser campaign are different. In this case, N-sigma thresholding could be applied only to the elevation differences belonging to this laser campaign.
- Our current estimates are influenced by the combined effect of surface slope and roughness. The poor resolution and quality of the GLOBE digital elevation model did not allow to apply a correction for the influence of surface slope. Possibly a high-resolution digital elevation model can be obtained from ICESat data in order to correct for this influence. Furthermore, when the raw waveforms are used (the GLA01 standard data product) the estimated slope bias could be applied to correct the waveform for the influence of surface slope. After correction it might be possible to estimate the roughness parameter independently.

- When for new releases a roughness parameter is available, it can be tried to use this in a weighting scheme.
- In the conversion to mass changes, two different averaged densities are used. In reality these densities are strongly varying both in the spatial and the temporal domain, resulting in a high uncertainty of these values and so in the estimated mass change rates. Possibly the densities can be incorporated as unknown parameters into the joint inversion scheme.
- Variable accumulation rates hamper the estimation of a mass change using altimetry datasets. When short time series are used this causes an additional unknown that cannot be separated from elevation changes caused by the real mass balance change and PGR. Possibly the snow accumulation can be derived from an independent source. In that case, this trend can be estimated independently too.
- Current estimates are not corrected for the compaction of firn, which causes elevation change but no mass change. Zwally et al., [77] show that this correction is significant, so a correction is necessary. Models are available that allows to calculate the contribution of this term.
- It turns out that the ablation pattern is very inhomogeneous over the Greenland ice sheet. Strong mass losses are located in relatively small patches in the coastal area. This makes a representative estimation of the mass change rate difficult. In order to solve this problem, a high-resolution map of the ablation and accumulation signals is necessary. This map can be used for making an integrated estimation of ice mass variations for the entire Greenland.
- One might consider to improve the sampling of spots that show strong signals with the help of airborne laser altimetry. When an ablation signal is related to a particular glacier, also satellite radar interferometry could be used. Drawback of this last method is that it requires additional information about the width and thickness of the glacier.
- In order to obtain a more realistic accuracy, different approaches could be tried. When more laser campaigns become available, it might be possible to split the dataset in two separate datasets and estimate the mass change rates for those datasets separately. The difference in both estimates can be used to quantify the uncertainty caused by the differences in sampling of the area. Information about the stochastic properties of the observed elevation differences might be estimated with variance component estimation.

7.2.2 Recommendations for GRACE processing

- Currently, isotropic or degree-dependent filters are used to smooth the monthly gravity field variations. With non-isotropic or degree-and-order-dependent-errors these filters do not perform well. Improvements are expected when more advanced filters are used that are degree-and-order dependent. A statistically optimal solution might be obtained when all the information of the variance-covariance matrix is exploited. For the DEOS solutions, these matrices are available, so here this approach could be implemented.
- The first thing to do with the current estimates is to correct them for the so-called leakage error. We think that simulations that recover the measured signal might be used to define a proper scaling factor. If a proper hydrological model is available this might be used to estimate the bias itself.

Appendix A

Maps Case Studies

This appendix contains the figures related to the case studies, discussed in section 4.1.

The figures are built up from four elements. The upper left element is a map of the elevation differences at the location of the case study. This location is marked on the inset map. In fact this map is a snapshot of figure 4.1 that shows all elevation differences for all laser campaigns. For the case studies, overlapping tracks are used, so the time difference between all overlapping track pairs (OTPs) is more or less constant. The overlapping tracks related to the case study at hand are plotted with an x symbol while the surrounding OPs are plotted with a dot. The letters B and E mark the first and last point respectively, of that part of the overlapping tracks that is visible in the elevation (difference) profile(s).

The upper right element contains a snapshot of a compilation of Landsat images, available from NASA's World Wind [37]. Here the pseudo color images are used with a ground resolution of 15 by 15 meter. Notice that these compilations are based on images acquired by Landsat from 1999 to 2003. The red arrow marks the path of the overlapping track points in the terrain. Not for all case studies clear Landsat images were available, especially at the center of the ice sheet, the images are entirely saturated and so no features are visible. In these cases the upper right element is empty.

The lower left element contains the elevation profiles, where the red profile represents the first track in time and the blue one the last track in time. The crosses mark the locations of the observations. The distances for the profiles are the cumulative distances between the successive points started from the first point in the track.

The lower right element contains the elevation difference profile.

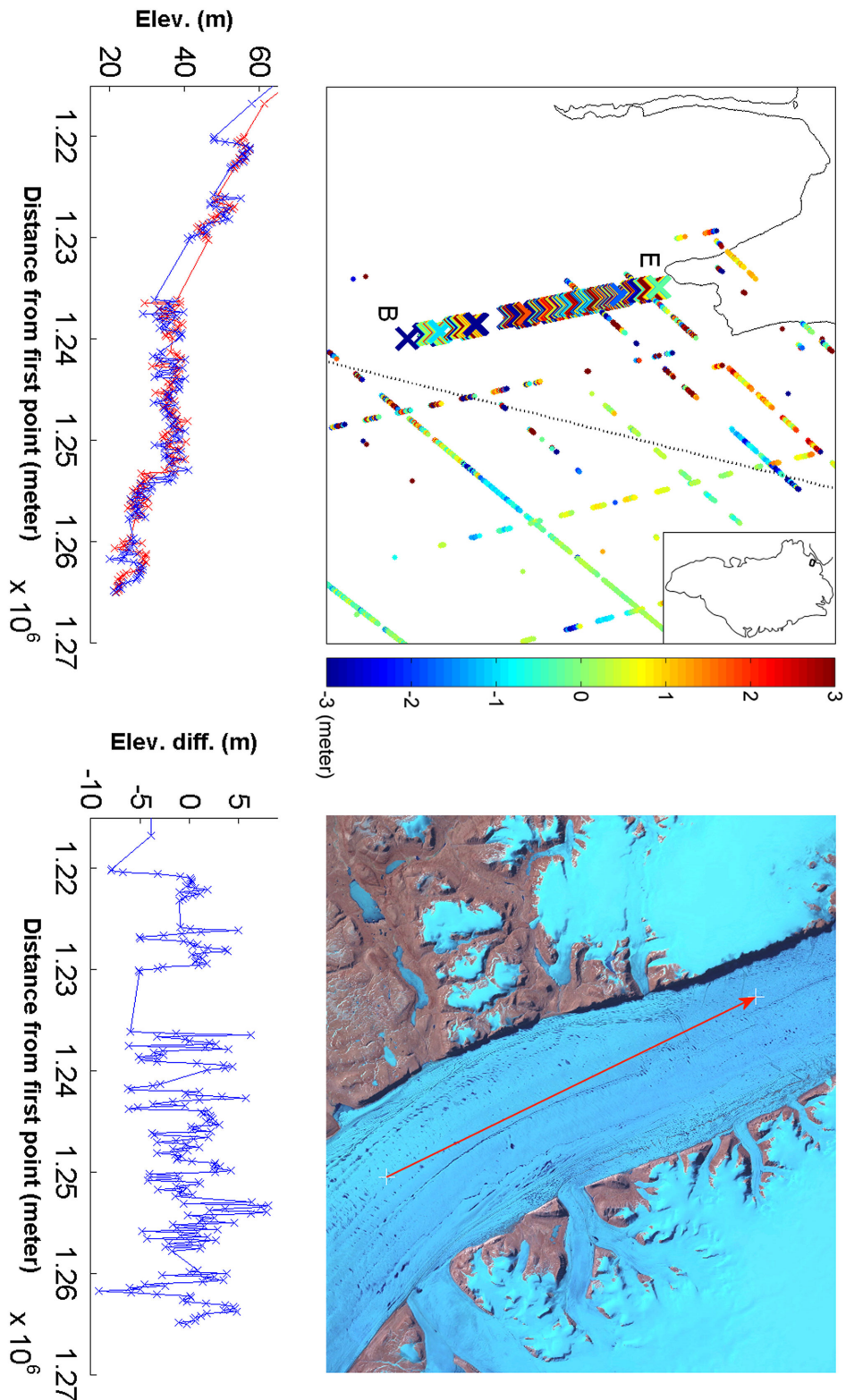


Figure A.1: First track acquired on 24-Feb-2004, second on 26-Feb-2005. The erratic behavior is probably due to the combined effect of surface slope and roughness in combination with the fact that the footprints do not overlap exactly. At the end of the elevation profiles we can probably see the effect of undulation, see section 4.1.4.

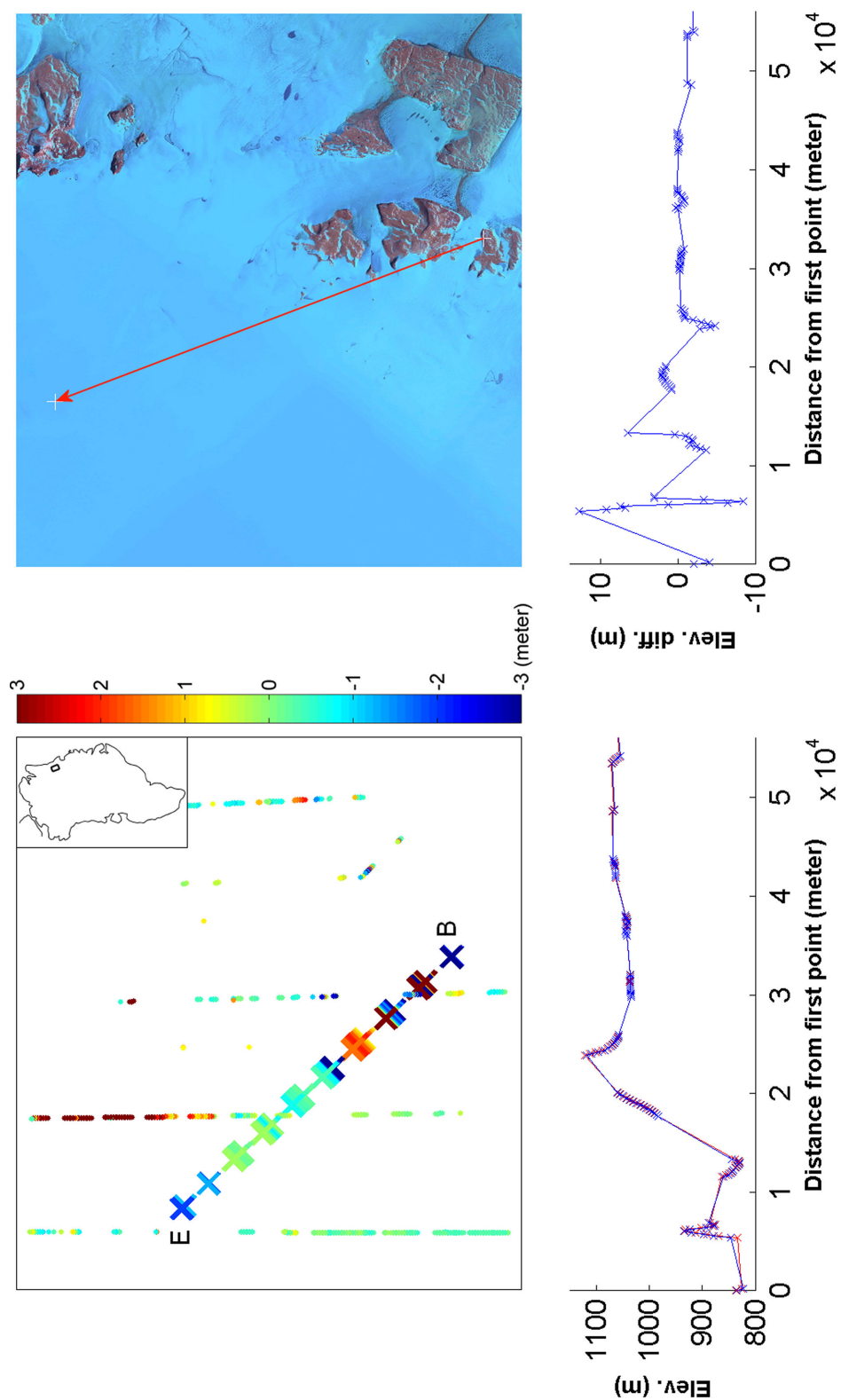


Figure A.2: First track acquired on 01-Mar-2004, second on 04-Mar-2005. Overlapping tracks located at the margin of the ice sheet. On the Landsat images we can see that a part of the OTPs are located on the rocks that rise above the ice sheet. Here steep slopes and roughness might explain the large elevation differences.

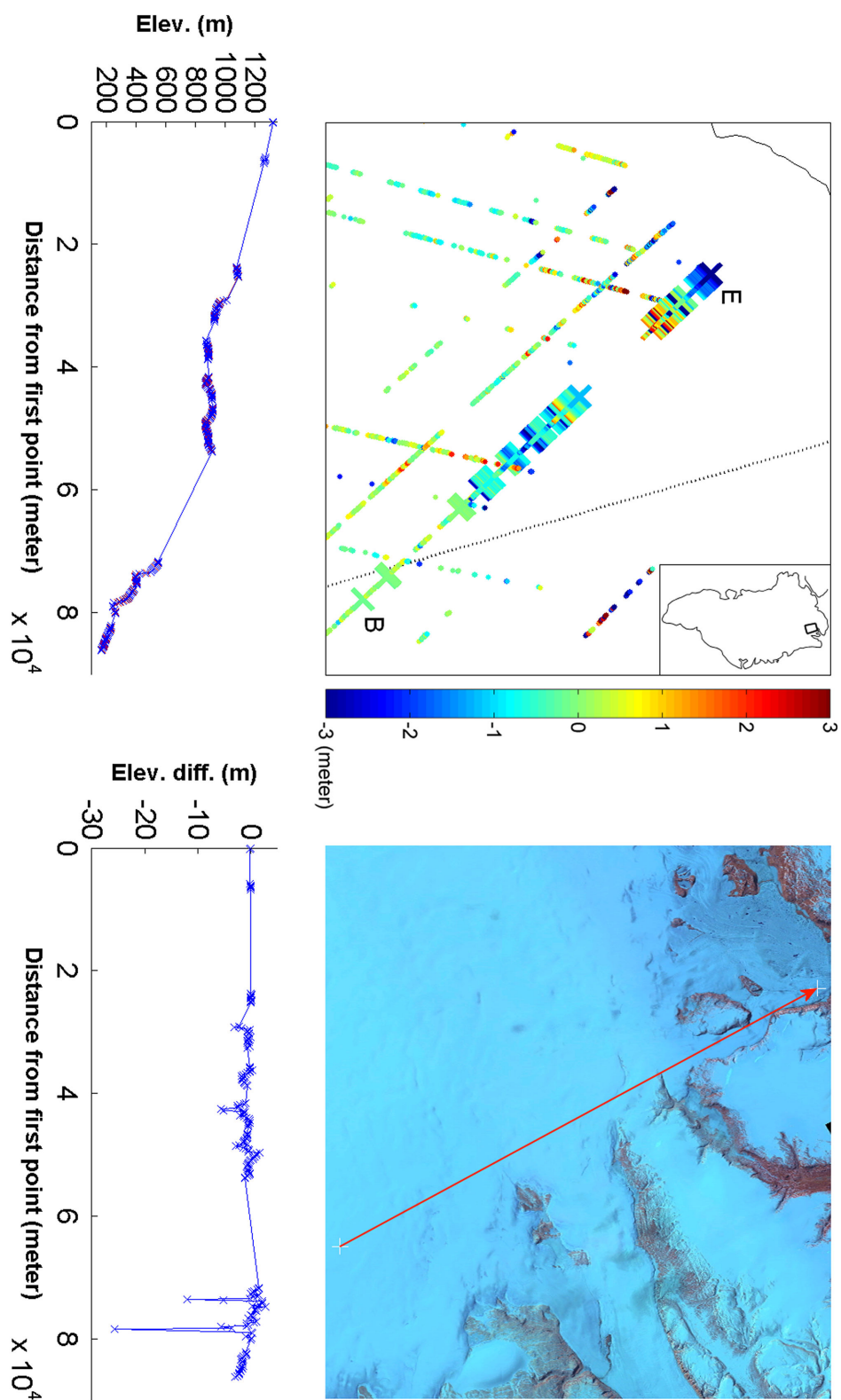


Figure A.3: First track acquired on 09-Mar-2004, second on 12-Mar-2005. Overlapping tracks located at the margin of the ice sheet. On the Landsat images we can see that a part of the OTPs are located on the rocks that rise above the ice sheet. Here steep slopes and roughness might explain the large elevation differences.

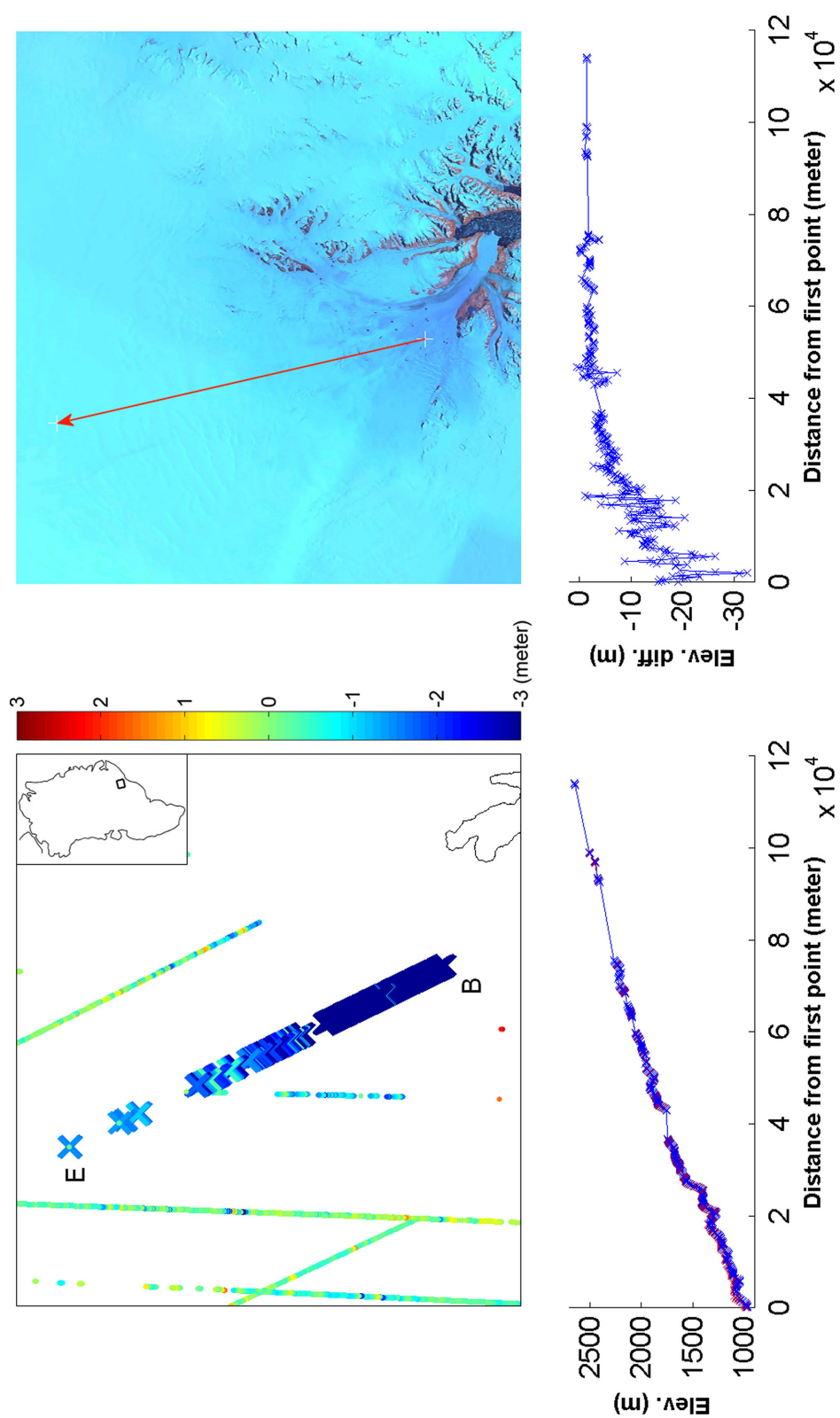


Figure A.4: First track acquired on 19-Oct-2003, second on 24-Oct-2005. The first increasing elevation differences that become constant and decrease after a while are probably due to the effect of saturation. Notice that for only one track a saturation correction is applied. Probably here also the glacier dynamics play a role.

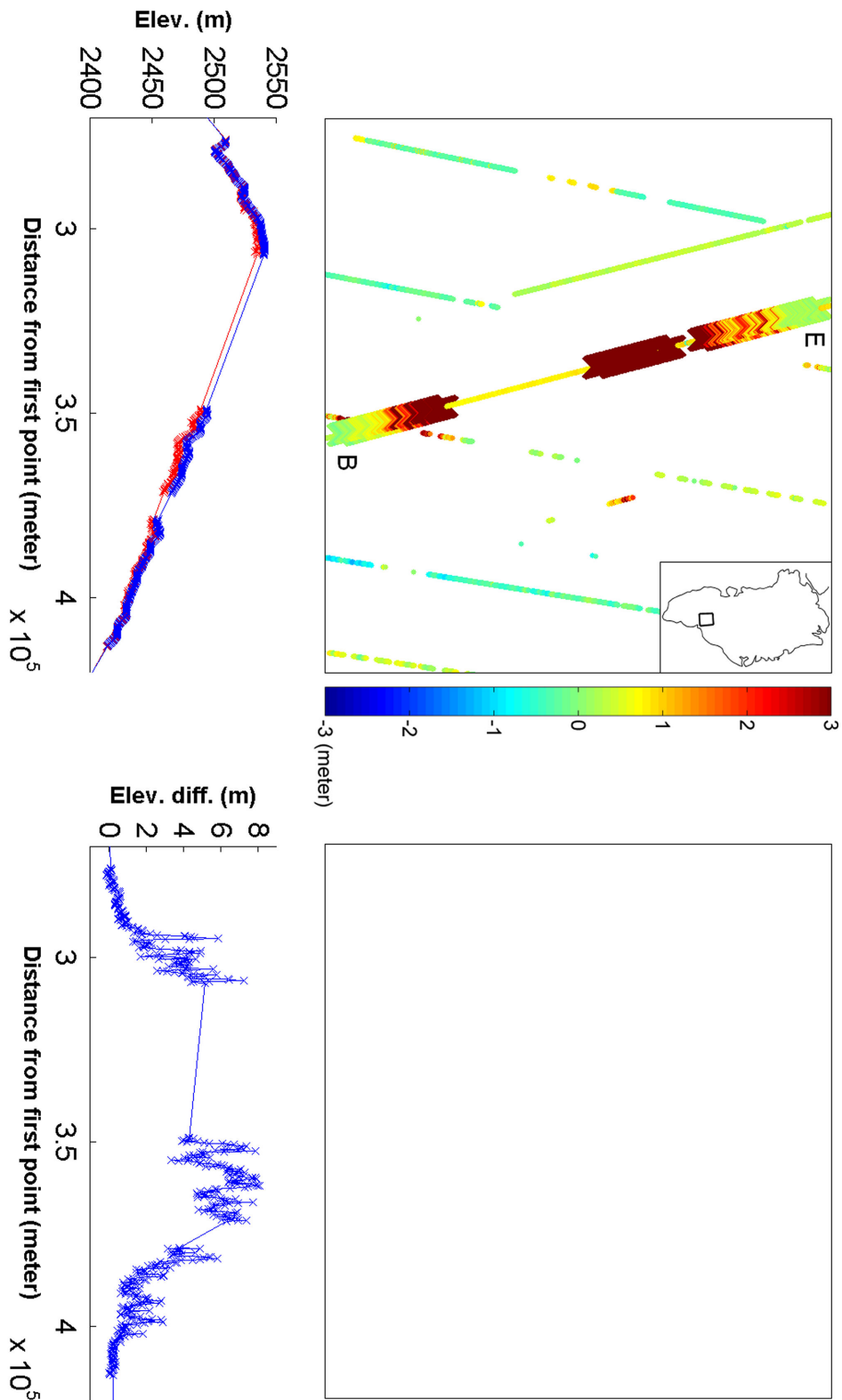


Figure A.5: First track acquired on 23-Oct-2003, second on 24-Feb-2004. The first increasing elevation differences that become constant and decrease after a while are probably due to the effect of saturation. Notice that for only one track a saturation correction is applied.

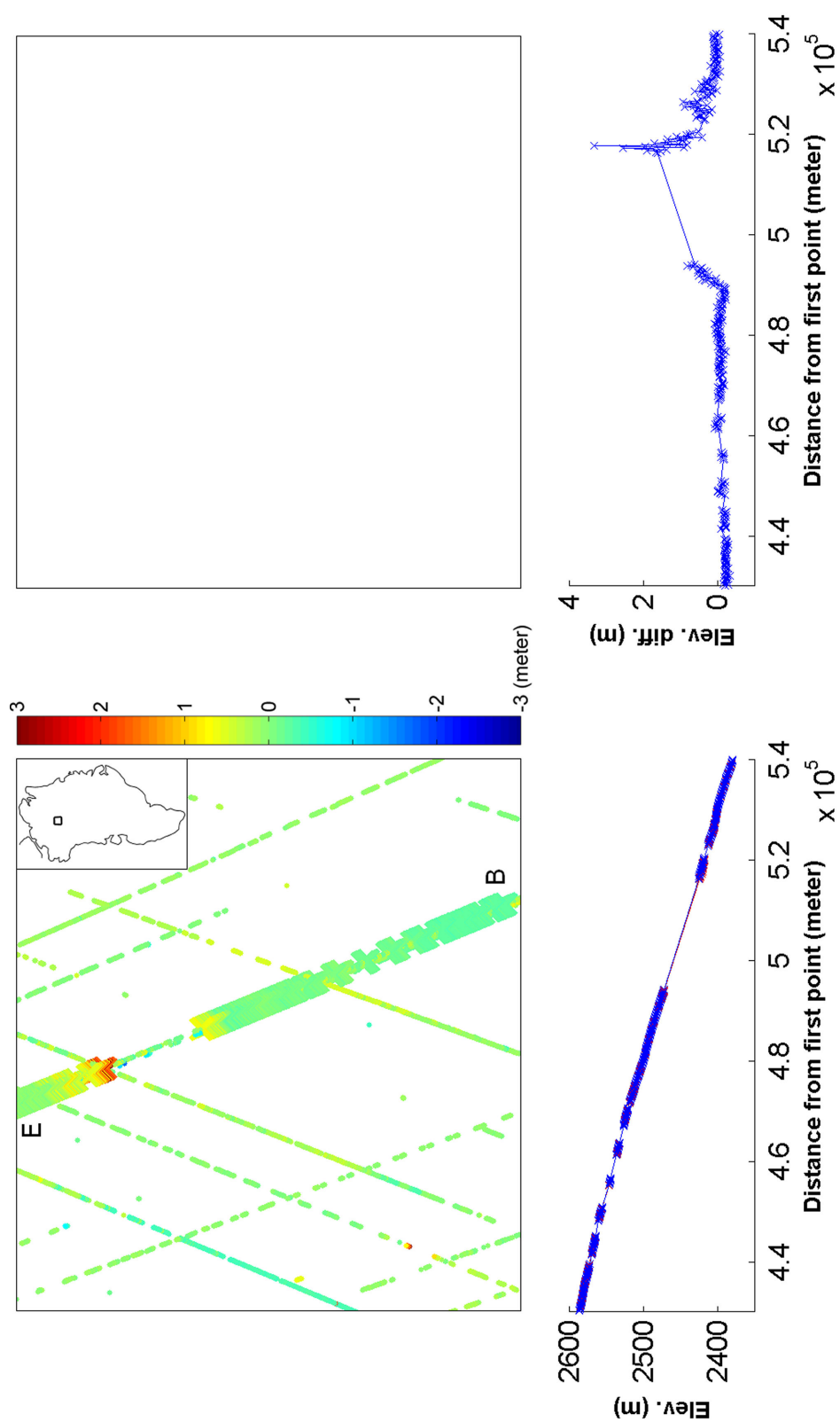


Figure A.6: First track acquired on 28-Oct-2003, second on 08-Mar-2004. The first increasing elevation differences that become constant and decrease after a while are probably due to the effect of saturation. Notice that for only one track a saturation correction is applied.

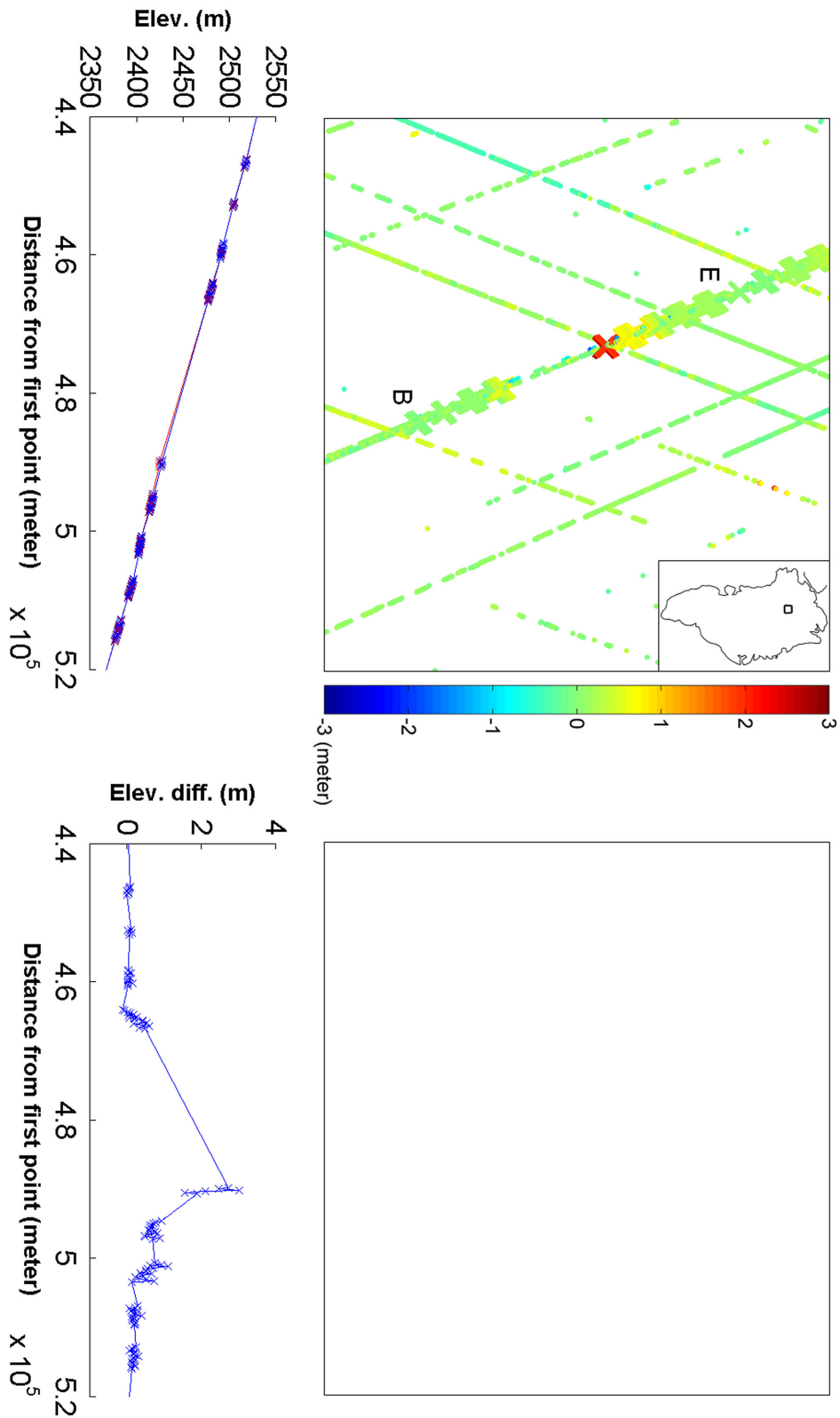


Figure A.7: First track acquired on 28-Oct-2003, second on 10-Nov-2005. The first increasing elevation differences that become constant and decrease after a while are probably due to the effect of saturation. Notice that for only one track a saturation correction is applied.

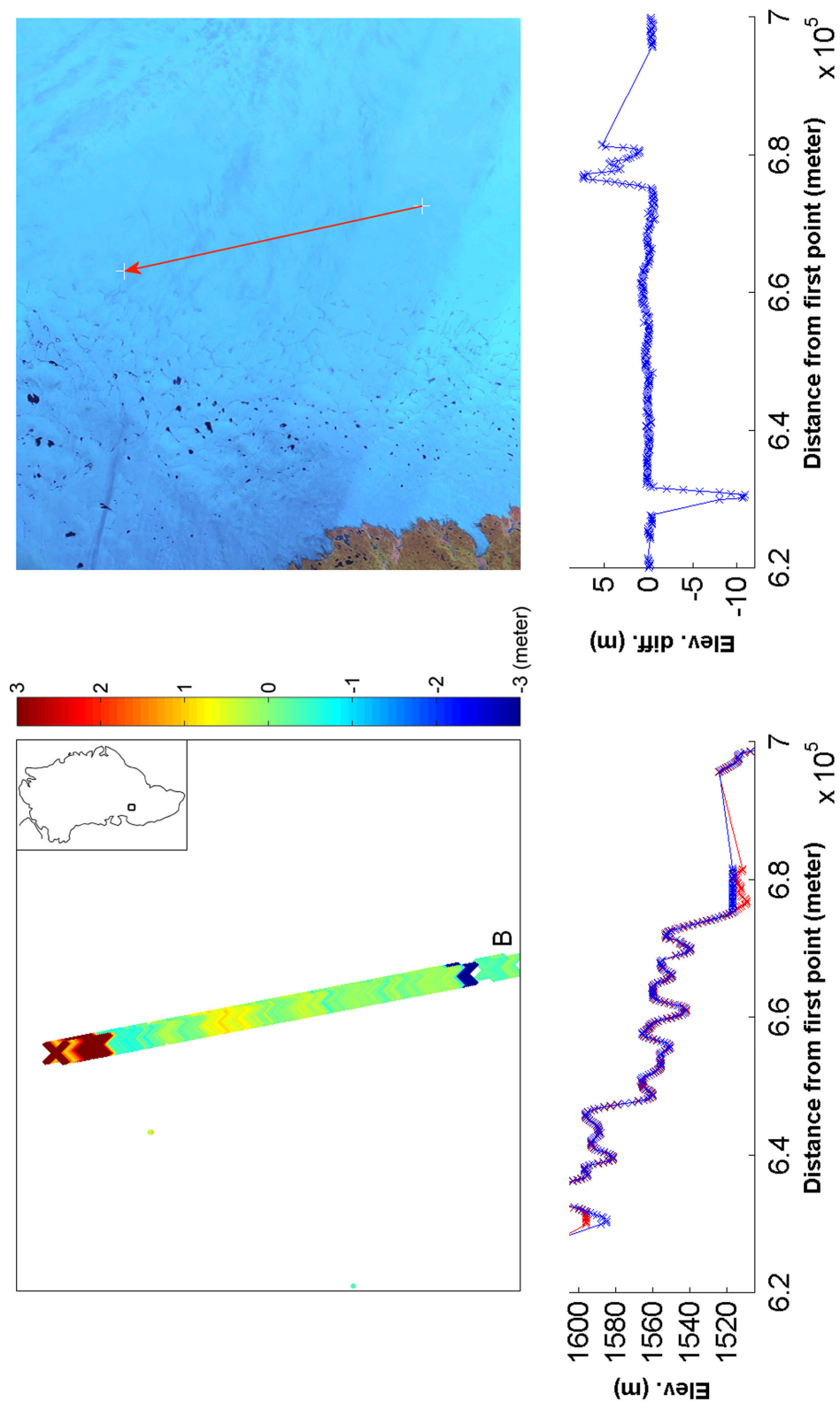


Figure A.8: First track acquired on 21-Mar-2004, second on 27-Mar-2006. Surface lakes at the West Greenland ice margin. The smoothness of the upper elevation profile can be interpreted as a water surface. In the left example the lake disappeared while in the right example a new lake is formed.

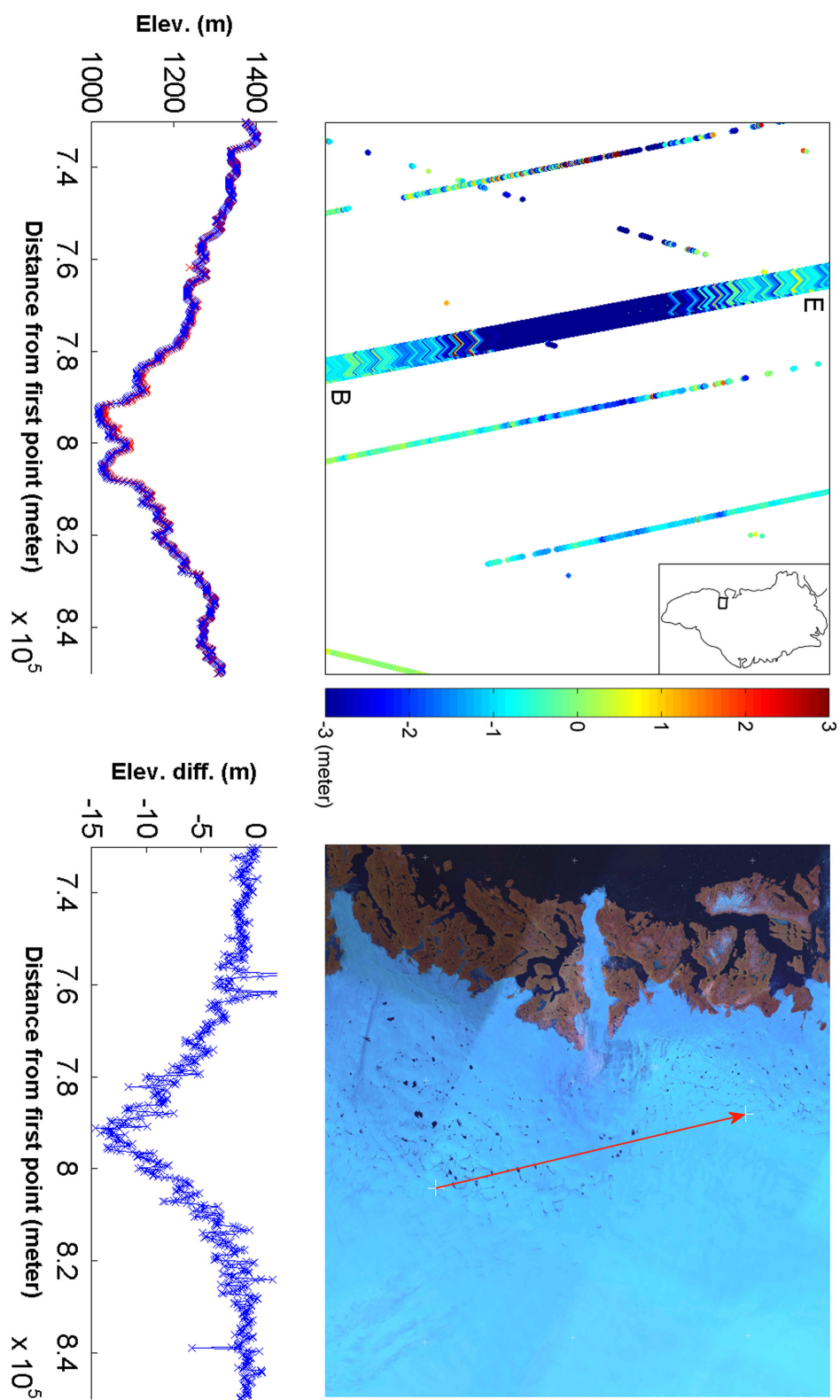


Figure A.9: First track acquired on 21-Mar-2004, second on 27-Mar-2006. Thinning inlet of Jakobshavn Isbræ glacier.

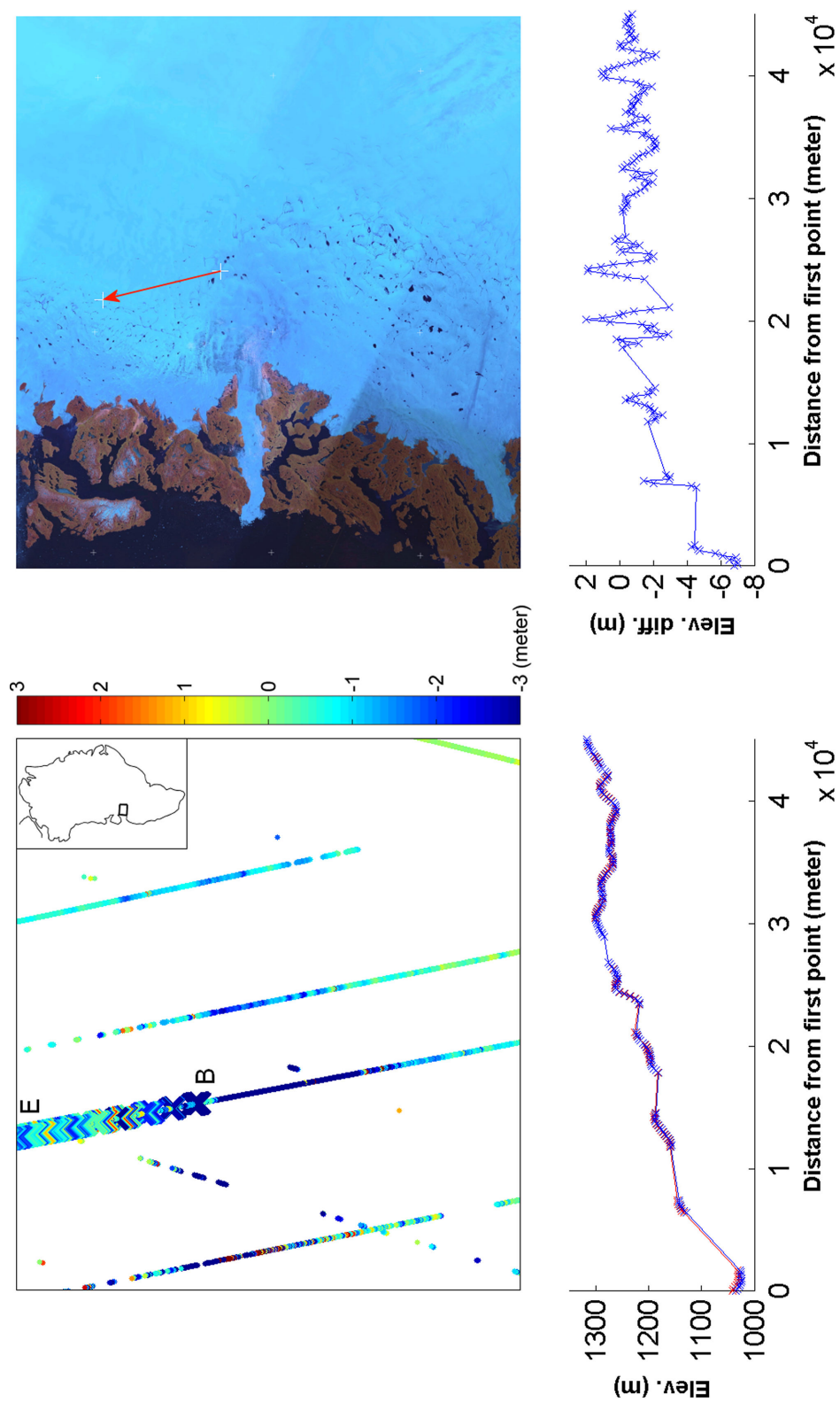


Figure A.10: First track acquired on 21-Mar-2004, second on 23-Nov-2005. Thinning inlet of Jakobshavn Isbræ glacier.

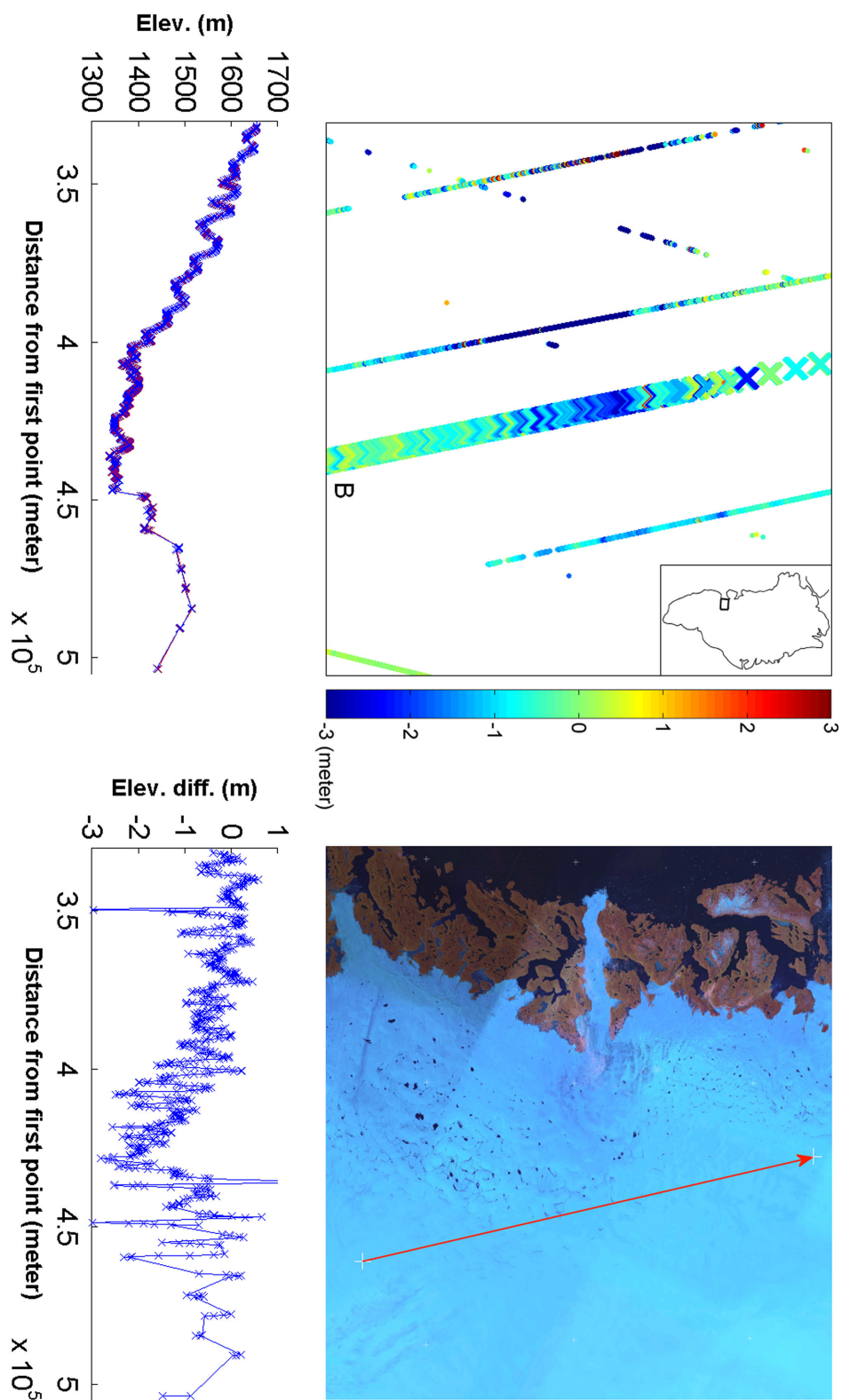


Figure A.11: First track acquired on 27-Feb-2005, second on 29-Oct-2005. Thinning inlet of Jakobshavn Isbrae glacier.

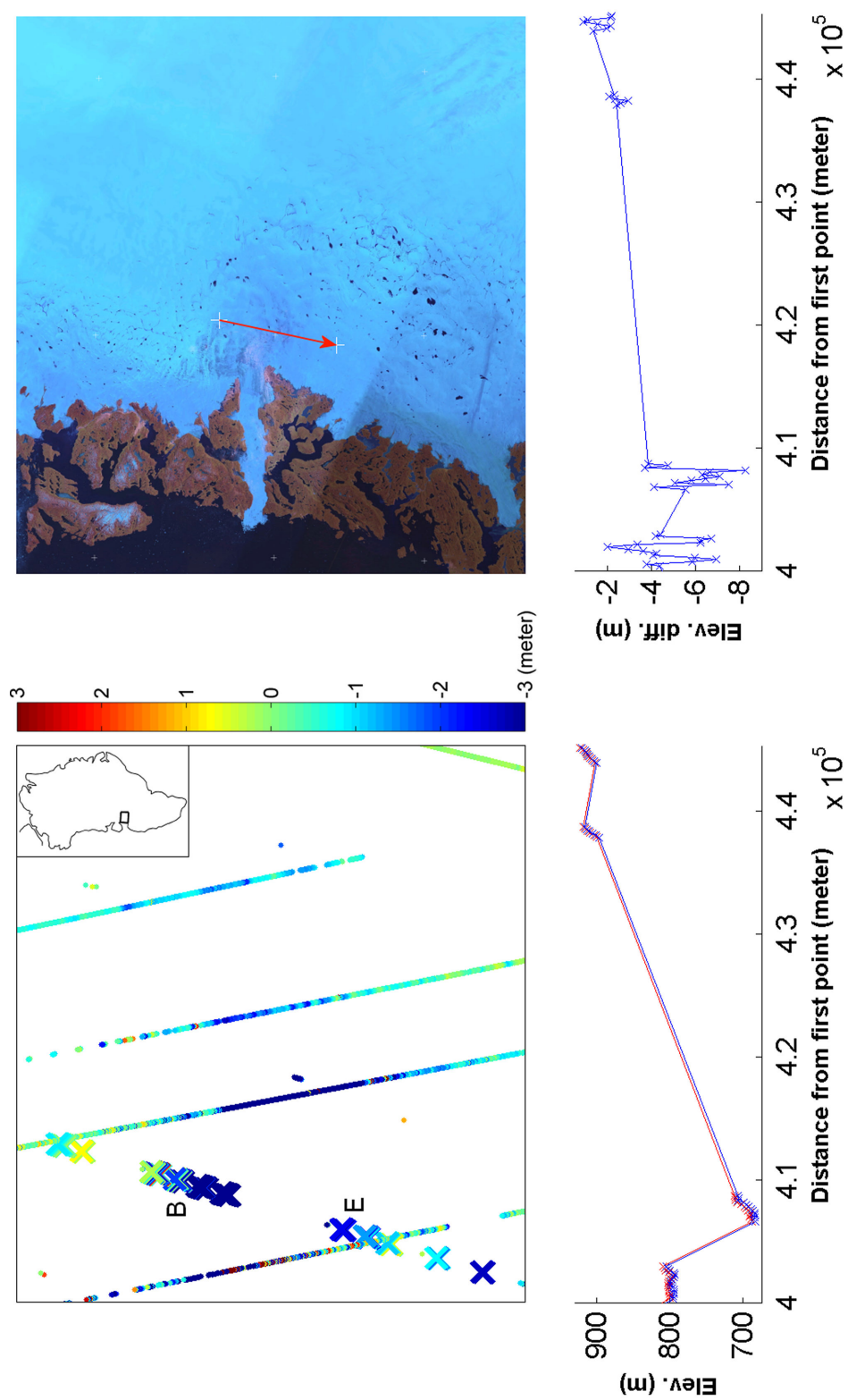


Figure A.12: First track acquired on 01-Mar-2005, second on 05-Mar-2006. Thinning inlet of Jakobshavn Isbræ glacier.

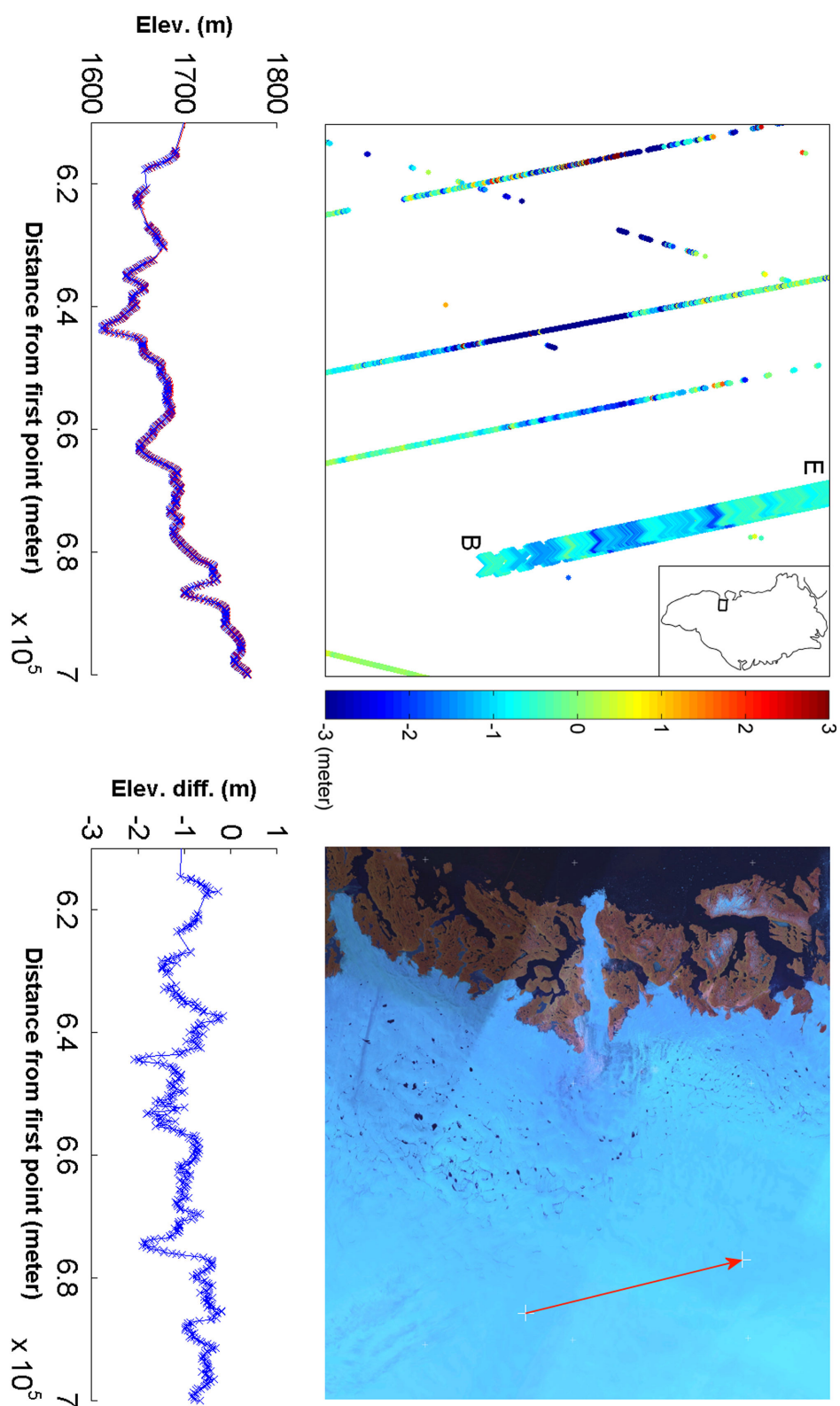


Figure A.13: First track acquired on 07-Mar-2005, second on 10-Mar-2006. Thinning inlet of Jakobshavn Isbræ glacier.

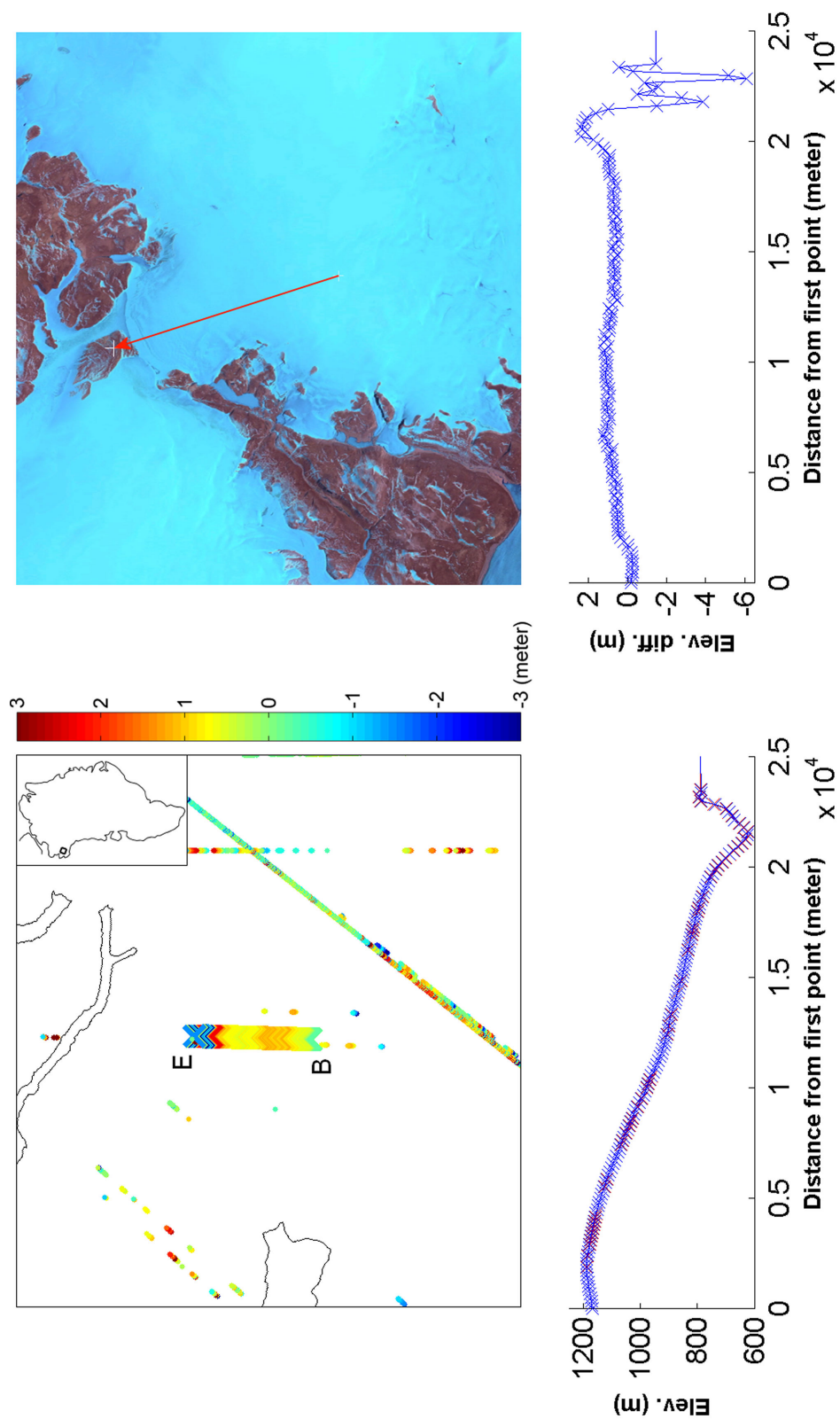


Figure A.14: First track acquired on 25-Sep-2003, second on 03-Oct-2003. Most likely explanation here is that the blocked flow of the glacier results in an uplift of the glacier.

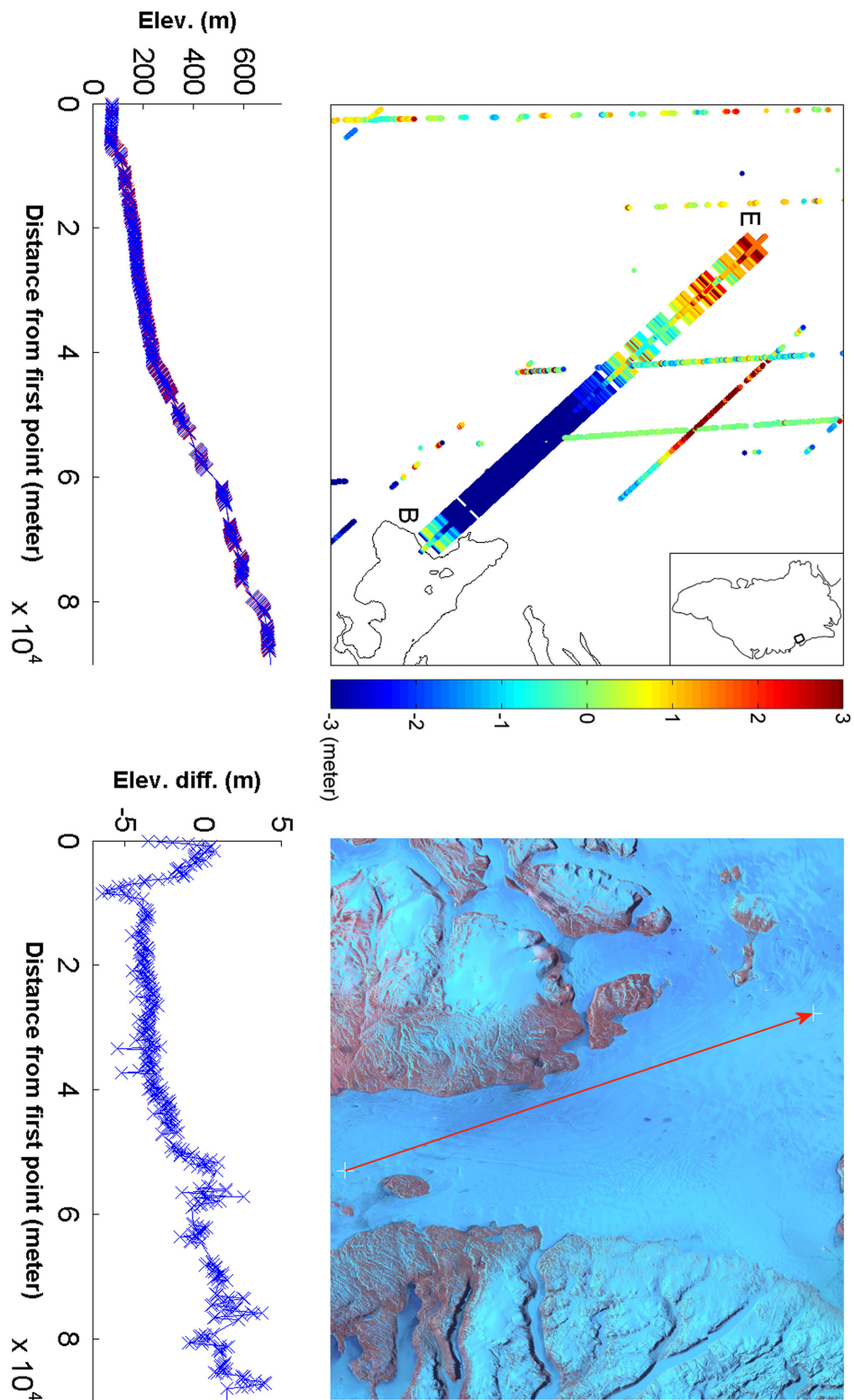


Figure A.15: First track acquired on 21-Oct-2003, second on 26-Oct-2005. Probable effect of undulation.

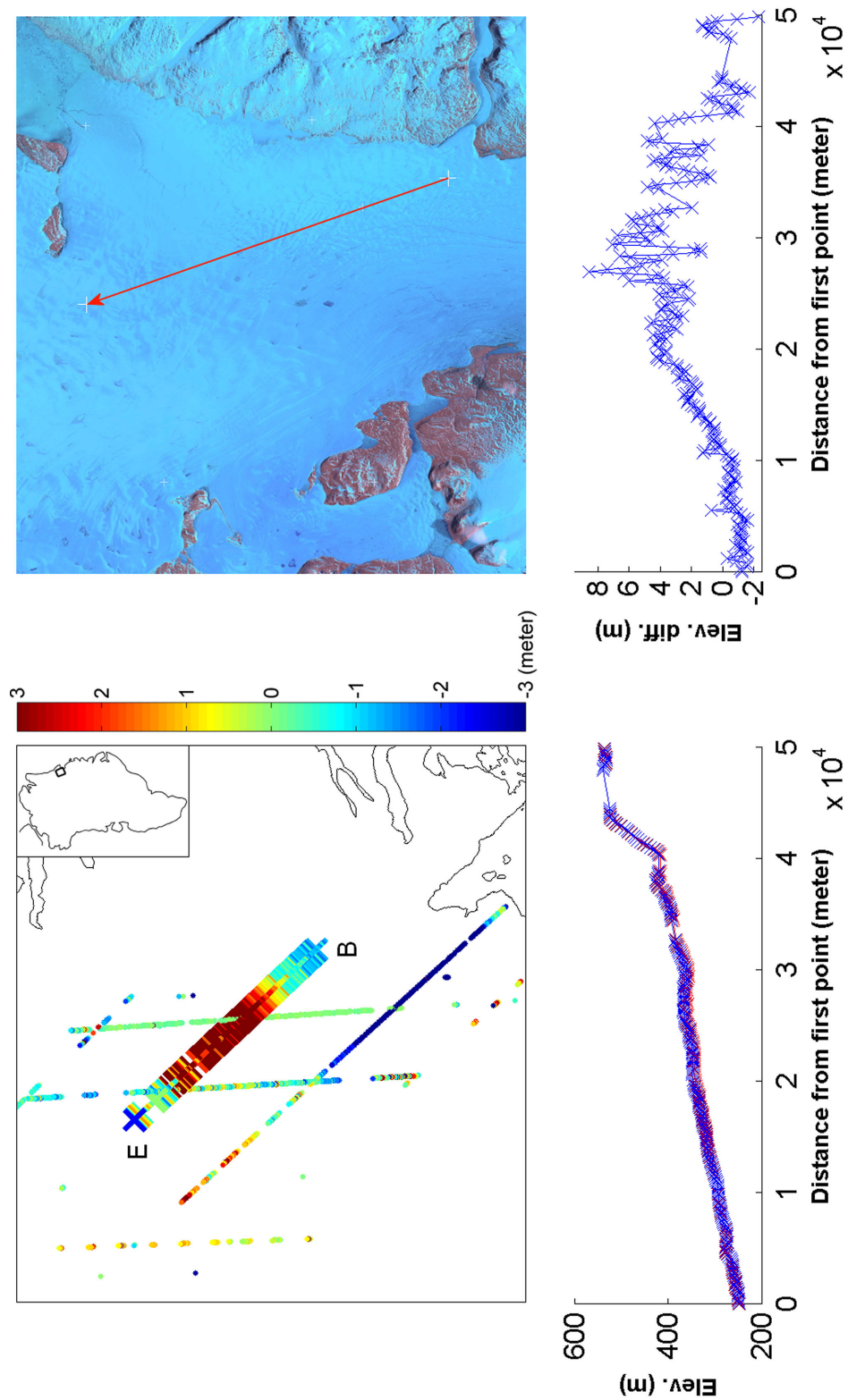


Figure A.16: First track acquired on 29-Oct-2003, second on 07-Mar-2006. Probable effect of undulation.

Appendix B

Time series ICESat

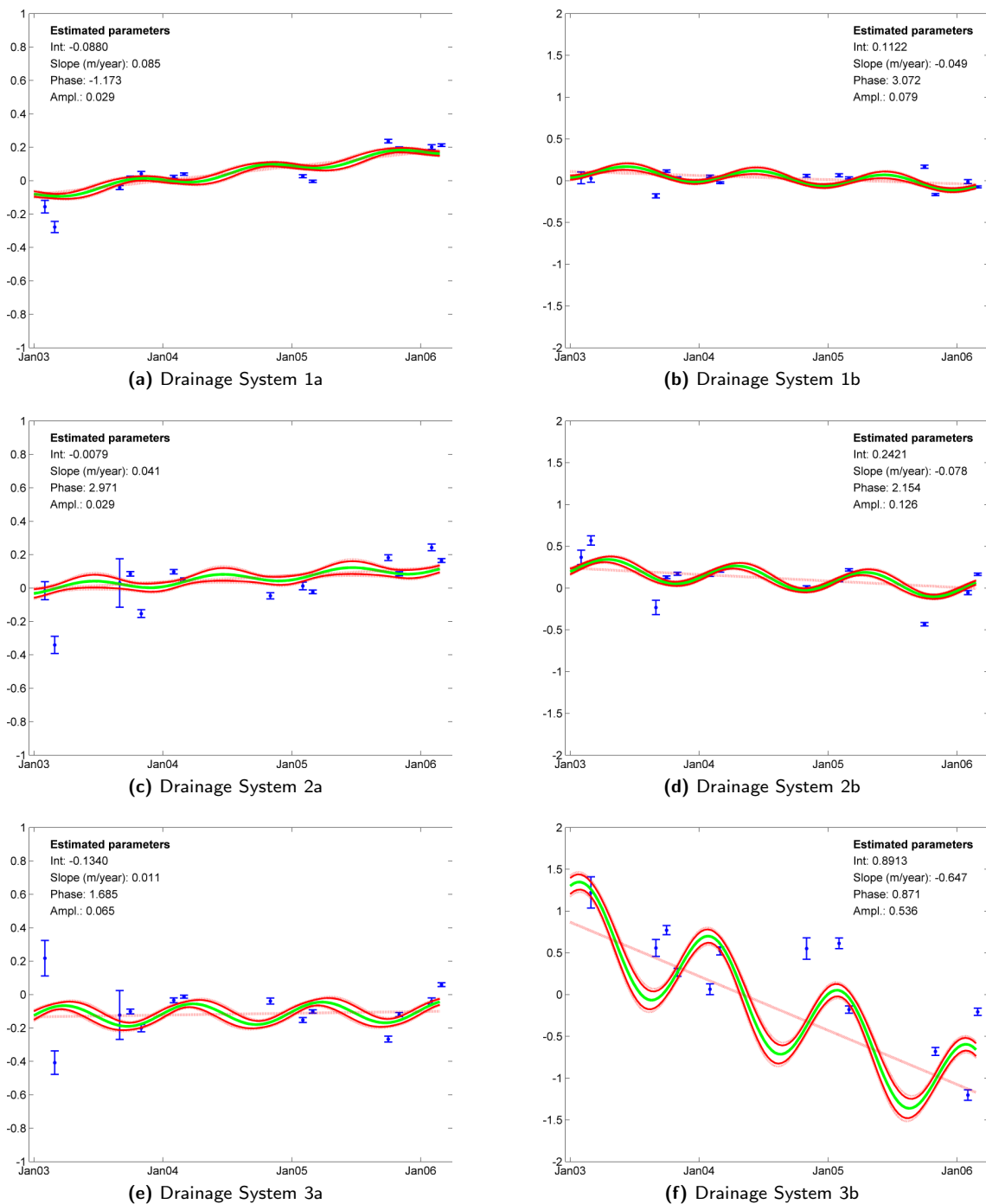


Figure B.1: Elevation change time series for drainage systems 1 to 3 based on ICESat data. Units of vertical axis are in meter. The letters a and b stand for above and below 2000 meter respectively. The time series are computed according to processing strategy 1c, see table 6.1. The estimated trend (straight dotted line) is computed using all available laser campaigns. The solid green line is the trend plus the seasonal cycle. The solid and dotted red curve represents the 95%- and 99%-confidence regions.

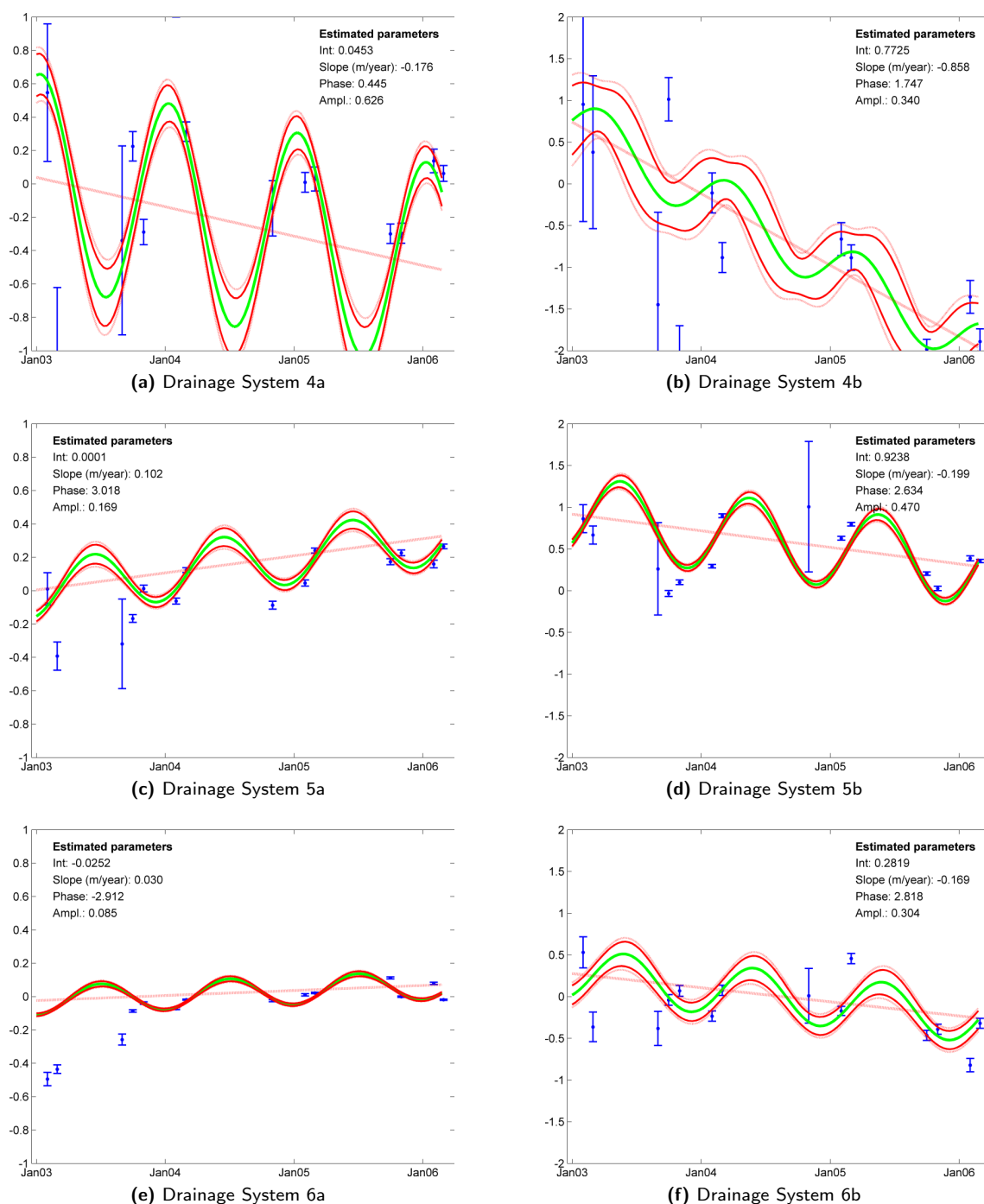


Figure B.2: Elevation change time series for drainage systems 4 to 6 based on ICESat data. Units of vertical axis are in meter. The letters a and b stand for above and below 2000 meter respectively. The time series are computed according to processing strategy 1c, see table 6.1. The estimated trend (straight dotted line) is computed using all available laser campaigns. The solid green line is the trend plus the seasonal cycle. The solid and dotted red curve represents the 95%- and 99%-confidence regions.

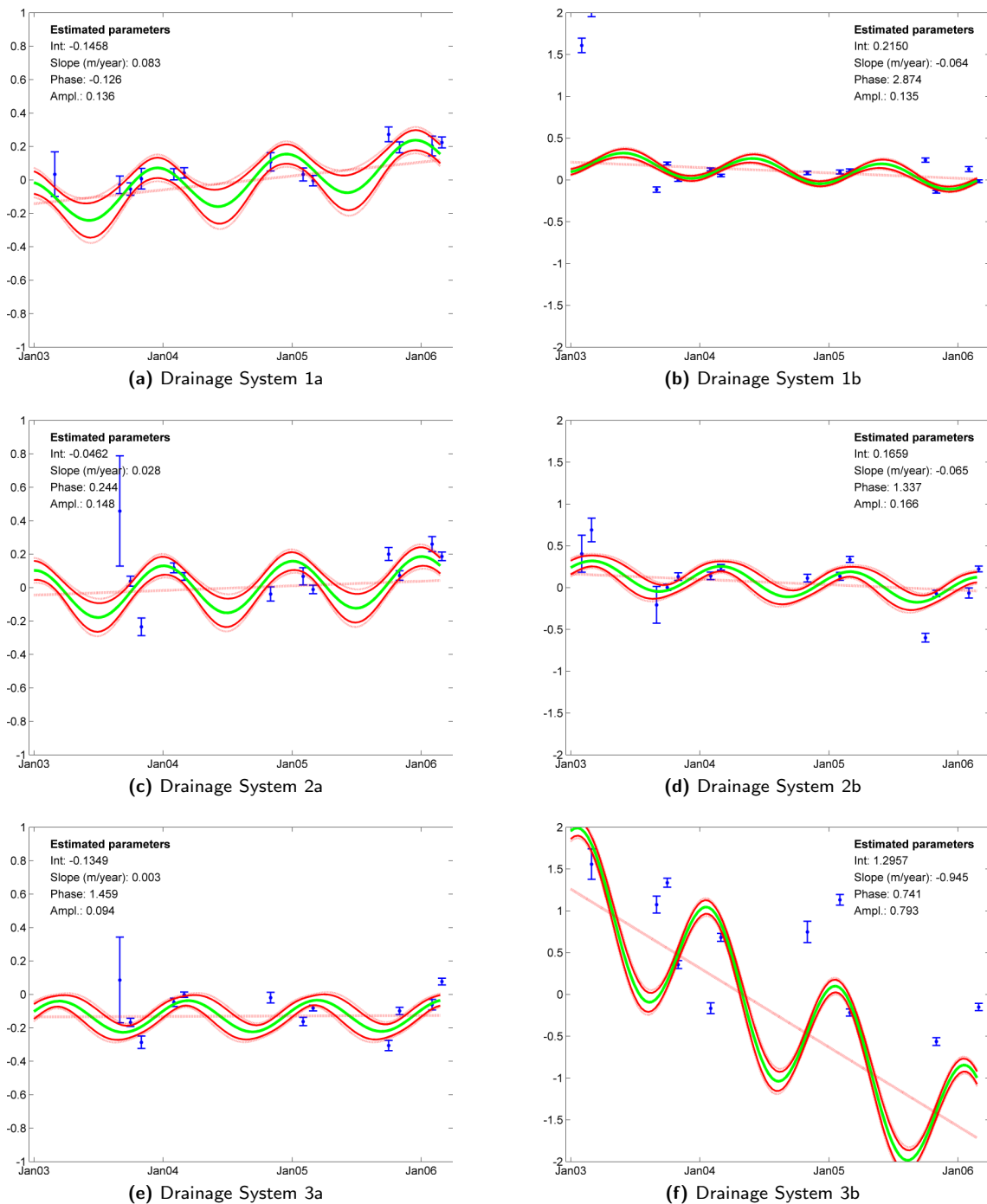


Figure B.3: Elevation change time series for drainage systems 1 to 3 based on ICESat data. Units of vertical axis are in meter. The letters a and b stand for above and below 2000 meter respectively. The time series are computed according to processing strategy 1d, see table 6.1. The estimated trend (straight dotted line) is computed using all available laser campaigns. However, due to the used processing strategy mostly the values of the first laser campaign are out of range. The solid green line is the trend plus the seasonal cycle. The solid and dotted red curve represents the 95%- and 99%-confidence regions.

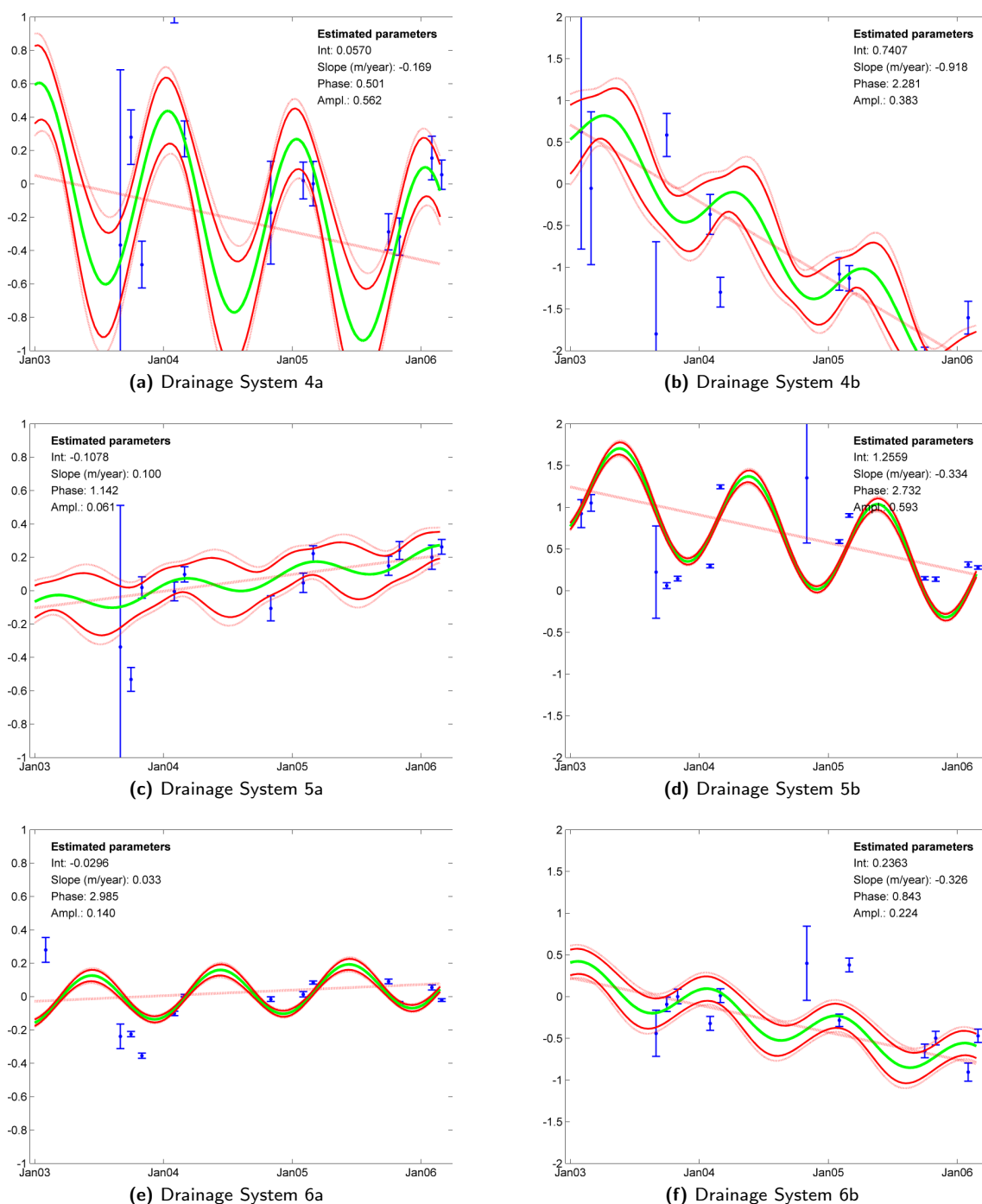


Figure B.4: Elevation change time series for drainage systems 4 to 6 based on ICESat data. Units of vertical axis are in meter. The letters a and b stand for above and below 2000 meter respectively. The time series are computed according to processing strategy 1d, see table 6.1. The estimated trend (straight dotted line) is computed using all available laser campaigns. However, due to the used processing strategy mostly the values of the first laser campaign are out of range. The solid green line is the trend plus the seasonal cycle. The solid and dotted red curve represents the 95%- and 99%-confidence regions.

Appendix C

Time series GRACE

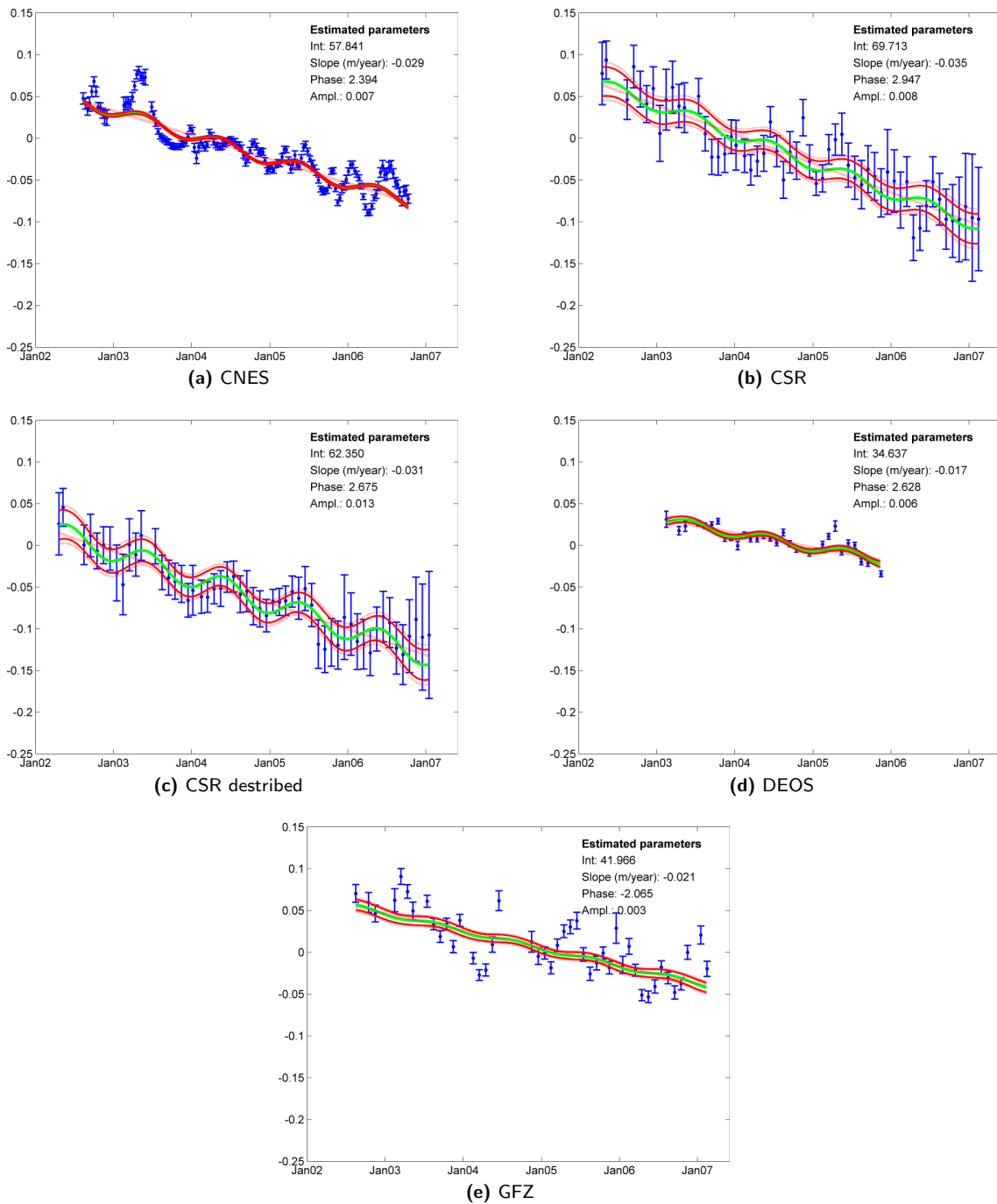


Figure C.1: Time series of all used GRACE solutions for the northern part of Greenland. This region is defined as the combination of the drainage systems 1, 2 and 6, see figure 4.11. The variations are expressed in terms of variations of thickness of an equivalent water layer, with units in meters. For spatial smoothing a Gaussian filter with a half-width of 500 km is used. Time series are corrected for PGR, see also table 5.3 and table 5.4. The estimated trend is represented as the straight dotted line. The solid green line is the trend plus the seasonal cycle. The solid and dotted red curve represents the 95%- and 99%-confidence regions.

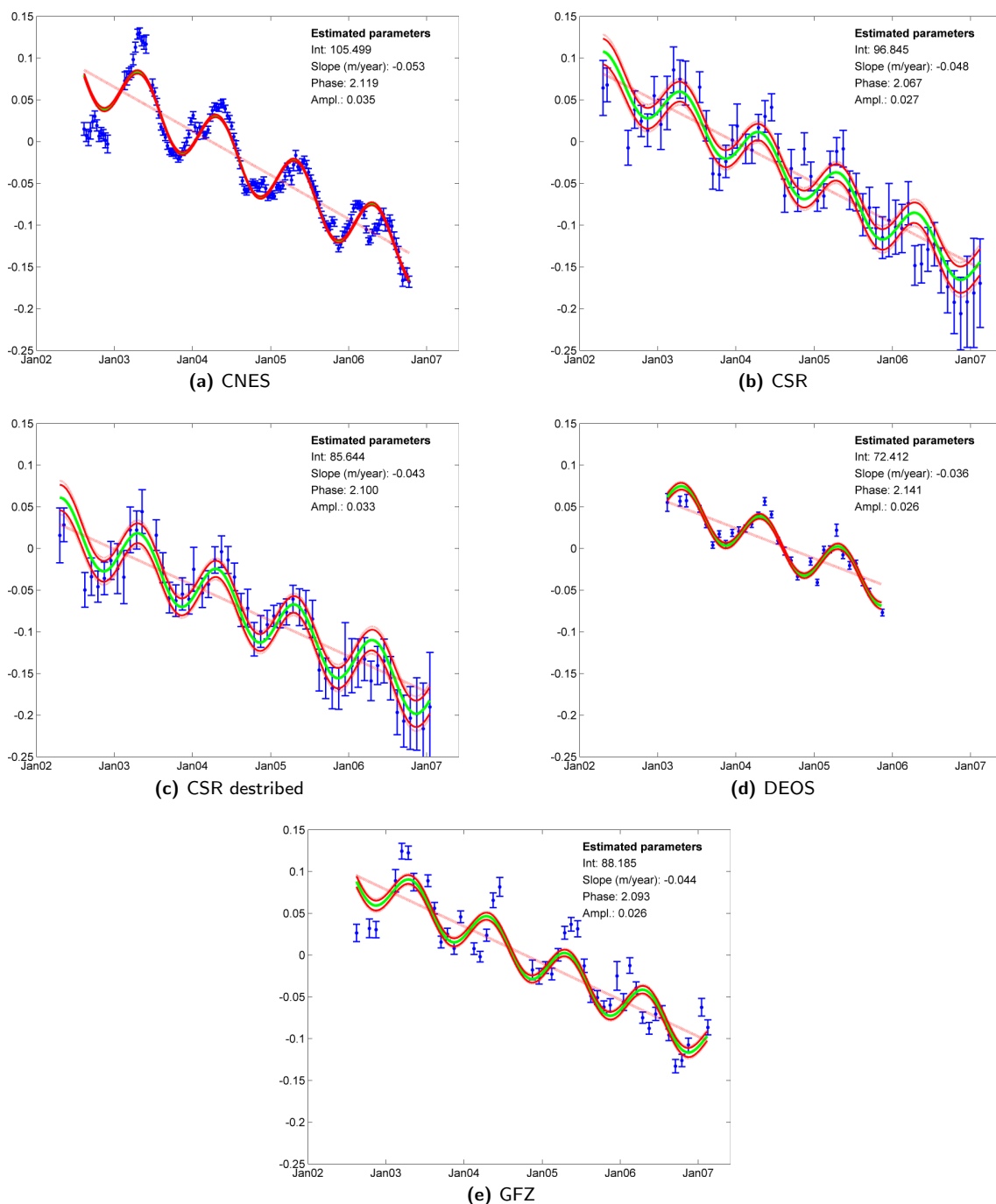


Figure C.2: Time series of all used GRACE solutions for the southern part of Greenland. This region is defined as the combination of the drainage systems 3, 4 and 5, see figure 4.11. The variations are expressed in terms of variations of thickness of an equivalent water layer, with units in meters. For spatial smoothing a Gaussian filter with a half-width of 500 km is used. Time series are corrected for PGR, see also table 5.3 and table 5.4. The estimated trend is represented as the straight dotted line. The solid green line is the trend plus the seasonal cycle. The solid and dotted red curve represents the 95%- and 99%-confidence regions.

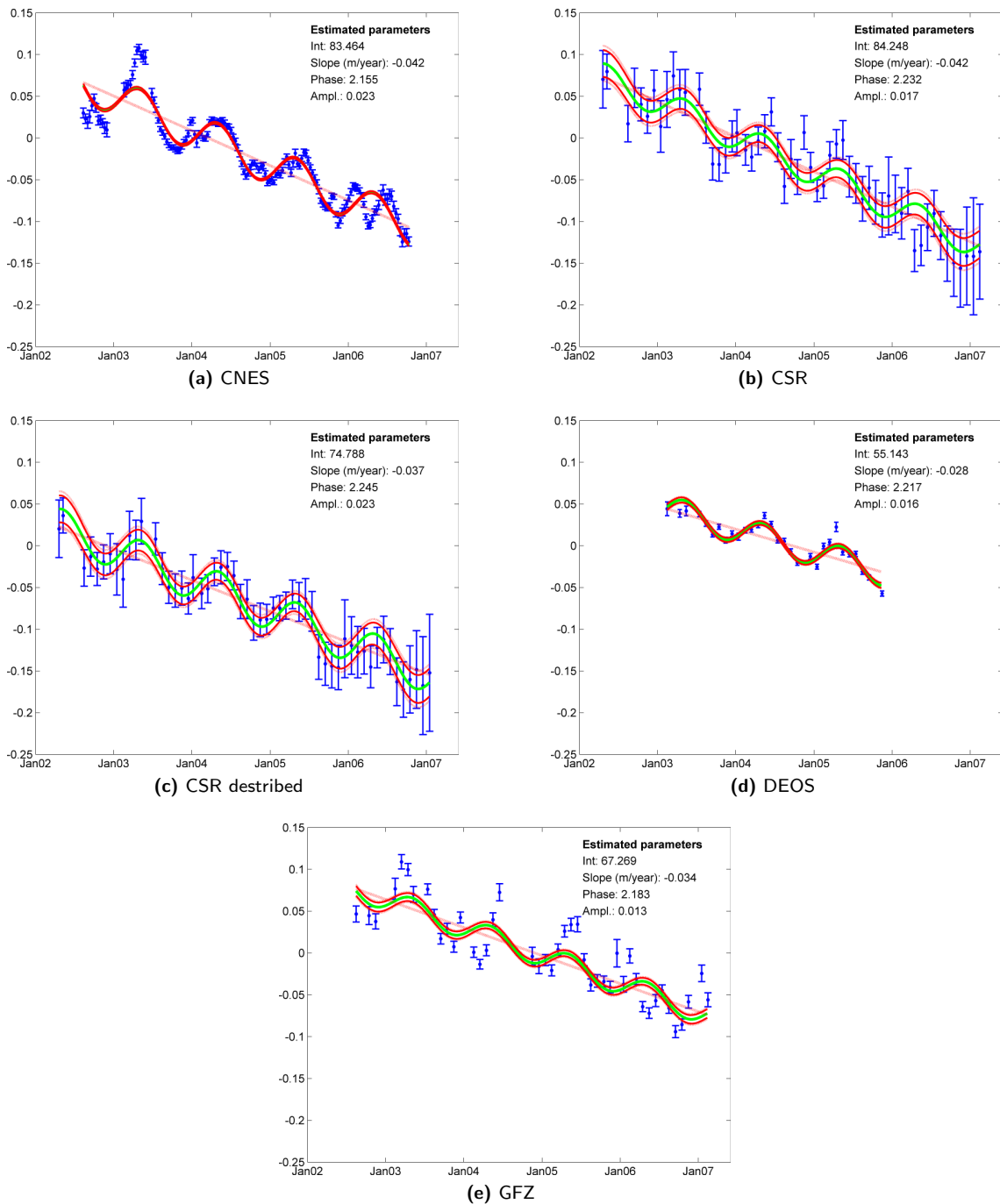


Figure C.3: Time series of all used GRACE solutions for whole Greenland. The variations are expressed in terms of variations of thickness of an equivalent water layer, with units in meters. For spatial smoothing a Gaussian filter with a half-width of 500 km is used. Time series are corrected for PGR, see also table 5.3 and table 5.4. The estimated trend is represented as the straight dotted line. The solid green line is the trend plus the seasonal cycle. The solid and dotted red curve represents the 95%- and 99%-confidence regions.

Appendix D

Time series joint inversion

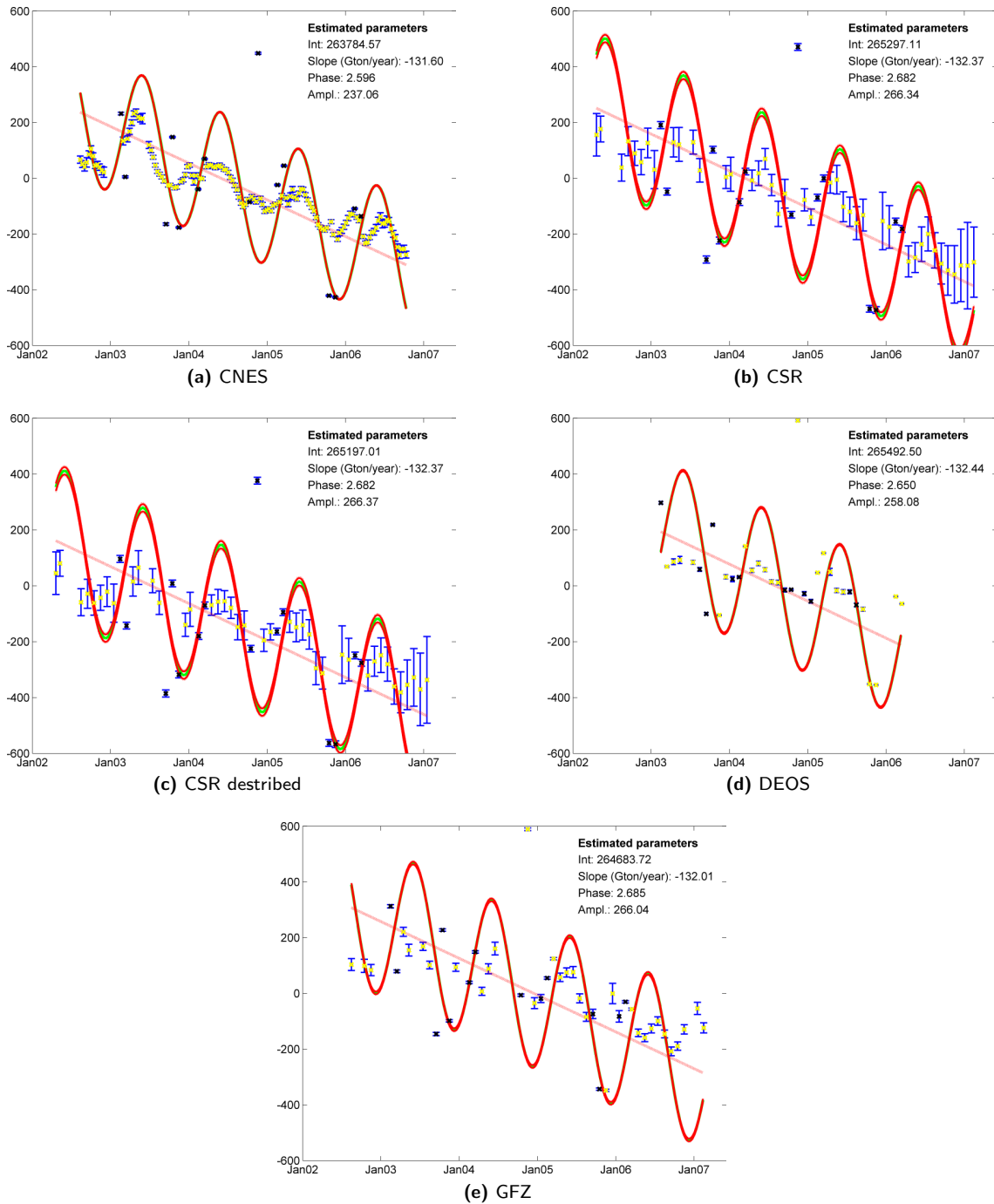


Figure D.1: Time series of the whole of Greenland based on joint inversion of the ICESat dataset (all releases + N -sigma thresholding applied) and all GRACE solutions. Here no variance component estimation is applied to estimate the relative weights between both datasets. The vertical axes are in terms of gigatons. For spatial smoothing of the GRACE data a Gaussian filter with a half-width of 500 km is used. Time series are corrected for PGR. The yellow crosses mark the epochs for which only GRACE data is available. The black crosses mark the epochs for which both ICESat and GRACE data is available. The estimated trend is represented as the straight dotted line. The solid green line is the trend plus the seasonal cycle. The solid and dotted red curve represents the 95%- and 99%-confidence regions.

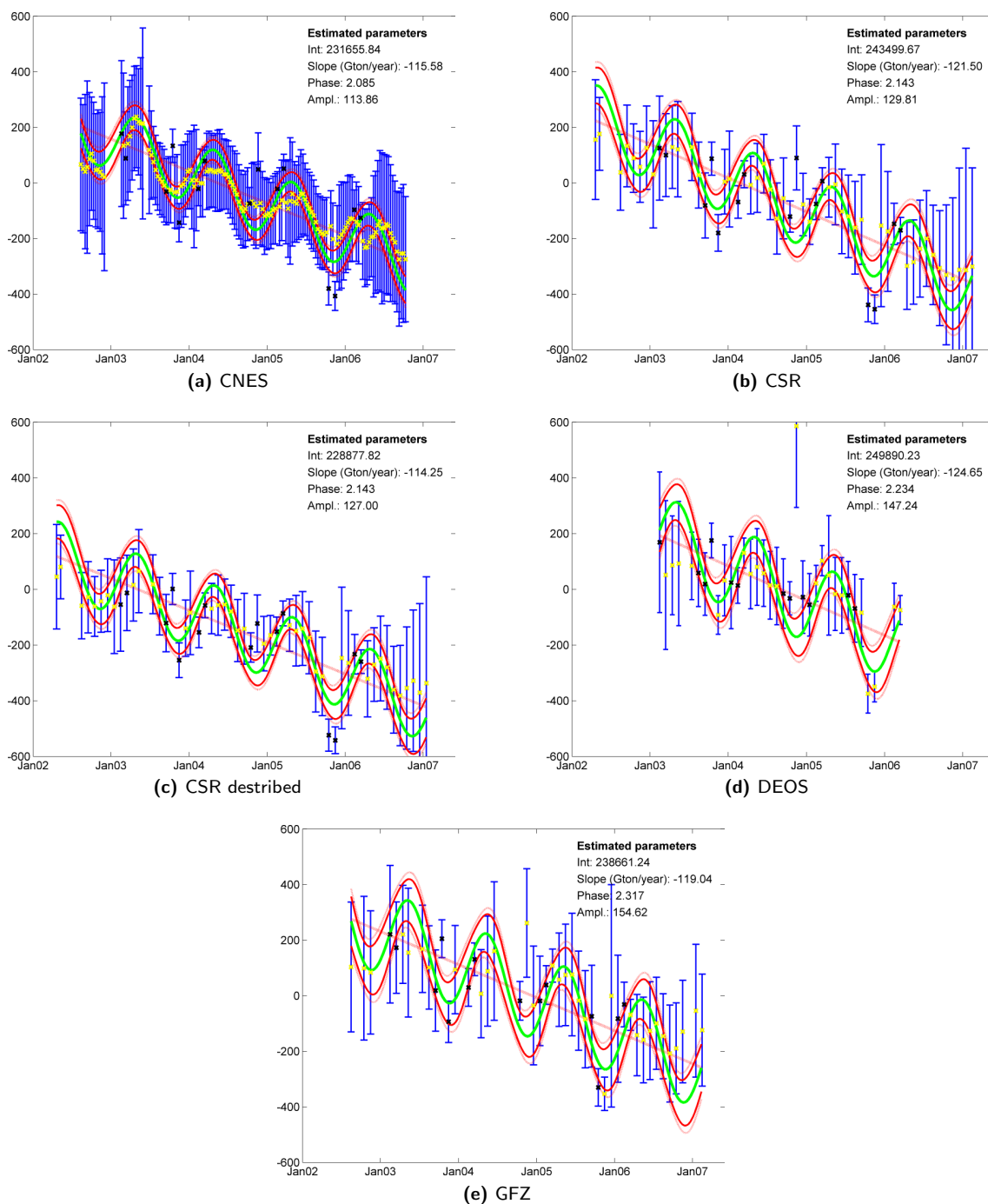


Figure D.2: Time series of the whole of Greenland based on joint inversion of the ICESat dataset (all releases + N -sigma thresholding applied) and all GRACE solutions. Here variance component estimation is applied to estimate the relative weights between both datasets. The vertical axes are in terms of gigatons. For spatial smoothing of the GRACE data a Gaussian filter with a half-width of 500 km is used. Time series are corrected for PGR. The yellow crosses mark the epochs for which only GRACE data is available. The black crosses mark the epochs for which both ICESat and GRACE data is available. The estimated trend is represented as the straight dotted line. The solid green line is the trend plus the seasonal cycle. The solid and dotted red curve represents the 95%- and 99%-confidence regions.

Bibliography

- [1] J. B. Abshire, X. Sun, H. Riris, J. M. Sirota, J. F. McGarry, S. Palm, D. Yi, and P. Liiva. Geoscience Laser Altimeter System (GLAS) on the ICESat Mission: On-orbit measurement performance. *Geophysical Research Letters*, 32:21–+, November 2005.
- [2] R. B. Alley, P. U. Clark, P. Huybrechts, and I. Joughin. Ice-Sheet and Sea-Level Changes. *Science*, 310:456–460, October 2005.
- [3] S. Bettadpur. Level-2 Gravity Field Product User Handbook. Technical report, Center for Space Research, University of Texas at Austin, 2007.
- [4] S. Bettadpur. *UTCSR Level-2 Processing Standards Document For Level-2 Product Release 0004, Gravity Recovery and Climate Experiment*. Center for Space Research, University of Texas at Austin, rev. 3.1 (draft), grace 327-742 (csr-gr-03-03) edition, 2007.
- [5] R. Biancale, J. M. Lemoine, S. Loyer, S. Bruinsma, F. Perosanz, J.-C. Marty, M. Sarrailh, N. Vales, and Balmino G. Monitoring variations of the geoid every 10 days from GRACE and LAGEOS satellite missions. *Geophysical Research Abstracts*, 8(05546), 2006.
- [6] A. C. Brenner, C. Bentley, B.M. Csatho, D.J. Harding, M.A. Hofton, J. Minster, L. Roberts, J.L. Saba, R. Schutz, R.H. Thomas, D. Yi, and H.J. Zwally. Derivation of range and range distributions from laser pulse waveform analysis for surface elevations, roughness, slope, and vegetation heights. Algorithm theoretical basis document. Version 4.1. Technical report, Goddard Space Flight Center, September 2003.
- [7] A. Cazenave and R. S. Nerem. Present-day sea level change: Observations and causes. *Reviews of Geophysics*, 42:3001–+, July 2004.
- [8] J. L. Chen, C. R. Wilson, R. J. Eanes, and R. S. Nerem. Geophysical interpretation of observed geocenter variations. *Journal of Geophysical Research*, 104:2683–2690, 1999.
- [9] J. L. Chen, C. R. Wilson, and B. D. Tapley. Satellite Gravity Measurements Confirm Accelerated Melting of Greenland Ice Sheet. *Science*, 313:1958–1960, September 2006.
- [10] J. A. Church, et. al. *Climate Change 2001: The Scientific Basis*. Cambridge Univ. Press, 2001.
- [11] C. H. Davis, C. A. Kluever, and B. J. Haines. Elevation Change of the Southern Greenland Ice Sheet. *Science*, 279:2086–+, March 1998.
- [12] P. G. Ditmar. AE4-E10: Inverse Problems, Lecture notes. Digital media., 2007.
- [13] P. G. Ditmar. AE4-E11: Satellite Gravity and the Geosphere, Lecture notes. Digital media., 2007.
- [14] G. Ekström, M. Nettles, and V. C. Tsai. Seasonality and Increasing Frequency of Greenland Glacial Earthquakes. *Science*, 311:1756–1758, March 2006.
- [15] GeoForschungsZentrum. Science objectives and applications. (Accessed September, 2007), <<http://www.gfz-potsdam.de/grace/science/objectives.html>>.

- [16] GLOBE Task Team & others. *The Global Land One-kilometer Base Elevation (GLOBE) Digital Elevation Model, Version 1.0. Digital data base on the World Wide Web and CD-ROMs.*, 1999.
- [17] GLOBE Task Team and others (Hastings, David A., Paula K. Dunbar, Gerald M. Elphinstone, Mark Bootz, Hiroshi Murakami, Hiroshi Maruyama, Hiroshi Masaharu, Peter Holland, John Payne, Nevin A. Bryant, Thomas L. Logan, J.-P. Muller, Gunter Schreier, and John S. MacDonald). The global land one-kilometer base elevation (globe) digital elevation model, version 1.0. digital data base on the world wide web (url: <http://www.ngdc.noaa.gov/mgg/topo/globe.html>) and cd-roms., 1999.
- [18] B. Gunn. Glaciers of antarctica. (Accessed June, 2007), <<http://www.rosssea.info/glaciers.html>>.
- [19] S.-C. Han, C. K. Shum, C. Jekeli, C.-Y. Kuo, C. Wilson, and K.-W. Seo. Non-isotropic filtering of GRACE temporal gravity for geophysical signal enhancement. *Geophysical Journal International*, 163:18–25, October 2005.
- [20] E. Hanna, P. Huybrechts, I. Janssens, J. Cappelen, K. Steffen, and A. Stephens. Runoff and mass balance of the Greenland ice sheet: 1958-2003. *Journal of Geophysical Research (Atmospheres)*, 110:13108–+, July 2005.
- [21] W. A. Heiskanen and H. Moritz. *Physical geodesy*. San Francisco, W. H. Freeman [1967], 1967.
- [22] M. M. Helsen, R. S. W. van de Wal, M. R. van den Broeke, W. J. van de Berg, E. van Meijgaard, and C. H. Davis. Effect of firn depth and density variations on ice sheet elevation changes in Antarctica. *European Geosciences Union 2007*, 2007.
- [23] I. M. Howat, I. Joughin, and T. A. Scambos. Rapid changes in ice discharge from Greenland outlet glaciers. *Science*, 315(5818):1559 – 1561, March 2007.
- [24] O. M. Johannessen, K. Khvorostovsky, M. W. Miles, and L. P. Bobylev. Recent Ice-Sheet Growth in the Interior of Greenland. *Science*, 310:1013–1016, November 2005.
- [25] I. Joughin, W. Abdalati, and M. Fahnestock. Large fluctuations in speed on Greenland's Jakobshavn Isbrae glacier. *Nature*, 432(7017):608–610, December 2004.
- [26] I. Joughin, S. Das, I. Howat, and T. Moon. Seasonal behavior of lakes on the surface of the Greenland Ice Sheet. *AGU Fall Meeting Abstracts*, pages A4+, December 2006.
- [27] R. Klees. Gravity Field and Geoid Determination, part 1-3 (Lecture notes). Digital media., 2006.
- [28] R. Klees, E. A. Zapreeva, H. C. Winsemius, and H. H. G. Savenije. The bias in GRACE estimates of continental water storage variations. *Hydrology and Earth System Sciences*, 11:1227–1241, May 2007.
- [29] W. B. Krabill, W. Abdalati, Frederick E. B., Manizade S. S., Martin C. F., Sonntag J. G., Swift R. N., Thomas R. H., and Yungel J. G. Aircraft laser altimetry measurement of elevation changes of the greenland ice sheet: technique and accuracy assessment. *Journal of Geodynamics*, 34(3):357–376, October 2002.
- [30] W. B. Krabill, W. Abdalati, E. Frederick, S. Manizade, C. Martin, J. Sonntag, R. Swift, R. Thomas, W. Wright, and J. Yungel. Greenland Ice Sheet: High-Elevation Balance and Peripheral Thinning. *Science*, 289:428–430, July 2000.
- [31] W. B. Krabill, E. Hanna, P. Huybrechts, W. Abdalati, J. Cappelen, B. Csatho, E. Frederick, S. Manizade, C. Martin, J. Sonntag, R. Swift, R. Thomas, and J. Yungel. Greenland Ice Sheet: Increased coastal thinning. *Geophysical Research Letters*, 31:24402–+, December 2004.
- [32] Jet Propulsion Laboratory. Images of jpl spacecraft, artist's concept of grace. (Accessed September, 2007), <http://www.jpl.nasa.gov/images/spacecraft/grace_083002_caption.html>.
- [33] X. Liu, P. Ditmar, Q. Zhao, and R. Klees. An acceleration approach for gravity field modeling from GRACE range measurements. (in preparation), 2007.

- [34] S. B. Luthcke, H. J. Zwally, W. Abdalati, D. D. Rowlands, R. D. Ray, R. S. Nerem, F. G. Lemoine, J. J. McCarthy, and D. S. Chinn. Recent Greenland Ice Mass Loss by Drainage System from Satellite Gravity Observations. *Science*, 314:1286–1289, December 2006.
- [35] The Matworks. Mapping toolbox, gradientm. (Accessed September, 2007), <www.mathworks.com/access/helpdesk/help/toolbox/map/gradientm.html>.
- [36] NASA. Glas image gallery. (Accessed April, 2007), <<http://glas.gsfc.nasa.gov/gallery.html>>.
- [37] NASA. World wind. (Accessed March, 2007), <<http://worldwind.arc.nasa.gov/>>.
- [38] NSIDC. Data releases. (Accessed April, 2007), <<http://www.nsidc.org/data/icesat/detailed-disclaimer.html>>.
- [39] NSIDC. Gla12 records. (Accessed February, 2007), <<http://nsidc.org/data/docs/daac/glas-altimetry/gla12-records.html>>.
- [40] NSIDC. Glas altimetry product usage guidance. (Accessed April, 2007), <<http://nsidc.org/data/docs/daac/glas-altimetry/usage.html>>.
- [41] NSIDC. Tools. (Accessed February, 2007), <<http://nsidc.org/data/icesat/tools.html>>.
- [42] D. G. Simons P. J. G. Teunissen and C. C. J. M. Tiberius. Probability and observation theory, 2005. lecture notes.
- [43] W. R. Peltier. Global Glacial Isostasy and the Surface of the Ice-Age Earth: The ICE-5G (VM2) Model and GRACE. *Annual Review of Earth and Planetary Sciences*, 32:111–149, May 2004.
- [44] G. Ramillien, A. Lombard, A. Cazenave, E. R. Ivins, M. Llubes, F. Remy, and R. Biancale. Inter-annual variations of the mass balance of the Antarctica and Greenland ice sheets from GRACE. *Global and Planetary Change*, 53:198–208, September 2006.
- [45] E. Rignot and P. Kanagaratnam. Changes in the Velocity Structure of the Greenland Ice Sheet. *Science*, 311:986–990, February 2006.
- [46] E. Rignot and R. H. Thomas. Mass Balance of Polar Ice Sheets. *Science*, 297:1502–1506, Augustus 2002.
- [47] M. Rodell, P. R. Houser, U. Jambor, J. Gottschalck, K. Mitchell, C.-J. Meng, K. Arsenault, B. Cosgrove, J. Radakovich, M. Bosilovich, J. K. Entin*, J. P. Walker, D. Lohmann, and D. Toll. The Global Land Data Assimilation System. *Bulletin of the American Meteorological Society*, vol. 85, Issue 3, pp.381-394, 85:381–394, March 2004.
- [48] D. D. Rowlands, S. B. Luthcke, S. M. Klosko, F. G. R. Lemoine, D. S. Chinn, J. J. McCarthy, C. M. Cox, and O. B. Anderson. Resolving mass flux at high spatial and temporal resolution using GRACE intersatellite measurements. *Geophysical Research Letters*, 32:4310–+, February 2005.
- [49] I. Sasgen, Z. Martinec, and K. Fleming. Wiener optimal filtering of GRACE data. *Studia Geophysica et Geodaetica*, 50(4):499–508, October 2006.
- [50] R. Schmidt. Static Field Geopotential Coefficients estimated from Satellite Data only. Digital media., 2007. GFZ Potsdam GRACE Science Data System, Oberpfaffenhofen, Germany.
- [51] E. J. O. Schrama and P. N. A. M. Visser. Accuracy assessment of the monthly GRACE geoids based upon a simulation. *Journal of Geodesy*, 81:67–80, January 2007.
- [52] B. E. Schutz, H. J. Zwally, C. A. Shuman, D. Hancock, and J. P. DiMarzio. Overview of the ICESat Mission. *Geophysical Research Letters*, 32:21–+, November 2005.
- [53] J. M. Sirota, S. Bae, P. Millar, D. Mostofi, C. Webb, B. Schutz, and S. Luthcke. The transmitter pointing determination in the Geoscience Laser Altimeter System. *Geophysical Research Letters*, 32:22–+, November 2005.

- [54] J. D. Spinhirne, S. P. Palm, W. D. Hart, D. L. Hlavka, and E. J. Welton. Cloud and aerosol measurements from GLAS: Overview and initial results. *Geophysical Research Letters*, 32:22–+, September 2005.
- [55] S. Swenson and J. Wahr. Methods for inferring regional surface-mass anomalies from Gravity Recovery and Climate Experiment (GRACE) measurements of time-variable gravity. *Journal of Geophysical Research (Solid Earth)*, 107:3–1, September 2002.
- [56] S. Swenson and J. Wahr. Post-processing removal of correlated errors in GRACE data. *Geophysical Research Letters*, 33:8402–+, April 2006.
- [57] S. Swenson, J. Wahr, and P. C. D. Milly. Estimated accuracies of regional water storage variations inferred from the Gravity Recovery and Climate Experiment (GRACE). *Water Resources Research*, 39:11–1, August 2003.
- [58] GFZ Potsdam GRACE Science Data System, 2007. (Accessed May, 2007), <http://www.gfz-potsdam.de/pb1/op/grace/results/index_RESULTS.html>.
- [59] B. Tapley, J. Ries, S. Bettadpur, D. Chambers, M. Cheng, F. Condi, B. Gunter, Z. Kang, P. Nagel, R. Pastor, T. Pekker, S. Poole, and F. Wang. GGM02 - An improved Earth gravity field model from GRACE. *Journal of Geodesy*, 79:467–478, November 2005.
- [60] P. J. G. Teunissen. *Network quality control*. Series on Mathematical Geodesy and Positioning. Vereniging voor Studie- en Studentenbelangen te Delft, 2006.
- [61] P. J. G. Teunissen and A. R. Amiri-Simkooei. Least-squares variance component estimation. *Journal of Geodesy*, pages 39–+, May 2007.
- [62] R. Thomas, E. Frederick, W. Krabill, S. Manizade, and C. Martin. Progressive increase in ice loss from Greenland. *Geophysical Research Letters*, 33:10503–+, May 2006.
- [63] R. H. Thomas. Remote sensing reveals shrinking Greenland ice sheet. *EOS Transactions*, 82:369–369, 2001.
- [64] R. H. Thomas, W. Abdalati, E. Frederick, W. B. Krabill, S. Manizade, and K. Steffen. Investigation of surface melting and dynamic thinning on Jakobshavn Isbrae, Greenland. *Journal of Glaciology*, 49:231–239, 2003.
- [65] I. Velicogna and J. Wahr. A method for separating Antarctic postglacial rebound and ice mass balance using future ICESat Geoscience Laser Altimeter System, Gravity Recovery and Climate Experiment, and GPS satellite data. *Journal of Geophysical Research (Solid Earth)*, 107, October 2002.
- [66] I. Velicogna and J. Wahr. Greenland mass balance from GRACE. *Geophysical Research Letters*, 32:18505–+, September 2005.
- [67] I. Velicogna and J. Wahr. Acceleration of Greenland ice mass loss in spring 2004. *Nature*, 443:329–331, September 2006.
- [68] I. Velicogna and J. Wahr. Measurements of Time-Variable Gravity Show Mass Loss in Antarctica. *Science*, 311:1754–1756, March 2006.
- [69] I. Velicogna and J. Wahr. Seasonal and long term ice mass variations from GRACE. presentation at IUGG XXIV 2007, July 2007.
- [70] J. Wahr, M. Molenaar, and F. Bryan. Time variability of the Earth's gravity field: Hydrological and oceanic effects and their possible detection using GRACE. *Journal of Geophysical Research*, 103:30205–30230, December 1998.
- [71] J. Wahr, S. Swenson, V. Zlotnicki, and I. Velicogna. Time-variable gravity from GRACE: First results. *Geophysical Research Letters*, 31:11501–+, June 2004.
- [72] J. Wahr, D. Wingham, and C. Bentley. A method of combining ICESat and GRACE satellite data to constrain Antarctic mass balance. *Journal of Geophysical Research*, 105:16279–16294, 2000.

- [73] A. Weidick, N. Mikkelsen, C. Mayer, and S. Podlech. Jakobshavn Isbræ, West Greenland: the 2002-2003 collapse and nomination for the UNESCO World Heritage List. *Geological Survey of Denmark and Greenland Bulletin*, 4:85–88, 2003.
- [74] D. J. Wingham, A. J. Ridout, R. Scharroo, R. J. Arthern, and C. K. Shum. Antarctic Elevation Change from 1992 to 1996. *Science*, 282:456–+, October 1998.
- [75] D. J. Wingham, A. Shepherd, A. Muir, and et al. Mass balance of the Antarctic ice sheet. *Royal Society of London Philosophical Transactions Series A*, 364:1627–1635, July 2006.
- [76] X. Wu, M. M. Watkins, E. R. Ivins, R. Kwok, P. Wang, and J. M. Wahr. Toward global inverse solutions for current and past ice mass variations: Contribution of secular satellite gravity and topography change measurements. *Journal of Geophysical Research (Solid Earth)*, 107:2291–+, November 2002.
- [77] H. J. Zwally, M. B. Giovinetto, J. Li, H. G. Cornejo, M. A. Beckley, A. C. Brenner, J. L. Saba, and D. Yi. Mass changes of the Greenland and Antarctic ice sheets and shelves and contributions to sea-level rise: 1992-2002. *Journal of Glaciology*, 51:509–527, 2005.
- [78] H. J. Zwally and L. Jun. Seasonal and interannual variations of firn densification and ice-sheet surface elevation at Greenland summit. *Journal of Glaciology*, 48:199–207, 2002.
- [79] H. J. Zwally, B. Schutz, W. Abdalati, J. Abshire, C. Bentley, A. Brenner, J. Bufton, J. Dezio, D. Hancock, D. Harding, T. Herring, B. Minster, K. Quinn, S. Palm, J. Spinhirne, and R. Thomas. ICESat's laser measurements of polar ice, atmosphere, ocean, and land. *Journal of Geodynamics*, 34(3):405–445(41), October 2002.
- [80] H. J. Zwally, R. Schutz, C. Bentley, J. Bufton, T. Herring, B. Minster, J. Spinhirne, and R. Thomas. GLAS/ICESat L2 Antarctic and Greenland Ice Sheet Altimetry Data V001. Digital media.
- [81] H. J. Zwally and C. A. Shuman. *ICESat brochure*. NASA/GSFC, 2002. (Accessed 19 December, 2006), <<http://icesat.gsfc.nasa.gov/>>.

